UNIVERSITY OF CALIFORNIA SAN DIEGO

SAN DIEGO STATE UNIVERSITY

# Fundamental Investigation of Novel Graphene-Glassy Carbon (GrGC) MetaMaterial through Synthesis, Characterizations, Molecular Dynamics Simulation, and Neural Interface Testbed

A dissertation submitted in partial satisfaction

of the requirements for the degree Doctor of Philosophy

in

Engineering Science (Bioengineering)

by

Surabhi Nimbalkar

Committee in charge:

University of California San Diego

Professor Todd Coleman, Co-Chair

Professor Gert Cauwenberghs

Professor Darren Lipomi

San Diego State University

Professor Sam Kassegne, Chair

Professor Parag Katira

2021

The Dissertation of Surabhi Nimbalkar is approved, and it is acceptable in quality and form for publication on microfilm and electronically:

---

---

---

---

Co-Chair

---

Chair

University of California San Diego

San Diego State University

2021

# TABLE OF CONTENTS

Dissertation Approval Page ..... iii

Table of Contents ..... iv

List of Figures ..... v

List of Tables ..... vii

Acknowledgments ..... viii

Vita ..... x

Abstract of the Dissertation ..... xii

Chapter I: Introduction ..... 1

Chapter II: Ultra-capacitive carbon neural probe allows simultaneous long-term electrical stimulations and high-resolution neurotransmitter detection ..... 11

Chapter III: Glassy carbon microelectrodes minimize induced voltages, mechanical vibrations, and artifacts in magnetic resonance imaging ..... 45

Chapter IV: Novel Graphene-Glassy Carbon (GrGC) MetaMaterial Synthesis: Fundamental Investigation through Experimental Validation and Molecular Dynamics Simulation ..... 69

Chapter V: Graphene on Glassy Carbon Microelectrodes Demonstrate Long-Term Structural and Functional Stability in Neurophysiological Recording and Stimulation ..... 98

Chapter VI: Discussion ..... 135

Appendix ..... 146

# LIST OF FIGURES

Figure 1.1 Graphene- Glassy carbon microstructure synthesis by pyrolysis. ..... 4

Figure 2.1 Lithography steps for microfabricating glassy carbon (GC) microstructures on a polymer ..... 15

Figure 2.2 Details of the GC neural probe ..... 21

Figure 2.3 Details of fracture planes following mechanical testing of GC and thin-film metal probes ..... 22

Figure 2.4 Electrochemical characterization of GC electrodes. ..... 26

Figure 2.5 Equivalent Circuit for GC electrode. ..... 27

Figure 2.6 Effect of accelerated aging through bi-phasic pulsing in PBS for 42 days (1000 hours). ..... 28

Figure 2.7 SEM and AFM image of microelectrode surface ..... 28

Figure 2.8 GC microelectrodes array implantation site on the left forelimb sensory cortex with electrical stimulation on the skin of the right wrist ..... 30

Figure 2.9 Color plot showing changes in current following 20 nM DA injection in PBS in-vitro ..... 32

Figure 3.1 Probes with GC and Pt ground microelectrodes of 2cm x 1cm geometry and UV Photo lithography steps for microfabrication of GC microelectrodes ..... 50

Figure 3.2 The experimental setup used for MR imaging ..... 52

Figure 3.3 Details of the experimental setup for the measurement of gradient induced vibrations in the field of a permanent magnet 1.5T MRI system ..... 54

Figure 3.4 Experimental setup to investigate the dependence of microelectrode materials on the induced eddy currents ..... 55

Figure 3.5 Pt electrode showed darkened rectangular shape along the width of Pt electrode in the axial view as compared to the GC electrode ..... 57

Figure 3.6 Strong B1-field distortions are observed for the Pt for high 11.7 T MR scanner ..... 58

Figure 3.7 Comparison of the simulated behavior for the 2cm x 1cm rectangular GC and Pt ground microelectrodes ..... 59

Figure 3.8 Measurement results from induction experiments. ..... 61

Figure 3.9 Measurement results of vibration measurements and their comparison to theoretical values ..... 63

Figure 4.1 GC Microstructure and STEM Image ..... 72

Figure 4.2 Synthesis of Metamaterial GrGC microstructure ..... 75

Figure 4.3 MD Simulation box and setup ..... 77
Figure 4.4 SEM and STEM images of GrGC microstructure ..... 81
Figure 4.5 STEM EELS analysis of GrGC Metamaterial ..... 82
Figure 4.6 HAADF imaging of GrGC microstructure ..... 83
Figure 4.7 Raman spectrum comparison of GrGC Vs GC ..... 84
Figure 4.8 FTIR spectrum comparison of GrGC Vs GC ..... 85
Figure 4.9 Overview of Evolution of GrGC nanostructure in simulation box ..... 87
Figure 4.10 GrGC evolution ..... 88
Figure 4.11 GrGC Microstructure models ..... 88
Figure 4.12 Functional groups of GrGC microstructure ..... 89
Figure 4.13 Evolution of GC Metamaterial ..... 92
Figure 4.14 GC nanostructure ..... 93
Figure 5.1 Graphene -Glassy Carbon microelectrode array ..... 102
Figure 5.2 Schematic of setup for in vivo recording and region of interest for fluorescent imaging ..... 108
Figure 5.3 Adhesive tape peeling test on microstructure ..... 112
Figure 5.4 SEM, STEM, and AFM images of the microstructure ..... 113
Figure 5.5 FTIR and Raman spectra of GrGC Metamaterial ..... 114
Figure 5.6 Electrochemical impedance spectrum, cyclic voltammogram, Voltage transient response of GrGC microstructure ..... 115
Figure 5.7 Acute in vivo validation of the Gr on GC device consistency ..... 117
Figure 5.8 Acute stimulation in vivo validation of the Gr on GC device ..... 119
Figure 5.9 Chronic in vivo validation of the Gr on GC microelectrode device stability ..... 119
Figure 5.10 Representative GFAP and IBA-1 images. ..... 120
Figure 5.11 Gr on GC microelectrode surface morphology post explant after 18 weeks ..... 121
Figure 5.12 Comparison of magnetic resonance imaging artifact of Gr on GC and GC microelectrode. 128
Figure 5.13 DA Detection using Gr on GC microelectrode ..... 129

# LIST OF TABLES

Table 2.1 Summary of key parameters in voltage transients for GC and Pt microelectrodes..... 27

Table 2.2 Average SNR value and impedance of GC microelectrodes arrays ..... 31

Table 6.1 Comparison between GrGC Vs GC material properties and testbed results..... 140

# ACKNOWLEDGEMENTS

I would like to thank my Ph.D. advisor, Dr. Sam Kassegne for supporting my doctoral degree research and for the constant motivation. I would also like to thank my co-advisor, Dr. Todd Coleman, for his encouragement and guidance. I would like to acknowledge my committee members Dr. Gert Cauwenberghs, Dr. Darren Lipomi, and Dr. Parag Katira for their advice and suggestions on the research. I thank all my mentors, mentees, collaborators, and lab-mates of NanoFab Lab SDSU for their endless support throughout this journey.

Chapter 2, in full, is a reprint of materials as it appears in **Nimbalkar S**, Castagnola E, Balasubramani A, Scarpellini A, Samejima S, Khorasani A, Boissenin A, Thongpang S, Moritz C and Kassegne S, 2018. "Ultra-capacitive carbon neural probe allows simultaneous long-term electrical stimulations and high-resolution neurotransmitter detection." Scientific Reports, 8(1), pp.1-14. The dissertation author was the co-primary author of this paper.

Chapter 3, in full, is a reprint of materials as it appears in **Nimbalkar S**, Fuhrer E, Silva P, Nguyen T, Sereno M, Kassegne S, Korvink J. "Glassy carbon microelectrodes minimize induced voltages, mechanical vibrations, and artifacts in magnetic resonance imaging." Microsystems & nanoengineering. 2019 Nov 18;5(1):1-1. The dissertation author was the co-first author of this paper.

Chapter 4, in partial, is in preparation or submission for publication as: **Nimbalkar S**, Montgomery-Walsh R, Kassegne S. "Novel Graphene-Glassy Carbon (GrGC) MetaMaterial Synthesis: Fundamental Investigation through Experimental Validation and Molecular Dynamics Simulation." The dissertation author is the primary author of this manuscript.

Chapter 5, in partial, is in submission or revision for publication as: **Nimbalkar S**, Samejima S, Hunt T, Nunez O, Moritz C, Kassegne S. "Graphene on Glassy Carbon Microelectrodes Demonstrate Long-

Term Structural and Functional Stability in Neurophysiological Recording and Stimulation." The dissertation author was the primary author of this chapter.

# VITA

| | |
|---|---|
| 2013 | Bachelor of Engineering, University of Pune, India |
| 2018 | Master of Science, Bioengineering, San Diego State University |
| 2017-2021 | Research Assistant, NSF-ERC Center for Neurotechnology, San Diego State University |
| 2021 | Doctor of Philosophy, Engineering Science (Bioengineering),<br>University of California San Diego and San Diego State University |

## PUBLICATIONS

**Nimbalkar S**, Montgomery-Walsh R, Galindo SL, Bunnell J, Kassegne S. "Novel Graphene-Glassy Carbon (GrGC) MetaMaterial Synthesis: Fundamental Investigation through Experimental Validation and Molecular Dynamics Simulation" (under preparation)

Montgomery-Walsh R, **Nimbalkar S**, Bunnell J, Galindo SL, Kassegne S. Molecular dynamics simulation of evolution of nanostructures and functional groups in glassy carbon under pyrolysis. Carbon. 2021 Oct 30;184:627-40.

**Nimbalkar S,** Samejima S, Dang V, Hunt T, Nunez O, Moritz C, Kassegne S. Graphene on glassy carbon microelectrodes demonstrate long-term structural and functional stability in neurophysiological recording and stimulation. Journal of Neural Engineering. 2021 Sep 22;18(5):056035.

Devi M, Vomero M, Fuhrer E, Castagnola E, Gueli C, **Nimbalkar S**, Hirabayashi M, Kassegne S, Stieglitz T, Sharma S. Carbon-based neural electrodes: promises and challenges. Journal of Neural Engineering. 2021 Aug 17.

Castagnola E, Thongpang S, Hirabayashi M, Nava G, **Nimbalkar S**, Nguyen T, Lara S, Moritz C, Kassegne S. "Glassy Carbon microelectrode arrays enable voltage-peak separated simultaneous detection of dopamine and serotonin using fast scan cyclic voltammetry." Analyst 146, no. 12 (2021): 3955-3970

Vahidi NW, Rudraraju S, Castagnola E, Cea C, **Nimbalkar S**, Hanna R, Arvizu R, Dayeh SA, Gentner TQ, Kassegne S. "Epi-intra neural probes with glassy carbon microelectrodes help elucidate neural coding and stimulus encoding in 3D volume of tissue". Journal of Neural Engineering. 2020.

**Nimbalkar S**, Fuhrer E, Silva P, Nguyen T, Sereno M, Kassegne S, Korvink J. "Glassy carbon microelectrodes minimize induced voltages, mechanical vibrations, and artifacts in magnetic resonance imaging." Microsystems & nanoengineering. 2019 Nov 18;5(1):1-1.

**Nimbalkar S**, Castagnola E, Balasubramani A, Scarpellini A, Samejima S, Khorasani A, Boissenin A, Thongpang S, Moritz C and Kassegne S, 2018. "Ultra-capacitive carbon neural probe allows simultaneous long-term electrical stimulations and high-resolution neurotransmitter detection." Scientific Reports, 8(1), pp.1-14.

Castagnola, E., Vahidi, N.W., **Nimbalkar, S**., Rudraraju, S., Thielk, M., Zucchini, E., Cea, C., Carli, S., Gentner, T.Q., Ricci, D. and Fadiga, L., 2018. In vivo dopamine detection and single unit recordings using intracortical glassy carbon microelectrode arrays. MRS advances, 3(29), p.1629.

# ABSTRACT OF THE DISSERTATION

Novel Graphene-Glassy Carbon (GrGC) MetaMaterial Synthesis: Fundamental Investigation through Experimental Validation, Molecular Dynamics Simulation, and Neural Interface Testbed

by

Surabhi Nimbalkar

Doctor of Philosophy in Engineering Science (Bioengineering)

University of California San Diego, 2021
San Diego State University, 2021

Professor Sam Kassegne, Chair
Professor Todd Coleman, Co-chair

There is a growing interest in the use of carbon and its allotropes for microelectrodes in neural probes because of their inertness, long-term electrical and electrochemical stability, and versatility. Building on that interest, we introduce a new electrode material system consisting of an ultra-thin mono layer of graphene (Gr) mechanically supported by a relatively thicker layer of glassy carbon (GC). Gr has impressive electrical and electrochemical properties. On the other hand, GC is one of carbon's important allotropes and consists of 3D microstructures of graphene fragments. Further, GC has exceptional chemical

inertness, good electrical properties, high electrochemical stability, purely capacitive charge injection, and fast surface electrokinetics coupled with lithography patternability. This makes GC an ideal candidate for addressing Gr's lack of out-of-plane rigidity through providing a matching sturdier and robust mechanical backing. Combining the strengths of these two allotropes of carbon, we introduce a new metamaterial Graphene- Glassy Carbon (GrGC) synthesis. We present the fabrication technology for the microelectrodes and the accompanying pattern transfer technology on flexible substrate and report on the bond between these two allotropes of carbon through FTIR, surface morphology through SEM, topography through AFM, and nanostructure study through molecular dynamics and STEM imaging. A long-term (18-weeks) *in vivo* study of the use of these *GrGC* microelectrodes assessed the quality of the ECoG-based neural signal recording and stimulation through electrophysiological measurements. The probes were demonstrated to be functionally and structurally stable over the 18-week period with minimal glial response – the longest reported so far for graphene-based microelectrodes

CHAPTER I

# Introduction

## 1.1 Carbon, the 'New' Material for Micro and Nanomanufacturing

While silicon has been dominant material of choice in the semi-conductor and the broad emerging micro and nanomanufacturing industries for sometimes now, carbon is fast emerging as a serious competitor. Looking ahead, with Moore's Law now significantly challenged in maintaining its validity in the silicon-dominated semi-conductor industry, the emergence of 2D materials like graphene is further laying the ground work for an industry where carbon will be among the most dominant materials.

Unlike its competition in the form of silicon, germanium, and the like, carbon's unique tunable mechanical and electronic properties help position it as a versatile material of choice for a variety of applications including as promising material in semi-conductor and energy storage technologies, specifically in supercapacitors, microelectrodes, batteries, fuel-cells, magnetic thin-films, and bio-chemical sensors [1-3]. Various allotropes of carbon are known for their unique characteristics that have further expanded the use of this important material. For example, graphene possesses excellent conductivity, large surface area, and in-plane stiffness [4], Q-carbon has excellent hardness and excellent strength [5,6], and glassy carbon has demonstrated superior electrochemistry [7-8]. Graphene, few-layer graphene (FLG), and graphene nanoribbons (GNR) are used in thermal phase change materials (PCM) for battery and energy storage application [9]. Additionally, modification of carbon electrodes has demonstrated improved chemical sensitivity foe bio-chemical sensing applications. In addition, multiwall carbon nanotube (MW-CNTs) modified glassy carbon electrodes have been used for detecting glucose oxide as non-enzymatic sensor, lactic acid, ascorbic acid, and NADH detection, further expanding the reach of carbon and its allotropes in the sensing discipline [10-12]. Further, carbon nanotubes (CNTs) grown on diamond like carbon (DLC) thin film have shown improved sensitivity and selectivity towards dopamine sensing [13].

Therefore, carbon's promise as a competitive engineering material is now well established and poised for even further expansion in the emerging are of micro and nanomanufacturing industry. Leveraging its current expansion and future potentials, there is still room for even more significant innovations in expanding the use of carbon and its allotropes.

## 1.2 Motivation

Among some of the most compelling application areas of carbon and its various allotropes, carbon's use as a probe material in devices that interface with tissues carries the most visible and impactful one. This is, of course, driven by carbon's (and its allotropes) chemical inertness, biocompatibility, good electrical conductivity, high charge injection capacity, and excellent long-term electrochemical stability [7-8, 21-22]. Carbon-based neural microelectrode arrays have been reported for neural electrical recording [14-16, 21-23], electrical stimulation [24-26], magnetic resonance compatibility [27], and neurotransmitter detection [28-30].

Further, the multimodality capability of carbon electrodes has raised interest in neurophysiological applications specially for long term implantation. This multi-modality includes ability to record electrical and electrochemical signals and to electrically stimulate tissues. However, in the same time, there is an increasing need of advanced microelectrode material in neural engineering applications that require a new generation of multimodal neural microelectrode arrays with electrochemical stability and sturdiness, excellent conductivity, high charge storage and injection capacity, and exceptional electrochemistry, a mixture of rare properties tough to be obtained from in a single material. In this dissertation, an argument is forwarded regarding the notion that a carbon material synthesized from various allotropes combining high charge storage capacity for energy storage application, high conductivity for superior signal to noise performance, and functional groups for improved electrochemical sensing in biosensors could be the answer to the current need in neural interface materials.

Among the various allotropes of carbon, graphene (Gr) and glassy carbon (GC) stand out in their potential in revolutionizing several industries including energy storage. Gr is a 2D monolayer material and is considered the gold-standard for electrical conductivity (1700 S/m) and has high in-plane mechanical strength, excellent thermal conductivity (4840–5300 W/mK), large surface area (2630 $m^2/g$), and high double layer capacitance (21 $\mu F/cm^2$) [31]. GC with a cage-like 3D microstructure of ribbons of graphene has been used for electrochemistry and has exceptional chemical inertness, high mechanical stiffness [6],

good electrical properties, high electrochemically stability, high charge storage capacity (61.5 mC/cm$^2$), and fast surface electrokinetics coupled with lithography patternability [32-33]. Independently, the two allotropes of carbon Gr and GC have certain compelling distinctive properties suitable for semi-conductor and energy-storage applications.

In this dissertation, we investigate the possibility of leveraging the unique strengths of these two allotropes of carbon to introduce a new composite "made of tailored building blocks, which are composed of one or more constituent bulk materials, leading to effective medium properties beyond those of their ingredients" – and hence form a metamaterial [34]? This fundamental question inspires a hypothesis on whether combining the unique strength of the 'gold-standard' materials- graphene and glassy carbon as show in Figure 1.1 will help introduce a new metamaterial system that brings the best qualities of these materials in a single material bonded through strong covalent bonds. A metamaterial that combines graphene with its excellent conductivity and glassy carbon with its high charge storage capacity could be the answer for demanding requirement of carbon-based neural interface and ultrasensitive biochemical sensors.

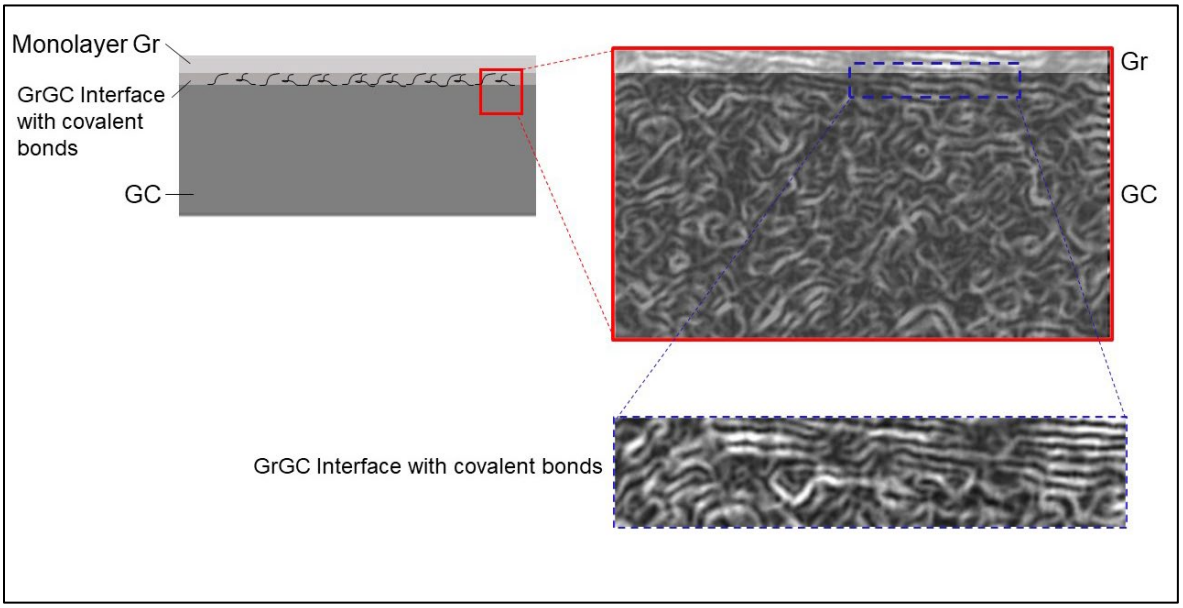



**Figure 1.1** Graphene- Glassy carbon microstructure and representative nanostructures indicating carbon layers within the metamaterial

## 1.2 Outline of the dissertation

To test this hypothesis of a GrGC metamaterial, first we introduce the synthesis process of the GrGC metamaterial. The synthesis process will then be validated through molecular dynamics simulation. Material properties of the GrGC such as disordered carbon structures, functional groups on material surface, nanostructure at the GrGC interface by STEM imaging and bonding between Gr and GC will then be investigated. Electrochemical properties of the metamaterial such as impedance and charge storage capacity will also be tested for micro- electrocorticography. After validating in vitro electrochemical performance, micro-ECoG electrodes will be tested for *in vivo* recording and stimulation. Further, neurotransmitter detection capability and magnetic resonance compatibility will be demonstrated. Altogether, multimodality of the micro array will be established through this study.

The research plan for the dissertation contains 3 research objectives.

1. Introduction of GrGC synthesis process and material characterization of GrGC including surface defects, functional groups, bonds, and nanostructure of the metamaterial
2. Background work on the GC synthesis and neural interface test bed
3. Multimodal GrGC testbed for neurophysiology application. This will involve ECoG recording, stimulation, neurotransmitter detection, MR compatibility

The dissertation consists of 6 chapters. Chapter 1 introduces Graphene-Glassy Carbon hypothesis, research motivation and outline of the dissertation. Chapter 2 to chapter 5 will include reprinted or submitted manuscripts. Chapters 2 and 3 consist of background work done on Glassy carbon where multimodality of microelectrode material was studied. Chapters 4 and 5 contain of studies of synthesis of Graphene- Glassy carbon metamaterial and its application in neural interface devices respectively.

In chapter 2, we presented a carbon-based neural microelectrode array consisting of homogeneous glassy carbon microelectrodes, interconnects and connecting pads and established GC as capacitive

material. The electrode array showed purely capacitive behavior and lasted more than 3.5 billion cycles of bi-phasic pulses at charge density of 0.25 mC/cm$^2$. These probes enabled high SNR (>16) for *in vivo* recordings and high-resolution real-time neurotransmitter detection using same microelectrode array. These arrays showed potential to be served as a multi-modal platform for long-term applications of neural probe technology in clinical neuroscience. [8]

In chapter 3, we further investigated multimodal performance of glassy carbon electrodes testing magnetic resonance compatibility of glassy carbon material and established GC's compelling advantage for clinical use. In this study, GC and thin film Pt were compared through induced vibration, induced voltage, and MRI experiments and finite element modeling. GC microelectrodes demonstrated superior magnetic resonance compatibility over standard metal thin-film microelectrodes. Due to low magnetic susceptibility and lower conductivity, GC microelectrodes caused no susceptibility shift artifacts and no eddy-current-induced artifacts compared to Pt microelectrodes. [27]

In chapter 4, we introduced Graphene-Glassy Carbon metamaterial synthesized from graphene (Gr) and glassy carbon (GC) - two allotropes of carbon - possessing superior electrical, power density, energy density, and specific capacitance properties. Novel fabrication process for the metamaterial is presented where a substrate with monolayer of Gr transferred was used to deposit a layer of negative-tone polymer precursor for GC that was patterned and then pyrolyzed in the furnace to synthesize a new metamaterial called GrGC. The formation of this novel metamaterial is validated through molecular dynamics modeling and comprehensive mechanical and surface characterizations. The chemical bond of the metamaterial was characterized through Raman Spectroscopy, its surface morphology through SEM and STEM. MD simulation validated the formation of a unique metamaterial that consisted of a planar Gr component, transition region, and a 3D-shaped cage-like GC component. The MD simulation results also showed formation of functional groups and covalent bond between the two allotropes.

In chapter 5, we introduce a new neural probe as a testbed to test new material that consists of ~1 nm thick layer of patterned Gr microelectrodes supported by another layer of 3-5 μm thick patterned GC. We present the fabrication technology for the new GrGC microelectrodes and the accompanying pattern

transfer technology on flexible substrate. A long-term (18-weeks) in vivo study of the use of these Gr on GC microelectrodes assessed the quality of the ECoG-based neural signal recording. Acute SEP recording and MEP stimulation were also tested through electrophysiological measurements. The probes were demonstrated to be functionally and structurally stable over the 18-week period with minimal glial response – the longest reported so far for graphene-based microelectrodes. Additionally, magnetic resonance compatibility study and neurotransmitter detection capability of GrGC metamaterial is demonstrated

In chapter 6 as discussion, a comparative study between GC and GrGC metamaterial was conducted based on the results obtained from chapter 2 to 5. Overall, capability of GrGC metamaterial for potential clinical neural interface microelectrode applications is discussed.

**References:**


[1] Lin PC, Park BY, Madou MJ. Development and characterization of a miniature PEM fuel cell stack with carbon bipolar plates. Journal of power sources. 2008 Jan 21;176(1):207-14.

[2] Wang Y, Pham L, de Vasconcellos GP, Madou M. Fabrication and characterization of micro PEM fuel cells using pyrolyzed carbon current collector plates. Journal of Power Sources. 2010 Aug 1;195(15):4796-803.

[3] Martinez-Duarte, R., Gorkin III, R.A., Abi-Samra, K. and Madou, M.J., 2010. The integration of 3D carbon-electrode dielectrophoresis on a CD-like centrifugal microfluidic platform. Lab on a Chip, 10(8), pp.1030-1043.

[4] Novoselov KS, Geim AK, Morozov SV, Jiang DE, Zhang Y, Dubonos SV, Grigorieva IV, Firsov AA. Electric field effect in atomically thin carbon films. science. 2004 Oct 22;306(5696):666-9..

[5] Narayan J, Bhaumik A. Novel phase of carbon, ferromagnetism, and conversion into diamond. Journal of Applied Physics. 2015 Dec 7;118(21):215303.

[6] Hu M, He J, Zhao Z, Strobel TA, Hu W, Yu D, Sun H, Liu L, Li Z, Ma M, Kono Y. Compressed glassy carbon: An ultrastrong and elastic interpenetrating graphene network. Science advances. 2017 Jun 1;3(6):e1603213.

[7] Vomero M, Castagnola E, Ciarpella F, Maggiolini E, Goshi N, Zucchini E, Carli S, Fadiga L, Kassegne S, Ricci D. Highly stable glassy carbon interfaces for long-term neural stimulation and low-noise recording of brain activity. Scientific reports. 2017 Jan 13;7(1):1-4.

[8] Nimbalkar S, Castagnola E, Balasubramani A, Scarpellini A, Samejima S, Khorasani A, Boissenin A, Thongpang S, Moritz C, Kassegne S. Ultra-capacitive carbon neural probe allows simultaneous

long-term electrical stimulations and high-resolution neurotransmitter detection. Scientific reports. 2018 May 3;8(1):1-4.

[9] Renteria JD, Nika DL, Balandin AA. Graphene thermal properties: applications in thermal management and energy storage. Applied sciences. 2014 Dec;4(4):525-47..

[10] Sainio S, Palomäki T, Rhode S, Kauppila M, Pitkänen O, Selkälä T, Toth G, Moram M, Kordas K, Koskinen J, Laurila T. Carbon nanotube (CNT) forest grown on diamond-like carbon (DLC) thin films significantly improves electrochemical sensitivity and selectivity towards dopamine. Sensors and Actuators B: Chemical. 2015 May 1;211:177-86.

[11] Gupta VK, Jain AK, Shoora SK. Multiwall carbon nanotube modified glassy carbon electrode as voltammetric sensor for the simultaneous determination of ascorbic acid and caffeine. Electrochimica Acta. 2013 Mar 30;93:248-53.

[12] Musameh M, Wang J, Merkoci A, Lin Y. Low-potential stable NADH detection at carbon-nanotube-modified glassy carbon electrodes. Electrochemistry communications. 2002 Oct 1;4(10):743-6.

[13] Kang X, Mai Z, Zou X, Cai P, Mo J. A sensitive nonenzymatic glucose sensor in alkaline media with a copper nanocluster/multiwall carbon nanotube-modified glassy carbon electrode. Analytical biochemistry. 2007 Apr 1;363(1):143-50.

[14] Cogan SF. Neural stimulation and recording electrodes. Annu. Rev. Biomed. Eng.. 2008 Aug 15;10:275-309.

[15] Stieglitz T. Neural prostheses in clinical practice: biomedical microsystems in neurological rehabilitation. Operative Neuromodulation. 2007:411-8.

[16] Navarro X, Krueger TB, Lago N, Micera S, Stieglitz T, Dario P. A critical review of interfaces with the peripheral nervous system for the control of neuroprostheses and hybrid bionic systems. Journal of the Peripheral Nervous System. 2005 Sep;10(3):229-58.

[17] Alba NA, Du ZJ, Catt KA, Kozai TD, Cui XT. In vivo electrochemical analysis of a PEDOT/MWCNT neural electrode coating. Biosensors. 2015 Dec;5(4):618-46.

[18] Kolarcik CL, Catt K, Rost E, Albrecht IN, Bourbeau D, Du Z, Kozai TD, Luo X, Weber DJ, Cui XT. Evaluation of poly (3, 4-ethylenedioxythiophene)/carbon nanotube neural electrode coatings for stimulation in the dorsal root ganglion. Journal of neural engineering. 2014 Dec 8;12(1):016008.

[19] Cui X, Lee VA, Raphael Y, Wiler JA, Hetke JF, Anderson DJ, Martin DC. Surface modification of neural recording electrodes with conducting polymer/biomolecule blends. Journal of Biomedical Materials Research: An Official Journal of The Society for Biomaterials, The Japanese Society for Biomaterials, and The Australian Society for Biomaterials and the Korean Society for Biomaterials. 2001 Aug;56(2):261-72.

[20] Petrossians A, Whalen JJ, Weiland JD, Mansfeld F. Surface modification of neural stimulating/recording electrodes with high surface area platinum-iridium alloy coatings. In2011 Annual International Conference of the IEEE Engineering in Medicine and Biology Society 2011 Aug (pp. 3001-3004). IEEE.

[21] Chen YC, Hsu HL, Lee YT, Su HC, Yen SJ, Chen CH, Hsu WL, Yew TR, Yeh SR, Yao DJ, Chang YC. An active, flexible carbon nanotube microelectrode array for recording electrocorticograms. Journal of neural engineering. 2011 Apr 8;8(3):034001.

[22] Castagnola E, Maiolo L, Maggiolini E, Minotti A, Marrani M, Maita F, Pecora A, Angotzi GN, Ansaldo A, Boffini M, Fadiga L. PEDOT-CNT-coated low-impedance, ultra-flexible, and brain-conformable micro-ECoG arrays. IEEE Transactions on Neural Systems and Rehabilitation Engineering. 2014 Jul 25;23(3):342-50.

[23] Park DW, Schendel AA, Mikael S, Brodnick SK, Richner TJ, Ness JP, Hayat MR, Atry F, Frye ST, Pashaie R, Thongpang S. Graphene-based carbon-layered electrode array technology for neural imaging and optogenetic applications. Nature communications. 2014 Oct 20;5(1):1-1.

[24] Wang K, Fishman HA, Dai H, Harris JS. Neural stimulation with a carbon nanotube microelectrode array. Nano letters. 2006 Sep 13;6(9):2043-8.

[25] Vitale F, Summerson SR, Aazhang B, Kemere C, Pasquali M. Neural stimulation and recording with bidirectional, soft carbon nanotube fiber microelectrodes. ACS nano. 2015 Apr 28;9(4):4465-74.

[26] Lu Y, Lyu H, Richardson AG, Lucas TH, Kuzum D. Flexible neural electrode array based-on porous graphene for cortical microstimulation and sensing. Scientific reports. 2016 Sep 19;6(1):1-9.

[27] Nimbalkar S, Fuhrer E, Silva P, Nguyen T, Sereno M, Kassegne S, Korvink J. Glassy carbon microelectrodes minimize induced voltages, mechanical vibrations, and artifacts in magnetic resonance imaging. Microsystems & nanoengineering. 2019 Nov 18;5(1):1-1.

[28] Castagnola E, Vahidi NW, Nimbalkar S, Rudraraju S, Thielk M, Zucchini E, Cea C, Carli S, Gentner TQ, Ricci D, Fadiga L. In vivo dopamine detection and single unit recordings using intracortical glassy carbon microelectrode arrays. MRS advances. 2018;3(29):1629-34.

[29] Castagnola E, Thongpang S, Hirabayashi M, Nava G, Nimbalkar S, Nguyen T, Lara S, Oyawale A, Bunnell J, Moritz C, Kassegne S. Glassy carbon microelectrode arrays enable voltage-peak separated simultaneous detection of dopamine and serotonin using fast scan cyclic voltammetry. Analyst. 2021;146(12):3955-70.

[30] Zachek MK, Takmakov P, Moody B, Wightman RM, McCarty GS. Simultaneous decoupled detection of dopamine and oxygen using pyrolyzed carbon microarrays and fast-scan cyclic voltammetry. Analytical chemistry. 2009 Aug 1;81(15):6258-65.

[31] Xia J, Chen F, Li J, Tao N. Measurement of the quantum capacitance of graphene. Nature nanotechnology. 2009 Aug;4(8):505-9..

[32] Mardegan A, Kamath R, Sharma S, Scopece P, Ugo P, Madou M. Optimization of carbon electrodes derived from epoxy-based photoresist. Journal of The Electrochemical Society. 2013 Jun 1;160(8):B132.

[33] Sharma S, Kamath R, Madou M. Porous glassy carbon formed by rapid pyrolysis of phenol-formaldehyde resins and its performance as electrode material for electrochemical double layer capacitors. Journal of analytical and applied pyrolysis. 2014 Jul 1;108:12-8.

[34] Kadic M, Milton GW, van Hecke M, Wegener M. 3D metamaterials. Nature Reviews Physics. 2019 Mar;1(3):198-210.

# CHAPTER II

## Ultra-Capacitive Carbon Neural Probe Allows Simultaneous Long-Term Electrical Stimulations and High-Resolution Neurotransmitter Detection

**Abstract**

We present a new class of carbon-based neural probes that consist of homogeneous glassy carbon (GC) microelectrodes, interconnects and bump pads. These electrodes have purely capacitive behavior with exceptionally high charge storage capacity (CSC) and are capable of sustaining more than 3.5 billion cycles of bi-phasic pulses at charge density of 0.25 mC/cm$^2$. These probes enable both high SNR (>16) electrical signal recording and remarkably high-resolution real-time neurotransmitter detection, on the same platform. Leveraging a new 2-step, double-sided pattern transfer method for GC structures, these probes allow extended long-term electrical stimulation with no electrode material corrosion. Cross-section characterization through FIB and SEM imaging demonstrate strong attachment enabled by hydroxyl and carbonyl covalent bonds between GC microstructures and top insulating and bottom substrate layers. Extensive in-vivo and in-vitro tests confirmed: (i) high SNR (>16) recordings, (ii) highest reported CSC for non-coated neural probe ($61.4 \pm 6.9$ mC/cm$^2$), (iii) high-resolution dopamine detection (10 nM level - one of the lowest reported so far), (iv) recording of both electrical and electrochemical signals, and (v) no failure after 3.5 billion cycles of pulses. Therefore, these probes offer a compelling multi-modal platform for long-term applications of neural probe technology in both experimental and clinical neuroscience.

## 1. Introduction

Carbon is increasingly finding wider acceptance in micro and nanofabrication of a variety of sensors, actuators, microelectrodes, wires, batteries, fuel cells, thin-films, and neural interfaces [1-6]. Its unique tunable mechanical and electronic properties enabled by the availability of a range of possible hybridized bonds ($sp^2$ and $sp^3$) make it a versatile material. Further, carbon has a potential to assume even more far-reaching importance in applications varying from sensors to energy conversion and storage with discovery of newer carbon allotropes such as graphene (excellent conductivity and strength) [7], Q-carbon (excellent hardness) [8] and compressed glassy carbon (excellent strength) [9]. Specifically, in recent developments, the ability to microfabricate photolithographically patterned carbon features has further driven innovation in wider application of GC, one of the allotropes of carbon [1,2]. This technology

involves pyrolyzing pre-patterned polymeric structure made from negative tone resists at high temperatures and inert environment in a tube furnace [1,2].

Carbon is a compelling material for chronically implanted devices aiming to minimize tissue damage due to its chemical inertness, biocompatibility, good electrical properties, electrochemical stability, purely capacitive charge injection (no irreversible reactions and byproducts), and fast surface electrochemical kinetics [1-6]. We recently demonstrated neural probes with GC microelectrodes for electrocorticography (ECoG), intracortical recording and stimulation [3-5]. Brain stimulation applications require high performance microelectrode materials capable of sustaining hundreds of millions of cycles of electrical stimulations pulses (corresponding to implantations lasting 3–5 years) at clinically relevant charge densities without corrosion, tissue damage, or delamination of insulating and substrate layers. Meeting this requirement will enable the transition of neural probe technology from lab to clinical use, particularly with applications requiring long-term electrical stimulation, such as deep brain stimulation or spinal stimulation used for neuromodulation and induction of neuroplasticity [10].

As a response to this need, we introduce here a new class of GC neural probes exclusively fabricated from a single homogeneous material of GC with no intermediate layers such as adhesion and conducting metal layers. This process removes any sources of potential mechanical or electrical discontinuities or failures at large cycles of electrical stimulations and extended period of in-vivo use. The new fabrication method presented here allows for a 2-step double-sided patterning, subsequent transfer to a polymeric supporting layer and final insulation of GC microelectrodes, interconnects and bump pads using a single material. In this new approach, therefore, there is no intermediate metal deposition process involved allowing–for the first time–all GC neural probes (aGC neural probes) made of a single homogenous material and supported on flexible polymeric substrate. The final aGC neural probes are housed in a flexible, thin-film polyimide substrate that leverage the superior electrochemical stability of GC material along with the improved biocompatibility of thin-film devices. To establish the robustness and superiority of the technology, extensive in-vivo and in-vitro mechanical, electrical, and electrochemical characterizations

coupled with aggressive long-term stability and corrosion tests under electrical stimulations were carried out. This study demonstrates robustness and multi-modal recording capability for both neuronal electrical signals and neurotransmitter electrochemical signals. These probes are also capable of delivering balanced-charge pulsing over 3.5 billion cycles in extended accelerated aging process lasting more than 1000 hours. We demonstrate that these new probes have compelling advantages over existing technologies in almost all key metrics from mechanical and electrical properties to electrochemical kinetics, which is quite remarkable for probes fabricated from a single material without any surface coating.

## 2. Materials and Methods

### 2.1 Microfabrication

To demonstrate the technology, we microfabricated a 15-channel neural probe specifically designed for electrocorticography (ECoG) reading and a 4-channel penetrating probe designed and sized for neurotransmitter detection. The geometry of the ECoG device consisted of 300 μm diameter surface microelectrodes with 180 μm wide interconnects and a total width of 3.5 mm [2,3]. The neurotransmitter detection version had 4 penetrating microelectrodes of exposed area of 25 μm × 20 μm (500 $\mu m^2$) spaced at 220 μm (see Supplementary Figures S1 and S2).

As shown in Fig. 1, the microfabrication process started with spin-coating 6 μm thick SU8–10 negative photoresist (Microchem, MA) and patterning it following conventional negative lithography process steps [1,2]. The patterned SU-8 microstructures were then pyrolyzed in a quartz furnace (MTI Corp., CA) under inert atmosphere of nitrogen gas with flow rate of 50 ml/min. For pyrolysis, the temperature was ramped to 1000 °C over a period of 6 hours and then held at this temperature for 90 minutes. Following this, the furnace was allowed to cool down to room temperature over a period of several hours.

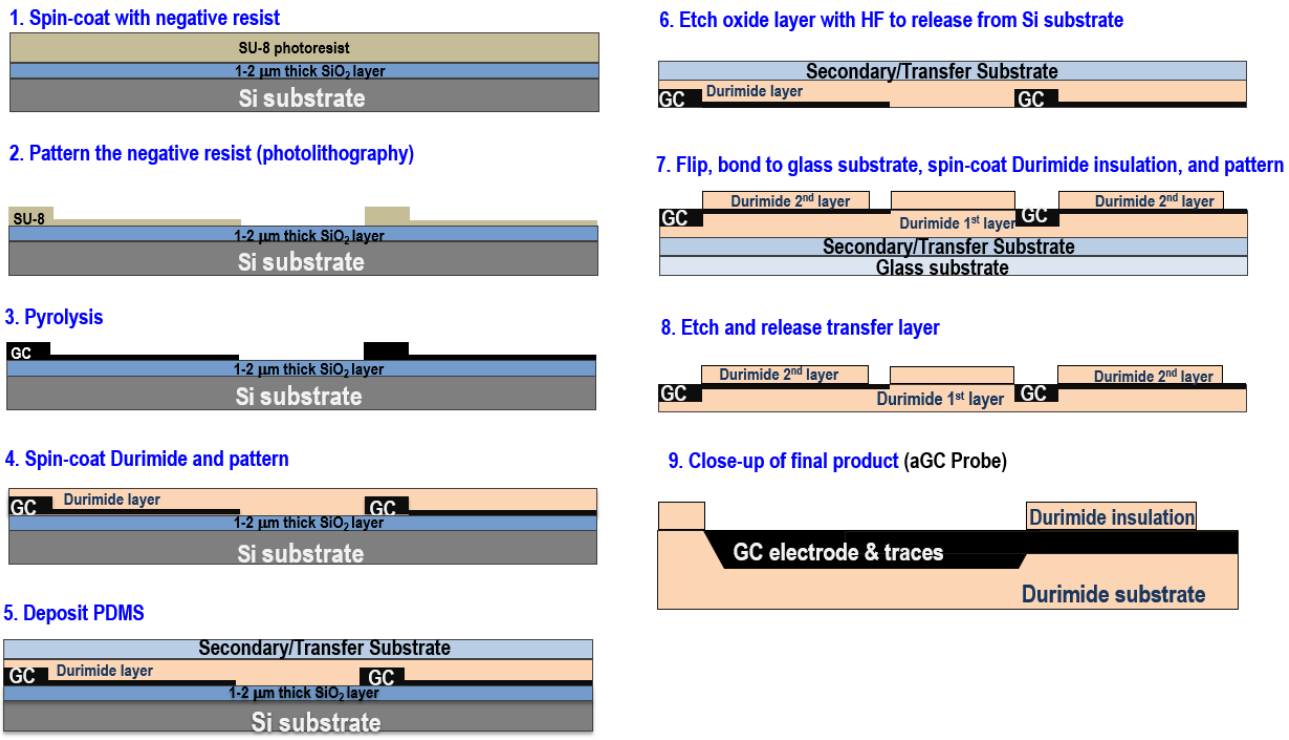



**Figure 2.1** Lithography steps for microfabricating all glassy carbon (aGC) microstructures on a polymeric substrate. Two-step double-sided lithography patterning was used in addition to pyrolysis. Complete probes are referred as aGC probes whereas glassy carbon material is referred to simply as GC.

Subsequently, the first base layer of ~8 µm thick non-photo sensitive polyimide (Durimide 115a) (Fujifilm, Japan) was spin-coated on top of GC microstructures at 2500 rpm for 45 seconds. This was then soft baked at 135 °C for 2.5 min and cooled down to room temperature. Patterning of Durimide was done through dry reactive ion etching (Technics Series 85 Reactive Ion Etcher, Pleasanton, CA) using Shipley positive resist (Microchem, MA) as a soft mask. The patterned Durimide layer was partially cured at 200 °C for 30 mins in $N_2$ environment. A sacrificial transfer layer was then deposited as a secondary substrate on top of the Durimide layer. Polymers such as PMMA (Polymethyl methacrylate) or PDMS (Polydimethylsiloxane) could be used for this purpose. Here, we describe the use of PDMS (Dow Corning, USA) as one example. PDMS mixed with curing agent in 10:1 proportion was spin-coated at 300 rpm for 45 secs and then cured at 90 °C for 30 mins followed by BHF etching of oxide layer to release it from the silicon substrate. Subsequently, a glass substrate was bonded to the released structure to offer an additional

temporary support for improved alignment. The wafer was then flipped and an insulation layer of Durimide spin-coated. After patterning this top insulation layer of Durimide, it was subsequently partially cured under $N_2$. A final BHF etching removed the sacrificial layer and released all devices. The final aGC probes are shown in Supplementary Figures S1 (μECoG probe) and S2 (intracortical penetrating probe).

### 2.2 Mechanical and Cross-Sectional Characterizations

The mechanical strength of the ensuing device was measured using Instron's 1500HDX Universal Testing Machine (Instron, USA) where tensile load was applied till failure, and the resulting extension measured. Tensile test specimen probes with dimensions of 17 mm in length, 0.5 mm in width and 50 μm in thickness were used for the experimental study. Since the devices were too thin, attachment of strain gauge extensometers directly to the probes was not practical. Instead, linear displacement due to the crosshead motion of Instron was used to obtain displacement values. Thread-rolled C-clamps with clamping capacity of 0–25 mm were used to grip the probe. C-clamps provide greater precision for easy adjustment of position and prevent marring of the probe surface. The frame of C-clamps was then held between the jaws of upper and lower clamps of the Instron machine (ca. Supplementary Figure S4). The cross-head extension rate was set at 0.5 mm/min. The specimen was then loaded to failure at this rate and the load-deflection curve plotted. For comparison purposes, probes of similar geometry but consisting of 200 nm thick metal (Pt) microelectrodes and wire traces were microfabricated through standard metal lift-off process. Subsequently, the load-deflection curves and ultimate load carrying capacity of the thin-film metal probes were determined in a similar fashion. Young's Modulus was determined by taking the mean slope of ten points in the elastic region of the stress-strain curve. The modulus of plain Durimide substrate with no metal or GC interconnects and microelectrodes was also determined separately to de-couple its effect from the composite structure. FEI Quanta 450 FEG SEM (ThermoScientific, OR) was used for scanning electron microscopy images. Cross sectioning was obtained through Focused Ion Beam (FIB) milling using a dual beam microscope system (Nova 600 NanoLab; FEI, Netherlands). This system is equipped with a

field emission gun for scanning electron imaging and a focused ion beam of gallium ions for milling. The sectioning process was done in two steps: ion current milling (working at 30 kV and 7.7 pA) followed by a cleaning step of the section. Imaging was done at an acceleration voltage of 20 kV (0.4 nA of emission current).

### 2.3 Electrical, Electrochemical, and Stability Characterizations

The electrochemical behavior of the microelectrodes was studied in Phosphate-Buffered Saline solution (PBS; 0.01 M, pH 7.4; Sigma Aldrich, USA). Cyclic voltammetry (CV) was used to quantify capacitive charging and microelectrode stability while electrochemical impedance spectroscopy (EIS) was used to determine the electrical properties of the probes over a large range of frequencies. For both CV and EIS tests, we used a potentiostat (Reference 600+, Gamry Instruments, USA) connected to a three-electrode electrochemical cell with a platinum wire as a counter electrode and a saturated Ag/AgCl reference electrode. During CV tests, the working electrode potential was swept between 1.3 V and −0.9 V (water window of GC [4]), maintaining a scan rate of 100 mV/s. The total charge storage capacity (CSC) was calculated from the time integral of a CV cycle. During EIS measurements, 10 mV RMS amplitude sine wave was superimposed on 0 V potential with frequency sweep from 0.1 to $10^5$ Hz. Equivalent circuit modeling of the EIS data was done through Gamry Echem Analyst Vn 7.05 software (Gamry Instruments, USA). For the accelerated aging test consisting of prolonged current stimulation patterns, we used a cathodic-first charge balanced bi-phasic current pulses with 450 µA amplitude, 400 µsec cathodic half-phase period and a frequency of 1 kHz in saline solution (0.01 M PBS) using a Gamry Instruments Virtual Front Panel (Gamry Instruments, PA, USA). This accelerated aging test corresponds to charge density of 0.25 mC/cm$^2$ and was applied over a period of 1000 hours. Voltage transient responses during stimulation were acquired using the same potentiostat by simultaneously injecting stimulation current pulses and recording the corresponding voltage excursions between working and counter electrodes. In regular intervals, impedance was measured, and the integrity of the electrodes checked. The buffer pH was measured regularly during accelerated aging test using pH/mv/ion benchtop meter (Jenco Electronics, TX).

Fast-Scan Cyclic Voltammetry (FSCV) was used to evaluate the electrodes' dopamine detection performance with a WaveNeuro Potentiostat System (Pine Research, NC). For in-vitro dopamine calibration, the FSCV waveform was used with a pyramidal excursion from −0.5 V to +1.3 V potential and back to baseline with respect to the Ag/AgCl reference electrode at a scan rate of 400 V/s and 10 Hz frequency [11]. The duration of each scan was 9 ms (900 data points). Prior to the beginning of each experiment, the same voltage waveform was applied to the microelectrodes at 60 Hz for 1 hour for activating the carbon surface of the microelectrodes. Known concentrations of dopamine (10 nM–1 μM) were then infused over 5 seconds while changes in current were recorded for 20 seconds.

### 2.4 *In-vivo* Tests

**Micro-ECoG Implantation**:

All animal experiments were performed in accordance with the Association for Assessment and Accreditation of Laboratory Animal Care (AAALAC) Guide for the Care and Use of Laboratory Animals (8th Edition) and approved by the University of Washington Institutional Animal Care and Use Committee (IACUC) under protocol number 4265-01. Adult female Long-Evans rats (300 g) were used in this study and anesthesia was induced with a mixture of ketamine and xylazine. The animal was placed in a stereotaxic frame and a craniotomy made 1.5 mm rostral and 4.5 mm caudal to the bregma and 1 mm lateral and 7 mm lateral to the midline, targeting the left forelimb sensorimotor cortex. The microelectrode array was then placed on the dura and stabilized by gel foam dental cement. A reference wire was connected to a screw on the right parietal bone while a ground wire was connected to a screw on the occipital bone. Throughout the entire procedure, body temperature of the animal was maintained with a heating pad placed under it.

**Electrophysiology Recording**

Brain signal recording sessions were carried out under anesthesia, 4 days after array implantation. The implanted ECoG microarray was connected to a multichannel data acquisition system (Tucker-Davis Technologies, FL) through an active (unity-gain) head-stage. Sensory evoked potentials (SEP) were

obtained by applying bipolar surface stimulation to the surface of skin of the right wrist of an anesthetized rat. Recorded data was digitized at 24.4 kHz and stored on a PC for further analysis. Subsequently, raw signals were bandpass filtered (1–450 Hz, 4th order Butterworth, zero-phase) and down-sampled to 1 kHz using Matlab software (Mathworks, Inc., MA). Low-frequency brain activity in evoked SEPs were eliminated by a high-pass filter (30 Hz, 4th order Butterworth, zero-phase). In each recording session, 15 single, bi-phasic, squared wave stimulation pulses (pulse width: 500 µs, pulse amplitude: 0.5 mA − 2 mA, 0.5 Hz) were applied to the surface electrodes and evoked response from 5 ms to 55 ms after stimulation onset were averaged to obtain average SEPs12. The extracted evoked response between 5 ms to 55 ms after stimulation onset was considered as an estimate for the signal, while the extracted spontaneous activity corresponding to 65 ms to 115 ms after stimulation onset was taken as an estimate for the background noise. Subsequently, SNR (signal-to-noise ratio) of ECoG electrodes placed in six different positions across forelimb sensory cortex were evaluated. The SNR value for each trial was defined as the ratio between the variance of selected signal (evoked response) and the variance of selected noise (spontaneous activity). The calculated SNR (mean ± standard deviation) of all channels was used as a useful indication of the quality of brain-signal recording. Furthermore, to show temporal-spectral representation of recorded data by GC microelectrodes, the spectrogram of each ECoG channel were computed by applying 256 ms Hanning window on each ECoG time-series. The corresponding short-time Fourier transform of each segment were then computed using 200 ms overlap.

## 3. Results

In this section, we present the outcomes of the mechanical, electrical, and electrochemical characterizations.

### 3.1 Optical and Cross-Sectional Characterizations

Optical microscopy and SEM were used to visually investigate the structural integrity of the probes. As shown in Fig. 2a and Supplementary Figures S1–S3, the microelectrodes and interconnects (wire traces and bump pads) look sharp and well-defined after a two-stage, double-sided, pattern transfer procedure.

Both the top and bottom insulation layers appear structurally robust. As can be seen in Fig. 2b, d, FIB characterizations of GC microelectrode/substrate and GC interconnect/substrate interfaces demonstrate that the top insulation and bottom substrate polymer layers have an almost seamless interface with GC suggesting a strong bond between GC and polymer layers. This smooth and seamless interface is an important requirement for a tight integration and composite action between GC and the polymer layers.

### 3.2 Mechanical Characterizations

Results from mechanical characterization are summarized in Fig. 3 showing failure planes at maximum load carrying capacity. Load-deflection curves under a tensile load are reported along with calculated modulus (Supplementary Figure S4). For comparison purposes, tensile load tests were carried out on probes with thin-film metal (Pt) microelectrodes and interconnects with similar geometry as their aGC counterparts. The load carrying capacity for both types of probes was directly obtained from the load-deflection curves and the resulting failure planes in transverse direction were further investigated using SEM. The aGC probes failed at a tensile load of ~12 N at 1 mm extension with clearly defined elastic and plastic regions observed in the load-deflection curves. On the other hand, probes microfabricated with thin-film metal (Pt) microelectrodes and traces failed at an ultimate tensile load of 5 N at 0.7 mm extension. For both thin-film metal and GC traces, the failure plane as shown in Fig. 3a, b passes through the traces with no jagged discontinuity, suggesting a strong bond between durimide and the respective metal or GC layer. The Young's Modulus of the composite structure with GC microelectrodes and traces was calculated to be ~2.65 GPa whereas it was ~2.59 GPa for probes with Pt microelectrodes and traces. The modulus of aGC probes was slightly higher than that of plain Durimide (2.5 GPa) suggesting a strong composite action between GC and polyimide3. Optical observation revealed several micro-cracks in the thin-film metal traces near the failure plane (Fig. 3a), whereas only a single additional crack was seen in the otherwise intact GC trace (Fig. 3b), indicating different failure modes in the two types of probes. The extent of micro cracks in the thin-film metal electrodes suggests that they were progressively produced during loading resulting in earlier onset of electrical connection failure. For aGC probes, failure in the traces under tensile

load seems to have occurred at higher load levels preceding plastic failure. Stiffness of aGC probes in compression was determined through the Euler buckling load: $Pcr = \pi 2EI/(KL)^2$, where E = Young's modulus, I = area moment of inertia (500 µm width and 50 µm depth), K = effective length factor (usually 1) and L = length of probe. For the intracortical penetrating probes reported here, Pcr = 2.13 mN, which is substantially higher than ~1.5 mN force required to penetrate the cerebral cortex of a rat [13].

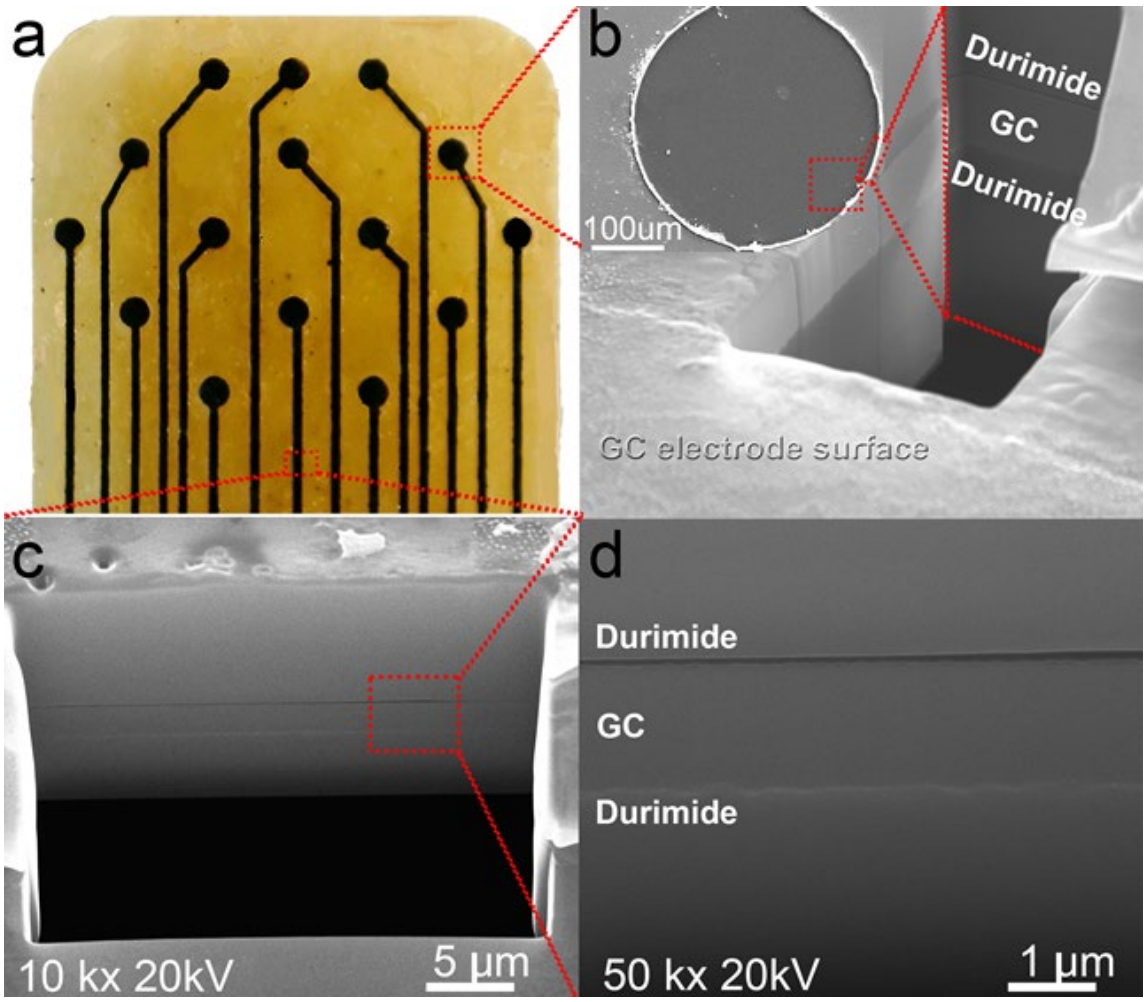



**Figure 2.2** Details of the aGC neural probe. (a) 16-channel ECoG probe, (b) FIB cross-section near one of GC electrodes showing embedding of electrodes between PI and Durimide. (c) FIB cross-section taken at GC traces, (d) close-up of FIB image at GC trace. Box in (a) shows the location where FIB was taken. Note that there are no adhesion layers or metal layers in aGC probes.

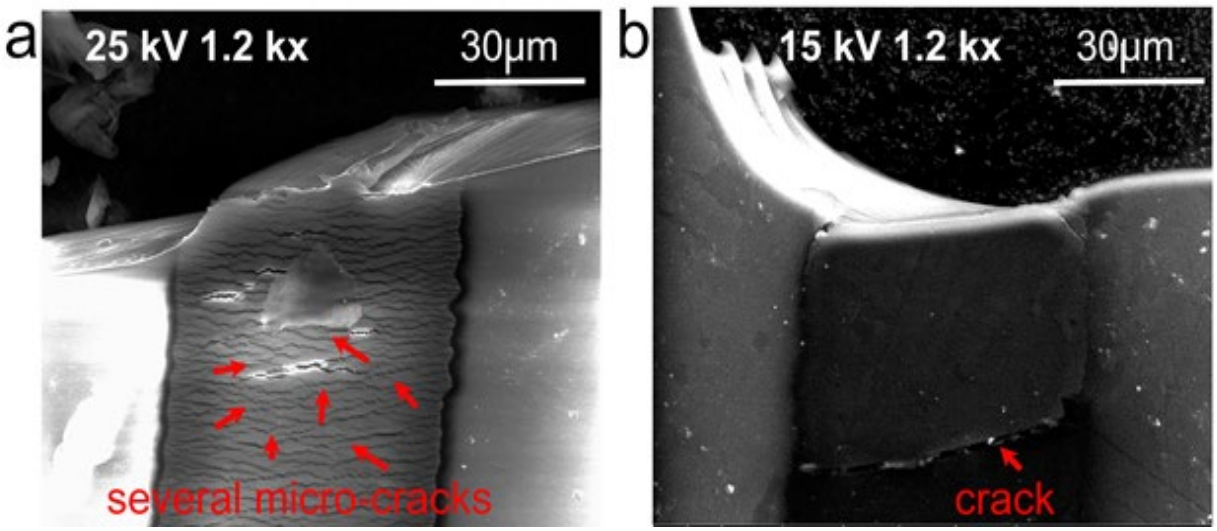



**Figure 2.3** Details of fracture planes following mechanical testing of aGC and thin-film metal (Pt) probes. (a) SEM image highlighting failure plane in probes with metal interconnects where numerous micro-cracks were developed prior to and at time of failure. (b) SEM image of failure plane in aGC probes. Apart from the failure plane, a single crack is observed at failure while the rest of GC interconnects remain intact. This micro-crack extends through the width of the specimen consistent with cracks that form during failure of homogeneous materials.

### 3.3 Electrical, Electrochemical and Stability Characterizations

Electrical characterization results are shown in Fig. 4. The impedance values at 10 Hz, 100 Hz and 1 kHz are (42.5 ± 27.6) kΩ, (10.7 ± 4.9) kΩ and (5.8 ± 1.2) kΩ, respectively (mean and standard deviation, n = 10). These indicate an excellent range for micro-ECoG recording applications. The corresponding EIS plots are reported in Fig. 4a. As the phase plot in Fig. 4a shows, impedances at frequencies higher than 4 kHz are dominated by almost exclusively a resistive component. Results from cyclic voltammetry of GC microelectrodes are summarized in Fig. 4b demonstrating an approximately rectangular shape, characteristic of microelectrodes exhibiting a predominantly double-layer capacitance. This is consistent with several other reports showing that this type of behavior is exhibited by only purely carbon materials, indicating that no faradaic reactions occur during the charging and discharging process [4, 14-17]. CSC,

calculated as the time-integral of an entire CV cycle between the water oxidation and reduction potential limits, is $61.4 \pm 6.9$ mC/cm$^2$ (mean and standard deviation, n = 10).

This capacitive charge injection mechanism is also confirmed by the voltage transient shape (Fig. 4c) illustrating the comparison of voltage transients between GC and Pt microelectrodes with the same dimension of 300 μm diameter and comparable impedance. Traces are in response to a biphasic, symmetric current pulse of 450 μA amplitude and 400 μsec of half-phase period. Due to the capacitive charge injection mechanism of GC microelectrodes, the amplitude of voltage transient for the same current level applied to both types of probes is much less in GC microelectrodes, producing maximum negative voltage ($V_{max,neg}$) of −1.03 V and maximum positive voltage ($V_{max,pos}$) of 0.25 V. These correspond to $E_{mc}$ (most negative polarization voltage) across electrode-electrolyte interface of −0.75 V and $E_{ma}$ (most positive polarization voltage) close to 0 V [18]. These values are safely within the maximum potential limits of water reduction and oxidation for GC microelectrodes (i.e., −0.9 to 1.3 V; Fig. 4b). In contrast, for Pt microelectrodes, the corresponding $V_{max,neg}$, $E_{mc}$, $V_{max,pos}$ and $E_{ma}$ values are −2.25 V, −1.75 V, 1.07 V and 0.7 V, respectively. These values are substantially outside the maximum potentials corresponding to the water window of Pt at −0.6 V to 0.8 V. Note that the maximum negative potential excursion ($E_{mc}$) is calculated by subtracting the access voltage ($V_a$) associated with the Ohmic electrolyte resistance and overpotential terms from the maximum negative voltage in the transient (i.e., $E_{mc} = V_{max,neg} - V_a$ and $E_{ma} = V_{max,pos} - V_a$)18. $V_a$ is defined as the near-instantaneous voltage change at either the onset of the current pulse or immediately after the current pulse is terminated [18]. In this condition, $V_a$ is 0.36 V for GC and 0.48 V for Pt (33% higher for Pt), suggesting a substantially lower overpotential to be overcome in GC microelectrodes (Fig. 4c,d). Table 1 summarizes these results.

Further, to gain better insight regarding the charge transfer properties of the electrode, equivalent circuit model is used to analyze experimental EIS data as shown in Figure 5. The optimal circuit model is composed of the electrolyte resistance ($R_{sol}$) in parallel with a constant phase element ($Z_{CPE}$) and the Warburg diffusion impedance ($Z_w$; Fig. 5, inset). Representative EIS bode plots of experimental data and

equivalent circuit models are reported in Figure 5. The corresponding EIS parameters obtained by fitting the experimental data to the model are: $R_{sol}$ = 4.095 kΩ, $Z_{CPE}$ ($Z_{CPE} = \frac{1}{(j\omega)^{\alpha}Y_0}$) Y0 = 4.07e−11 S*s$^{\alpha}$ and α= 0.91, and $Z_W$ = 4.55e$^{-5}$ S*s$^{1/2}$. Experimentally, capacitors often do not behave ideally but they act like a constant phase element, define as: $Z_{CPE} = \frac{1}{(j\omega)^{\alpha}Y_0}$ where $Y_o$ represents the capacitance and α is a constant related to the angle of rotation in the complex plane compared to the purely capacitive behavior ($Y_o$=1 for a pure capacitor).

Results from accelerated aging test with cycles of electrical pulse applied over period of 1000 hours are reported in Fig. 6a,b. Figure 6 summarizes EIS plots, CV cycles and voltage transients of GC microelectrodes before and after 0.2, 1, 2, 2.5 and 3.5 billion cycles of electrical stimulation pulses. Prior to pulsing, for example, the impedance value at 1 kHz was ~5.2 kΩ. After 2, 2.5 and 3.5 billion cycles of pulses, the impedance at 1 kHz was measured to be 5.75, 6.3, 8.8 kΩ, respectively. In general, we observed a decrease in impedance at low frequency ranges with a shift of the low frequency pole and a corresponding increase in CSC. The CSC values increased from 45 mC/cm$^2$ to 180 mC/cm$^2$ after 0.2–3.5 billion cycles of pulsing. This increase in capacitance is predominantly due to continued surface activation that is very common in carbon microelectrodes [22]. The corresponding CV cycles are reported in Fig. 6b, exhibiting the expected rectangular shape of capacitive microelectrodes. Again, as CV diagrams demonstrate, there are no observable faradaic reactions occurring during charging and discharging processes.

As part of this accelerated aging test, pH value of ~7.55 was measured at several locations in the flow-cell, well within the buffer's initial pH of 7.4. This is expected due to the buffering action of the PBS solution. Moreover, our findings are consistent with pH levels predicted by a transient FEA model in our previous work where pH near the microelectrode surface returned back to the initial conditions after each charge-balanced cycle [23].

SEM and AFM inspections of GC microelectrodes demonstrate that the mechanical integrity of the microelectrode was still intact after 3.5 billion cycles of biphasic 0.25 mC/cm$^2$ pulses in PBS solution over

a period of 42 days (Fig. 7). SEM images confirm that the insulation and substrate polymeric layers remained intact and well attached to GC microelectrodes at the end of this accelerated aging under electrical stimulation. Further, as shown in Fig. 7, AFM images of the microelectrodes were taken at 25 μm × 25 μm area before and after aging to determine if there was any quantifiable and visible corrosion of the exposed microelectrodes. AFM morphology analysis indicated that, before stimulation, mean roughness of the microelectrode surface was 43.55 ± 3.09 nm (n = 4) while after stimulation, it was 44.00 ± 6.69 nm (n = 4). A corresponding t-test gave a nonsignificant difference (P value > 0.05) between the mean roughness of the surfaces under the two conditions, confirming that there was no discernible corrosion after the aging process.

To test GC microelectrodes at near their charge injection limit, we applied a cathodic-first charge balanced bi-phasic current pulses with 5.1 mA amplitude, 400 μsec cathodic half-phase period and a frequency of 1 kHz in saline solution (0.01 M PBS) for 50 million cycles of pulses (3 mC/cm$^2$). Voltage transients of a GC microelectrode in response to this biphasic pulse together with impedance spectra and the corresponding CV plots before and after 20, 40, 50 billion stimulation pulses are reported in Supplementary Figure S5, demonstrating that the microelectrode was able to sustain aggressive stimulation without significant changes in electrochemical performances.

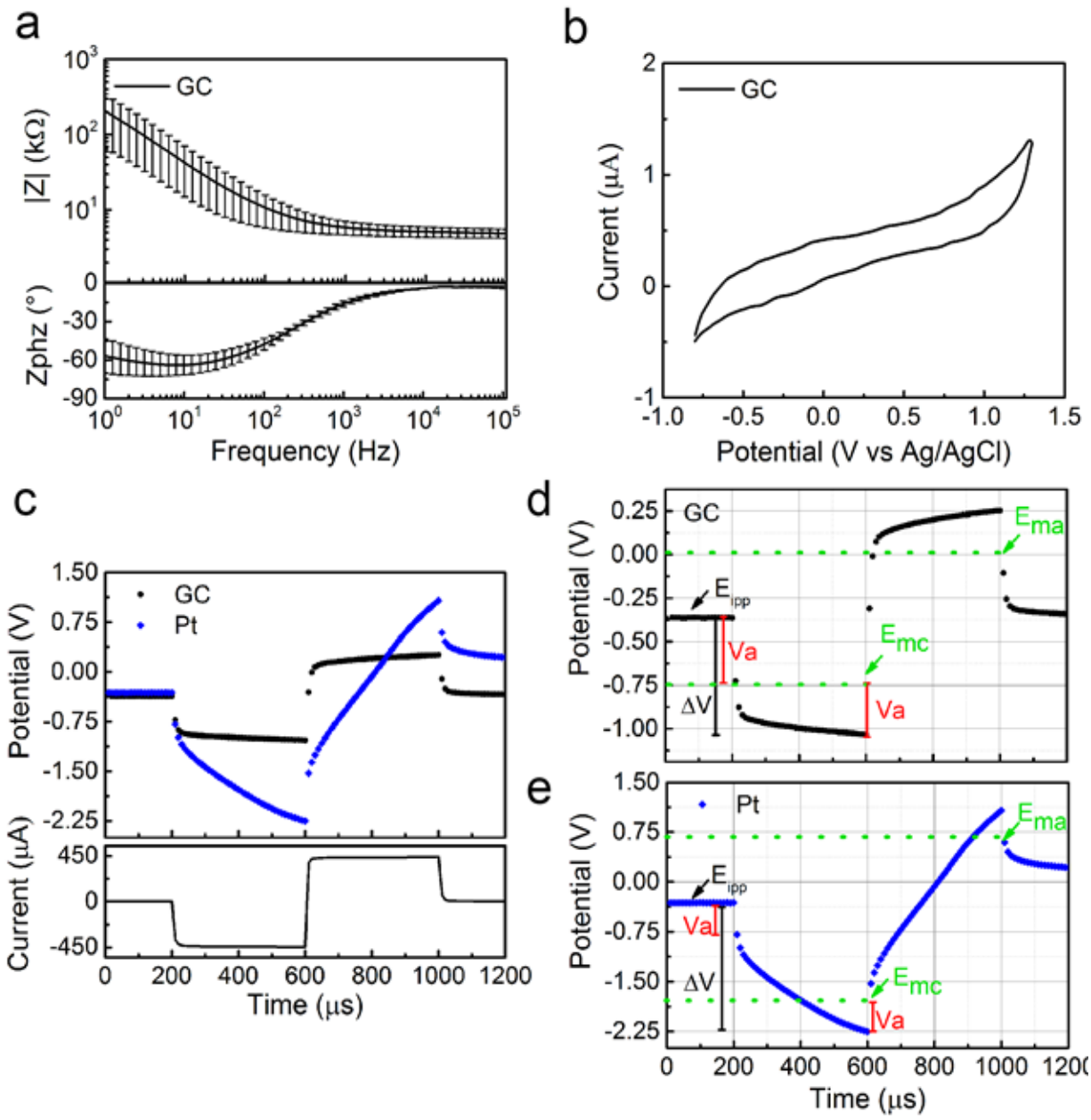



**Figure 2.4** Electrochemical characterization of GC electrodes. (a) EIS plot (mean and standard deviation, n=10), (b) representative cyclic voltammogram, (c) comparison of the voltage transient of **GC** versus **Pt** 300 µm diameter microelectrodes in response to a biphasic, symmetric 450 µA current pulse. (d) magnification of the voltage transients of the GC, (e) magnification of the voltage transients of Pt. Both plots show underlying the elements that contribute to the voltage transient, used for the calculation of the maximum positive polarization (Ema) and the maximum negative polarization (Emc) possible across the electrode-electrolyte interface. The values of Emc and Ema for GC and Pt are (-0.75 V, 0 V) and (-1.75 V, 0.75 V) respectively, indicating a lower overpotential and, hence, lower-threshold for electrokinetics for GC microelectrodes.

**Table 2.1** Summary of key parameters in voltage transients for GC and Pt microelectrodes

| Material | ΔV | $E_{ipp}$ | $V_a$ | $\Delta E_p$ | $E_{mc}$ | $E_{ma}$ | $V_{max,neg}$ | $V_{max,pos}$ |
|---|---|---|---|---|---|---|---|---|
| GC | 0.72 | −0.36 | 0.36 | 0.36 | −0.75 | 0.05 | −1.03 | 0.25 |
| Pt | 1.88 | −0.31 | 0.48 | 1.4 | −1.75 | 0.71 | −2.25 | 1.07 |

Emc = (Vmax,neg − Va), Ema = (Vmax,pos − Va), and ΔEp = ΔV − Va

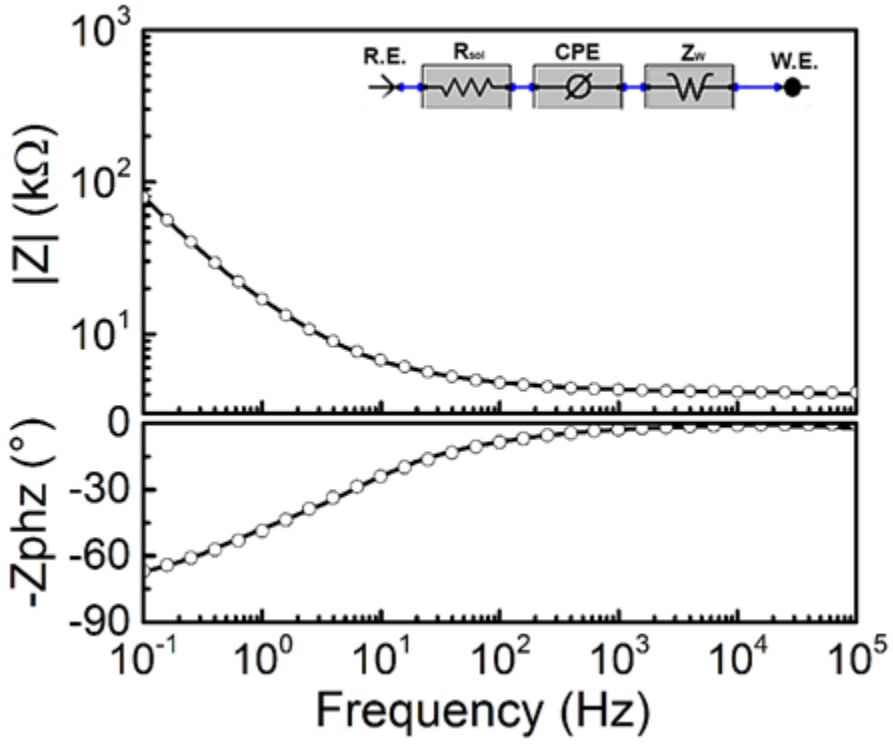



**Figure 2.5** Equivalent Circuit for aGC electrode. EIS parameters obtained by fitting the experimental data to the model are: $R_{sol}$ = 4.095 kΩ, CPE with a $Y_0$= 2.847e$^{-5}$ S*s$^{\alpha}$ and α = 0.91 & $Z_W$ = 4.55e$^{-5}$ S*s$^{1/2}$.

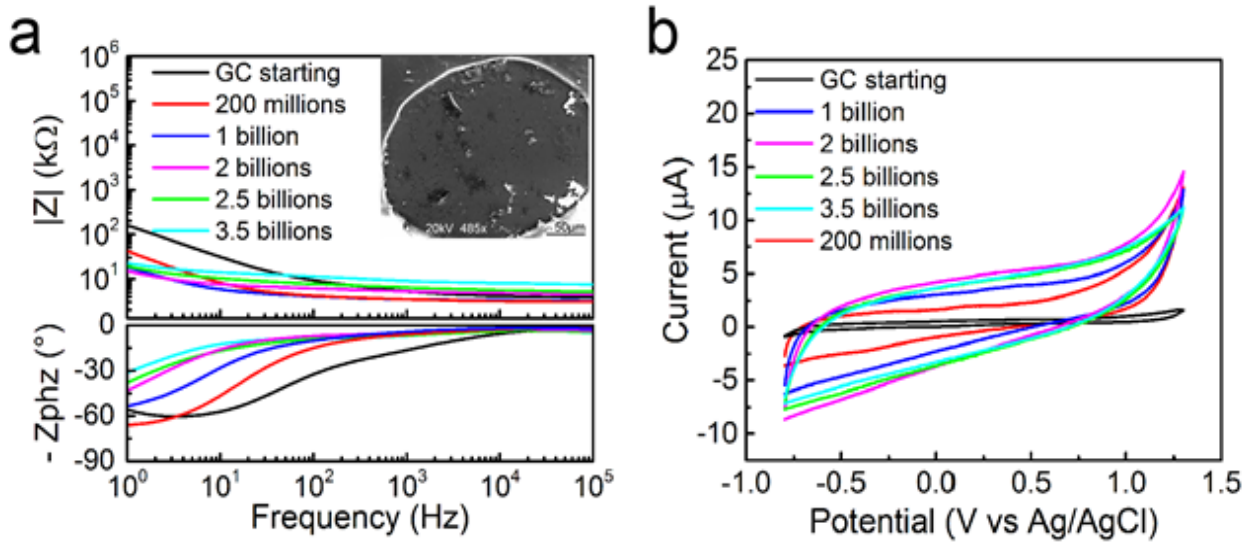



**Figure 2.6** Effect of accelerated aging through bi-phasic pulsing in PBS for 42 days (1000 hours). (a) Impedance spectra before and after 0.2, 1, 2, 2.5 and 3.5 billion of 0.25 mC/cm$^2$ stimulation pulses in PBS. The SEM picture of the GC microelectrodes after 3.5 billion pulses is reported in the inset. (b) Corresponding cyclic voltammograms over the range of stimulation pulses.

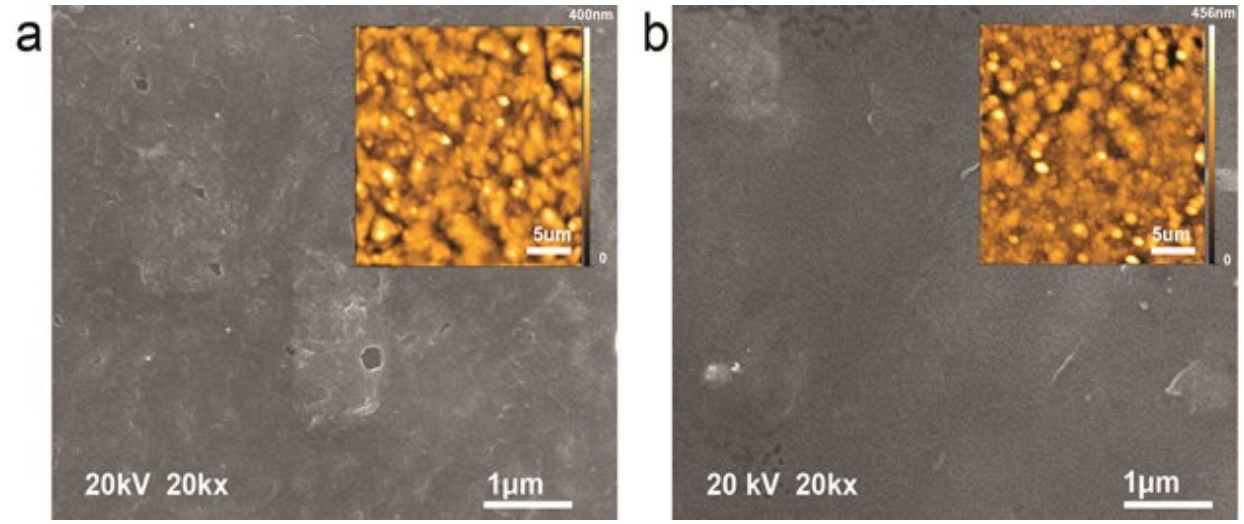



**Figure 2.7** SEM and AFM image of microelectrode surface (a) before stimulation and (b) after 3.5 billion pulses of stimulation.

### 3.4 *In-Vivo* Electrophysiology Tests

SEPs caused by the bi-phasic stimulation pulses on the right wrist were recorded via the ECoG microelectrode array implanted on the left forelimb sensory cortex of an anesthetized rat. Figure 8a shows

the craniotomy made targeting the left forelimb sensorimotor cortex where the probes were implanted. Plots of brain activities sampled from six channels of GC microelectrodes implanted in the sensory cortex four days after the implantation surgery are shown in Fig. 8b. To verify the quality of brain recording using GC microelectrodes, the average-SEP of different channels were calculated in response to the surface electrical stimulation of hand area. Figure 8c shows a typical average-SEP (mean ± standard error) of a single ECoG channel for 5 ms to 55 ms after stimulation onset, with average-spontaneous activity of the same ECoG channel for 65 ms to 115 ms after stimulation onset. The time frame between 5 ms to 55 ms was considered adequate to cover the entire SEP response, as all SEPs were observed in this time range. The large positive and negative response corresponding to 15 ms after stimulation onset demonstrates that the ECoG microelectrodes successfully recorded early response of sensory neurons in somatosensory cortex in the presence of background spontaneous activity. Figure 8d shows the power spectrum of the same six channels. As can be seen, all of the microelectrodes recorded brain activities in physiological spectral range without interference from non-physiological noise such as power line noise. Further, Supplementary Figure S6 shows that the spectrograms representing brain signals could be recorded across different frequency bands using GC microelectrodes. In Table 2, the mean (±standard deviation) SNR value (16 ± 6) and impedance of all ECoG channels are shown. Collectively, the in-vivo tests demonstrate that the GC ECoG microarray can successfully record multi-site, temporal and spectral brain information with high SNR.

**3.5 Neurotransmitter (Dopamine) Detection**

Figure 9 summarizes the results obtained from a series of FSCV characterizations on a 500 $\mu m^2$ net surface area penetrating GC microelectrode probes (Supplementary Figure S2). Figure 9a shows an example of dopamine signals detected using a standard pyramidal FSCV waveform in which the applied voltage was ramped from the holding potential of −0.5 V to the switching potential of +1.3 V and then back to −0.5 V at 400 V/s scan-rate. In particular, the color plots show changes in current following the injection of 10 nM of dopamine (DA) at t = 15 secs first and subsequently an additional 10 nM at t = 25 sec in the base PBS buffer. These changes in currents occurred at the known reduction and oxidation peaks of DA

(i.e., −0.18 V and 0.62 V), as clearly shown in the background subtracted CVs for 10 nM and 20 nM DA given in Fig. 9b. Further, to determine a calibration curve over a wider range of concentrations, additional sets of FSCV were carried out at 10, 20, 50, 100, 200, 500, 700 nM and 1 µM concentration of dopamine in PBS. As shown in Fig. 9c, the background subtracted CVs corresponding to these range of concentrations demonstrate reduction and oxidation peaks at (−0.18 V) and (0.62 V). In addition, the calibration curve for these concentrations of DA varying from 10 nM to 1 µM follows a linear trend as reported in Fig. 9d. This low detection limit of dopamine at 10 nM represents one of the lowest reported limits in the literature.

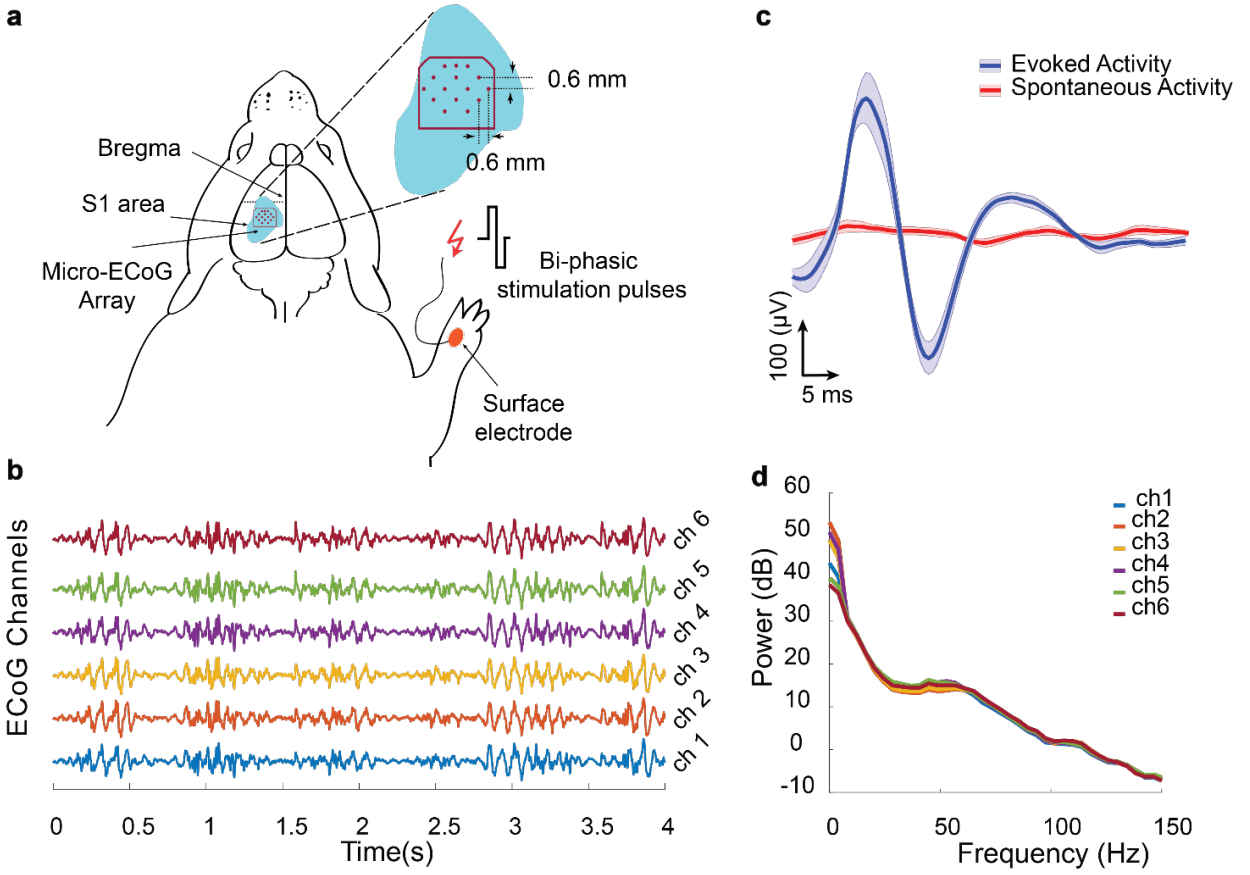



**Figure 2.8** (a) Schematic figure of the GC microelectrodes array implantation site on the left forelimb sensory cortex with electrical stimulation on the skin of the right wrist (b) Example of raw ECoG data recorded using **GC** microelectrodes arrays implanted in the forelimb area of rat sensory cortex (c) Average-SEP response related 5 - 55 ms after surface electrical stimulation of hand skin with the average-spontaneous activity related to 65 - 115 ms after stimulation. (d) Corresponding power spectrum of the same ECoG channels.

**Table 2.2** Average SNR value and impedance of **GC** microelectrodes arrays implanted in the forelimb area of rat sensory cortex in the recording session.

| SNR (mean ± std) | Impedance of all electrodes (KΩ) (mean ± std) | Impedance of Ground electrode (KΩ) |
|---|---|---|
| **16 ± 6** | **81 ± 16** | **<0.1** |

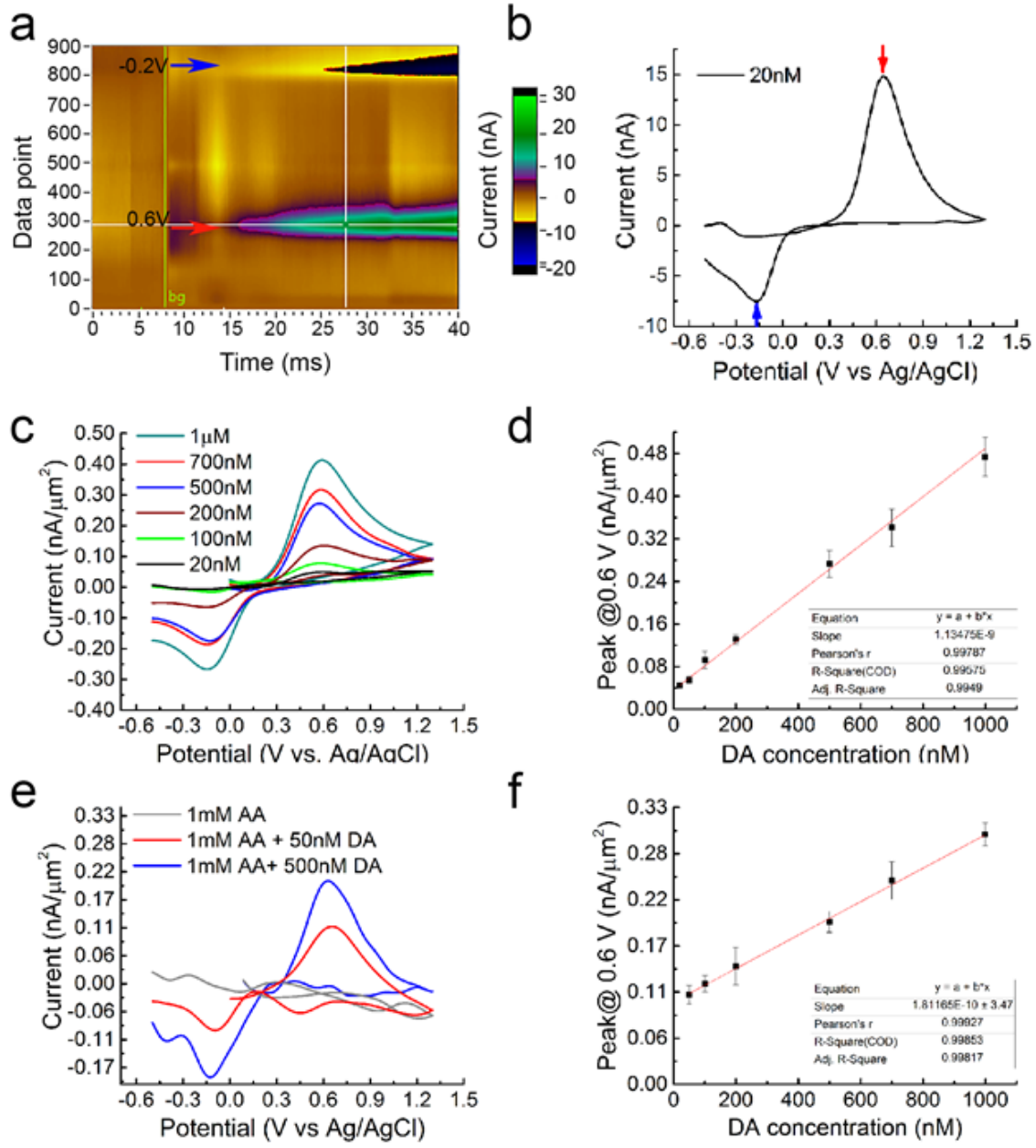



**Figure 2.9** (**a)** Representative color plot showing changes in current following 20 nM DA injection in PBS in-vitro; **(b)** correspondent background subtracted CV, showing reduction (-0.2 V) and oxidation (0.6 V) peaks of DA. Dopamine signals were measured using a standard pyramidal FSCV waveform in which the applied voltage was ramped from the holding potential of −0.5 V to the switching potential of +1.3 V and then back to −0.5 V at 400 V/s. **(c)** Background subtracted CVs, showing reduction (-0.2 V) and oxidation (0.6 V) peaks of respectively 20,100, 200, 500, 700 nM and 1 μM DA concentration in PBS, **(d)** calibration curve corresponding to conditions in d. **(e)** Background subtracted CVs, showing reduction (-0.2 V) and oxidation (0.6 V) peaks of 50 and 500 nM of DA in presence of 1 mM AA in PBS; **(f)** Calibration curve of the oxidation (0.6 V) peak of respectively 50, 100, 200, 500, 700 nM and 1 μM DA concentration in 1 mM AA in PBS.

Further, the capability of this aGC platform for selective detection of dopamine in the presence of Ascorbic Acid (AA) was also investigated. AA typically occurs in much higher concentration than that of DA (100–1000 times) and strongly interferes with DA detection24. Hence, the determination of DA with high selectivity and sensitivity in presence of AA is desirable for diagnostic applications. GC microelectrodes were able to detect 50 nM DA in the presence of 1 mM AA with high resolution. Background subtracted CVs showing reduction (−0.2 V) and oxidation (0.6 V) peaks of 50 nM and 500 nM of DA in presence of 1 mM AA in PBS are reported in Fig. 9e. The corresponding calibration curve shows a linear trend (Fig. 9f). This capability uniquely underscores an additional strong asset of GC microelectrodes in neurotransmitter detection through FSCV, a capability that is not matched by thin-film metal or metal oxide microelectrodes.

**Discussions**

This study aims to overcome key barriers towards long-term clinical translation of neural probe technology. We demonstrate (i) long-term stimulation of electrodes at biologically relevant charge densities, (ii) ability to electrochemically sense neurotransmitters with the same platform as electrical signal recording, and hence potentially enable understanding of the interplay between the two signaling modalities, (iii) no corrosion of the electrode material and, (iv) no delamination of layer. The extensive characterizations reported here are targeted towards investigating these capabilities and establishing the suitability and superiority of GC microelectrodes towards advancing clinical translation of neural interfaces. Below, we review these in light of key results reported in the literature for other competing probe materials.

The mechanical and electrical integrity of the aGC probes, when exposed to aggressively large number of electrical stimulations cycles, is documented via SEM, AFM, FIB, EIS and CV characterizations. AFM and SEM images taken at several locations on the microelectrodes after accelerated aging show that

there is no measurable and statistically significant difference on the surface roughness of the microelectrodes before and after aging. This strongly supports the observation that GC experiences no corrosion for voltage excursions applied within its wide electrochemical window of 2.4 volts [4]. Further, the maintenance of strong mechanical integrity of the probes after 1000 hours of accelerated aging under active electrical stimulation indicate that the attachment between GC microstructures and polyimide remains excellent. We had previously shown that the interface between GC and polyimide is dominated by strong hydrogen bonds through hydroxyl and carbonyl groups as well as covalent bonds through anhydride groups [25].

It is important to closely examine if this exceptional performance in mechanical integrity is accompanied with equally superior electrical and electrochemical performance. For that, a closer examination of surface electrochemical kinetics in GC microelectrodes will provide useful parameters for assessing the performance of these microelectrodes under recording and electrical stimulation conditions. For example, CSC is typically an excellent indicator of the type of dominant current transduction in a microelectrode (i.e., faradaic Vs double-layer charging). In this study, we show that for GC microelectrodes made of a single and homogenous material with no coating of any kind, CSC is as high as $61.4 \pm 6.9\ mC/cm^2$. This value is slightly lower than that of carbon nanotubes (CNT) directly grown on metal microelectrodes ($70.8 \pm 1.1\ mC/cm^2$)14,15, but much larger than porous graphene ($50\ mC/cm^2$)17. For further comparison, CSC for PEDOT-PSS coatings is $40.4 \pm 4.8\ mC/cm^2$ while it is $893.5 \pm 137.8\ mC/cm^2$ for PEDOT-PSS-CNT coatings and ~$90\ mC/cm^2$ for AIROF (Activated Iridium Oxide Film) microelectrodes [26-30]. All these microelectrode materials, however, utilize a coating on top of a thin-film metal layer. In the case of AIROF, it has an additional drawback of transferring charges through faradaic reactions that could result in microelectrode degradation and tissue damage. Therefore, our data support the interpretation that GC has the highest reported CSC for a single and homogenous probe material. In fact, if the surface of GC could be made porous through plasma etching or similar processes, the CSC value may further increase significantly.

Additional insight into electrode kinetics in GC microelectrodes can be obtained from voltage transients. The voltage transients in GC, in both negative and positive excursions, show a rapid and almost instantaneous convergence in the voltages suggesting a very fast electrode polarization. Pt microelectrodes, on the other hand, show a steep slope and slower polarization before Vmax-neg or Vmax-pos are reached. The voltage residuals at the end of each pulse cycle are also revealing in terms of the speed of charging and discharging. GC microelectrodes almost instantaneously converge back to starting potential whereas Pt still has significant voltage residual. In addition, electrode overpotential ($\eta$), which represents the deviation from the equilibrium potential ($E - E_{eq}$), is mainly driven by redox process and is a very good indicator of surface electrode kinetics [18,29-31]. The net voltage drop at the electrode is a sum of the Ohmic IR drop, electrode overpotential (drives redox at electrode/electrolyte interface), solution overpotential (due to transient charge distribution), and the shift in the equilibrium potential of the electrode (i.e., $\Delta V = IR + \eta_{electrode} + \eta_{sol} + \Delta E_o$)18. Here, the same buffer is used for GC and Pt microelectrodes. Therefore, the differences in $\Delta V$ between the two materials are mostly due to electrode overpotential ($\eta_{electrode}$), and to a lesser extent on solution overpotential ($\eta_{sol}$). The overpotential of GC is significantly lower than that of Pt (0.38 Vs 0.48 V) suggesting that the voltage drop at the GC microelectrode surface due to overpotential accompanied by double layer charging and discharging is low (i.e., no reaction occurs). This is expected as overpotential is mainly influenced by faradaic reactions that are dominant in Pt microelectrodes.

With regard to accelerated aging under electrical stimulation, the charge density used in the experiments reported here (i.e., 0.25 mC/cm$^2$) is consistent with the charge density used to evoke sensations in humans using millimeter-scale ECoG electrodes [32]. In the literature, there have been several reports of accelerated aging tests with and without electrical stimulation. With respect to passive (non-electrical) accelerated aging, thin-film Pt microelectrodes with adhesion promoters (i.e., polyimide-DLC-SiC-Pt) subjected to constant temperature of 37 °C for a period of 1 year [33], silicon carbide microelectrodes immersed in a buffer heated to 96 °C for 1600 hours [34], and PEDOT-coated microelectrodes immersed in buffer for 4 weeks have been reported [28]. These tests, however, were limited to either mechanical shear

strength or current leakage of the probes. Electrical stimulation tests were reported for iridium microelectrodes with 2 billion cycles applied over ~167 hours (0.25 mC/cm$^2$) [35], porous graphene microelectrodes under 1 million biphasic current pulses [17], GC with adhesion promoters (SiC and DLC) under 20 million pulses (0.2 mC/cm2) [36], CVD-CNT-coated electrodes under 1 million pulses (1.6 mC/cm$^2$) [15], and PEDOT-coated electrodes subjected to 24-hour biphasic stimulation (3 mC/cm$^2$) [29]. In general, the use of coatings is often a point of weakness, especially in cases where there is active electrical stimulation. A variety of materials such as titanium nitride, iridium oxide, PEDOT, and carbon nanotube composites have been adopted as coating layers [37-47]. However, these materials are prone to delamination during stimulation and long-term implantations, caused typically by poor adhesion between the coating material and the metal electrode [37,38,45]. Our current work is the first reported case where any neural probe, either with or without a coating, is subjected to 1000 hours and 3.5 billion cycles of active electrical current pulses. During these tests our probe exhibited no corrosion, delamination, or any sort of mechanical or electrical failure. Furthermore, on the same GC microelectrodes, we carried out an even more aggressive test at charge injection limit of 3 mC/cm$^2$ with a cathodic-first charge balanced bi-phasic current pulses consisting of 5.1 mA amplitude, 400 μsec cathodic half-phase period and a frequency of 1 kHz in saline solution (0.01 M PBS) applied for 50 million pulses. Once again, GC microelectrodes survived this extreme test with no delamination of polymeric layers and no corrosion of electrodes. Further comparisons are given in Supplementary Table 1.

What drives this resistance to corrosion in GC microelectrodes? In the case of GC microelectrodes reported here, the ability to withstand such a high number of cycles of pulses can be explained by the fact that (i) GC is a homogeneous material with no crystalline structure; hence devoid of granular surfaces that could act as points of initiation of corrosive chemical reactions during stimulation [1,2] and (ii) weaker metal adhesion layers have been eliminated. A previous study using AFM and SEM characterization demonstrated that surface roughness of GC is only a few nanometers, an order of magnitude smaller than typical thin-film metal electrodes [4,47]. In addition to this smoothness in surface, the current study has

demonstrated that absence of a thin-film adhesion (Cr or Ti) and thin-film metal layer (Pt or Au) eliminates any potential Galvanic corrosion in probes [48]. This is a key distinguishing aspect of the technology presented here.

In addition, our demonstration of high-resolution real-time in-vitro neurotransmitter detection through background-subtracted FSCV using GC microelectrodes highlights the versatility and multi-modal (electrical and electrochemical) recording capabilities of the platform. Driven by its high spatiotemporal resolution and ability to detect sub-second fluctuations in neurotransmitter concentrations, FSCV has become a technique of choice for neurotransmitter detection. The 10 nM limit of detection (LOD) for dopamine reported here is one of the lowest ever reported in the literature. Given that biologically relevant dopamine concentration characteristic of living systems is within 26–40 nM [49], such a low LOD represents significant progress in this area. There are several reports in the literature that document similar level of sensitivity. For example, CNT directly grown on metal microelectrodes (CNT-Nb) have shown dopamine detection limit of $11 \pm 1$ nM[50], whereas SWCNT (Single Walled CNTs) on metal microelectrodes have shown LOD of 17 nM[51]. Further, for carbon nanofibers modified by PEDOT/graphene oxide coating, LOD of 85 nM was reported[52] while laser-treated CNT yarn microelectrodes (CNTYMEs) have been shown to have LOD down to $13 \pm 2$ nM[53]. Further comparisons are given in Supplementary Table 2. As shown in the table, the GC LOD of 10 nM is superior to all other probes measured. Further, it is noteworthy that the majority of FSCV experiments reported in the literature were performed using carbon-fiber microelectrodes or single microelectrodes, allowing only single measurements. Glassy carbon microelectrodes, on the other hand, are suited for multi-site FSCV detection, similar to reported 3D carbon nanofiber microelectrode arrays (MEAs) fabricated through $O_2$ plasma-assisted pyrolysis [54], and pyrolyzed carbon MEAs using thin positive resists on non-biocompatible silicon substrates that were used for dopamine detection [55].

An obvious question is what drives this high neurotransmitter sensitivity? GC surfaces–as reported here –- are ideal for detecting neurotransmitter electrochemical activity due to the intrinsic hydroxyl groups

that form on their surfaces [25]. These hydroxyl groups are favorable for adsorption of cationic species such as dopamine whose amine side chain gets protonated at physiological pH [56]. Further, the strength of adsorption of dopamine at GC surface (and hence sensitivity) has been shown to correlate with increased heterogeneous electron transfer kinetics. This is an advantage of GC, as demonstrated in the voltage transients of Fig. 4c–e.

## 4. Conclusions

In this study, we introduced the first use of all glassy carbon probe structure where microelectrodes, traces, and bump-pads are all fabricated from a single and homogeneous GC material. The probe experienced no measurable corrosion after a very aggressive accelerated aging test that involved 3.5 billion cycles of pulses. Through extensive characterizations, the versatility of this material, that may accelerate the translation of neuroprosthetic devices to clinical use, was demonstrated.

The following points highlight some of the key findings reported in this work:

1. The process introduced is compatible with MEMS and semi-conductor processes making the fabrication of these electrodes and their integration with CMOS a possibility.

2. GC microelectrodes have high SNR (>16) in-vivo recordings capability.

3. The accelerated aging introduced here is a record-setting 3.5 billion cycles of bi-phasic charge-balanced pulse train over period of 1000 hours. To the best of our knowledge, this is the first report on pulsing at this level and duration.

4. The corrosion rate in GC is very minimal and there was no difference between new and aggressively aged microelectrodes.

5. There was no failure at the GC and polyimide interface after 3.5 billion pulses and 1000 hours of immersion in a buffer. This suggests a strong mechanical robustness at the interface of microelectrodes and

the supporting as well as insulating substrates aided by both hydrogen bonds (hydroxyl and carboxyl groups) and covalent bonds (anhydride groups).

6. GC microelectrodes have one of the highest reported CSC for single material non-coated neural probe (i.e., $61.4 \pm 6.9$ mC/cm$^2$).

7. GC microelectrodes have one of the lowest limits of detection for dopamine at 10 nM. This is a significant finding.

8. The same probe materials are capable of stimulating, as well as recording both electrical and electrochemical signals (neurotransmitters). Therefore, GC microelectrodes offer a multi-modal platform that may accelerate investigation into the interplay between electrical and electrochemical signaling in the brain.

Collectively, our results demonstrate that GC may be an ideal microelectrode material for neuroprosthetics devices given its good impedance, excellent electrochemical response, high fidelity recordings, strong resistance to corrosion after billions of pulses of electrical stimulations, and ability to electrochemically detect neurotransmitters at one of the lowest concentrations reported. It is rare to find all these attributes in a single platform.

**References**


1. O. J. A. Schueller, S. T. Brittain, C. Marzolin, and G. M. Whitesides, "*Fabrication and Characterization of Glassy Carbon MEMS*," Chem. Mater., vol. 9, pp. 1399–1406, 1997.

2. S. Ranganathan, R.L. McCreery, S.M. Majji, M. Madou, J. "*Photoresist-Derived Carbon for Microelectromechanical Systems and Electrochemical Applications,*" Electrochem. Soc. 147 (2000) 277-282.

3. Vomero, M. et al. "*Novel Pattern Transfer Technique for Mounting Glassy Carbon Microelectrodes on Polymeric Flexible Substrates*", *Journal of Micromechanics and Microengineering* **26** (2016).

4. M. Vomero, E. Castagnola, F. Ciarpella, E. Maggiolini, N. Goshi, E. Zucchini, S. Carli, L. Fadiga, S. Kassegne, D. Ricci, "*Highly Stable Glassy Carbon Interfaces for Long-Term Neural Stimulation and Low-Noise Recording of Brain Activity*", Nature Sci. Rep 7 (2017) 40332. doi: 10.1038/srep40332.

5. Kassegne, S. et al. "*Electrical impedance, electrochemistry, mechanical stiffness, and hardness tunability in glassy carbon MEMS μECoG electrodes*", *Microelectronic Eng.* **133,** 36–44 (2015).

6. Kozai, T.D.; Kipke, D.R. Insertion shuttle with carboxyl terminated self-assembled monolayer coatings for implanting flexible polymer neural probes in the brain. J. Neurosci. Methods 2009, 184, 199–205

7. Novoselov, K.S., et al, Science*,* 306, 666–669 (2004).

8. Narayan, Jagdish; Bhaumik, Anagh (2015-12-07). *"Novel phase of carbon, ferromagnetism, and conversion into diamond*". *Journal of Applied Physics*. **118** (21): 215303.

9. Hu, M., He, J., Zhao, Z., Strobel, T.A., et al, "*Compressed glassy carbon: An ultrastrong and elastic interpenetrating graphene network", SCIENCE ADVANCES*, 2017, E1603213.

10. Ievins. A. and Moritz, C. T., "*Therapeutic Stimulation for Restoration of Function After Spinal Cord Injury," Physiology (Bethesda)* **32** 391-8, 2017.

11. Bucher, E. S., Brooks, K., Matthew D. Verber, Richard B. Keithley, Catarina Wesson-White, Susan Carroll, Pavel Takmakov, Collin J. McKinney, and R. Mark Wightman, "*A Flexible Software Platform for Fast-Scan Cyclic Voltammetry Data Acquisition and Analysis*," Anal Chem. 2013 Nov 5;85(21):10344-53. doi: 10.1021/ac402263x.

12. Song, W., Truong, D. Q., Bikson, M. & Martin, J. H. Trans-Spinal Direct Current Stimulation Immediately Modifies Motor Cortex Sensorimotor Maps. Brain Stimulation: Basic, Translational, and Clinical Research in Neuromodulation 10(1), e18 (2017).

13. Winnie, J., Yoshida, K. & Hofmann, U. G. In-vivo implant mechanics of flexible, silicon-based ACREO microelectrode arrays in rat cerebral cortex. IEEE Transactions on Biomedical Engineering 53(5), 934–940 (2006).

14. Ansaldo, A., Castagnola, E., et al., "*Superior Electrochemical Performance of Carbon Nanotubes Directly Grown on Sharp Microelectrodes*," ACS Nano, 2011, 5 (3), pp 2206–2214.

15. E Castagnola, A Ansaldo, L Fadiga, D Ricci, "*Chemical vapour deposited carbon nanotube coated microelectrodes for intracortical neural recording*," physica status solidi (b), 2010

16. K. Wang, H. A. Fishman, H. Dai, and J. S. Harris Neural Stimulation with a Carbon Nanotube Microelectrode Array, Nano Lett., 2006, 6 (9), pp 2043–2048, DOI: 10.1021/nl061241t

17. Lu, Y., Lyu, H., Richardson, A. G., Lucas, T. H. & Kuzum, D. Flexible Neural Electrode Array Based-on Porous Graphene for Cortical Microstimulation and Sensing. Scientific Reports, 6:33526, https://doi.org/10.1038/srep33526.

18. Cogan, S. F. Neural stimulation and recording electrodes. Annu. Rev. Biomed. Eng. 10, 275–309 (2008).

19. Cui, X. & Martin, D. C. Fuzzy gold electrodes for lowering impedance and improving adhesion with electrodeposited conducting polymer films. Sens. Actuators. 103, 384–399 (2003)

20. Macdonald, J. R. Impedance Spectroscopy: Emphasizing solid materials and systems (Wiley, 1987)

21. Parker, J. R. et al. Testing of thin-film electrode arrays for cochlear implants of the future, Biomedical Research in the 3rd Millennium. Proceedings of the Inaugural Conference of the Victorian chapter of the IEEE Engineering in Medicine and Biology Society, Caulfield, Victoria (1999)

22. Purnakala V.Samanta, Filomena Gonçalves, Maria Madalena A.Freitas, Manuel Fernando R.Pereira, José L.Figueire, "*Surface activation of a polymer based carbon*," J. Carbon, Volume 42, Issue 7, 2004, Pages 1321-1325.

23. Goshi, N., Vomero, N., Dryg, I. & Kassegne, S. Modeling and Characterization of Tissue/Electrode Interface in Capacitive μECoG Glassy Carbon Electrodes. ECS Trans. 72(1), 83–90, https://doi.org/10.1149/07201.0083 (2016).

24. Veera Manohara Reddy Y, Prabhakara Rao V, Vijaya Bhaskar Reddy A, Lavanya M, Venu M, Lavanya M, Madhavi G., "*Determination of dopamine in presence of ascorbic acid and uric acid using poly (Spands Reagent) modified carbon paste electrode*," Mater Sci Eng C Mater Biol Appl. 2015 Dec 1;57:378-86. doi: 10.1016/j.msec.2015.08.005.

25. M Hirabayashi, B Mehta, NW Vahidi, A Khosla, S Kassegne, "*Functionalization and characterization of pyrolyzed polymer based carbon microstructures for bionanoelectronics platforms,*" Journal of Micromechanics and Microengineering 23 (11), 115001

26. Castagnola, E., Biso, M. & Ricci, D. "*Improvement of polypyrrole and carbon nanotube co-deposition techniques for high charge transfer electrodes*," Phys. Status Solidi (B). 246, 2469–2472 (2009).

27. Castagnola, V., Bayon, C., Descamps, E. & Bergaud, C. "*Morphology and conductivity of PEDOT layers produced by different electrochemical routes*." Synth. Met. 189, 7–16 (2014).

28. Castagnola, E. et al. "*PEDOT-CNT-coated low-impedance, ultra-flexible, and brain-conformable micro-ECoG arrays". Neu Sys and Rehab Eng,* IEEE Trans, 23, 342-350 (2015).

29. Venkatraman, S., Jeffrey Hendricks, Zachary A. King, Andrew J. Sereno, Sarah Richardson-Burns, David Martin, and Jose M. Carmena, "*In Vitro and In Vivo Evaluation of PEDOT Microelectrodes for Neural Stimulation and Recording*," IEEE TRANSACTIONS ON NEURAL SYSTEMS AND REHABILITATION ENGINEERING, VOL. 19, NO. 3, JUNE 2011 307

30. Beebe X, Rose TL. 1988. "*Charge injection limits of activated iridium oxide electrodes with 0.2 ms pulses in bicarbonate buffered saline"*. IEEE Trans. Biomed. Eng. 35:494–95

31. Kassegne, S.K., Reese, H., Hodko, D., Yang, JM., Sarkar, K., Smolko, S., Swanson, P., Raymond, D., Heller, M.J., and Madou, M.J., "Numerical Modeling of Transport and Accumulation of DNA on Electronically Active Biochips", Journal of Sensors and Actuators B: Chemical, Volume 94, pp. 81–98, Elsevier Science B.V, 2003

32. Johnson, L. A. Wander JD, Sarma D, Su DK, Fetz EE, Ojemann J.G. "*Direct electrical stimulation of somatosensory cortex in humans using electrocorticography electrodes: a qualitative and quantitative report*". *J. Neural Eng.* 10, 036021 (2013).

33. J.S. Ordonez, C. Boehler, M. Schuettler, and T. Stieglitz. "*Long-term adhesion studies of polyimide to inorganic and metallic layers,*" In Symposium TT Interfaces in Materials, Biol. and Phys., Volume 1466 of MRS Proceedings, 2012.

34. Diaz-Botia et al, 2017, J. Neural Eng., doi.org/10.1088/1741-2552/aa7698.

35. Arreaga-Salas, D.E., Avendaño-Bolívar, A., Simon, D., Reit, R., Garcia-Sandoval, A., Rennaker, R.L., Voit, W., "*Integration of High-Charge-Injection-Capacity Electrodes onto Polymer Softening Neural Interface*s", American Chemical Society (2015).

36. M. Vomero, E. Castagnola, J. S. Ordonez, S. Carli, E. Zucchini, E. Maggiolini, C. Gueli, N. Goshi, F. Ciarpella, C. Cea, L. Fadiga, D. Ricci, S. Kassegne, T. Stieglitz, *Incorporation of Silicon Carbide and Diamond-Like Carbon as Adhesion Promoters Improves In Vitro and In Vivo Stability of Thin-Film Glassy Carbon ECoG Arrays,* Advanced Biosystems (No. adbi.201700081R2), accepted October **2017**

37. Weiland, J. D., Anderson, D. J. & Humayun, M. S. "*In vitro electrical properties for iridium oxide versus titanium nitride stimulating electrodes*," Biomedical Engineering, IEEE Transactions on 49, 1574–1579 (2002).

38. Cogan, S. F., Guzelian, A. A., Agnew, W. F., Yuen, T. G. & McCreery, D. B. "*Over-pulsing degrades activated iridium oxide films used for intracortical neural stimulation,*" Journal of Neuroscience Methods 137, 141–150 (2004).

39. Cui, X. T. & Zhou, D. D. "*Poly (3,4-ethylenedioxythiophene) for chronic neural stimulation,"* Neural Systems and Rehabilitation Engineering, IEEE Transactions on 15, 502–508 (2007).

40. Wilks, S. J., Richardson-Burns, S. M., Hendricks, J. L., Martin, D. C. & Otto, K. J. "*Poly (3,4-ethylenedioxythiophene) as a microneural interface material for electrostimulation*," Frontiers in Neuroengineering 2, 7 (2009).

41. Rose, T., Kelliher, E. & Robblee, L. "*Assessment of capacitor electrodes for intracortical neural stimulation,"* Journal of Neuroscience Methods 12, 181–193 (1985).

42. Jan, E. et al. "*Layered carbon nanotube-polyelectrolyte electrodes outperform traditional neural interface materials*," Nano Letters 9, 4012–4018 (2009).

43. Castagnola, E. et al. "*PEDOT-CNT-Coated Low-Impedance, Ultra-Flexible, and Brain-conformable Micro-ECoG Arrays*," IEEE Transactions on Neural Systems and Rehabilitation Engineering, 23 342–350 (2015).

44. Bullara, L., McCreery, D., Yuen, T. and Agnew, W. "*A microelectrode for delivery of defined charge densities*," Journal of Neuroscience Methods 9, 15–21 (1983).

45. A Prasad, QS Xue, R Dieme, V Sankar, RC Mayrand, "*Abiotic-biotic characterization of Pt/Ir microelectrode arrays in chronic implants*", Frontiers in Neuroengineering, 2014.

46. Kozai, TDY., Catt, K., Du, Z., Na, K., Srivannavit, O., Haque, RM., Seymour, J., Wise, KD., Yoon, E., and Cui, XT., "*Chronic In Vivo Evaluation of PEDOT/CN*T", IEEE TRANSACTIONS ON BIOMEDICAL ENGINEERING, VOL. 63, NO. 1, JANUARY 2016 111.

47. NU Huynh, N Yamada, H Furukawa, G Youssef, A Khosla, S Kassegne, "*Effect of Thin Film Platinum Microelectrode Granularity on Corrosion under Electrical Stimulation*", ECS Meeting Abstracts, 1064-106.

48. Erin Patrick, Mark E.Orazem, Justin C.Sanchez, Toshikazu Nishida, "Corrosion of tungsten microelectrodes used in neural recording applications", Journal of Neuroscience Methods, Volume 198, Issue 2, 15 June 2011, Pages 158-171

49. K. Jackowska and P. Krysinsky, Anal Bioanal Chem 405, 3753-3771 (2013)

50. C.Yang, C. B. Jacobs, M. D. Nguyen, M. Ganesana, A. G. Zestos, I. N. Ivanov, A. A. Puretzky, C. M. Rouleau, D. B. Geohegan, and B. J. Venton, Carbon Nanotubes Grown on Metal Microelectrodes for the Detection of Dopamine, Anal. Chem., 88, 645−652, 2016, DOI: 10.1021/acs.analchem.5b01257

51. Ning Xiao and B. Jill Venton, "*Rapid, sensitive detection of neurotransmitters at microelectrodes modified with self-assembled SWCNT forests*," Anal Chem. 2012 Sep 18; 84(18): 7816–7822.doi: 10.1021/ac301445w)

52. Taylor IM, Robbins EM, Catt KA, Cody PA, Happe CL, Cui XT. "Enhanced dopamine detection sensitivity by PEDOT/graphene oxide coating on in vivo carbon fiber electrodes," Biosens Bioelectron. 2017;89(Pt 1):400-410. doi: 10.1016/j.bios.2016.05.084.

53. C. Yang, E. Trikantzopoulos, M. D. Nguyen, C. B. Jacobs, Y. Wang, M. Mahjouri-Samani, I. N. Ivanov, and B. J. Venton, "*Laser Treated Carbon Nanotube Yarn Microelectrodes for Rapid and Sensitive Detection of Dopamine in Vivo*," DOI: 10.1021/acssensors.6b00021 ACS Sens. 2016, 1, 508−515).

54. Wenwen Yi, Yuanyuan Yang, Parastoo Hashemi, Mark Ming-Cheng Cheng, "*3D carbon nanofiber microelectrode arrays fabricated by plasma-assisted pyrolysis to enhance sensitivity and stability of real-time dopamine detection*," Biomed Microdevices (2016) 18: 112 DOI 10.1007/s10544-016-0136-1).

55. Matthew K. Zachek, Pavel Takmakov, Ben Moody, R. Mark Wightman, Gregory S. McCarty, "*Simultaneous Decoupled Detection of Dopamine and Oxygen using Pyrolyzed Carbon Microarrays and FSCV*," Anal Chem. 2009 Aug 1; 81(15): 6258–6265.doi: 10.1021/ac900790m)

56. Bath, B. D. et al. Sub-second Adsorption and Desorption of Dopamine at Carbon-Fiber Microelectrodes. Anal. Chem. 72(24), 5994–6002, https://doi.org/10.1021/ac000849y (2000).

**Acknowledgments**

Chapter 2, in full, is a reprint of materials as it appears in Nimbalkar, Surabhi, Elisa Castagnola, Arvind Balasubramani, Alice Scarpellini, Soshi Samejima, Abed Khorasani, Adrien Boissenin, Sanitta Thongpang, Chet Moritz, and Sam Kassegne. "Ultra-capacitive carbon neural probe allows simultaneous

long-term electrical stimulations and high-resolution neurotransmitter detection." *Scientific reports* 8, no. 1 (2018): 1-14. The dissertation author was the co-primary author of this paper.

# CHAPTER III

## Glassy Carbon Microelectrodes Minimize Induced Voltages, Mechanical Vibrations and Artifacts in Magnetic Resonance Imaging

**Abstract**

The recent introduction of glassy carbon (GC) microstructures supported on flexible polymeric substrates has motivated the adoption of GC in a variety of implantable and wearable devices. Neural probes such as electrocorticography and penetrating shanks with GC microelectrode arrays used for neural signal recording and electrical stimulation are among the first beneficiaries of this technology. With the expected proliferation of these neural probes and potential clinical adoption, the magnetic resonance imaging (MRI) compatibility of GC microstructures needs to be established to help validate this potential in clinical settings. Here, we present GC microelectrodes and microstructures—fabricated through the carbon micro-electro-mechanical systems process and supported on flexible polymeric substrates—and carry out experimental measurements of induced vibrations, eddy currents, and artifacts. Through induced vibration, induced voltage, and MRI experiments and finite element modeling, we compared the performances of these GC microelectrodes against those of conventional thin-film platinum (Pt) microelectrodes and established that GC microelectrodes demonstrate superior magnetic resonance compatibility over standard metal thin-film microelectrodes. Specifically, we demonstrated that GC microelectrodes experienced no considerable vibration deflection amplitudes and minimal induced currents, while Pt microelectrodes had significantly larger currents. We also showed that because of their low magnetic susceptibility and lower conductivity, the GC microelectrodes caused almost no susceptibility shift artifacts and no eddy-current-induced artifacts compared to Pt microelectrodes. Taken together, the experimental, theoretical, and finite element modeling establish that GC microelectrodes exhibit significant MRI compatibility, hence demonstrating clear clinical advantages over current conventional thin-film materials, further opening avenues for wider adoption of GC microelectrodes in chronic clinical applications.

## 1 Introduction

Increasingly, carbon is becoming a compelling material of choice for the micro- and nanofabrication of a variety of micro devices with applications varying from biochemical sensors to microcapacitors and batteries [1-3]. The recent introduction of neural probes consisting of glassy carbon

(GC) microelectrodes microfabricated through carbon micro-electro-mechanical systems (C-MEMS) technology and transferred to flexible polymer substrates has opened up significant opportunities in wearable and implantable carbon devices. This trend will continue as more evidence supporting the superior performance of GC microstructures in applications requiring extended electrical, electrochemical, and mechanical stability under chronic in vivo conditions emerge [4].

In the meantime, magnetic resonance imaging (MRI) is increasingly being used under pre- and post-surgery conditions for the brain imaging of patients as well as animal models already implanted with electrocorticography (ECoG) or deep brain stimulation (DBS)-type neural probes. These MRI modalities are typically needed to investigate outcomes of DBS or chronic sulcus electrode placement and to evaluate pathological abnormalities related to electrode implantation [5]. They are also used for guiding surgery in chronically implanted microelectrode arrays in inaccessible areas of the cortical sulcus where a magnetization-prepared rapid acquisition with gradient-echo (MPRAGE) sequence is acquired for stereotaxically positioning the array [6]. In addition, the 3D atlas MRI co-registration method has been used to localize stimulating electrodes of DBS systems in Parkinson's disease patients [7].

However, there is a significant number of documented cases where neural implants give rise to visible artifacts in MRI images [8]. Specifically, these MR images have shown distortion artifacts due to mismatches in the magnetic susceptibility of electrode materials and brain tissue, leading to inaccurate observations of electrodes in MR images due to hypo or hyper signals at these interfaces [7]. Furthermore, the interaction between conductive materials and radio frequency (RF) fields results in the heating of electrode surfaces, in which the transmitted RF field is absorbed in the electrode material, causing heating [9,10]. An increase in temperature up to 7 °C due to RF electrical field induction of current in the leads of electrodes has been reported11. In addition, since neural implant materials are usually tested under high magnetic fields (up to 3 T), excitation by RF and rapidly switching gradients cause not only imaging artifacts but also eddy currents. The use of MRI, therefore, understandably raises concerns about risks such as heating of the cortex due to induced currents [11,12] and mechanical movements of electrodes due to gradient-induced vibrations.

In general, while designing cortical electrode arrays compatible with MRI, the hazards to be considered are (1) forces generated due to the interaction between gradient fields and the static $B_0$ field with the implanted electrode, (2) induced voltages due to a changing gradient field and RF field and movement of the electrode inside the scanner, (3) heating of the electrode due to RF pulses and electric fields generated by a time-varying magnetic field, and (4) imaging artifacts originating from (a) susceptibility mismatch between the electrode material and surrounding brain tissue and/or (b) $B_1$-field distortion due to induction8. To avoid or minimize the imaging artifacts, electrode materials with magnetic susceptibility matching that of brain tissue have been introduced, such as printed carbon ink electrodes on organic polymer substrates [13], titanium-based microelectrodes [14], silicon microelectrodes for neural recording and stimulations[15], and carbon nanotube yarn electrodes[16]. However, while these materials have good MRI compatibility, they nonetheless suffer from a lack of long-term electrical and electrochemical stability. In this study, therefore, we build upon the excellent magnetic susceptibility performance of carbon materials and the excellent stability of GC4 and investigate the response of GC microelectrodes to MRI from the perspective of induced voltages, mechanical forces, and vibrations, as well as artifacts. We additionally create a finite element model (FEM) to validate the experimental measurements of induced voltages, currents, and mechanical forces. The aim is, therefore, to extend the application of GC to implantable devices, where other modalities such as live and simultaneous MRI are required for clinical purposes on subjects with implanted neural devices.

## 2 Materials and Methods

### 2.1 Microfabrication of GC Microelectrodes

To investigate and compare the MRI compatibility of GC microelectrodes and thin-film metal microelectrodes, we fabricated probes made of both GC and Pt microelectrodes in two sets as shown in Fig. 1. The first set consisted of a ground electrode of an ECoG probe (one with GC and another with Pt with a rectangular geometry of 2 cm × 1 cm) supported on a polymer substrate, while the second set consisted of ring electrodes of 5 cm outer diameter and 3 cm internal diameter supported on a silicon wafer. Ground microelectrodes were selected for the MRI study because they represented microelectrodes with the largest

surface area in an array of recording and stimulation electrodes in neural probes. The core C-MEMS microfabrication technology that is used for these GC devices supported on polymeric substrates is described in detail elsewhere [17]. Briefly, a SU8-10-negative photoresist (Microchem, Westborough, MA, USA) with a final thickness of 6 μm was spin coated, and a ground microelectrode (2 cm × 1 cm) was patterned. Pyrolysis of the negative resist layer was conducted following protocols described elsewhere [18,19]. In brief, the pyrolysis of the patterned microelectrode array was carried out in a quartz furnace under a vacuum or an inert atmosphere of nitrogen gas with a flow of 50 ml/min at 1000 °C for 90 min. The ensuing GC layer was then covered with a layer of non-photosensitive Durimide 115a and patterned (protocol described elsewhere)4. Subsequently, a thicker layer of Durimide 7520 (Fujifilm USA, Inc., Mesa, AZ, USA) was photolithographically patterned to provide a stiffer substrate for the ground microelectrode. This was followed by etching of the silicon dioxide in a buffered hydrofluoric acid bath. For the probes with Pt ground microelectrodes, conventional metal lift-off on a polymer layer was carried out. The details are given in the Supplementary Section (Fig. S1).

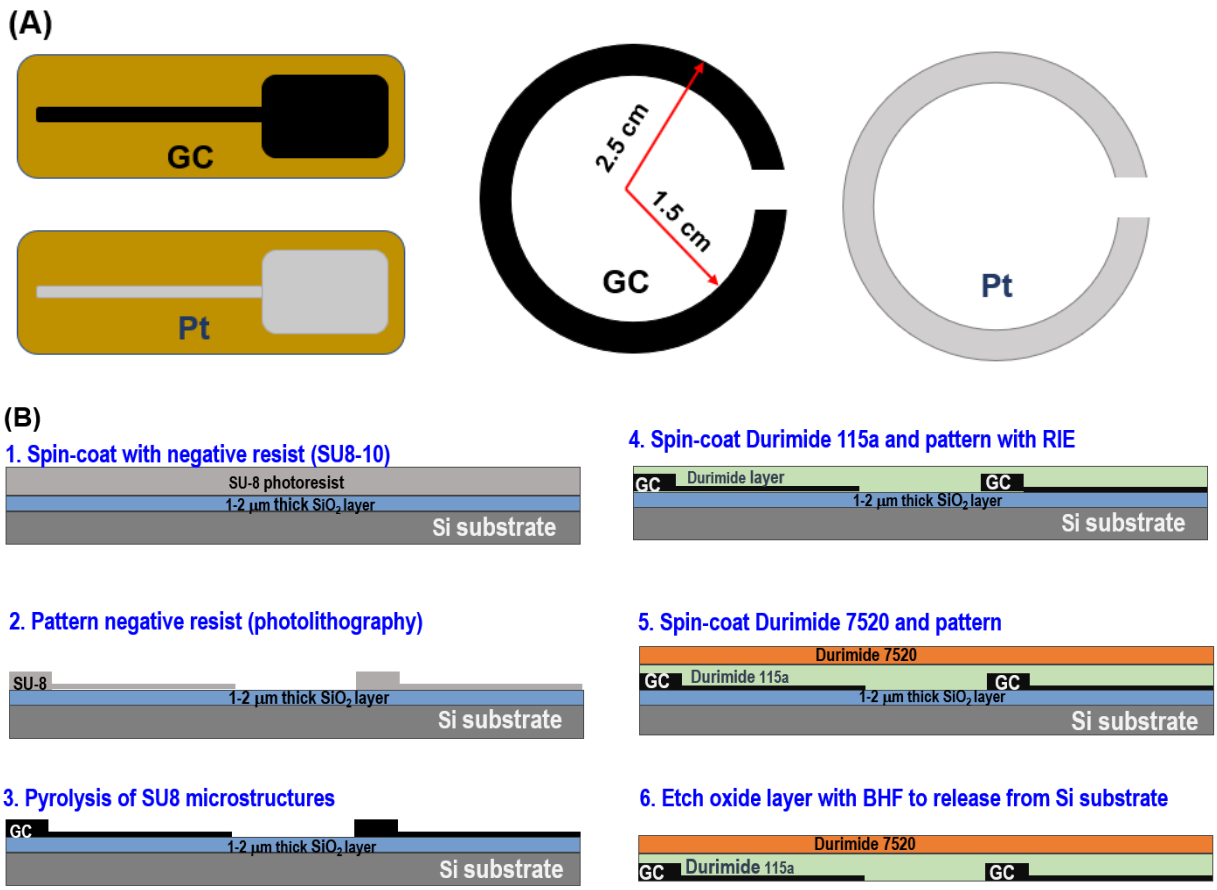



**Figure 3.1** (A) Probes with GC and Pt ground microelectrodes of 2cm x 1cm geometry supported on polyimide substrate, and circular GC and Pt microelectrodes (OD = 5 cm, ID = 3 cm) supported on silicon substrate, (B) UV Photo lithography steps for microfabrication of GC microelectrodes on flexible substrate.

**MRI Measurements**

MR images of GC and Pt microelectrodes of identical dimensions (2cm x 1cm) shown in Figure 1A were acquired by a Siemens 3T Prisma scanner that is commonly used for clinical imaging (**Siemens GmbH, Erlangen, Germany**). In order to simulate the brain tissue environment, a phantom was prepared by dissolving phosphate buffered saline (PBS, 0.01 M) in agarose in a glass petri dish, where subsequently GC and Pt microelectrodes were immersed. The agarose gel solution was allowed to solidify to avoid trapping of bubbles**.** As shown in **Figure 2,** the agarose phantom with the microelectrodes was then placed on top of the MRI phantom (Solution N per 1000g $H_2O$ dist.: 3.75g $NiSO_4 \times 6H_2O$, 5g NaCl, 5300 ml, Siemens Healthcare GmbH, Germany) to position the microelectrode near the isocenter of the coil. MR

images of the PBS-Agarose phantom with GC and Pt microelectrodes were collected to test for MRI artifacts (Figure 2A). The following MR sequences were run with the 3T scanner: (i) T1-weighted images were acquired using an inversion-prepared 3D gradient echo sequence (MPRAGE) with 0.8×0.8×0.8 $mm^3$ resolution, flip-angle=9°, TE=3.15 ms, TR=7.7 ms, TI=900 ms, FOV=200x200x179 mm, inversion repeat time=2300 ms, (ii) T2-weighted images were collected using a variable flip angle 3D turbo spin-echo sequence (SPACE) with 0.9×0.9×0.9 $mm^3$ resolution, TE=408 ms, TR=3200 ms, FOV=230x230x173 mm, averages=1.4, (iii) 2D dual echo $B_0$ field map with 3x3x2 $mm^3$ resolution, TE1 = 4.92 ms, TE2 = 7.38 ms, TR = 600 ms, FOV = 192x192 mm, flip-angle=60°, and (iv) gradient echo multiband EPI sequence (fMRI) images were acquired using a multi-band echo planar imaging sequence with 2×2×1 $mm^3$ resolution, TR=1.02 s, TE=31 ms, flip angle=60°.

Further, for higher spatial resolution, we acquired 3D gradient-echo images (GRE) and $B_0$-field maps using an 11.7T scanner (500 MHz Bruker Avance III, Ettlingen, Germany). Due to limited sample space, we trimmed the GC and Pt microelectrodes to quarter pieces and mounted them onto a sample holder that was placed inside the wide-bore magnet as shown in Figure 2b. We used a standard 3D Cartesian GRE sequence with TR = 30 ms, TE = 2.02 ms, FA = 15°, and an isotropic resolution of 100 μm. To investigate effect of $B_1$ distortion, the sample was oriented such that the $B_1$ vector was orthogonal to the surface of the electrodes [20]. The $B_0$-field map was acquired using a predefined integrated protocol in the machine software (ParaVision, FieldMap) which uses two GRE sequences with varying echo times. In this case, the samples were oriented such that the $B_1$ vector was parallel to the surface of the microelectrodes to suppress $B_1$ field distortions. The $B_0$ map parameters were identical to the GRE sequence except TE1 = 1.675 ms and TE2 = 26.811 ms.

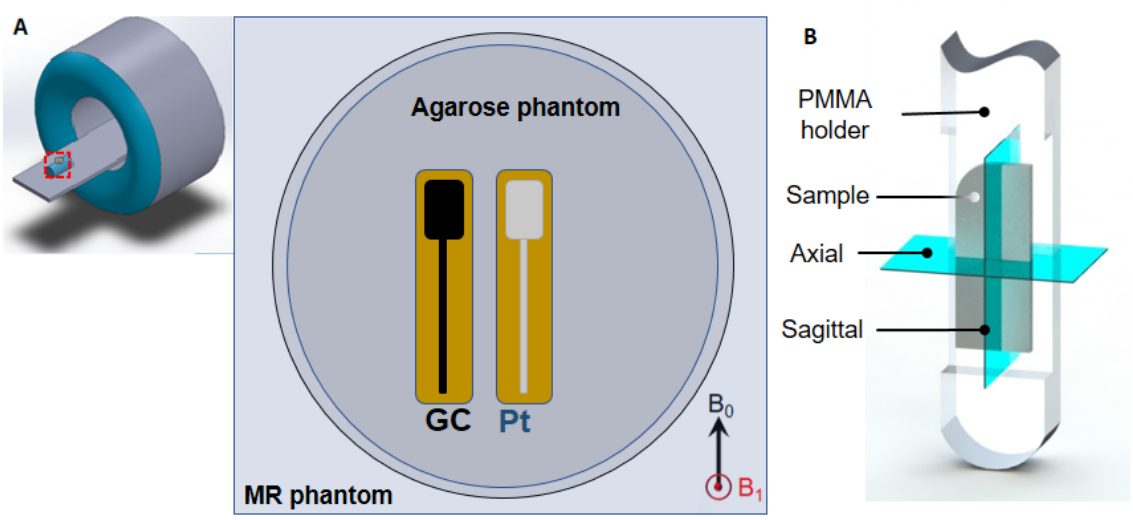



**Figure 3.2** The experimental setup used for MR imaging (A) 3T Human MRI scanner with glassy carbon and platinum microelectrodes placed on an MRI phantom and GC and Pt cortical microelectrodes immersed in an agarose, (B) quarter of microelectrode specimen mounted in 11.7 T scanner.

## 2.2 Finite Element Modelling of $B_0$-Field Map

FEM simulations of the effects observed were modeled in COMSOL Multiphysics (COMSOL AB, Sweden) using the 2cm x 1cm rectangular microelectrodes as a domain (Figure S2). Static magnetic fields ($B_0$ effects) were obtained by solving for the magnetic scalar potential using Gauss´ Law, dynamic electromagnetic behavior (gradient effects) by solving for the magnetic vector potential and current fields using Ampere's and Faraday's Laws and the radiofrequency behavior ($B_1$ effects) by solving for the electric field of the Maxwell equations. The materials simulated were Pt ($\varepsilon_r$ ~=0.735, $\chi$= 279 ppm, $\sigma$= 9.43x$10^6$ S/m), GC ($\varepsilon_r$ ~= 12.5, $\chi$ = -1.2 ppm, $\sigma$ = 6803 S/m), and PMMA ($\varepsilon_r$ ~= 2.6, $\chi$ = -1.2 ppm, $\sigma$ ~= 0 S/m) in a water phantom ($\varepsilon_r$ ~= 80, $\chi$ = -9.05 ppm, $\sigma$ ~= 0 S/m) [21-24].

## 2.3 Gradient Induced Vibration Measurements

All vibrational experiments were conducted within a 1.5T permanent magnet system (Bruker, ICON). A custom-built probe [25,26] was used to investigate the torque produced by the ground microelectrode when exposed to gradient switching. The main experimental setup is illustrated in Figure 3.

Vibration occurs if conductive structures are placed inside a static magnetic field where additional time-variable magnetic field featuring a linear gradient is superimposed. In the setup presented here, the produced torque leads to a mechanical deflection which could be precisely measured by reflection of a laser beam using a segmented photo diode.

To acquire the torque produced by different implants, we fixed the microelectrodes on a PMMA substrate and mounted it on the coil-sample interface. Then, we followed a three-step measurement protocol to determine the torque produced by the implants. The protocol is described in supplementary section C.

The mechanical setup illustrated in Figure 3 is modelled by a harmonic oscillator using Equation 1.

$$\mathrm{J}\ddot{\theta} + \Gamma\dot{\theta} + \mu\theta = \tau(t) \qquad \text{Equation 1}$$

where $J$ is the moment of inertia, $\Gamma$ is the rotational friction, $\mu$ is the torsion constant, $\tau$ is the external torque, and $\theta$ is the measured deflection angle. We designed the setup to produce the externally applied torque in two ways. The first one involved a precisely controlled current *I(t)* with respect to amplitude and frequency that was passed through an actuation coil with a determined surface area $A$. This produces a controllable torque shown in Equation 2. The normal vector of the surface $A$ with the vector of $B_0$ forms the angle $\alpha$.

$$\tau_1(t) = I(t)A\sin(\alpha)B_0. \qquad \text{Equation 2}$$

The second one involves the gradient-switching-produced eddy currents which leads to a torque $\tau_2(t)$ as given by Equation 3.

$$\tau_2(t) = -\frac{1}{8}\dot{G}_z z\pi\sigma t r_s^4 B_0 \sin(\alpha)\cos(\alpha) \qquad \text{Equation 3}$$

where $\dot{G}_z$ is the gradient slew rate, $z$ is the position of implant (center of gravity), $\sigma$ is the electrical conductivity, $t$ is the thickness of the conductive layer, $r_s$ is the largest dimension of implant, and $\alpha$ is the angle between normal vector of the implant surface with $B_0$ and $G_z$ ($B_0 \parallel G_z$). As a control group, we prepared an additional set of samples with (i) a sample exhibiting very high conductivity using a 40 µm thick copper foil (Chomerics CCK-18-101-0200) and (ii) a non-conductive empty PMMA substrate (Figure 3).

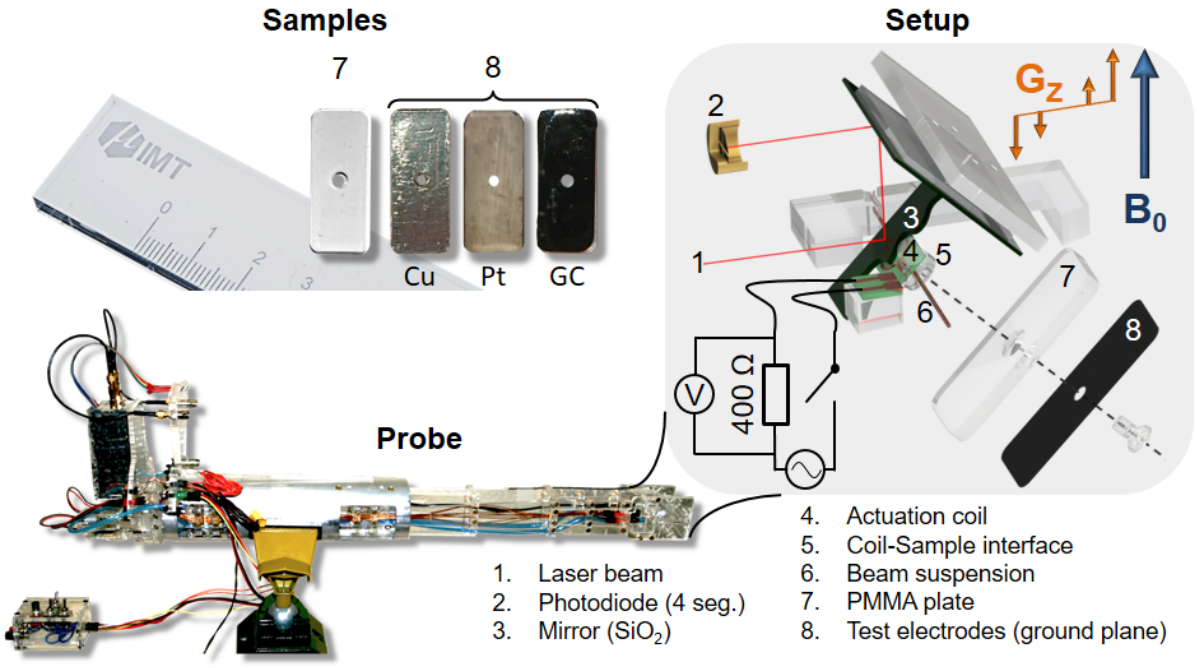



**Figure 3.3** Details of the experimental setup for the measurement of gradient induced vibrations in the field of a permanent magnet 1.5T MRI system (ICON, Bruker, Germany). *Top left:* Image with cm scale bar of the test samples. *Top right:* Illustration of the measurement head. The microelectrode (8) is fixed on a PMMA plate (7) and mounted onto a coil-sample interface. The coil-sample interface is suspended on a torsion beam for which the static angular deflection is proportional to the second moment of the cross-sectional area of the beam. The vibration is recorded by measuring the deflection of a laser beam using a segmented photodiode (2). *Bottom:* Photograph of the complete measurement probe. (Cu: Copper foil 40µm thick, Pt: Platinum microelectrode 300 nm thick, and GC: Glassy Carbon microelectrode 2 µm thick).

## 2.4 MR Induced Current and Voltage Measurements

To further investigate the performance difference between GC and Pt, we microfabricated open-loop circular dummy microelectrode structures (outer radius = 2.5 cm and inner radius 1.5 cm) out of these two materials, as shown in Figure 1. The planar geometry for both GC and Pt was the same, with Pt ≈ 300 nm thick and GC ≈ 2 µm thick. For the vibration experiments, we also prepared a highly conductive sample out of Cu tape as a control experiment. The open loop microstructures enabled direct measurement of the induced voltages and currents, as shown in Figure 4. First, we measured the resistance $R_i$ of the dummy structure using the four-terminal method (Rhode-Schwarz HM 8112-3). In a next step, we measured the induced voltage due to gradient switching in the open loop configuration, followed by a current measurement using a shunt resistor of 1Ω. In these measurements, the surface was placed orthogonal to the gradient field. Direct voltage measurements helped to avoid acoustic coupling.

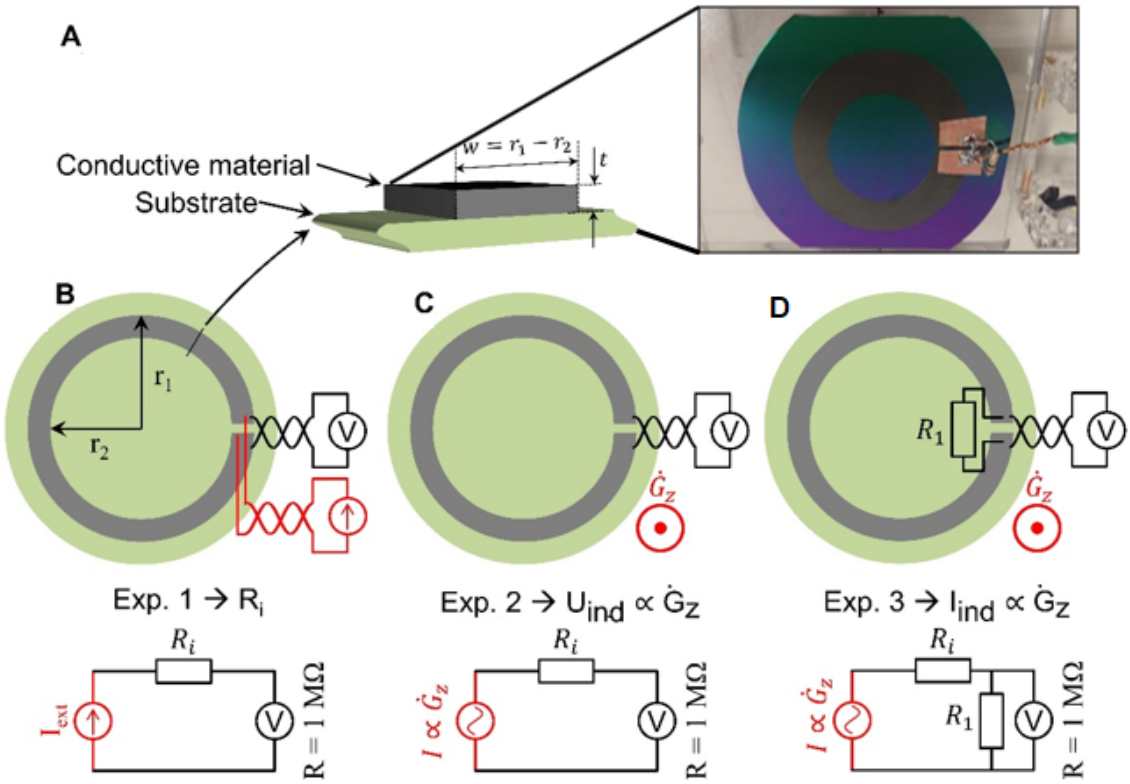



**Figure 3.4** Experimental setup to investigate the dependence of microelectrode materials on the induced eddy currents. Preparation of conductive rings using Cu (thickness t = 40 µm), Pt (t = 300 nm) and GC (t = 2 µm). The radii are $r_1$ = 2.5 cm and $r_2$ = 1.5 cm. (A) Sample on a silicon wafer (B) Measurement of $R_i$ by means of four-terminal sensing. (C) Measurement of the induced voltage due to gradient switching in open circuit mode. (D) Measurement of the induced current using a shunt resistor of 1 Ω.

# 3 Results

## 3.1 MRI Measurement

The imaging artifacts produced in the 3T scanner by the GC and Pt microelectrodes were compared in the phantom using clinical MRI sequences. In Figure 5, the first row shows T1-weighted images taken with the MPRAGE sequence, the second column shows T2-weighted images taken with the turbo spin echo (TSE) sequence. T1 and T2 weighted images are commonly used in clinical sequences and are represented in axial, sagittal and coronal views in Figure 5. The darkened rectangular shape on right side of the phantom artifact shows loss of signal or hyperintense signals (Figure 5) corresponding to an imaging artifact produced by the Pt microelectrode. High signals or bright spots are observed at the interface of the Pt microelectrode and the polyimide substrate. Since PBS saline has the same magnetic susceptibility as brain tissue, it mimics the MR environment of the brain [27]. On the left side of the phantom, an outline of the GC electrode is barely visible (Figure 5 E-F). The Pt electrode sites were ≈ 300 nm in thickness, but the distortions in MR images observed near the Pt electrode were more spread throughout the thickness of agarose phantom (4 mm) in the axial and sagittal views (Figure 5 A-D). The MR imaging in Figure 5 show that GC microelectrodes ($\chi$= -1.2 ppm [22]) have significantly less artifacts than Pt microelectrode ($\chi$=279 ppm [27]). Similarly, images captured with EPI sequence showed loss of signal at the location of the Pt microelectrode, whereas the GC microelectrode position was not differentiable from the phantom background (Supplementary Figure S.6). There is no visible differentiation between the $B_0$ field map of the GC and Pt microelectrodes, as shown in Supplementary Figure S.6b.

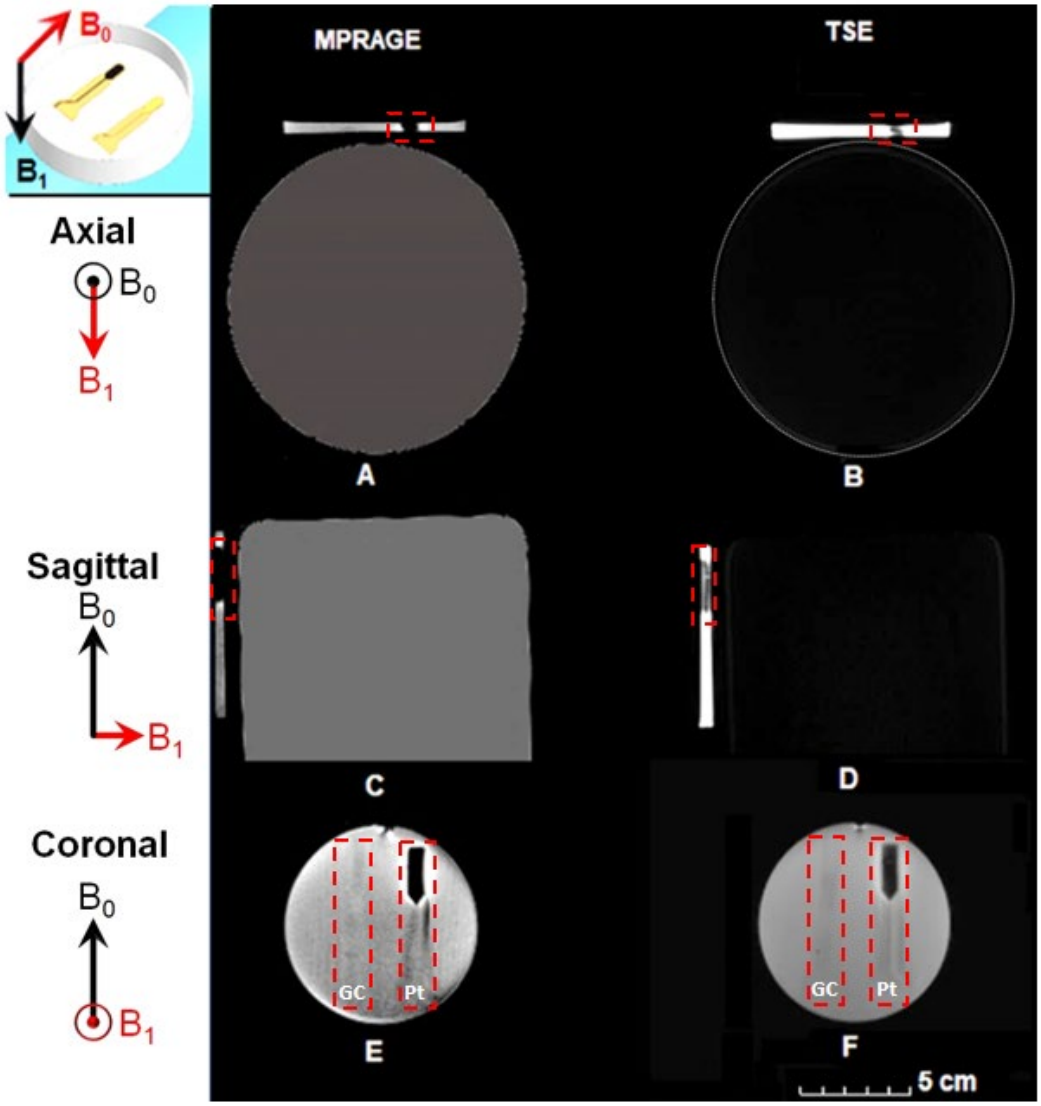



**Figure 3.5** Pt electrode placed on right side of the agarose phantom showed darkened rectangular shape along the width of Pt electrode in the axial view as compared to the GC electrode (a, b) for both T1- and T2-weighted images. Similarly, imaging artifact is recorded at Pt electrode along the length in sagittal view of agarose phantom placed on top of MRI phantom (c, d). In the coronal view, bright spots were observed at Pt and polyimide interface, while no artifacts were observed at GC electrode

### 3.2 High-Field MRI

The results of the $B_0$-field measurements and the image experiments conducted in the high field (11.7 T) magnet are summarized in Figure 6. The artifacts are mainly due to $B_1$-field distortion based on induced eddy currents. This conclusion is supported by the fact that there are no severe $B_0$-field distortions

in the $B_0$-field map, but there are large intensity distortions in the MR images. These intensities are a result of opposing magnetic fields to the $B_1$-field and induced eddy currents. Compared to the Pt microelectrode, the GC microelectrode sample does not show any image distortions because the smaller conductivity inhibits the formation of considerable adverse eddy currents. This is consistent with what was observed with the 3T scanner.

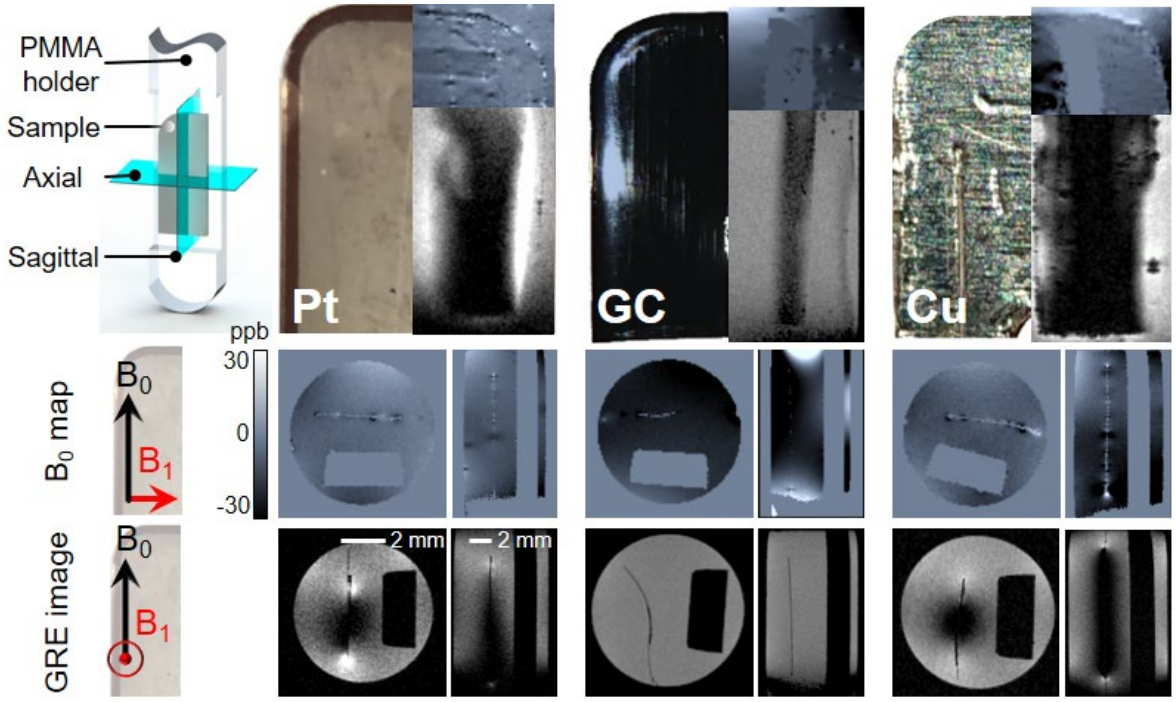



**Figure 3.6** For the B0-field map acquisition, the metal samples were oriented such that the B1 vector is parallel to the electrode surface and orthogonal for the GRE image sequences. For all samples, no significant field distortion is visible. The color map used for the B0-field maps varies from −30 to 30 p.p.b. (−15 to 15 Hz) (blue encoded images). Slight distortions in the range of a few Hz are visible for the Pt microelectrode. The background field for the GC electrodes shows slight inhomogeneity, but there are no measurable field distortions. Strong B1-field distortions are observed for the Pt as well as the Cu dummy samples. This is due to the high conductivity of the materials, which yields considerable eddy currents that counteract the B1 field

### 3.3 FEA Simulations

From the results obtained and shown in Figure 7, it can be observed that a reduced susceptibility mismatch ($\Delta\chi_{H20\text{-}GC} \sim= 0.04\ \Delta\chi_{H20\text{-}Pt}$) and drastically reduced area conductivity ($\sigma_{tGC} \sim= 0.005\ \sigma_{tPt}$) lead to a significant reduction in artifacts arising from $B_1$ and $B_0$ inhomogeneity. The relative contribution of these will depend on the imaging sequence used. Similarly, the decreased conductivity led to a reduction in the

mechanical response coming from gradient switching, in the same ratio as that of the resistances of each microelectrode. Furthermore, due to the reduced conductivity, the microelectrodes have a smaller interaction with the RF fields, meaning the dielectric heating response will be more accurately described by standard RF/SAR simulations, as optimized for safety. Similarly, any Joule heating coming from current dissipation in the microelectrodes will potentially also be reduced by a similarly proportional factor.

When applying a current/force-generating gradient field on the electrodes $B_G = t\left(\vec{G}.\overrightarrow{\Delta r}\right)$, the behavior on a microelectrode can be split into two separate contributions as:

$$B_G = t\vec{G}.\left(\overrightarrow{\Delta r_{CE-G}} + \overrightarrow{\Delta r_{PE-CE}}\right) \qquad \text{Equation 4}$$

where $\overrightarrow{\Delta r_{G-CE}}$ is a function of the distance from the center of the electrode to the center of the gradient's origin, and $\overrightarrow{\Delta r_{PE-CE}}$ is the distance from a point in the electrode to its center. The first effect was experimentally measured with the resulting torque; but can be fully removed by placing the center of the microelectrode in the gradient's origin, whereas the second effect could not be measured and cannot be removed. Given that it is impossible to precisely position an implant in a patient relative to the magnet, introducing a displacement in the cm range, the same order of magnitude of the microelectrode itself, the two effects mentioned will be comparable in magnitude.

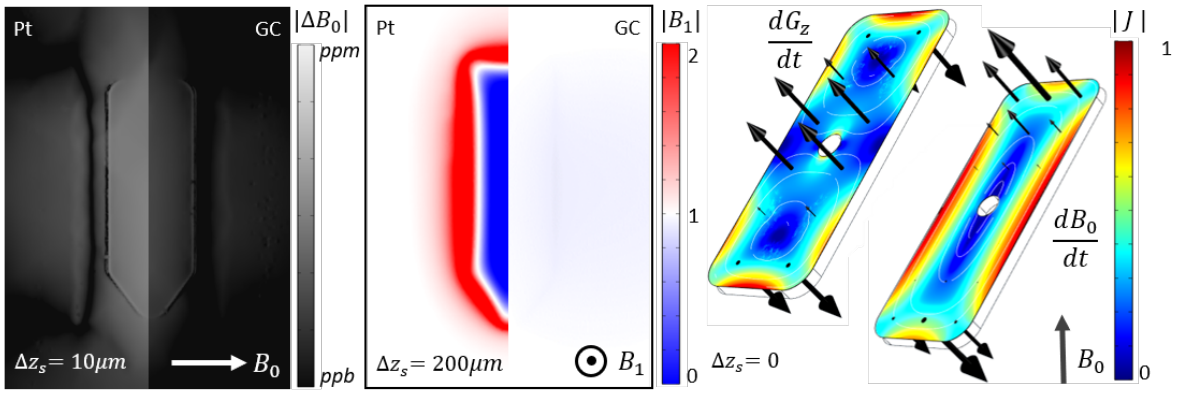



**Figure 3.7** Comparison of the simulated behavior for the 2cm x 1cm rectangular GC and Pt ground microelectrodes. On the left, one can see the $B_0$ relative-inhomogeneity map, at the center, the normalized $B_1$ inhomogeneity map and, on the right, the induced currents and forces generated by each effect of a unitary gradient's slew rate, as described above. Results are for a water phantom in a 1.5T field, shown for varying distances to the electrode's surface, $\Delta z_s$, where the effects are at magnitudes relevant to the experiment: 1ppm for inhomogeneity (left image), hundreds of micrometers for a slice thickness (middle image), and current dissipation on the surface of the electrode (right image).

### 3.4 Artifacts Measurement – Currents

Investigating the induced voltages in the ring structures allowed the examination of the gradient field interaction without acoustic noise distortions. Similar to the microelectrode design, the GC and the Pt sample had the same geometry, except that the thickness of the layers were different (Pt ≈ 300 nm and GC ≈ 2 µm). The resistances of the test structures were $R_{pt}$ = 25 Ω for the Pt-based microstructure and $R_{GC}$ = 280 Ω for the GC microstructure, and $R_{Cu} \leq 0.006$ Ω for the Cu tape. As expected, the induced voltage depended only on the surface through which the magnetic flux changed. The theoretical value presented in Figure 8 is computed through Equation 5.

$$U[V] = \pi(r_1^2 - r_2^2)\dot{G}_z z \qquad \text{Equation 5}$$

The gradient slew rate in this experiment was 2046.6 T/m/s which leads to the theoretical voltage value displayed in Figure 8 that shows that the measured induced voltage in the rings are in good agreement with the theoretical value (solid line). The measurements with the short end are also presented in the same figure to highlight the amplitude of erroneous induced voltage in the measurement lines. The induced currents measured with a 1 Ω resistor are also given in the same figure indicating that the current in GC is at least a factor of 10 less than that of the Pt sample. It has to be noted that the current induced in the GC was below the limit of detection when using a resistor of 1 Ω.

### 3.5 Vibration Measurements

In Figure 9, the results of the experimental results are displayed against the theoretical values. The acoustic coupling was measured using empty PMMA plates which allowed us to determine the limit of detection. This means that samples with conductive structures are beyond the limit of detection if their vibration amplitude is not distinguishable from the non-conductive PMMA plates. This is the case for both the Pt and GC microelectrode samples. The sample with copper foil (Cu), in contrast led to strong

vibrational amplitudes of more than two orders of magnitudes above the LOD. With this sample, the common mode vibration is clearly detectable where the vibration approaches zero at the gradient center. The acoustic vibration on the other hand, is strongest inside the MR scanner (-40 mm) which leads to the fact that the best LOD is achieved at around 30-40 mm. At this point the gradient slew rate is strongest, whereas the acoustic coupling is minimal. Using theoretical analysis, we can estimate how much the torque of the implants is beyond the LOD. The quality of this analysis is benchmarked by comparing the prediction and experimental value of the Cu sample.

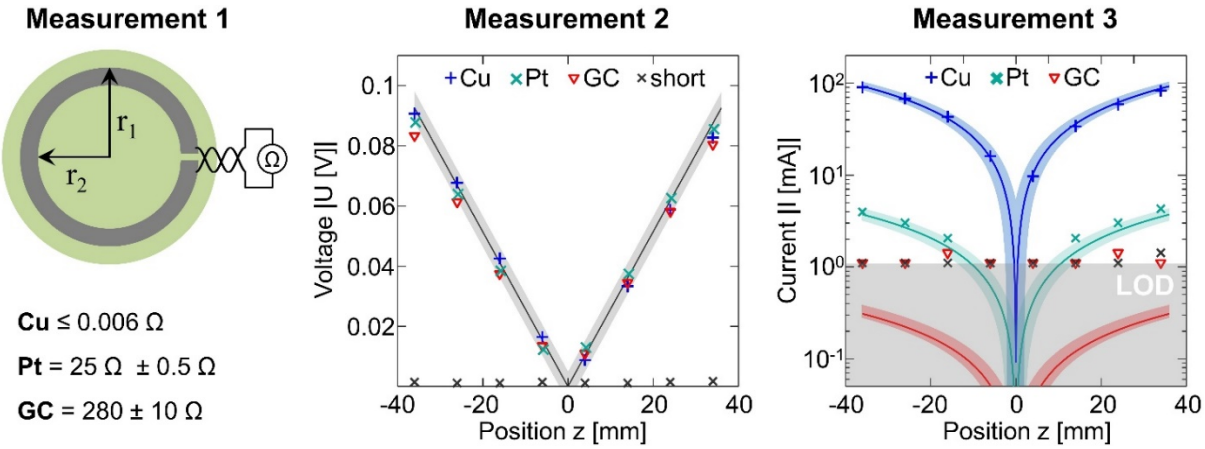



**Figure 3.8** Measurement results from induction experiments. Continuous lines show the interpolated mean values and the corresponding color encoded areas represent the standard deviation. Actual measurement points are indicated by one set of data points per sample. The first experiment was conducted to measure the resistance of the disc. Middle: The second experiment shows the induced voltage in the rings. The measured values are in good agreement with the theoretical value (solid line). Additionally, short-circuit measurements are presented to highlight the amplitude of erroneous induced voltage in the measurement lines. Right: Induced currents measured with a 1 Ω resistor. The solid lines are the theoretical values using the measured resistances from experiment 1. The limit of detection (LOD) is derived from the deviation of the measurement from the theoretical curve.

Interestingly, the platinum microelectrode appears to be at the limit of the detection, whereas the GC has an approximately 40-fold weaker response (see Figure 9 B). In contrast, the copper foil results in a response three orders of magnitude larger than the tested electrodes. We want to emphasize that, due to the linearity of electromagnetism, the derived value of TPSR may serve as a figure of merit for an implant,

which allows a simple derivation of the worst case torque at any MR scanner. As an example, we may take the Cu foil with a TPSR = 4 $\frac{\mu Nm}{T \cdot T/s}$. Then, in a 3T human MR scanner with slew rate of max. 300 T/m/s and largest dimension of 0.3 m (e.g. in the z-direction) the maximum expected torque evaluates to:

$$\tau_{max} = \text{TPSR} \cdot B_0 \cdot \dot{G}_z \cdot z = 4 \frac{\mu\text{Nm}}{\text{T} \cdot \frac{\text{T}}{\text{s}}} \cdot 3\ \text{T} \cdot 300\ \text{T/m/s} \cdot 0.3\ m = 1080\ \mu\text{Nm}. \quad (6)$$

According to ASTM, critical torque is reached when the MR induced torque is larger than the gravitational induced torque [28]. Gravitational induced torque can be computed using the weight (m) of an object multiplied with its longest dimension (l). Hence, for the Cu foil, the gravitational torque $\tau_g$ is:

$$\tau_g = mgl = 8960 \frac{kg}{m^3} \cdot (0.04 \cdot 25 \cdot 11) \cdot 10^{-9} m^3 \cdot 9.81 \frac{m}{s^2} \cdot 25 \cdot 10^{-3} m = 24.2\ \mu Nm \ll 1080 \mu Nm \quad (6)$$

Because $\tau_{max} >> \tau_{g,}$ the Cu foil is clearly MR incompatible. On the other hand, the upper limit for MR induced torque of Pt and GC microelectrodes will be in the range of $5 \times 10^{-3}$ * 3T *300 T/m/s = 4.5µNm, which is safe.

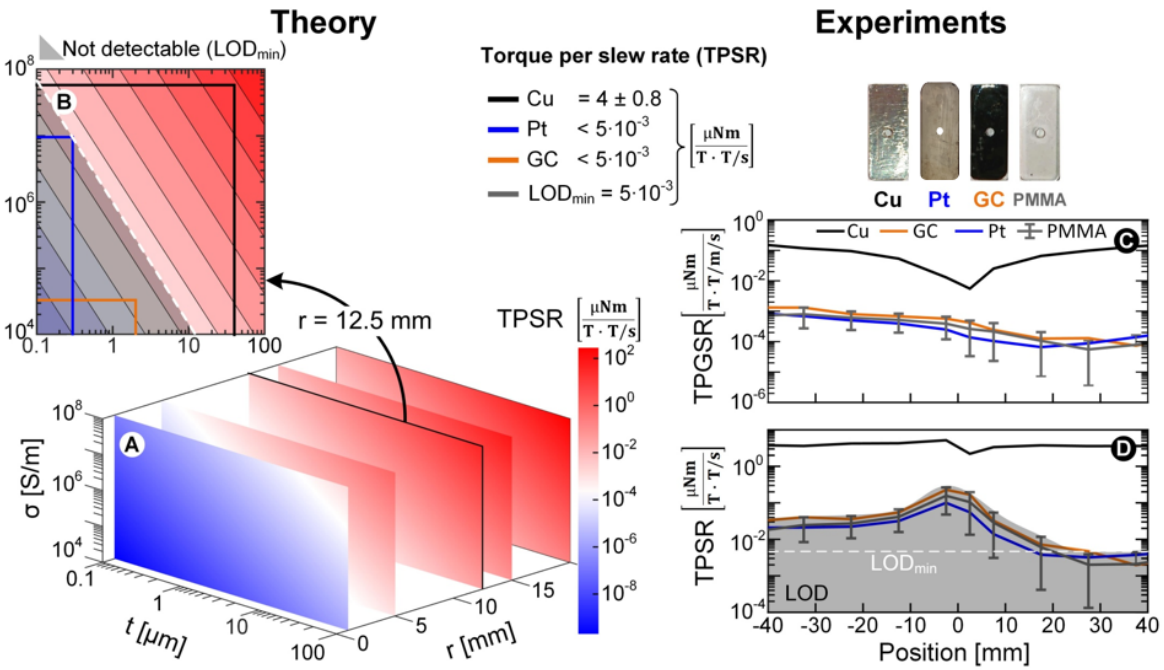



**Figure 3.9** Measurement results of vibration measurements and their comparison to theoretical values. (A) Graph of the torque per unit slew rate (TPSR) as a function of conductivity σ, metal layer thickness t and largest dimension size r. The value range of TPSR covers 10 orders of magnitude. (B) A slice of (A) that corresponds to a radius of 12.5 mm. The theoretical values for the tested sites are highlighted as well as the limit-of-detection due to superimposed acoustic vibration for implants of this size. The contour lines are per decimal power. The theoretical TPSR for Pt electrode (blue) and the GC electrode (orange) differ by one order of magnitude (~40x). (C) Graph of the torque per gradient slew rate and field strength that acts on the implants is displayed as a function of the position alongside the bore inside the MR scanner. PMMA samples were used to determine the acoustic dependent deflection. The vibration of Pt and GC samples do not show significant vibration beyond acoustic coupled amplitudes. The values are within the standard deviation of the non-conductive samples (error bars for GC and Pt are not plotted here for clarity). The Cu sample, in contrast, shows clear gradient induced vibration. (D) The torque per slew rate and field strength which is obtained by normalizing the results from (C) by the position.

## 4 Discussion/Conclusion

In this work, the MR interactions of GC and Pt based microelectrodes were investigated with respect to their adverse effects in producing MR artifacts and gradient induced vibrations. The specific aim of the MR characterization was to test whether GC microelectrodes used for deep brain stimulation (DBS) or the less-invasive intracortical recording (ECoG) produce any artifacts while mapping functional or morphological information of the brain with MR. With regard to gradient-induced vibrations, calculations show that the induced eddy currents are much larger for the Pt microelectrodes as compared to the GC microelectrodes. However, for both types of microelectrodes, the measurable forces were below the

detection limit. In our experimental scanner, the gradient field slew-rates are up to a factor of ten larger than in comparable human MRI machines, hence, the expected forces with the presented microelectrodes should remain within a non-hazardous range even in human scanners with up to 7 T. We want to emphasize, however, that the gradient-induced vibration scales to the power of four with the radius of the implants and thus, for larger electrodes the positive effect of smaller conductance of GC will be advantageous to obtain electrode designs that are not prone to vibration induction. We also emphasize the introduction of a new figure of merit which is independent of field strength and gradient slew rate. It provides an important tool to compare the tendency of different implants to vibrate and enables the straightforward computation for worst case torque of an implant for any field strength and slew rate.

In contrast to vibrations, MR artifacts depend on the conductivity as well as the magnetic susceptibility of the applied material. In summary, our findings show that the larger magnetic susceptibility of platinum does not produce considerable field distortions especially because of the small volume of the thin-film electrodes. Both GC microelectrodes showed field distortions with less than 30 ppb at even 11.7T, and from this viewpoint both microelectrode types may even allow for use within field-sensitive applications such as localized spectroscopy in human MR machines operating with smaller static magnetic fields ($\leq$ 3T). On the other hand, the Pt microelectrode shows considerable B1-field distortions due to RF-induced eddy currents, which lead to large position-dependent obscuration or hyperintensity. The GC microelectrode is clearly superior with respect to this type of artifact, showing no measurable distortion of the image. The reason is also the much smaller electrical conductivity of GC. It should be noted here that the geometries of these microelectrodes affect their resistance (and hence conductivity), as the resistance R is a function of length L and cross-sectional area A (i.e., $R = \rho L/A$ or $R = L/(\sigma A)$), suggesting that the contribution of geometry alone to the resistance R is ~6.6× for Pt compared to GC (since the thickness of Pt = 300 nm and of GC = 2 μm). However, the conductivity ($\sigma$) of Pt is $9.43 \times 106$ S/m, which is almost 1400× that of GC (6803 S/m), in effect making the resistance R of the Pt microelectrode ~1/200th that of GC. Therefore, despite the smaller thickness, Pt microelectrodes experienced higher induced currents, as demonstrated here. For eddy currents, on the other hand, where the RF resistance is more relevant, length

plays a larger role than does thickness due to skin effects; hence, the resistance of Pt and GC microelectrodes will be dominated by their inherent conductivities [29].

Therefore, we submit that GC microelectrodes demonstrate superior behavior with respect to MR safety compared to Pt-based electrodes. There is strong indication that this statement will be further corroborated by an analysis of RF-induced heating, which was not conduced in this investigation. One large source of RF-induced heating is RF-induced eddy currents; the same currents lead to large MR image artifacts only in the Pt microelectrode and not in the GC microelectrode. We anticipate that the introduced figure of merit will be of great significance as an implant-specific value for labeling torque-related interactions.

Taken together, this study demonstrated that (i) GC microelectrodes experienced no considerable vibration deflection amplitudes and minimally induced currents (below the LOD), while Pt microelectrodes had considerably larger currents, (ii) GC microelectrodes had almost no susceptibility shift artifacts compared to Pt microelectrodes because GC has 1/20th the magnetic susceptibility of Pt and (iii) GC microelectrodes had no eddy-current-induced artifacts, unlike the Pt microelectrodes, mainly because of the lower conductivity of GC (~1/1000th that of Pt) that inhibits the formation of considerable eddy currents. Since GC has recently been demonstrated to have a compelling advantage over other materials for neural stimulation, recordings, and electrochemical sensing of neurotransmitters through voltammetry4,19, this MRI compatibility validated in this study offers an additional advantage for long-term in vivo use in clinical settings.

**References**


1. Ranganathan, S., McCreey, R., Majji, S.M., Madou, M., "*Photoresist-derived Carbon for Microelectromechanical Systems and Electrochemical Applications,*" J Electrochem Soc, 147 (2000), pp. 277–282.

2. Majid Beidaghi, Wei Chen, Chunlei, Wang, "*Electrochemically activated carbon micro-electrode arrays for electrochemical micro-capacitors,*" Journal of Power Sources, Volume 196, Issue 4, 15 February 2011, Pages 2403-2409

3. Wang, C., Taherabadi, L., Jia, G., Kassegne, S., Zoval, J., and Madou, M., "*Carbon-MEMS Architecture for 3D Microbatteries,"* Proceedings of SPIE-Photonics Europe, Strasbourg, France, April 2004.

4. Nimbalkar, S., Castagnola, E., Balasubramani, A., Scarpellini, A., Samejima, S., Khorasani, A., Boissenin, A., Thongpang, S., Moritz, C., and Kassegne, S., "*Ultra-Capacitive Carbon Neural Probe Allows Simultaneous Long-Term Electrical Stimulations and High-Resolution Neurotransmitter Detection,"* Nature Scientific Reports 8 (1), 6958, 2018.

5. Arantes, Paula R., Ellison F. Cardoso, Maria A Barreiros, Manoel J. Teixeira, Márcia R. Gonçalves, Egberto R. Barbosa, Sukhi Shergill Sukwinder, Claudia C. Leite, and Edson Amaro Jr. "*Performing functional magnetic resonance imaging in patients with Parkinson's disease treated with deep brain stimulation*." Movement disorders: official journal of the Movement Disorder Society 21, no. 8 (2006): 1154-1162.

6. Scherberger, H., I. Fineman, S. Musallam, D. J. Dubowitz, K. A. Bernheim, Bijan Pesaran, B. D. Corneil, B. Gilliken, and R. A. Andersen. "*Magnetic resonance image-guided implantation of chronic recording electrodes in the macaque intraparietal sulcus*." *Journal of neuroscience methods* 130, no. 1 (2003): 1-8.

7. Yelnik, Jérôme, Philippe Damier, Sophie Demeret, David Gervais, Eric Bardinet, Boulos-Paul Bejjani, Chantal François et al. "*Localization of stimulating electrodes in patients with Parkinson disease by using a three-dimensional atlas—magnetic resonance imaging coregistration method*." *Journal of neurosurgery* 99, no. 1 (2003): 89-99

8. Erhardt, Johannes B., Erwin Fuhrer, Oliver G. Gruschke, Jochen Leupold, Matthias C. Wapler, Jürgen Hennig, Thomas Stieglitz, and Jan G. Korvink. "*Should patients with brain implants undergo MRI?*" *Journal of neural engineering* 15, no. 4 (2018): 041002.

9. Shellock, Frank G. "Radiofrequency energy-induced heating during MR procedures: a review." *Journal of Magnetic Resonance Imaging* 12, no. 1 (2000): 30-36.

10. Dempsey, Mary F., and Barrie Condon. "*Thermal injuries associated with MRI*." *Clinical radiology* 56, no. 6 (2001): 457-465.

11. Finelli, Daniel A., Ali R. Rezai, Paul M. Ruggieri, Jean A. Tkach, John A. Nyenhuis, Greg Hrdlicka, Ashwini Sharan, Jorge Gonzalez-Martinez, Paul H. Stypulkowski, and Frank G. Shellock. "*MR imaging-related heating of deep brain stimulation electrodes: in vitro study*." *American journal of neuroradiology* 23, no. 10 (2002): 1795-1802.

12. Rezai, Ali R., Daniel Finelli, John A. Nyenhuis, Greg Hrdlicka, Jean Tkach, Ashwini Sharan, Paul Rugieri, Paul H. Stypulkowski, and Frank G. Shellock. "*Neurostimulation systems for deep brain stimulation: In vitro evaluation of magnetic resonance imaging–related heating at 1.5 tesla.*" *Journal of Magnetic Resonance Imaging: An Official Journal of the International Society for Magnetic Resonance in Medicine*15, no. 3 (2002): 241-250.

13. Bonmassar, Giorgio, Kyoko Fujimoto, and Alexandra J. Golby. "*PTFOS: flexible and absorbable intracranial electrodes for magnetic resonance imaging.*" *PloS one* 7, no. 9 (2012): e41187.

14. Yoon, H., Deshpande, D.C., Kim, T.H., Jeong, E.K., Harbaugh, R.E. and Varadan, V.K., 2010. "*Development of titanium needle probes for neural recording and evaluation of magnetic*

*resonance imaging artifacts,*" *Journal of Nanotechnology in Engineering and Medicine*, *1*(1), p.011004.

15. Santiesteban, Francisco M. Martínez, Scott D. Swanson, Douglas C. Noll, and David J. Anderson. "*Magnetic resonance compatibility of multichannel silicon microelectrode systems for neural recording and stimulation: design criteria, tests, and recommendations,*" *IEEE transactions on biomedical engineering* 53, no. 3 (2006): 547-558.

16. Jiang, C. Q., H. W. Hao, and L. M. Li. "*Artifact properties of carbon nanotube yarn electrode in magnetic resonance imaging,*" *Journal of neural engineering* 10, no. 2 (2013): 026013.

17. Kassegne, S., Vomero, M., Gavuglio, R., Hirabayashi, M., Özyilmaz, E., Nguyen, S., Rodriguez, J., Özyilmaz, E., Niekerk, P., Khosla, A. "*Electrical impedance, electrochemistry, mechanical stiffness, and hardness tunability in glassy carbon MEMS μECoG electrodes*," *Microelectronic Eng.* 133, 36–44 (2015).

18. Vomero, M., van Niekerk, P., Nguyen, V., Gong, N., Hirabayashi, M., Cinopri, A., Logan, K., Moghadasi, A., Varma, P., Kassegne, S. *Novel Pattern Transfer Technique for Mounting Glassy Carbon Microelectrodes on Polymeric Flexible Substrates*, *Journal of Micromechanics and Microengineering* 26, 36-44 (2016).

19. Vomero, M., Castagnola, E., Ciarpella, F., Maggiolini, E., Goshi, N., Zucchini, E., Carli, S., Fadiga, L., Kassegne, S., Ricci, D. "*Highly Stable Glassy Carbon Interfaces for Long-Term Neural Stimulation and Low-Noise Recording of Brain Activity*," *Nature Sci. Rep.* 7:40332 (2017) doi: 10.1038/srep40332

20. Camacho, Christopher R., Donald B. Plewes, and R. Mark Henkelman. "*Nonsusceptibility artifacts due to metallic objects in MR imaging*," *Journal of Magnetic Resonance Imaging* 5, no. 1 (1995): 75-88.

21. Windt, D. L. et al. Optical constants for thin films of Ti, Zr, Nb, Mo, Ru, Rh, Pd, Ag, Hf, Ta, W, Re, Ir, Os, Pt, and Au from 24Å to 1216Å. Appl. Opt. 27, 246–278 (1988).

22. Noto, K., K. Saito, K. Kawamura, and T. Tsuzuku. "*Diamagnetism of Glassy Carbons*," Japanese Journal of Applied Physics 14, no. 4 (1975): 480.

23. *Raymond A. Serway (1998). Principles of Physics (2nd ed.). Fort Worth, Texas; London, Saunders College Pub. p. 602.*

24. Wapler, M. C. et al. Magnetic properties of materials for MR engineering, micro-MR and beyond. J. Magn. Reson. 242, 233–242 (2014).

25. Fuhrer, E., M. Jouda, O. G. Gruschke, and J. G. Korvink. "*Optical gauge head to evaluate gradient field induced vibrations of conductive structures during MRI*," Electromagnetics in Advanced Applications (ICEAA), 2017 International Conference on, pp. 1555-1558. IEEE, 2017.

26. Fuhrer, E., Jouda, M., Klein, C. O. & Korvink, J. G. Gradient-induced mechanical vibration of neural interfaces during MRI. In: Pan, X. (ed) IEEE Trans. Biomed. Eng. (Early Access) (2019). https://doi.org/10.1109/TBME.2019.2923693.

27. Zhao, Siyuan. et al. Graphene encapsulated copper microwires as highly MRI compatible neural electrodes. Nano Lett. 16, 7731–7738 (2016).

28. ASTM, “ASTM F2213 - 06: Standard Test Method for Measurement of Magnetically Induced Torque on Passive Implants in the Magnetic Resonance Imaging,” 2016.

29. Johnson, H. & Graham, M. High-Speed Signal propagation Advanced Black Magic 3rd edn, ISBN 978-0-13-084408-8, 58–78 (Prentice-Hall, 2003).

**Acknowledgment**

Chapter 3, in full, is a reprint of materials as it appears in Nimbalkar, S., Fuhrer, E., Silva, P., Nguyen, T., Sereno, M., Kassegne, S. and Korvink, J., 2019. Glassy carbon microelectrodes minimize induced voltages, mechanical vibrations, and artifacts in magnetic resonance imaging. *Microsystems & nanoengineering*, *5*(1), pp.1-11. The dissertation author was the co-first author of this paper.

# CHAPTER IV

## Novel Graphene-Glassy Carbon (GrGC) MetaMaterial: Synthesis, Characterization, and Molecular Dynamics Simulation

**Abstract**

Using graphene (Gr) and glassy carbon (GC) - two allotropes of the abundantly available material carbon - as building blocks, we introduce a new metamaterial that possesses superior electrical, and electrochemical properties. The accompanying scalable and novel fabrication process for this metamaterial is presented where a substrate with layer of Gr grown on it was used to deposit a layer of negative-tone polymer precursor that was subsequently patterned and then pyrolyzed in the same chamber to synthesize a new metamaterial referred to as GrGC. The formation of this novel metamaterial is demonstrated and validated through (a) synthesis and fabrication process, (b) molecular dynamics modeling of the synthesis process, and (c) comprehensive morphological, surface material characterizations. Specifically, the chemical bond of the metamaterial was characterized through Fourier Transform Infrared Spectroscopy (FTIR) and Raman Spectroscopy while its surface morphology were characterized through SEM. Further, the cross section of microstructure of the ensuing GrGC was imaged through scanning transmission electron microscopy (STEM) and compared with outcomes from molecular dynamics (MD) simulations. In addition, electron energy loss spectroscopy (EELS) provided useful insights to the chemical composition in the microstructure of the ensuing metamaterial where a combination of sp2 and sp3 characteristics are observed to be dominant at the interface of Gr and GC. The MD modeling also showed formation of carbonyl (C=O), ether (C–O–C), and epoxide (cyclic ether) functional groups in the metamaterial. The characterization and modeling outcomes confirm that 5- 6-, and 7-membered carbon rings formed a continuous covalent bond at the Gr and GC interface contributing to the formation of a unique metamaterial that consisted of a flat Gr component, a transition region, and a 3D-shaped cage-like GC component. Taken together, the metamaterial's capability to form 3D and complex components, and functional group presence will offer new possibilities in advanced semi-conductor devices and ultra-sensitive biochemical sensors that could substantially extend current detection limits.

## 1. Introduction

Carbon, which is one of the most abundant elements on the planet, continues to enjoy increasing and wider acceptance in a variety of application areas such as sensors, microelectrodes, batteries, fuel-cells, magnetic thin-films, and neural interfaces [1-6]. Further, carbon's unique tunable mechanical and electronic properties help position it as a versatile material of choice for a variety of applications including as promising material in semi-conductor and energy storage technologies. The relatively recent discovery of new allotropes of carbon such as graphene (excellent conductivity, large surface area, and high in-plane stiffness) [7], Q-carbon (excellent hardness [8] and excellent strength) [9]), and glassy carbon (gold-standard for electrochemistry) [1-2] will further drive far-reaching importance of carbon for an expanding array of applications. Out of the several allotropes of carbon, graphene (Gr) and glassy carbon (GC) stand out in their potential in revolutionizing a wide variety of industries. The introduction of Gr, for example, with its high charge storage capacity and fast charge and discharge (C&D) has already contributed to increased interest in electrochemical supercapacitors for energy storage where fast C&D cycles are sought [10-15]. Further, the ability to photolithographically pattern GC and Gr features continues to drive innovation in wider application of these key allotropes of carbon [1-2, 16-18]. Gr is a 2D monolayer material and is considered the gold-standard for electrical conductivity (1700 S/m) with high in-plane mechanical strength, excellent thermal conductivity (4840–5300 W/mK), large surface area (2630 $m^2/g$), and high double-layer capacitance (21 μF/cm2) [19]. However, its monolayer thickness lacking 3-dimensionality introduces a severe weakness in overall 3D mechanical strength, particularly in transverse direction. Further, its imperviousness to molecules leaves much to desire in its charge storage capacity [10]. On the other hand, GC which has a cage-like 3D molecular structure of bands of Gr is the gold-standard for electrochemistry and has exceptional chemical inertness, high mechanical stiffness (in all planes) [6], good electrical properties, high electrochemically stability, high charge storage capacity (61.5 $mC/cm^2$), and fast surface electrokinetics coupled with lithography patternability [20-21].

It is, therefore, clear that by themselves, the two allotropes of carbon, i.e., Gr and GC, possess some strong unique properties suitable for applications in a wider variety of areas. Then, could the unique

strengths of these two carbon allotropes be further leveraged for introducing new composite "made of tailored building blocks, which are composed of one or more constituent bulk materials, leading to effective medium properties beyond those of their ingredients" – and hence form a metamaterial [22]? This fundamental question has inspired this work where we hypothesize that combining the strength of these 'gold-standard' materials will help introduce a new metamaterial that incorporates their best qualities to a single material. The combination of high surface area and double-layer capacitance of Gr coupled with high charge storage capacity of GC could help achieve high energy density, for example [19]. Further, we hypothesize that the merging of 2D monolayer Gr and 3D cage-like GC molecules introduces a versatile '2.5D' metamaterial with 2D planar microstructures of 6-ring carbon and 3D cagey microstructure with mix of 6-ring carbon rings and Gr monolayer (Figure 2). In this study, therefore, the feasibility of this metamaterial and the validity of the hypothesis presented is investigated and established through (a) characterization of synthesized GrGC metamaterial and (b) first-principle molecular dynamics simulation.

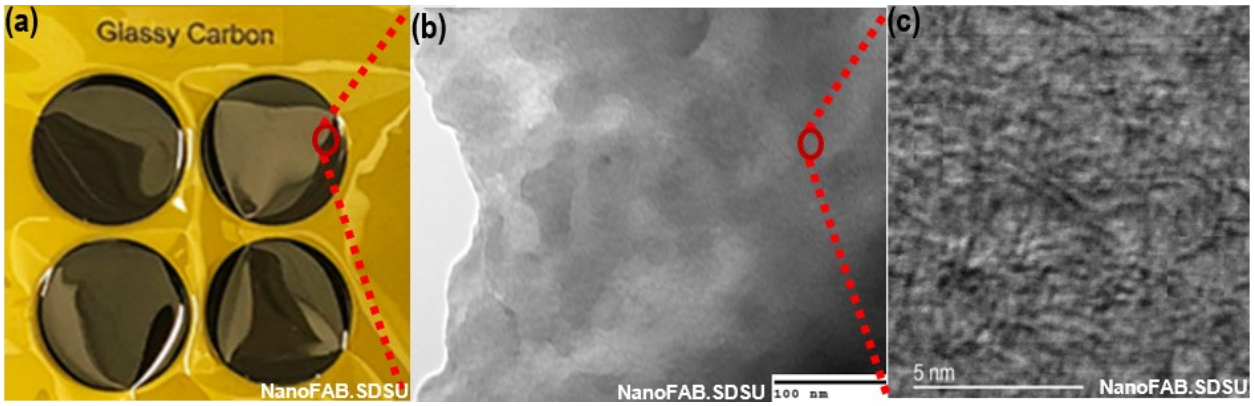



**Figure 4.1** (a) microfabricated GC structures (c) TEM image of GC (c) STEM image of GC

As shown in Figure 1b/1c, GC gets its superior capacitive behavior due to each of its 3-dimensional Gr cage-like structures acting as capacitors separated by a very small distance of ~3Å [23]. Further, the porosity that is associated with even more charge storage capacity can be increased through high flow rates of forming gases [24-25]. However, recent experimental work has raised some fundamental question regarding the true 3D molecular structure of GC [26-27]. In addition, how GC will interact with Gr to form

GrGC metamaterial during pyrolysis is, of course, unknown. Further, what emerges as an intriguing point is the fact that GC is structurally close to Gr leading to the natural speculation that, perhaps, creating the necessary chemical and physical environment for GC and Gr precursors may allow the formation of a new metamaterial that shares the property of these two materials. Therefore, a theoretical framework is needed to help gain a fundamental understanding of (a) the true 3D molecular structure of the ensuing metamaterial, (b) the process of evolution of the metamaterial, and (c) the type and distribution of active functional groups. For that, molecular dynamics (MD) simulation framework that will help shed light on the exact mechanism of microstructure formation on a molecular level of the metamaterial is presented.

## 2. Materials and Methods

To investigate the potential chemical bond that could form between GC and Gr layers and to test the ability of Gr layer to maintain its characteristics as GC layer is formed through pyrolysis of a polymer pre-cursor, a GrGC test structure in the shape of a serpentine was synthesized (Figure 2). Subsequently, scanning transmission electron microscopy (STEM) was used to image the cross-sectional microstructure of the material with cross-sectional thinning of the sample done using focused ion beam (FIB) assisted sample preparation. STEM was preferred here instead of TEM to avoid milling of the material which could cause significant stresses and alter the GrGC nanostructure. In addition, electron energy loss spectroscopy (EELS) was used to obtain elemental information at nanometer scale and analyze the bonds at the Gr and GC material interface.

### 2.1 Synthesis of GrGC Microstructure

The microfabrication process adopted here involved first transferring a monolayer of Gr on a silicon wafer with 0.2 – 0.5 μm thick oxide, applying a layer of negative-tone resist polymer precursor, UV patterning of the negative resist, removal of exposed Gr monolayer by dry oxygen plasma etching, and then pyrolyzing the precursor polymer and Gr together to form GrGC metamaterial (Figure 2). Silicon wafer with oxide layer that contained Gr monolayer transferred on it was used in this process (Grolltex Inc, San

Diego, CA). Negative photoresist SU8-10 (Microchem, MA) was used as precursor for forming GC microstructure. The photoresist was spun coated at 1200 rpm on the wafer that contained Gr monolayer. The photoresist was then pre-baked before UV exposure (400 mJ/cm2) in two steps at 65°C for 10 min and 95°C for 20 mins. The post-exposure bake consisted of heating at 65°C for 1 min and 95°C for 10 min. The patterned SU8 microstructures were then used as hard masks for patterning the underlying Gr layer. Following the development of microstructures, the SU8 microstructure on Gr monolayer underwent dry oxygen plasma etch treatment at 90 W, 300 mTorr for 1 min for removal of Gr from uncovered parts of the wafer. Subsequently, the patterned SU8/Gr microstructure was pyrolyzed in a furnace with nitrogen flow at 1000˚C for 90 mins [1-2, 20-21]. Polyimide (Durimide 115a, Fujifilm, Japan) was then spun-coated on top of the GrGC layer, and cured at 400˚C for 4 hrs in a vacuum furnace. Finally, the microstructure supported on a polyimide substrate was separated from silicon wafer by etching the oxide layer in buffered hydrofluoric acid (BHF) bath. Figure 2b shows the GrGC metamaterial microstructure.

**2.2 Surface Morphology, Topology, and Microstructure Characterization**

The morphologies of the ensuing microstructure were optically characterized via Keyence VHX-5000 optical microscopy (Keyence, Itasca, IL 60143, USA) and through SEM (FEI Quanta 450 FEG, Hillsboro, Oregon, USA). The microstructure of the GrGC metamaterial was investigated at the atomic scale through STEM using a cross-sectional specimen prepared by FIB milling. The cross-sectional sample was prepared using a FIB apparatus (Helios 5UX, Thermofisher Scientific) with a Ga+ ion beam of accelerating voltage 30 kV, probe current 20 nA. Prior to the FIB treatment, a thin layer of Au (~1 nm in thickness) was vacuum deposited using an external metal sputter for grounding the GrGC microstructure on polyimide sample. After the GrGC microstructures were located on the polyimide substrate through SEM, a layer of tungsten (~1 µm in thickness) was vacuum deposited with probe current of 0.26 nA on 11 µm x 1.5 µm area to protect the GrGC surface from bombardment by Ga+ ions during milling. Cross-section lamella was prepared using a standard lift-out procedure with a 30 kV Ga+ ion beam, then plucked out using micromanipulator and transferred on TEM grid at 30 kV energy and 90 pA probe current. After

bonding to the supporter through Pt deposition, the lamella was cut out from the micromanipulator. Once the sample lamella was transferred on grid, the energy was reduced to 2 kV and probe current to 0.26 nA during the final milling stage.

The atomic structure of the cross-sectioned samples was observed using STEM (Nion UltraSTEM 100). The bright field (BF) STEM images were obtained near a defocus condition of $\Delta f = 193.41$ nm and convergence angle of 33 mrad. EELS measurement of the cross-sectioned GrGC metamaterial was performed using the Nion UltraSTEM, 60 keV in STEM mode, using GatanGIF Quantum ERS with a collection angle of 58 mrad and a dispersion of 0.25 eV/ch. The HAADF (half angle annular dark field) images were obtained at 60 keV energy and collection angle of 80 mrad.

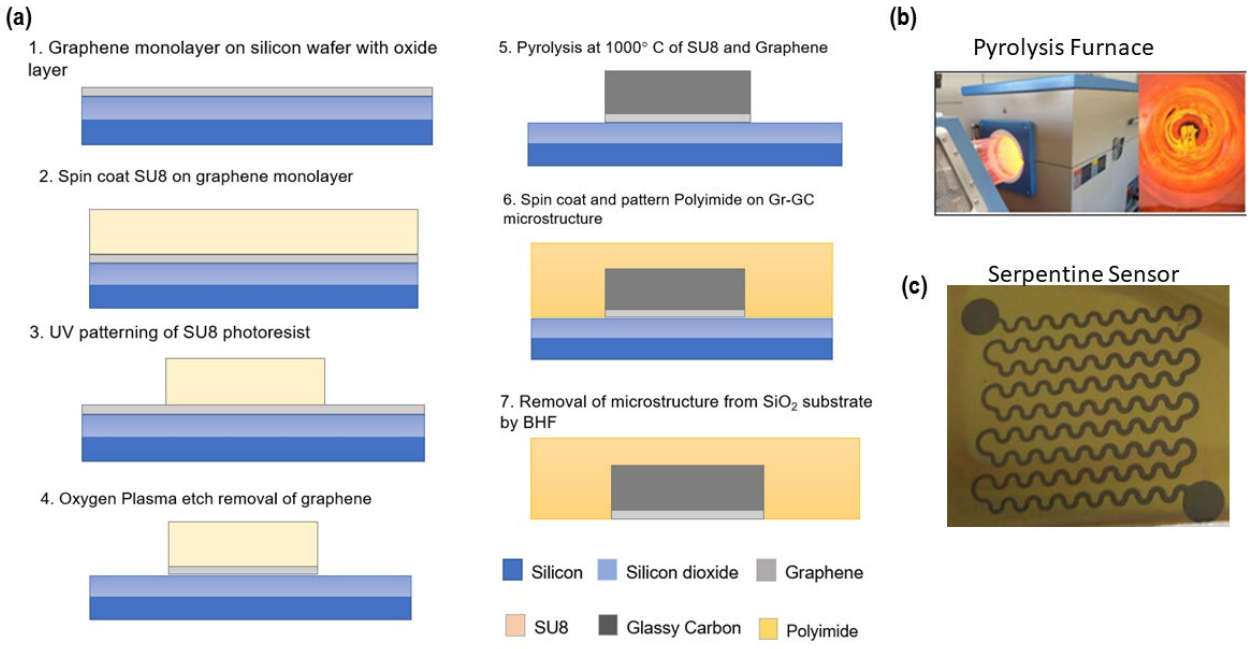



**Figure 4.2** (a) microfabrication process for GrGC microstructure, (b) tube-furnace for synthesis, (c) ensuing metamaterial.

## 2.3 Raman Spectroscopy

Raman spectra were recorded on the GrGC and GC microstructures using Thermo Nicolet DXR Raman Microscope (ThermoScientific Inc of Waltham, MA, USA). Argon ion laser operated at 532 nm

with average power of 1.5 mW focused through aperture of 25 μm in diameter with 50x objective was used for recording the Raman spectra.

### 2.4 FTIR Spectroscopy

FTIR-ATR spectroscopy was done using a Nicolet iS50 FT-IR Spectrometer equipped with a Smart iTR diamond ATR cell (Thermo Scientific, Court Vernon Hills, IL, USA). The microstructure was washed with methanol, dried, and placed on the diamond cell. 128 spectral scans were recorded. The scans were compiled from 4 diagonal areas of microstructure and all discrete Gr on GC spectra were averaged, resulting in a single spectrum.

### 2.5 Molecular Dynamics Model

To get insight to the synthesis of the metamaterial's molecular-level microstructure, the potential bonds between Gr and GC, and the type and distribution of functional groups formed in this metamaterial, atomistic-scale computational model using molecular dynamics (MD) was used. MD simulation techniques are powerful for "exploring, developing, and optimizing promising properties of novel materials" [28-30]. In this work, MD simulations will be performed using the ReaxFF software within SCM's Amsterdam Modeling Suite [29-31]. In the MD modeling with force field formulation, the potential energy function that allows for the calculation of the force experienced by any atom is used, given the positions of the other atoms. The motions of forced atoms affecting other atoms is determined by Newton's law. Within the simulation, time is divided into time steps (on a femtosecond scale). At each time step, the forces acting on each atom are computed, using molecular mechanics force field. The position and velocity of each atom and energy contributions to the potential are then updated using Newton's Equations of Motion.

The force field on each atom are derived from energy expression made of Ebond (energy associated with forming bonds between atoms), Eangle and Etors (energies associated with three-body valence angle strain and four-body torsional angle strain), Eover (energy penalty preventing the over coordination of atoms, ECoulomb (electrostatic) and EvdWaals (energy due to Van der Waals forces) [28-30].

However, while MD simulations allow for detailed observation of molecular structure and evolution, the time scale for simulations is extremely limited. One way to overcome this limitation is to use higher temperature for MD simulations than temperatures used in experimental conditions, thus accelerating the process and allowing reaction barriers to be overcome more easily. This method is widely used in reactive MD simulations, and results obtained by this method are typically consistent with experimental observations [32-37]. Here, we used simulation temperature of 3100K to speed up the computation.

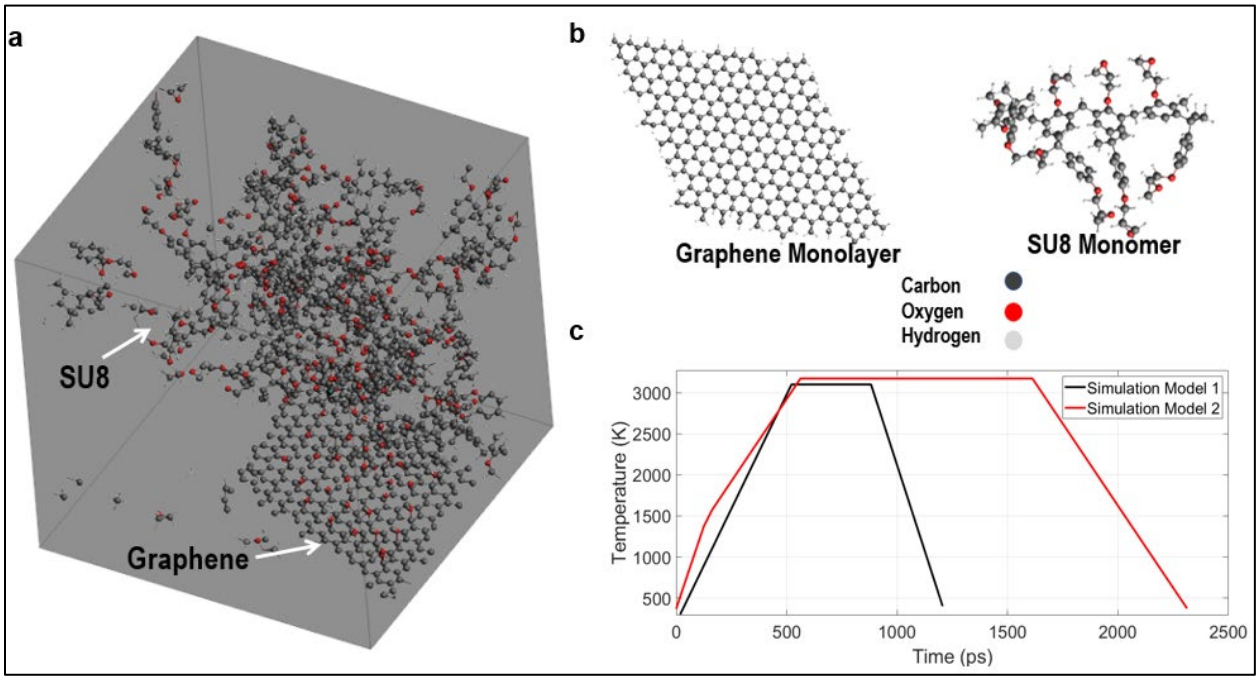



**Figure 4.3** (a) Simulation box for molecular dynamics model containing Gr monolayer and 20 SU-8 monomers, (b) Gr monolayer and SU-8 , precursor to GC, (c) temperature profile in simulation parameter Vs experimental parameters.

As shown in Figure 3, the simulation focuses on modeling the interaction of the monolayer Gr with SU8 negative tone resist, as it undergoes a complete pyrolysis process. A volume of 50Å x 50Å x 50Å forms the simulation box where 20 units of SU8 monomers and a monolayer Gr sheet were placed in it. Packmol was used to model the atomic structure of SU-8 [38]. The density of the box was 0.3546 g/mL. The simulations were performed using CHON reactive force fields module at constant temperature and

volume (NVT) i.e., canonical ensemble with Berendsen thermostat (damping constant of 100 fs). The equations were integrated with 0.25 fs time step. Experimental pyrolysis process involves the ramping up of temperature of a furnace to 1000°C (1273 K) in 6 hrs, holding it at final pyrolysis temperature for 90 mins, and ramping down to room temperature in 4 hrs.

To accelerate the reactions to a nanosecond time scale available to MD simulations and to allow the reaction energy barriers to be overcome more easily in nanoseconds as compared to experimental hour time scale, we employed pyrolysis temperature of 3173 K for simulations compared to 1273 K for experimental process. To determine the effect of holding time during the pyrolysis process at the maximum temperature, two sets of simulations were carried out, i.e., with Model I (annealing time = 400 ps) and Model II (annealing time = 1100 ps) with similar ramping up and down profiles. The total time for simulation was 1200 ps for Model I while it was 2350 ps for Model II.

## 3 Results

### 3.1 Surface Morphology, Topology, and Microstructure of GrGC MetaMaterial

Figure 4a shows SEM image of the GrGC metamaterial that suggests homogenous surface. As shown in Figure 4b, FIB was used to prepare a cross sectional sample of GrGC microstructure. Here, FIB assisted sample preparation was preferred to avoid stresses caused by milling that could potentially alter the microstructure of the material. Tungsten coating (~1 μm) preserved the underlying GrGC microstructure during FIB thinning process. Black lines in these images represent parts of the carbon sheets that are parallel to the incident electron beam. Figure 4b shows multiple Gr layers at the surface of GrGC metamaterial, underneath the thin Au layer. The interlayer distance between these Gr layer stacks was calculated through Fast Fourier Transform (FFT) of region of interest (ROI). Figure 4b I, II, II provides details of ordered (ROIs I and II) and disordered (ROI III) carbon sheets at various locations on the GrGC microstructure cross-sectional surface. At the surface of the microstructure (at ROIs I and II), ordered Gr layers were seen organized whereas on the inner side of the GrGC microstructure (~10 nm from surface at ROI III) more

disordered, randomly oriented carbon layers were observed. As shown in Figure 4c, the multilayer Gr stacking was observed at ~2 nm away from GrGC surface with thickness of few Gr layers ~2.5 nm and mean interlayer distance of 0.38±0.014 nm at locations marked 'I' and 'II'. The Gr stacks at ROI I are closer to the surface of the metamaterial. These Gr stacks might have originated from the original Gr monolayer In Figure 4c, at ROI III, multiple disordered Gr layer stacks were observed. The mean interlayer distance at stacks of Gr at 1 and 2 locations is observed to be 0.41 ± 0.023 nm.

**3.2 Electron Energy Loss Spectroscopy (EELS)**

EELS combined with STEM is a powerful technique to analyze the chemical composition of carbon materials. Figure 5 shows EELS data of the carbon core-loss edge at different regions of interest marked as A, B and C where 'A' represents Gr region, 'B' a transitional interface region, and 'C', a predominantly shows GC zone. The Carbon K-edge region shows two main peaks: the first one between 286 eV and 288 eV due to the 1s to π* orbital transition (characteristic feature of sp2 bonding) and the second one at 292 eV .The main maximum (σ* peak) of the Carbon-K edge located at ~ 292 eV is associated with 1s to σ* transitions for both sp2 – and sp3 -hybridized carbon atoms.

The 'A' or Gr stack region or has peaks that indicate significant sp2 character. As seen in Figure 5B and C, the intensity of the π* transition increases for B or interface region as compared to C or GC region indicating an increase in sp2 character identical to A or Gr region. The intensity of the σ* transition showed higher values for B or interface region as compared to only A or Gr region indicating higher sp3 character in B region indicating an increased graphitic order interface region. For C or GC region, σ* peak is even smeared out or appears featureless with an increase in the intensity as compared to A region and shows even more featureless broad hump starting above 292 eV and extending up to 305 eV due to the C 1s → σ* transition. This is typically seen for extremely disordered C-C bonds and the smearing of the edge is characteristic of amorphous carbon [41]. Below the π* excitations (<285 eV), the resonances of surface dangling bonds are observed [42,43]

Here, the π* peak can be used to identify sp2 bonded carbon atoms in C-materials, and to provide quantitative information about the sp2 to sp3 carbon – ratio by its relative intensity compared to σ* states. A procedure developed by Berger et al. [44] is used for determining the fraction of sp2-bonded carbon atoms in the material at the regions A, B and C shown in Figure 5. This method provides the ratio of integrated window centered on the π* peak (Iπ∗) to the integrated area containing both π* and σ* peaks (I π∗+σ∗), according to the equation (sp2/(sp2 + sp3) = Iπ∗/(I π∗+σ∗). Here, 6 eV window centered at 292 eV over both π* and σ* peaks was used. The ratio obtained is normalized to the factor determined from spectra of a 100% sp2- hybridized material and region. As the Gr region shows highest π* intensity, Gr region intensity was used as reference for normalization [45]. As shown in Table S1, if region A or Gr has 100% sp2 fraction, regions B or interface and C or GC have 91.5% and 86.7% of sp2 fraction respectively, demonstrating a clear transition from Gr area to an interface and GC zone.

Multi-acquire summed Low and core loss spectra were also studied along the regions marked as Gr and GC. The low-loss EELS chart shows two distinct peaks around 6.5 eV and 25 eV (Figure 5C). The first peak corresponds to the π–π* inter-band transition and the second one is due to the collective oscillation of the π + σ plasmon. The π–π* transition is mainly due to the in-plane mode, which appears at 7 eV for graphite and shifts to 4.8 eV for single layer Gr can be attributed to a π-valence band plasmon. For both regions Gr and GC, π–π* inter-band transition was observed at 6.5 eV. The π + σ plasmon peak was observed at 25.2 eV for region Gr, close to the value seen for graphite (27 eV). The plasmon losses could be seen in this region due to multiple Gr layers stacking [44]. At region GC, π + σ peak is observed close to 23 eV (Gr monolayer peak). Multi-acquire core loss spectra showed similar peaks as that of single acquire EELS (Figure 5a-c). From the core loss and low-loss spectra data, it is clear that the microstructure of the GrGC metamaterial consists of a few layers of highly graphitic material [45].

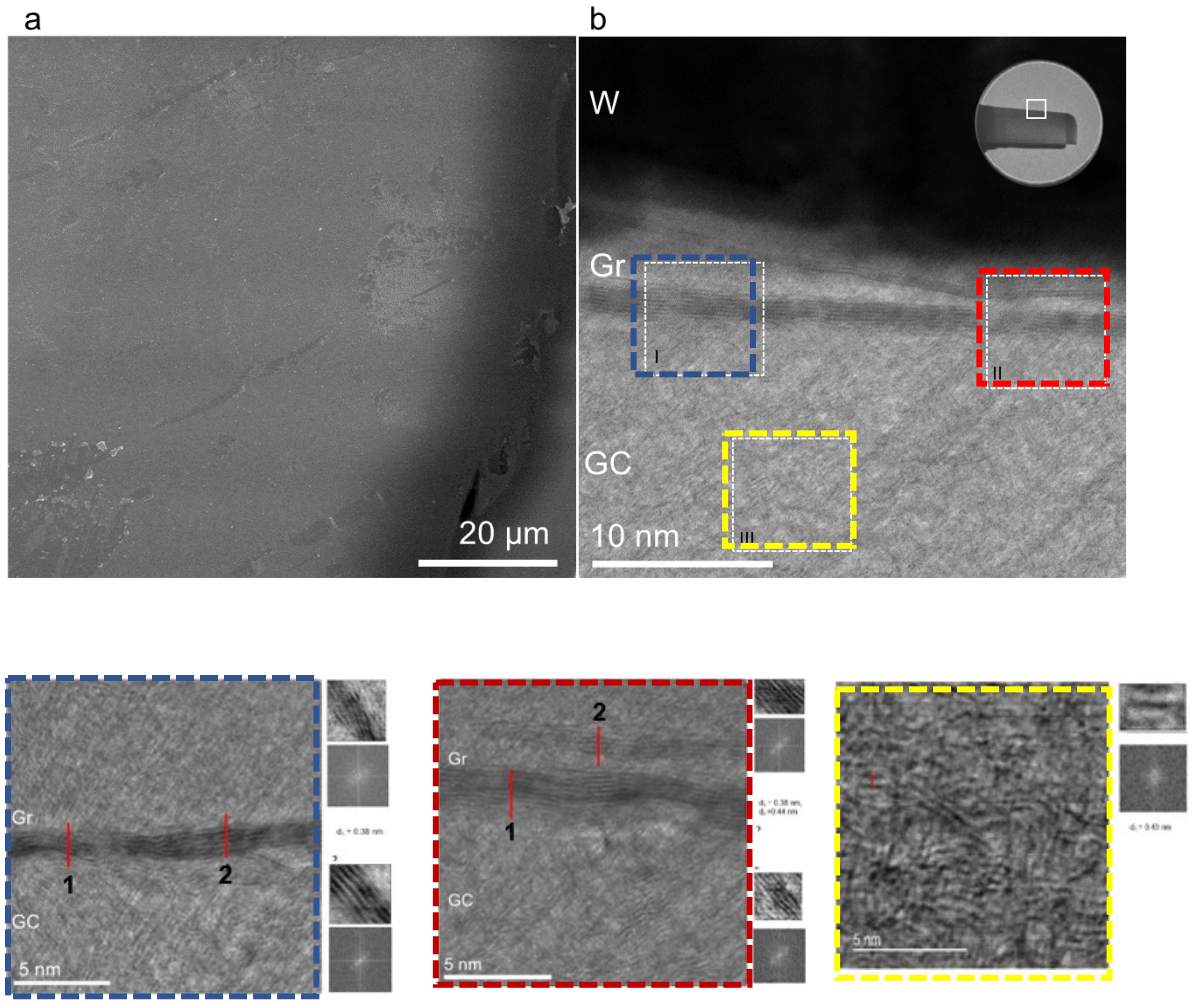



**Figure 4.4** (a) SEM image of GrGC microstructure on polyimide substrate (b) GrGC sample prepared by FIB for STEM imaging. STEM Image of GrGC FIB and interlayer distance of stacked graphene layers was studies at locations I, II and III.

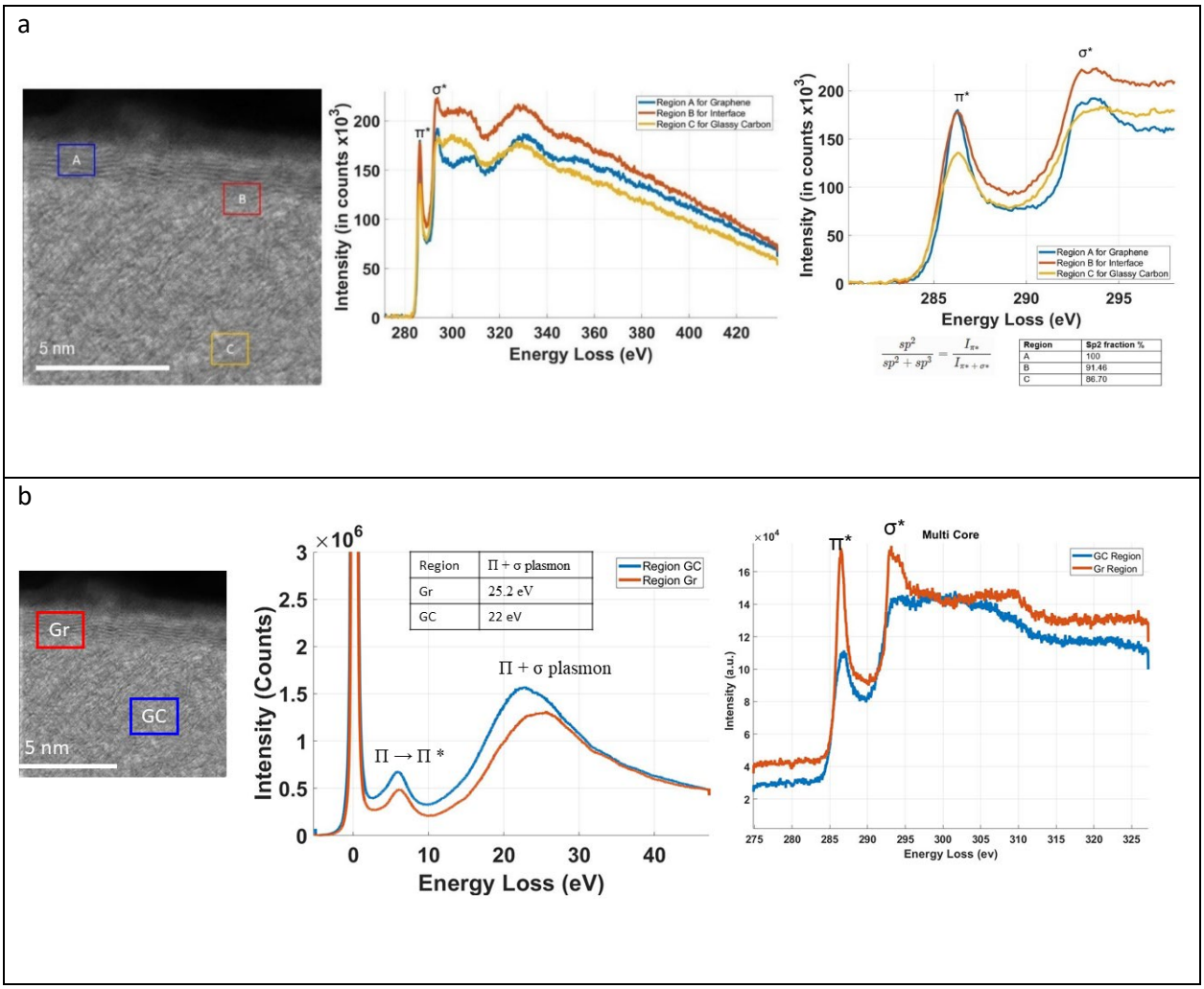



**Figure 4.5** (a) Bright field STEM image of stacked Gr layers and EEL spectra recorded at locations A, B and C. (b) Summed low-loss EEL spectra and multi-acquire high-loss EELS acquired at Gr and GC regions.

### 3.3 HAADF STEM:

Similarly, a DF STEM image can be generated by Nion UltraSTEM resulting in a high-angle annular dark-field (HAADF) image. HAADF image is formed by Rutherford scattered electrons, the intensity of which depends on the mean atomic number of the transmitted volume. HAADF images show distinct material (Z-) contrast, where the intensity of each image pixel is roughly proportional to the second power of atomic number, Z (Lebeau & Stemmer, 2008). In STEM HAADF image, the layer with bright contrast on the top is the Au protective layer (Figure 6). The metamaterial appears darker in contrast due to its low atomic number. A line-profile series is shown at Gr GC interface, for low loss spectrum, the layers

visible in Gr region with brighter contrast indicate increased thickness of the material. Transition in intensities of low and high loss spectra of HAADF is observed from Gr to Interface and from interface to GC region. Here, Gr region is indicated by highest intensity counts, whereas GC is indicated by lowest intensity.

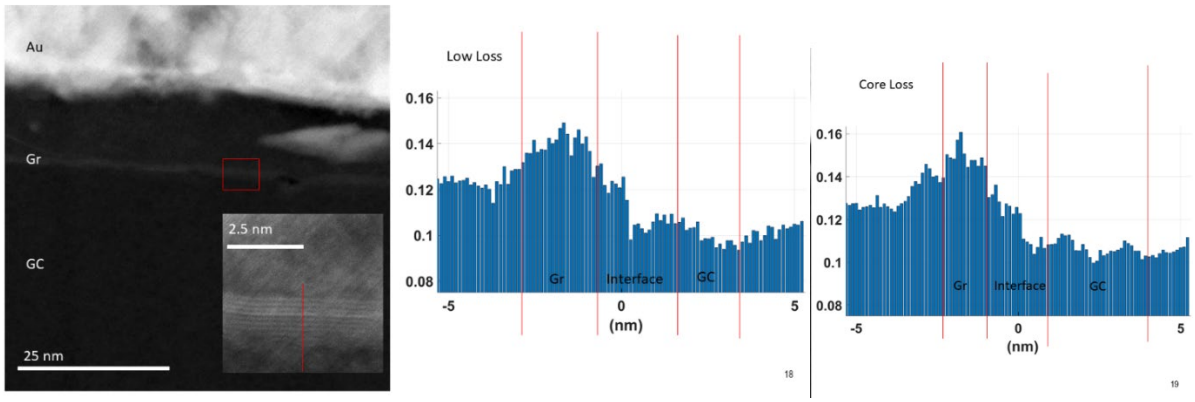



**Figure 4.6** (a) HAADF image of the GrGC material (b) Low loss HAADF spectrum (c) Core loss HAADF spectrum

### 3.4 Structural Disorder:

The graphitic and disorder peaks for both GrGC and GC were observed at 1340 cm-1 and 1583 cm-1. For the pristine glassy carbon, the 2D band merges with the surrounding bands to form a small, modulated bump. The intensity of the 2D peak increases for GrGC as compared to GC. The formation of greater and more uniform carbon hexagonal rings in GrGC causes significant rise in the 2D intensity. Small lateral size or smaller graphene layers may be the cause for not visible 2D peak for pristine GC.

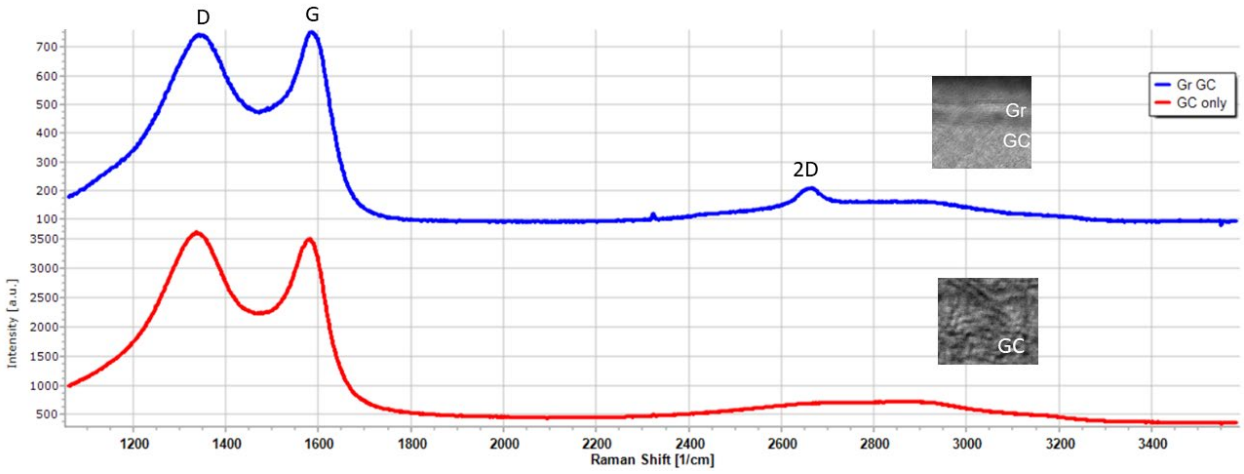



**Figure 4.7** Structural defects in GrGC Vs GC. GrGC material has shown similar D and G peaks as that of GC. 2D peak was observed for GrGC.

### 3.4 FTIR Spectroscopy

To understand surface bonds and functional groups on GrGC experimentally, we compared GC and GrGC FTIR spectrums. In the FTIR spectra (Figure 8), the boxed areas indicate the areas of interest, i.e., carbonyl and hydroxyl peaks. The potential presence of carbonyls, carboxylic acids, and hydroxyls was tested by analyzing their known corresponding peaks. The presence of carboxyl groups onto the surface of Gr-GC is indicated by peak in 1740–1720 cm-1. Carbonyl and carboxyl functional groups are observed in $sp^2$ hybrized carbon atoms in graphene sheet or on the edges. Peaks between wavenumber 3100–3000 $cm^{-1}$ (=C–H) corresponding to sp2 from aromatic ring are observed for GrGC (Figure 8)

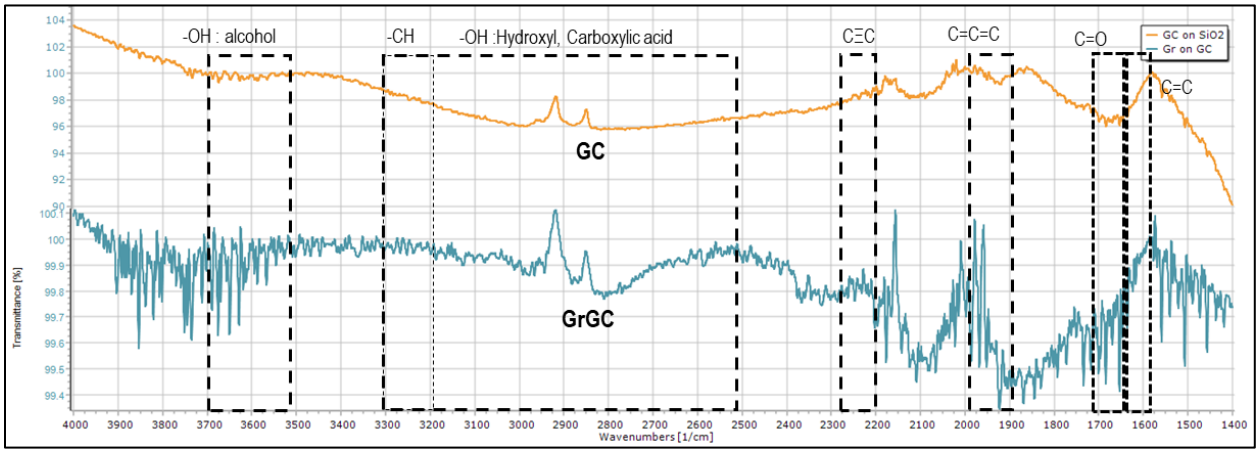



**Figure 4.8** FTIR spectrum of GrGC microstructure and corresponding hydroxyl, carboxyl, and carbonyl peaks

### 3.3 Molecular Dynamics Simulation of Evolution of GrGC

The MD simulation focused on modeling the interaction of the monolayer Gr with SU8 negative tone resist during a pyrolysis process to generate a GrGC metamaterial. The modeling showed that the evolution of the metamaterial in this process had several key stages, i.e., (i) binding of carbon molecule from the edge of Gr monolayer with oxygen molecules of epoxy group from SU8 monomer (ii) breakdown of hydrocarbons in SU8 monomers and (iii) formation of carbon rings that originate from SU8 monomers at Gr edges (aromatic groups), and (iv) formation of graphitic structure at the edges of Gr monolayer. Due to sp2 configuration, the surface carbon atoms of Gr are relatively inactive. However, dangling bonds located on the edges of Gr monolayer can form bonds with the SU8 polymer matrix. This provides catalytic seeds for the formation of larger graphitic structure in the pyrolysis process. During the early stage of temperature ramp-up at T = 600K, carbon atoms at the graphene monolayer edges were observed to bind with epoxy group of SU8. Towards the end of the ramping (T = 2300K), with further degradation of the polymer, formation of CO, $CO_2$, $H_2O$, $H_2$, and $CH_4$ were observed along. At T = 2700K, Gr nanosheets exhibited favorable edge chemistry with the formation of 5-, 6-, and 7-membered carbon rings. These carbon rings were formed from polymer as shown in Figure 10c. At the final pyrolysis temperature of

3100K, graphitic structure was observed along with stacked domains of graphitic plane. These graphitic planes are connected to each other by linear and branched C-C chains.

To determine the effect of holding time during the pyrolysis process at the maximum temperature, two sets of simulations were carried out, i.e., with Model I (400 ps) and Model II (1200 ps). Figure 10 shows evolution of GrGC structure for model II at 1000 K, 2000K, 3000K, 3100K showing binding of SU8 and 5-, 6-, and 7-membered carbon ring structures to the monolayer Gr. At 1000 K and 2000 K, favorable edge chemistry of graphene monolayer supports attachment of SU8 monomers at the edge of Gr (Figure 10 a and b). At T = 2300 K or at higher temperature, SU8 monomers degraded with significant formation of 5-, 6-, and 7-membered carbon rings. These carbon rings are bonded at the Gr edge as shown in Figure 10c at T = 3000 K. At the maximum pyrolysis temperature of 3100K, graphitic 3D cagey structures were formed around Gr. The chart shown in Figure S2 (a) indicated the C, H and O contents in the graphitic structure starting from Gr at 400 K. The carbon contents of the GrGC structure increase significantly till the pyrolysis temperature is reached. The CHO contents in the structure remain almost constant during ramping down phase. Similar trend is observed for simulation model 2 with longer pyrolysis temperature hold time representing the carbon content of the GrGC microstructure for both models remained similar. Figure 11 shows the GrGC microstructure at the room temperature, after the pyrolysis is completed. Carbon atoms from Gr monolayer are highlighted in blue for model I whereas, Gr carbon atoms from model II are represented in grey shade. Top view and side view along X axis of the both models I and II did not show significant difference in geometry (Figure 11a-b, d-e), however view along the Y axis for model II showed higher amount of curved structures as (Figure 11F) compared to Model I (Figure 11C). This indicated that with longer pyrolysis temperature hold in MD simulation resulted in curved structures in the graphitic structures originated from SU8 carbon radicals. 5- or 7- membered carbon rings contributed to higher curvature for model II.

### 3.4 Functional Groups Analysis

The atomic structure of the resulting material is mainly composed of both sp3 and sp2 hybridized carbons, with significant amount of C, H, O atoms originally present in SU8 polymer and Gr monolayer. Here, the sp3-hybridized carbons are associated with the carbon atoms connected with hydroxyl group, which are responsible for change of configuration from planar to stereo. After 3100K pyrolysis, the residual oxygen mainly exists in the form of hydroxyls, epoxy, carbonyl groups, and dangling bonds while residual hydrogen mainly exists in the form of hydroxyls (Figure 12).

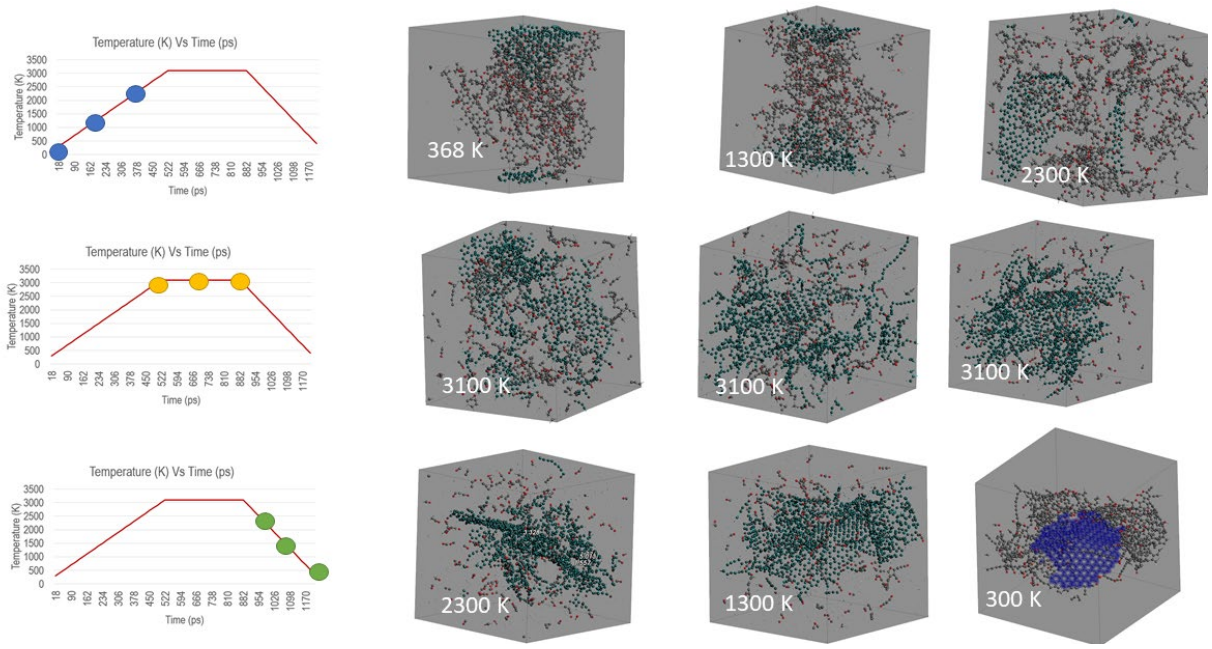



**Figure 4.9** Overview of Evolution of GrGC nanostructure in simulation box for model I

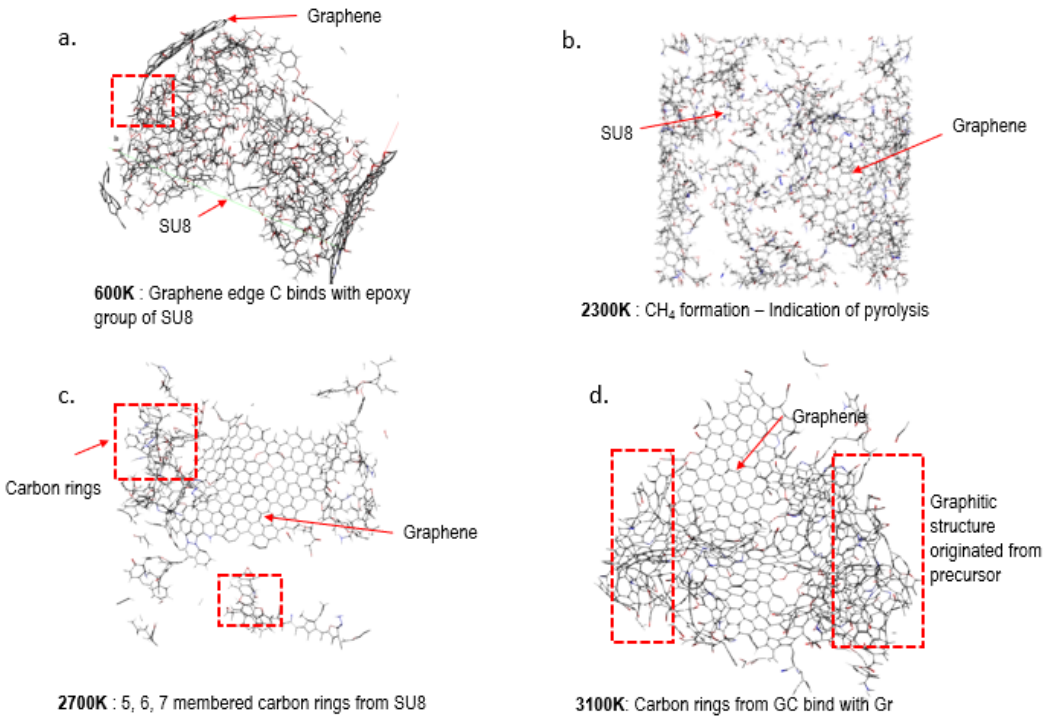



**Figure 4.10** Evolution of GrGC from Gr monolayer and SU8 monomers. Graphene and 20 SU8 monomers: (a) At 600K, graphene C at the edges bind with epoxy group of SU8 (b) At 2300K, CH4 formation was observed, an indicator of pyrolysis (c) At 2700 K, 5-, 6-, and 7-membered carbon rings start to grow at the edge of Gr as shown in red dotted box (d) At 3100 K, multiple carbon rings formation at Gr edge are observed.

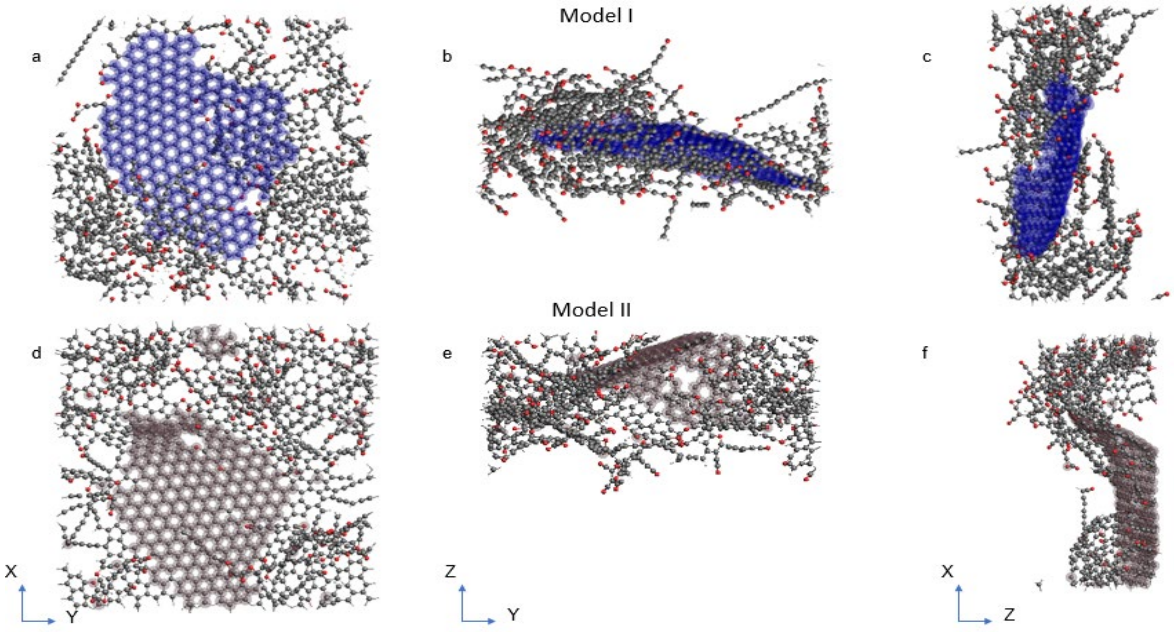



**Figure 4.11** (I) GrGC microstructure Model I (a: view along Z axis, b: view along X axis, (c) view along Y axis) and Model II (d, e, f).

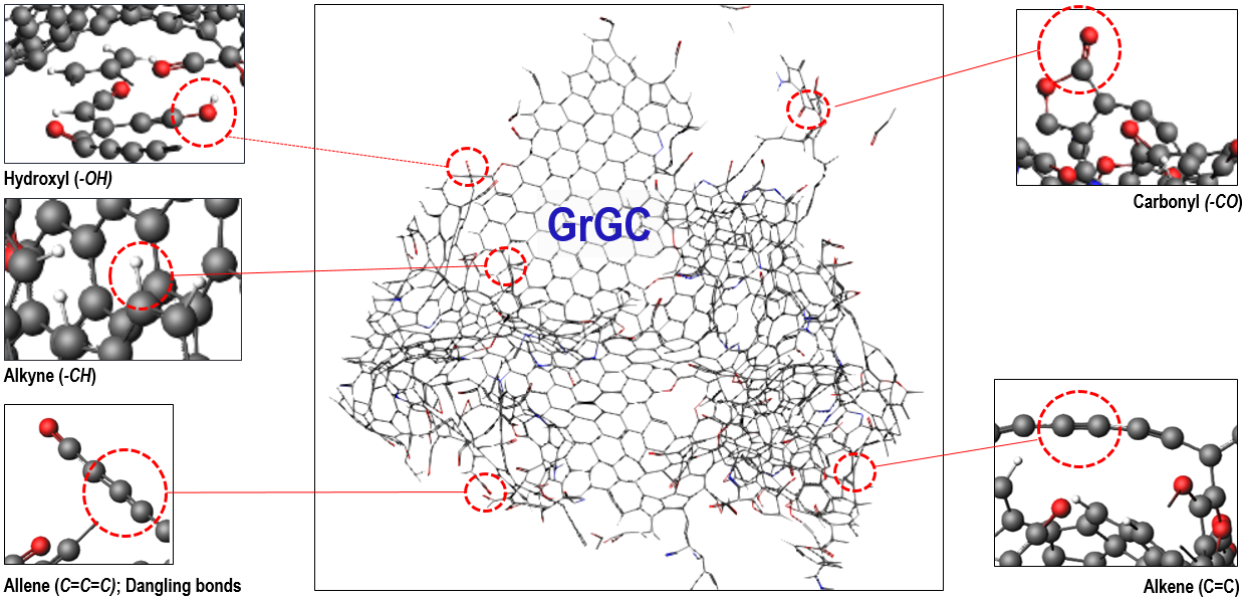



**Figure 4.12** Functional Groups developed on GrGC structure during pyrolysis of Gr monolayer and SU8 microstructure.

## 4 Discussions and Conclusions

The synthesis and fabrication process, the molecular dynamics modeling of the synthesis process, and the comprehensive morphological, and surface material characterizations presented here offer a validation of the introduction of a versatile '2.5D' metamaterial. High spatial (1 nm and less) and high energy resolution (<1 eV) imaging techniques such as STEM and EELS were instrumental in establishing the nanostructure and bonds in the metamaterial.

In STEM images of Figure 4, disordered graphene layers in region III extended up to 2-3 nm in length, whereas ordered graphene planes were observed throughout the surface of the GrGC microstructure. This indicated that by addition of Gr monolayer at the surface of the SU8 microstructure at the beginning of pyrolysis, longer ordered stacks of graphene were evolved. As discussed in Jurkieciz et al (2018), the longer and more ordered graphene nanostructures are observed in glassy carbon as the annealing temperature is increased from 980˚ C to 2500˚ C. Based on results suggested by BF STEM images of stacked Gr layers at the surface of GrGC, it can be inferred that adding Gr at surface of precursor polymer

provides similar ordered Gr stacking as observed by increasing the annealing temperature. However, as the graphene stacks are arranged parallel for GrGC, growth of pores observed with increasing annealing temperature from 980˚ to 2500˚C (Jurkiewicz et al) is not visualized in this study. In this study, graphene monolayer edge carbons to SU8 monolayer interaction were limited due to planar placement of the Gr monolayer at the beginning of the pyrolysis process. To understand the favorable edge chemistry between graphene and precursor polymer, in this case SU8, addition of graphene flakes to SU8 prior to pyrolysis process should be studied. The proposed study will also give insights on evolution of ordered graphene layers and porosity throughout the cross section of the microstructure.

### 4.1 Microstructure of GrGC from STEM Vs Simulation

Stacks of graphene multilayers close to surface of the material from STEM imaging:

Gr layer stacks were also observed in microstructure developed by simulation. The stacks of graphene are crosslinked by the presence of defects in the form of non-hexagonal rings, vacancies, isolated sp3 bonds or chains which introduce curvature in the interlayer connections. The interlayer distance from imaging is calculated to be ~0.38 nm whereas based on the model it is observed to be 0.35 nm. GC part of the microstructure mostly showed curved graphitic surfaces, similarly in simulation, GC curved surfaces indicated sp3 characteristic originated from carbon radicals separated from epoxy monomer precursor (SU8). With regard to sp3 and sp2 fractions, stacks of graphene close to surface show higher sp2 fractions and sp3 characters improves as the GC microstructures are observed predominantly at distance >4 nm from the surface.

Overall, the simulation results show that GrGC form covalent bonds along with functional groups on the edge plane. Hence, the 3D graphitic structure evolved from the process, could be capable of high charge storage, better electrochemical performance for neurotransmitter detection due to presence of functional groups and better conductivity contributed by Gr.

### 4.2 Metamaterial Rich with Functional Groups

The MD simulation demonstrated the unique graphene-induced edge chemistry, which favored the formation of 5/6/7-membered carbon rings along the graphene edges.

1. Longer pyrolysis duration in molecular dynamics simulation of model II did not affect the carbon, oxygen, and hydrogen contents significantly, however, it resulted in more curved structures in GrGC as compared to model I

2. Function groups such as epoxides or cyclic ether (C-O-C) and carbonyl (C=O) are predominantly observed at the GrGC microstructure from simulation whereas few traces of hydroxyl groups are also found

3. GrGC has shown comparable mechanical strength to GC as found in literature based on Young's Modulus. Addition of Gr monolayer to GC microstructure may increase mechanical strength of the material. It can be further investigated through future deformation studies.

4. The cross-links between neighboring graphene layers may have nature of nonplanar sp2-type bonds

### 4.3 Metamaterial Applications

The metamaterial's excellent conductivity and zero band-gap (derived from Gr) along with its capability to form 3D and complex conducting components (3D electrodes, antennas, resonators, etc.,) derived from GC will offer a compelling platform that could enable new possibilities in TTF (thin-film transistors), FET (field effect transistors), OFET, etc. The exceptional electrochemical sensing capability of GC together with the exceptional electrical conductivity of Gr could also offer pathway to ultra-sensitive biochemical sensors that could substantially extend current detection limits.

## 5. Discussion on background work of evolution of GC

5.1 MD Simulation Model:

The simulation box had a volume of 50Å x 50Å x 50Å. Random arrangements of the SU8 monomers (20 units) were arranged randomly in it. The density of the box was 0.375 mL/g. This was optimal possible density with the simulation software. Packmol was used to employ the atomic structure of SU8.

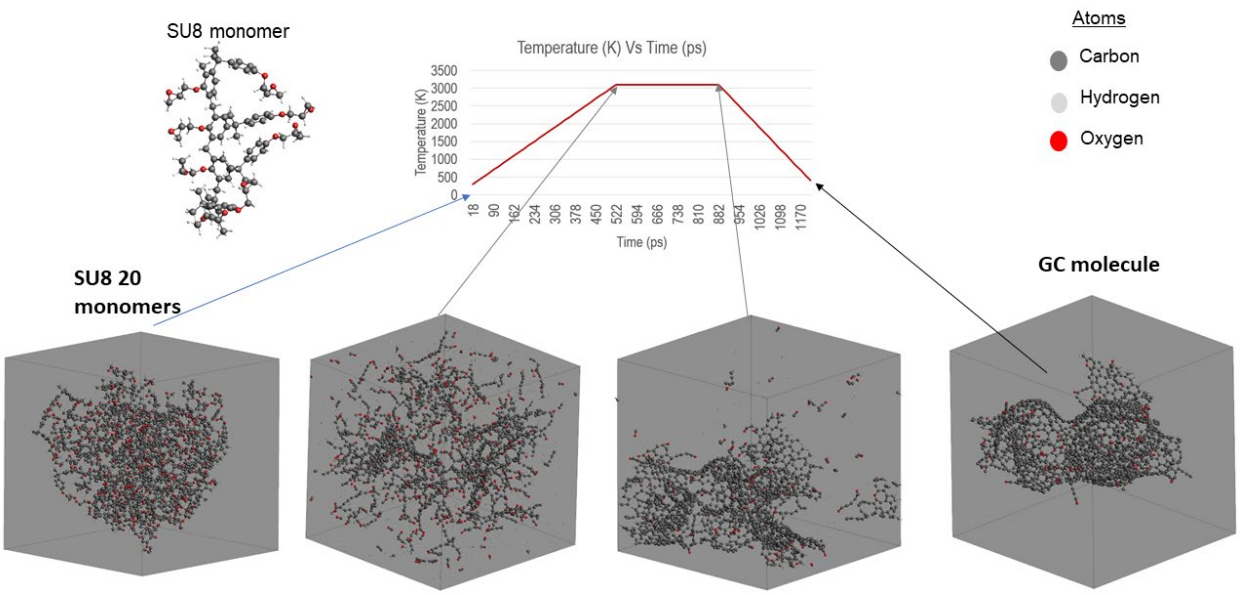



**Figure 4.13** Evolution of GC nanostructure represented in simulation boxes starting from i) T= 300 K and at t= 0 ps ii) T=3100K and t= 500 ps, iii) T = 3100 K and t = 900 ps, iv) T = 298 K and t= 1250

Similar to GrGC model, simulations were performed using CHON reactive force fields module at constant temperature and volume (NVT) with Berendsen thermostat. The equations were integrated with 0.25 fs time step and damping constant used was 100 fs. Here, we employed pyrolysis temperature of 3100 K for simulations. The total length of simulation was 1200 ps.

**5.2 Results:**

Similar to earlier model, we observed $CH_4$ formation at ~2300K. After exposing the polymer to high temperatures in an inert atmosphere, it resulted in the degradation of the SU8 monomers. This releases atoms in the form of gases such as CO, $CO_2$, $H_2O$, $H_2$, $CH_4$. Also, it creates carbon radicals containing aromatic rings originated from the SU8 polymer. At 3100K, at the beginning of holding phase of pyrolysis curve (t= 500 ps), the 5, 6, 7 membered carbon rings start to rearrange. At the end of holding phase (at 3100 K, t= 900 ps), the carbon radicals bonded together resulting in curved graphene multilayer structure. The curvature is added to structure due to 5, 7, 8 membered carbon rings. During the ramp down phase, the nanostructure further showed more curvature, and 2 layers of graphene stacks were observed in it (figure

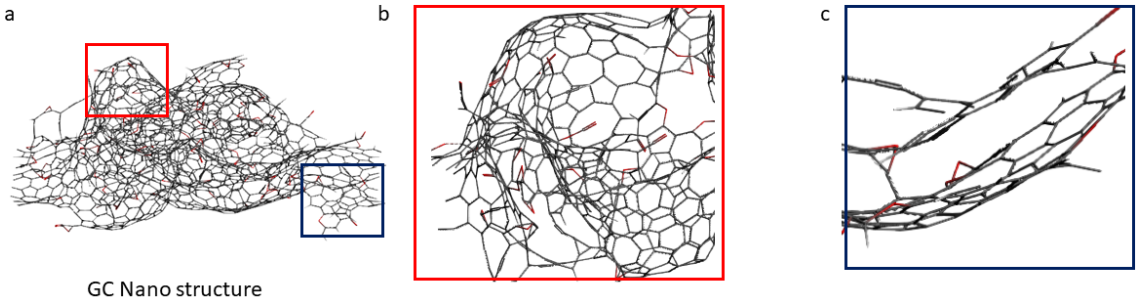



**Figure 4.14** (a) GC nano structure at room temperature (b) Curved region of the nanostructure containing 5 or 7 membered carbon rings (c) bilayer stacking of graphene with 5 or 7 membered carbon rings

As compared to GrGC model, GC synthesis model showed the nanostructure with higher degree of curvature. Due to the presence of planar graphene monolayer in GrGC model at the beginning of simulation, the carbon radicals originated from degradation of SU8 monomers bonded with Gr edge due to favorable edge chemistry. The O2 released around the 2300K attacks on the graphene monolayer, resulting into single or double vacancies, due to the vacancies slight curvature is added to Graphene monolayer. However, in case of GC nanostructure evolution, many dislocations represented by 5/7 carbon ring pairs. These 5/7 pairs are most energetically favorable edge dislocations and generate long range stress field with high strain energy resulting out of plane buckling achieved by releasing partial energy by graphene layer [48,49]. Dislocations can cause out-of-plane enfolding of monolayers, here in case of GC molecules graphene monolayers get enfolded due to 5/7 pairs dislocation [50-53]

**References**

1. Schueller, O.J.A., Brittain, S.T., Marzolin, C., and Whitesides. G.M., "Fabrication and Characterization of Glassy Carbon MEMS," Chem. Mater. 9, 1399–1406 (1997).
2. Ranganathan, S., McCreery, R.L., Majji, S.M., Madou, M.J., "Photoresist-Derived Carbon for Microelectromechanical Systems and Electrochemical Applications," Electrochem. Soc. 147:277-282, (2000).
3. Lin P., Park B., Madou M., "Development and Characterization of a Miniature PEM Fuel Cell Stack with Carbon Bipolar Plates", Journal of Power Sources, 176(1):207-14, 2008.

4. Wang Y, Pham L, de Vasconcellos GPS, Madou MJ. “Fabrication and Characterization of Micro PEM Fuel Cells Using Pyrolyzed Carbon Current Collector Plates”, Journal of Power Sources 2010; 195(15): 4796-4803, 2010.

5. Martinez-Duarte R, Gorkin Iii RA, Abi-Samra K, Madou MJ. “The Integration of 3D Carbon-Electrode Dielectrophoresis on a CD-like Centrifugal Microfluidic Platform”, Lab on a Chip, 10(8):1030-43, 2010.

6. Kassegne, S. et al. “Electrical impedance, Electrochemistry, Mechanical Stiffness, and Hardness, Tunability in Glassy Carbon MEMS μECoG Electrodes”. Microelectronic Eng. 133:36–44, 2015.

7. Novoselov, K.S., et al. “Electric Field Effect in Atomically Thin Carbon Films”, Science, 306: 666–669 (2004).

8. Narayan, J., Bhaumik, A., “Novel Phase of Carbon, Ferromagnetism, and Conversion into Diamond”, J. Applied Physics. 118(21):215303 (2015).

9. Hu, M., He, J., Zhao, Z., Strobel, T.A., et al., “Compressed Glassy Carbon: An Ultrastrong and Elastic Interpenetrating Graphene Network”, Science Advances (2017).

10. Geim, A. K.; Novoselov, K. S. (26 February 2007). "The Rise of Graphene". Nature Materials. 6 (3): 183–191.

11. Zhang, L.L., Zhao, X.S., “Carbon-based Materials as Supercapacitor Electrodes,” Chem. Soc. Rev. 38, 2520 (2009)

12. Yu, A., Roes, I., Davies, A., Chena, Z., "Ultrathin, Transparent, and Flexible Graphene Films for Supercapacitor Application", Appl. Phys. Lett. 96, 253105 (2010).

13. Zhang, L., Zhou, L.R., Zhao, X.S., “Graphene-based Materials as Supercapacitor Electrodes,” J. Mater. Chem. 20, 5983 (2010).

14. Brownson, D.A.C., Kampouris, D.K., Banks, C.E., “An Overview of Graphene in Energy Production and Storage Applications,” J. Power Sources 196, 4873 (2011).

15. Bose, S., Kuila, T., Mishra, A.K., et al., “Carbon-based Nanostructured Materials and their Composites as Supercapacitor Electrodes.,” J. Mater. Chem. 22, 767 (2012).

16. MacKenzie, J. D. & Ho, C. “Perspectives on Energy Storage for Flexible Electronic Systems,” Proc. IEEE 103, 535–553 (2015).

17. Gwon, H. et al. “Recent Progress on Flexible Lithium Rechargeable Batteries,” Energy Environ. Sci. 7, 538–551 (2014).

18. Kassegne, S., Moon, K., Martín-Ramos, P., Majzoub, M., Ozturk, G., Desai, K., Parikh, M., et al. "Organic MEMS/NEMS-based High-Efficiency 3D ITO-less Flexible Photovoltaic Cells", JMM, 22 (11), 115015, 2012.

19. Xia, J., Chen, F., Li, J. & Tao, N. “Measurement of the Quantum Capacitance of Graphene,” Nat. Nanotechnol. 4, 505–509 (2009).

20. Nimbalkar, S., Castagnola, E., Balasubramani, A., Scarpellini, A., Samejima, S., Khorasani, A., Boissenin, A., Thongpang, S., Moritz, C., and Kassegne, S., "Ultra-Capacitive Carbon Neural Probe Allows Simultaneous Long-Term Electrical Stimulations and High-Resolution Neurotransmitter Detection", Nature Scientific Reports 8 (1), 6958, 2018.

21. Vomero, Castagnola, E., Maggiolini, E., Ciarpella, F., Rembado, I., Goshi, N., Fadiga, L., Kassegne, S., Ricci, D., "A Direct Comparison of Glassy Carbon and PEDOT-PSS Electrodes for High Charge Injection and Low Impedance Neural Interfaces", Advances in Science and Technology 102, 68-76, Trans Tech Publications, 2016.

22. Kadic, M., Milton, G.W., van Hecke, M. et al. "3D Metamaterials", Nat Rev Phys 1, 198–210 (2019).

23. Mardegan, A., Kamath, R., Sharma, S., Scopece, P., Ugo, P., Madou, M. "Optimization of Carbon Electrodes Derived from Epoxy-based Photoresist", J. Electrochemical Society 160(8): B132-B137 (2013).

24. Sharma, S., Kamath, R., Madou, M. "Porous Glassy Carbon Formed by Rapid Pyrolysis of Phenol-Formaldehyde Resins and its Performance as Electrode Material for Electrochemical Double Layer Capacitors", J. Analytical and Applied Pyrolysis 108:12-18 (2014).

25. Kassegne, S., Vomero, M., Gavuglio, R., Hirabayashi, M., Özyilmaz, E., Nguyen, S., Rodriguez, J., Özyilmaz, E., van Niekerk, P., Khosla, A., "Electrical Impedance, Electrochemistry, Mechanical Stiffness, and Hardness Tunability in Glassy Carbon MEMS μECoG Electrodes," Microelectron. Eng. 133, 36–44 (2015).

26. Sharma, S., Shyam Kumar, C.N., Korvink, J.G. et al. "Evolution of Glassy Carbon Microstructure: In Situ Transmission Electron Microscopy of the Pyrolysis Process", Sci Rep 8, 16282 (2018).

27. Jurkiewicz, K., Pawlyta, M., Zygadło, D. et al. "Evolution of Glassy Carbon Under Heat Treatment: Correlation Structure–Mechanical Properties", J Mater Sci 53, 3509–3523 (2018).

28. Russo, M. F. Jr and van Duin, A. C. T. "Atomistic-Scale Simulations of Chemical Reactions: Bridging from Quantum Chemistry to Engineering," Nucl. Instrum. Methods Phys. Res. B 269, 1549–1554 (2011).

29. van Duin, A.C.T., Dasgupta, S., Lorant, F., Goddard, W.A., "ReaxFF: A Reactive Force Field for Hydrocarbons", J. Phys. Chem. A, 105, 9396-9409, 2001.

30. Senftle, T., Hong, S., Islam, M. et al. "The ReaxFF Reactive Force-Field: Development, Applications and Future Directions", NPI Comput Mater 2, 15011 (2016).

31. Kimberly Chenoweth, Adri C. T. van Duin, and William A. Goddard, "ReaxFF Reactive Force Field for Molecular Dynamics Simulations of Hydrocarbon Oxidation," The Journal of Physical Chemistry A, 112 (5), 1040-1053, 2008.

32. Sørensen, M. R., Voter, A.F., "Temperature-Accelerated Dynamics for Simulation of Infrequent Events," J. Chem. Phys. 2000, 112, 9599− 9606

33. Kristof M. Bal and Erik C. Neyts, "Merging Metadynamics into Hyperdynamics: Accelerated Molecular Simulations Reaching Time Scales from Microseconds to Seconds," Journal of Chemical Theory and Computation 2015 11 (10), 4545-4554.

34. Lianchi Liu, Yi Liu, Sergey V. Zybin, Huai Sun, and William A. Goddard, "ReaxFF-lg: Correction of the ReaxFF Reactive Force Field for London Dispersion, with Applications to the Equations of State for Energetic Materials", The Journal of Physical Chemistry A, 115 (40), 11016-11022, 2011.

35. Yalan Liu, Junxia Ding, Ke-Li Han, "Molecular Dynamics Simulation of the High-Temperature Pyrolysis of Methylcyclohexane," Fuel, Volume 217, Pages 185-192, 2018.

36. Hamm, JBS., Muniz, A.R., Pollo, L.D., Marcilio, N.R., Tessaro, I.C., “Experimental and Computational Analysis of Carbon Molecular Sieve Membrane Formation upon Polyetherimide Pyrolysis,” Carbon, Volume 119, 2017.

37. Kamat, A. M.; van Duin, A. C. T.; Yakovlev, A. “Molecular Dynamics Simulations of Laser-Induced Incandescence of Soot Using an Extended ReaxFF Reactive Force Field”, J. Phys. Chem. A 2010, 114 (48), 12561–12572. https://doi.org/10.1021/jp1080302.

38. Martínez L, Andrade R, Birgin EG, Martínez JM. “PACKMOL: A Package for Building Initial Configurations for Molecular Dynamics Simulations”, J Comput Chem., 30(13):2157-64, 2009.

39. Radovic, Ljubisa R., Alejandro B. Silva-Tapia, and Fernando Vallejos-Burgos. "Oxygen Migration on the Graphene surface. 1. Origin of Epoxide Groups." Carbon 49.13 (2011): 4218-4225.

40. D’Angelo, D., C. Bongiorno, M. Amato, I. Deretzis, A. La Magna, E. Fazio, and S. Scalese. "Oxygen functionalities evolution in thermally treated graphene oxide featured by EELS and DFT calculations." The Journal of Physical Chemistry C 121, no. 9 (2017): 5408-5414.

41. Kumar, CN Shyam, Venkata Sai Kiran Chakravadhanula, Adnan Riaz, Simone Dehm, Di Wang, Xiaoke Mu, Benjamin Flavel, Ralph Krupke, and Christian Kübel. "Understanding the graphitization and growth of free-standing nanocrystalline graphene using in situ transmission electron microscopy." Nanoscale 9, no. 35 (2017): 12835-12842.

42. Bressler, P. R., M. Lübbe, D. R. T. Zahn, and W. Braun. "X-ray absorption spectroscopy study of different solid carbon modifications." Journal of Vacuum Science & Technology A: Vacuum, Surfaces, and Films 15, no. 4 (1997): 2085-2087.

43. Rauwel, Protima, Augustinas Galeckas, Martin Salumaa, Frédérique Ducroquet, and Erwan Rauwel. "Photocurrent generation in carbon nanotube/cubic-phase HfO2 nanoparticle hybrid nanocomposites." Beilstein journal of nanotechnology 7, no. 1 (2016): 1075-1085.

44. Berger, S. D., D. R. McKenzie, and P. J. Martin. "EELS analysis of vacuum arc-deposited diamond-like films." Philosophical Magazine Letters 57, no. 6 (1988): 285-290.

45. Jurkiewicz, Karolina, Mirosława Pawlyta, Dorota Zygadło, Dariusz Chrobak, Stanisław Duber, Roman Wrzalik, Alicja Ratuszna, and Andrzej Burian. "Evolution of glassy carbon under heat treatment: correlation structure–mechanical properties." Journal of materials science 53, no. 5 (2018): 3509-3523.

46. Langer, T., Herbert Pfnür, H. W. Schumacher, and Christoph Tegenkamp. "Graphitization process of SiC (0001) studied by electron energy loss spectroscopy." Applied Physics Letters 94, no. 11 (2009): 112106.

47. LeBeau, James M., and Susanne Stemmer. "Experimental quantification of annular dark-field images in scanning transmission electron microscopy." Ultramicroscopy 108, no. 12 (2008): 1653-1658.Abstract

48. Komsa, H.-P., Kurasch, S., Lehtinen, O., Kaiser, U., and Krasheninnikov, A. V., 2013, “From Point to Extended Defects in Two-Dimensional MoS 2: Evolution of Atomic Structure Under Electron Irradiation,” Phys. Rev. B, 88(3), p. 035301.

49. Yang, G., Li, L., Lee, W. B., and Ng, M. C., 2018, “Structure of Graphene and its Disorders: A Review,” Sci. Technol. Adv. Mater., 19(1), pp. 613–64

50. Meyers, M. A., Mishra, A., and Benson, D. J., 2006, “Mechanical Properties of Nanocrystalline Materials,” Prog. Mater. Sci., 51(4), pp. 427–556.

51. Zou, X., Liu, Y., and Yakobson, B. I., 2013, "Predicting Dislocations and Grain Boundaries in Two-Dimensional Metal-Disulfides From the First Principles," Nano Lett., 13(1), pp. 253–258.

52. Yazyev, O. V., and Louie, S. G., 2010, "Topological Defects in Graphene: Dislocations and Grain Boundaries," Phys. Rev. B, 81(19), p. 195420.

53. Alem, N., Yazyev, O. V., Kisielowski, C., Denes, P., Dahmen, U., Hartel, P., Haider, M., Bischoff, M., Jiang, B., and Louie, S. G., 2011, "Probing the Out-of-Plane Distortion of Single Point Defects in Atomically Thin Hexagonal Boron Nitride at the Picometer Scale," Phys. Rev. Lett., 106(12), p. 126102

**Acknowledgments**

Chapter IV, in partial (sections 1 to 4), is a reprint of materials as it appears in **Nimbalkar S**, Montgomery-Walsh R, Lara-Galindo S, Bunnell J, Kassegne S. "Novel Graphene-Glassy Carbon (GrGC) MetaMaterial Synthesis: Fundamental Investigation through Experimental Validation and Molecular Dynamics Simulation" The dissertation author is the first author of this paper.

# CHAPTER V

## Graphene on Glassy Carbon Microelectrodes Demonstrate Long-Term Structural and Functional Stability in Neurophysiological Recording and Stimulation

**Abstract**

There is a growing interest in the use of carbon and its allotropes for microelectrodes in neural probes because of their inertness, long-term electrical and electrochemical stability, and versatility. Building on that interest, we introduce a new electrode material system consisting of an ultra-thin monoatomic layer of graphene (Gr) mechanically supported by a relatively thicker layer of glassy carbon (GC). Due to its high electrical conductivity and high double-layer capacitance, Gr has impressive electrical and electrochemical properties, two key properties that are useful for neural recording and stimulation applications. However, because of its 2D nature, Gr exhibits a lack of stiffness in the transverse direction and hence almost non-existent flexural and out-of-plane rigidity that will severely limits its wider use. On the other hand, GC is one of carbon's important allotropes and consists of 3D microstructures of graphene fragments with a natural molecular similarity to Gr. Further, GC has exceptional chemical inertness, good electrical properties, high electrochemical stability, purely capacitive charge injection, and fast surface electrokinetics coupled with lithography patternability. This makes GC an ideal candidate for addressing Gr's lack of out-of-plane rigidity through providing a matching sturdier and robust mechanical backing. Combining the strengths of these two allotropes of carbon, we introduce a new neural probe that consists of ~1 nm thick layer of patterned Gr microelectrodes supported by another layer of 3-5 μm thick patterned GC. We present the fabrication technology for the new *Gr on GC* (graphene on glassy carbon) microelectrodes and the accompanying pattern transfer technology on flexible substrate and report on the bond between these two allotropes of carbon through FTIR, surface morphology through SEM, topography through AFM, and microstructure imaging through STEM. A long-term (18-weeks) *in vivo* study of the use of these *Gr on GC* microelectrodes assessed the quality of the ECoG-based neural signal recording and stimulation through electrophysiological measurements. The probes were demonstrated to be functionally and structurally stable over the 18-week period with minimal glial response – the longest reported so far for graphene-based microelectrodes.

## 1. Introduction

Carbon, due to its chemical inertness, biocompatibility, good electrical conductivity, high charge injection capacity, and excellent long-term electrochemical stability [**1-5**], is proving to be a compelling material for applications that require microelectrodes to interface with tissue for long periods. Subsequently, carbon-based neural probes have been reported for neural recording [**1-5**], stimulation [**6-8]**, magnetic resonance compatibility [**9**], and neurotransmitter detection [**10-16**]. Carbon's multimodal capabilities permit not only electrical sensing and stimulation but also electrochemical recording due to its unique and yet paradoxical properties of chemical inertness and selective chemical activity. This is enabled by carbon's chemically active functional groups at edge planes and dangling bonds [**10-13**]. These capabilities have in turn raised significant interest in the wider use of carbon, predominantly for long-term applications. However, further advances in neural engineering applications require a new generation of multimodal neural probes with notable mechanical and electrochemical stability and durability, excellent conductivity, high charge storage and injection capacity, and exceptional electrochemistry – rare combination of properties difficult to find in a single material.

The two prominent allotropes of carbon, glassy carbon (GC) and graphene (Gr), may be ideal for chronically implanted multimodal neural probes. GC continues to demonstrate substantial success in neural probes due to its exceptional chemical inertness, good electrical properties, high electrochemical stability, purely capacitive charge injection, and fast surface electrokinetics coupled with lithography patternability **[2-4, 9-11**]. Although Gr has excellent electrical conductivity (**1700 S/m**) **[17,18]** and high double-layer capacitance (**21 µF/cm$^2$**) **[19]**, its major weakness is a lack of rigidity in the transverse direction due to its 2-dimensional monolayer nature with its thickness averaging only < 1 nm [**20**]. Therefore, Gr's inability to maintain versatility and mechanical robustness during extended periods of implantation may impede further advances in the use of Gr for microelectrodes.

Motivated by this need for a multi-material system with both in-plane and out-of-plane stiffnesses, we present a new approach where monolayer Gr microelectrodes are solidly supported on thicker lithographically patterned GC which has a natural molecular similarity with Gr and consists of 3D microstructures of graphene fragments and closed graphene-like cages [**21-22**]. The microfabrication of

these multi-material microelectrodes and their pattern transfer to a flexible substrate are presented. We also report on the investigation of the bonding between the two allotropes of carbon through Fourier Transform Infrared Spectroscopy (FTIR), their molecular structure through Raman Spectroscopy, their surface morphology and microstructure through Scanning Electron Microscopy (SEM) and Scanning Transmission Electron Microscopy (STEM) imaging, and their topography through Atomic Force Microscopy (AFM). A long-term (18 weeks) *in vivo* study involving an animal model is conducted to explore functional and structural stability of the multi-material microelectrodes.

## 2. Material and Methods

### 2.1 Microfabrication of Microelectrode Array of Graphene Supported on Glassy Carbon

We microfabricated a 12-channel neural probe specifically designed for electrocorticography (ECoG) applications. The geometry of the ECoG probe consisted of 300 μm diameter surface electrodes with 70 μm wide interconnects and a total width of 3 mm [**2-3**]. A silicon wafer with 0.5 μm thick oxide layer with a CVD grown graphene monolayer transferred on it was purchased from Grolltex (CA, USA). On top of this layer of Gr, 6 μm thick SU8–10 negative photoresist (Microchem, MA) was spin-coated at 1000 rpm. The SU8-10 layer was then patterned following conventional negative lithography process of microelectrodes described elsewhere [**2-3**]. Subsequently, the Gr underneath the patterned SU8 layer was itself patterned using the SU8 layer as a hard mask for oxygen plasma etching at 50 W and 300 mTorr oxygen pressure for 30 s. The wafer that contained patterned SU8 on Gr microelectrodes was then heated in a quartz furnace (MTI Corp., CA) under an inert atmosphere of nitrogen gas with flow rate of 50 ml/min. For pyrolysis of the patterned SU-8 polymer, the temperature was ramped to 1000 °C over a period of 6 hours and then held at this temperature for 90 minutes, similar to conventional carbon-MEMS processes widely reported in the literature [**2-3**,**23-24**]. Following this, the furnace was allowed to cool down to room temperature over a period of several hours. Subsequently, a layer of photosensitive polyimide (HD Microsystem) was spun and patterned onto the microelectrodes, as a substrate for the subsequent layers. Thin-film layers of Ti and Pt were then deposited on the substrate through lift-off process creating conductive traces, and finally a second layer of polyimide was spun on the metal traces for electrical

insulation [**2**]. Buffered hydrofluoric acid (BHF) etching was then carried out to release the final probe. As shown in **Figure 1**, in the final released probe, the Gr layer will be on top of GC layer which in turn will be supported by a polyimide substrate layer. The microelectrodes obtained will be referred to as "***Gr on GC***" to emphasize the specific mechanical backing that GC provides to Gr layer in the combined material system.

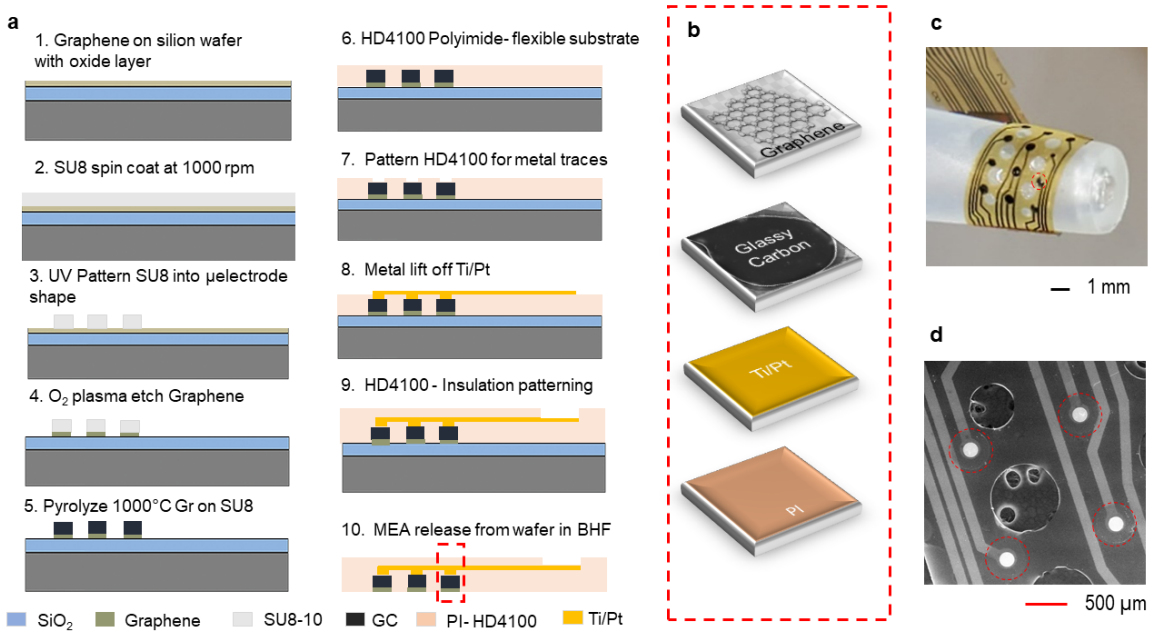



**Figure 5.1** Flexible "*Graphene on Glassy Carbon" (Gr on GC)* microelectrode array. (a) microfabrication steps using UV photolithography, (b) schematic of cross section of the microelectrode, (c) flexibility of probe with *Gr on GC* microelectrodes (represented by dotted circles), and (d) SEM image of probe.

## 2.2 Surface and Material Characterizations

### 2.2.1 SEM, AFM, and STEM Imaging

The morphologies of the ensuing microelectrodes were optically characterized *via* optical microscopy using Keyence VHX-5000 microscope (Itasca, IL, USA) and through SEM (Quanta 450, Hillsboro, OR, USA), using secondary electron detector and AFM (Signal Hill, CA, USA). Peel tests also were carried out to investigate the mechanical strength of the attachment between the *Gr and GC* microstructures of the ensuing probe. This involved attaching a clear tape to the *Gr on GC* thin-film and

applying a pulling force to separate it from the substrate. STEM characterization was also carried out to clearly identify how the Gr layer interfaces with GC. The sample for STEM was prepared by focused ion beam of gallium ions for milling of thickness ~40 nm (FEI Nova 200 Dual-Beam FIB). The sample was coated with 5 nm of gold (Au) initially to avoid electron charging of *Gr on GC*. In order to protect *Gr on GC* during current ion milling, the sample was further coated with 50 nm of Tungsten. The thinning of sample was done by ion current milling (at 30 kV and 5 nA). Nion UltraSTEM 100 (Kirkland, WA, USA) was used for recording high resolution scanning transmission electron microscope images of the cross-sectional sample prepared by FIB of *Gr on GC* microelectrode.

### 2.2.2 FTIR Spectroscopy

FTIR-ATR spectroscopy was done using a Nicolet iS50 FT-IR Spectrometer equipped with a Smart iTR diamond ATR cell (Thermo Scientific, Court Vernon Hills, IL, USA). The microstructure was washed with methanol, dried, and placed on the diamond cell. 128 spectral scans were recorded. The scans were compiled from 4 diagonal areas of microstructure **(**Supplementary **Figure S1),** and all discrete *Gr on GC* spectra were averaged, resulting in a single spectrum **[25].**

### 2.2.3 Raman Spectroscopy

Raman spectroscopy was carried out on the microelectrodes using Thermo Nicolet DXR Raman Microscope (ThermoScientific Inc of Waltham, MA, USA). Argon ion laser operated at 532 nm with average power of 1.5 mW focused through aperture of 25 μm in diameter with 50x objective was used for recording the Raman spectra.

## 2.3 Electrochemical Characterization

The electrochemical behavior of the microelectrodes was studied in Phosphate-Buffered Saline solution (PBS; 0.01 M, pH 7.4; Sigma Aldrich, USA). Cyclic voltammetry (CV) was used to quantify capacitive charging, while electrochemical impedance spectroscopy (EIS) was used to determine the electrical properties of the microelectrodes over a range of frequencies. For both CV and EIS tests, Potentiostat (Reference 600+, Gamry Instruments, USA) connected to a three-electrode electrochemical cell with a Pt wire as a counter electrode and a saturated Ag/AgCl reference electrode was used. During

CV tests, the working electrode potential was swept between 1.3 V and −0.9 V (water window of Gr and GC), maintaining a scan rate of 100 mV/s. During EIS measurements, 10 mV RMS amplitude sine wave was superimposed on 0 V potential with frequency sweep from 0.1 to 105 Hz. Equivalent circuit modeling of the EIS data was carried out through Gamry Echem Analyst Vn 7.05 software (Gamry Instruments, USA). Cathodic-first charge balanced bi-phasic current pulses with 400 µA amplitude, 200 µs cathodic half-phase period were applied using a Gamry Instruments Virtual Front Panel (Gamry Instruments, PA, USA) and voltage transient responses corresponding to voltage excursions between working and counter electrodes were recorded.

### 2.4 *In Vivo* Validation of Neural Recording and Stimulation

The *in vivo* study investigated neural recoding quality and stimulation performance of the *Gr on GC* Micro ECoG (µECoG) probe through acute and chronic recordings in adult female Long-Evans rats (250g-300g; Charles River Laboratories, MA). The acute sensory evoked potential (SEP) and motor evoked potential (MEP) recordings were performed in three animals and one animal, respectively. The chronic implantation was conducted in one animal. All procedures were approved by the Institutional Animal Care and Use Committee of the University of Washington under the protocol number 4265-01.

#### Surgical Procedure for Acute Brain Recording and Stimulation

Three µECoG probes (*Device 1-3*) were evaluated by acute SEP recordings in three animals (*n=3*). The animals were anesthetized using 2-3% isoflurane mixed with oxygen. Body temperature was maintained on a heating pad set at 37°C during and after the surgical procedure. The skin on the head and right forelimb was shaved and cleaned three times with alcohol and betadine. The skin incision was made on the skull, and the soft tissue was removed to expose the frontal and parietal bones. The head was fixed within a stereotaxic frame, and three screws were placed on the skull. One screw for a reference wire was placed on the right parietal bone and contacted the dura over the brain. Two screws for ground wires were placed on the bilateral frontal bones without contacting the brain. *6 mm x 4 mm* craniotomy was performed, centered 1.5 mm caudal to the bregma and 2.5 mm lateral to the midline to target the somatosensory area

for the right forelimb [**26**]. After removal of the dura mater, the µECoG device was placed on the brain surface and stabilized by gel form and acrylic dental cement.

Three µECoG probes (*Device 4-6*) delivered stimulation to assess the stimulation function by acute biceps MEP recordings in one animal (*n=1*). The animal was anesthetized using urethane 0.6g/kg [**27**]. In this brain stimulation study for MEPs in biceps muscles, *6 mm x 4 mm* craniotomy was performed, centered 1.5 mm rostral to the bregma and 2.5 mm lateral to the midline to target the motor area for the right forelimb. The devices were placed on the brain surface, and one screw on the right parietal bone was used as ground.

**Surgical Procedure for Chronic Implantation**

One animal was chronically implanted with the *Gr on GC* microelectrodes (*n=1*). Procedures were identical to the acute SEP recording implant describe above with the following exceptions. Sterile procedures were used throughout the implant surgery. Cement glue preparation with acrylic cement was used to fix the connector to the skull (C&B Metabond, Parkell Products Inc., NY). Postoperatively, Buprenorphine (0.05 mg/kg) was administered twice per day for three days to manage pain.

**Evoked Potential Recording and Offline Analysis**

In both acute and chronic impedance and SEP recordings, the same recording procedure was conducted under 2-3% isoflurane mixed with oxygen. Body temperature was maintained on the heating pad set at 37°C during recordings. Impedance of each microelectrode was measured at the frequency of 1 kHz (IMP-2A Single Channel, MicroProbes, MD, USA). The µECoG electrodes were then connected to a multichannel data acquisition system (Tucker-Davis Technologies, FL, USA) through an active, unity-gain head-stage. Two wires (0.27 mm diameter, 2 mm de-insulated tip, AS631, Cooner wire, CA, USA) were subcutaneously implanted 1 mm apart in the right biceps. Bipolar subcutaneous electrical stimulation of the periphery was delivered to evoke SEPs on the brain surface **(Figure 2a)**. Specifically, 40 single, biphasic, squared wave stimulation pulses were delivered with the following parameters: pulse width: cathodic-first 500 µs and anodic 500 µs, current amplitude: 5 mA, frequency: 2 Hz using an analog stimulus isolator (Model 2100 Isolated Pulse Stimulator, A-M System, WA, USA).

Recorded data were digitized at 24.4 kHz and stored on a PC for offline analysis. Subsequently, raw signals were bandpass filtered (30-450 Hz, 4th order Butterworth, zero-phase filter) and down-sampled to 1 kHz using MATLAB R2020a (MathWorks, MA, USA). The evoked response from 5 ms to 55 ms after stimulation onset were averaged to obtain average SEPs. The extracted evoked response between 5 ms to 55 ms after stimulation onset was considered as an estimate for the signal, while the extracted spontaneous activity corresponding to 105 ms to 155 ms after the stimulation onset was taken as an estimate for the background noise (**Figure S4**). Subsequently, signal-to-noise ratio (SNR) of the ECoG electrodes over forelimb sensory cortex were evaluated during SEPs. The SNR value for each trial was defined as the ratio between the average peak-to-peak response of SEPs at 5 mA biphasic biceps stimulation, and two standard deviations of the spontaneous activity [**28**]. The calculated SNR of all channels was used as a useful indication of the quality of brain-signal recording.

In the acute MEP recording, the data acquisition system was connected to the *Gr on GC* microarray through a passive head-stage. Bipolar electromyogram (EMG) electrodes were then inserted in the right biceps muscle for EMG recording (AS631, Cooner wire). Nine 100 μs stimulation pulses of monophasic (pulse width: anodic 100 μs, 3 ms interval, 9 pulses, current amplitude: 2 - 2.65 mA) were delivered to one electrode, located 2.9 mm rostral to the bregma and 3.4 mm lateral to the midline (location of channel), at 2 Hz for at least 50 pulses per parameter tested (**Figure 2b**). We performed the experiments using an analog stimulus isolator (Model 2100 Isolated Pulse Stimulator, AM System, Sequim, WA). The MEPs were analyzed offline using custom MATLAB scripts. Biceps EMG signals were filtered (4th order Butterworth band-pass; 10-500 Hz). A single trial of MEP was defined as evoked responses during the 30 ms following each stimulation event. MEPs were subsequently processed to compute peak to peak amplitudes.

**2.5 Immunohistochemical Analysis**

**Tissue Processing**

Brain tissue from the chronically implanted animal was used for immunohistochemistry after 18 weeks of implantation. The rat was deeply anesthetized with Beuthanasia (200mg/kg) injected intraperitoneally. During full sedation, the rat was perfused with 300mL of 0.9% saline followed by 300mL

of 4% paraformaldehyde in 0.1M phosphate buffered saline (PBS: pH, 7.4). The brain was dissected and stored in 10% paraformaldehyde at 4°C overnight. The implanted ECoG probe was explanted during the procedure. For the following three days, the brain and implant were moved to 30% sucrose buffer subsequently, 24 hours per buffer in 4°C. The brain was blocked into two different blocks covering the implanted area of the left hemisphere for the compared to the same area of the right hemisphere as a control. The blocks were frozen separately into Tissue Tek O.C.T. mounting media (Sakura, Netherlands) using liquid methanol and carbon dioxide. Serial sections (40 μm) were cut (Leica CM1850 cryostat; Leica Microsystems, Germany) into coronal sections. The sections were stored free floating in a 48-well plate with phosphate buffered saline (pH, 7.4) at 4°C, and then processed for immunohistochemical staining. The explanted probe was washed and dried with 90% isopropyl alcohol, then underwent surface and material characterizations.

Brain sections were washed with 1% Donkey Serum-PBS-Triton 2×10 min at room temperature followed by blocking with 5% normal donkey serum (Sigma-Aldrich) in PBS for one hour. Primary antibodies were then added to sections at the following dilutions: Anti-Glial Fibrillary Acidic Protein, GFAP (1:750; Millipore Sigma) and IBA-1 (1:600, Wako). Sections were incubated overnight with primary antibodies at 4°C. The following day, the sections were washed with 1% Donkey Serum-PBS-Triton 10 min twice and then incubated in secondary antibody, Alexa Fluor 594 - Donkey anti-rabbit (1:200; Thermo Fisher Scientific) for one hour at room temperature. The sections were then washed with regular PBS 10 min twice and mounted onto regular superfrost slides (Thermo Fisher Scientific). After the sections dried, cover slips were applied using Polyvinyl alcohol mounting medium with DABCO (Sigma-Aldrich).

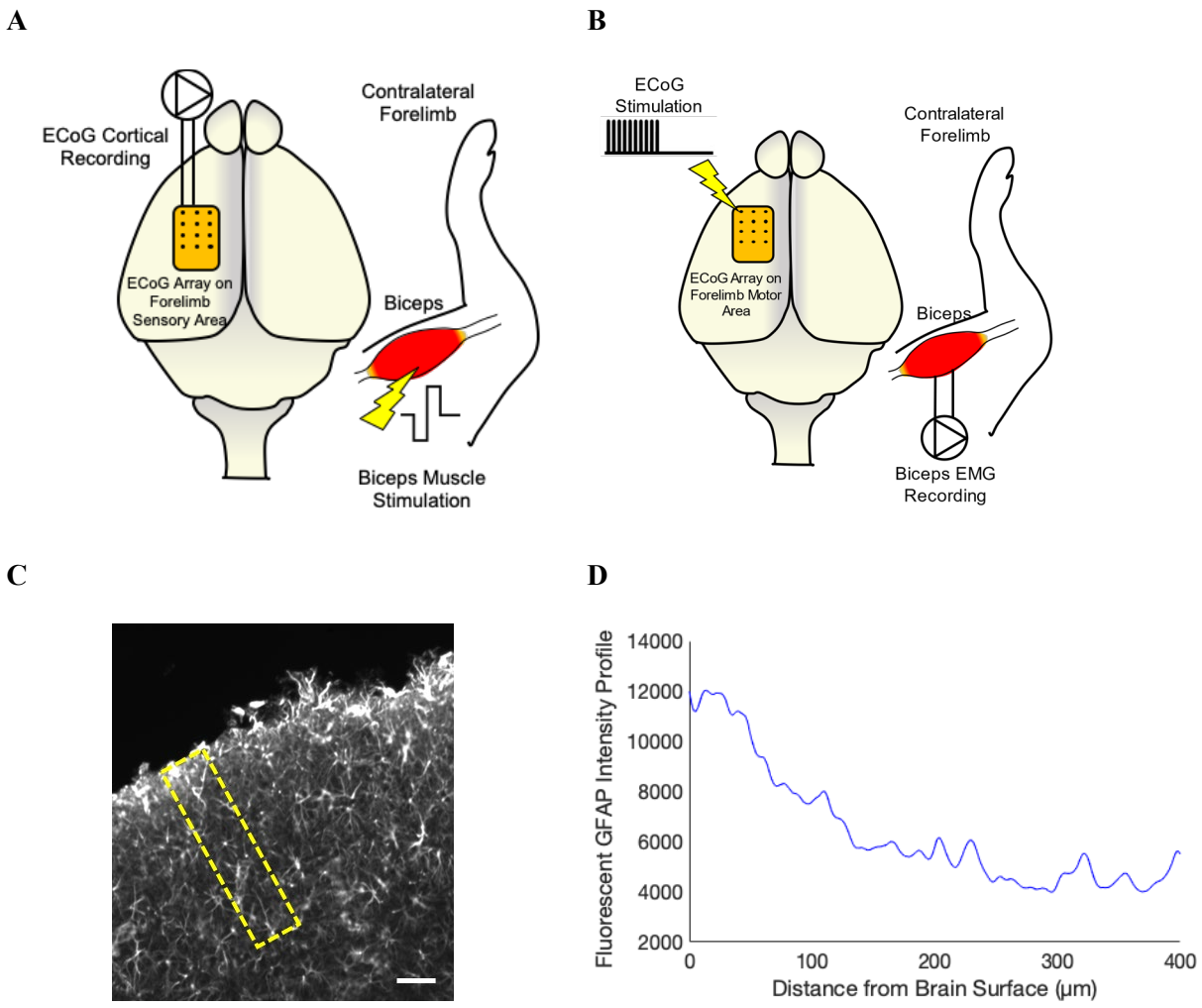



**Figure 5.2** Schematic of setup for *in vivo* recording and region of interest for fluorescent imaging. (a) diagram of the setup of multichannel sensory evoked potential recording using contralateral biceps muscle stimulation. (b) diagram of the setup of motor evoked potential recording of contralateral biceps muscle using ECoG stimulation. (c) an example of the grayscale GFAP immunostained horizontal section of the control tissue and the region of interest (yellow dash-line) used for quantification. Scale bar = 100 μm. (d) plot of the fluorescent intensity profile in the region of interest with respect to distance below the brain surface.

**Imaging and Analysis**

A total of four groups of tissue consisting of sections stained with GFAP or IBA-1 were prepared for both the implanted and control cortex. Fluorescent images were captured with a Leica fluorescent microscope with ZEN Pro software (Carl Zeiss Microscopy GmbH, Germany) under the same illumination level with 80x magnification, and then converted into grayscale images using ImageJ software. A 100 μm

× 400 μm rectangular shape window starting from the brain surface at the location of implant was marked (**Figure 2c**). The staining intensities within 20 rectangular windows for each group were quantified by averaging the pixels across the width of the rectangle in ImageJ and plotting them as a function of distance from the electrode in MATLAB R2020a (**Figure 2d**).

### 2.6 Statistical Analysis

All *in vivo* data are reported as mean ± standard error of mean, unless noted. All data were assessed for normality with the Kolmogorov–Smirnov test, and none of the data for the analysis were normally distributed. For the acute SEP and MEP recording analyses, difference between three devices were evaluated by Kruskal-Wallis test and Wilcoxon Rank-Sum test with Bonferroni correction. For the chronic recording analysis, differences within recorded on the same device over time were evaluated by Friedman's test and Wilcoxon Singed Rank test with Bonferroni correction. For the histological analysis, differences of the staining intensities between the implanted hemisphere and the control hemisphere were tested by Wilcoxon Singed Rank test with Bonferroni correction. All differences at the adjusted *p-value* based on the Bonferroni method (< 0.05 divided by the number of comparisons) were considered significant. All analyses were performed with MATLAB R2020a.

## 3. Results

In this section, we report the outcomes of these characterizations, with particular focus on the long-term stability of the microelectrodes.

### 3.1 Surface, Mechanical, AFM, SEM, and STEM Characterizations

First, we performed a '*peel test'* with clear pressure-sensitive tape to assess the adhesion between Gr layer and the supporting GC layer. The middle two images in **Figure 3** demonstrate outcomes of a peel test, while the last image shows the *Gr or GC* microstructure after the peel test. It was clearly noticed that there were no visible residues of *Gr or GC* left on the tape. This indicates that there is a strong bond between Gr and GC layers at scales larger than the weak bonds generated by typical *van der Waals* forces.

Subsequently, to visualize the structural disorders and defects on the surface of the Gr microstructure supported on GC, we analyzed SEM images (**Figure 4**). The wrinkles on a graphene surface

were formed due to the different thermal expansion coefficient between Cu and graphene during the wet transfer process of graphene onto a substrate. This also resulted in many line defects including ripples and folding. Point defects such as vacancies were also observed. STEM imaging of cross section of *Gr on GC* microelectrode indicated a distinct zone of graphene layers (~2 nm) on top of GC, while GC region showed disordered 3D graphitic structure stacking. Topography analysis by AFM of the surface of microelectrode indicated a lower roughness of *Gr on GC* material as compared to plain GC. This low surface roughness could contribute to higher impedance values of the microelectrodes of same dimensions. The mean surface roughness for GC alone microelectrodes was 40.15 ± 6.25 nm *(n* = 4), while that of *Gr on GC* microelectrodes was 9.64 ±2.67 nm.

**3.2 FTIR Spectroscopy**

In the FTIR spectra (**Figure 5a**), the boxed areas indicate the areas of interest, i.e., carbonyl and hydroxyl peaks. The potential presence of carbonyls, carboxylic acids, and hydroxyls was tested by analyzing their known corresponding peaks. The presence of carboxyl groups onto the surface of *Gr on GC* was confirmed by the stretching of the carboxyl group observed at 1740–1720 $cm^{-1}$. Carbonyl and carboxyl functional groups were observed in $sp^2$ hybridized carbon atoms in graphene sheets or on the edges. Peaks between 3100–3000 $cm^{-1}$ *(=C–H*) corresponding to $sp^2$ from the aromatic ring were observed in the *Gr on GC* microstructure. In general, *Gr on GC* showed several hydroxyl peaks between 3300-2500 $cm^{-1}$. Hydroxyl functional groups arranged on the top of the surfaces indicated $sp^3$ hybridization. Hydroxyl band between 1640–1620 $cm^{-1}$ was observed to be overlapped with in-plane vibrations of the skeletal *C=C* band of hexagonal aromatic ring from the graphene (**Figure S2**).

**3.3 RAMAN Spectroscopy**

We further studied structural disorders in the *Gr on GC* material through Raman spectroscopy and compared it to the microstructure of plain GC alone, as shown in **Figure 5b**. Both disorder-induced, amorphous band (*D-band*) and graphitic band (*G-band*), which are characteristics of carbon material were

observed both in GC and *Gr on GC* microelectrodes. Additionally, *Gr on GC* showed 2D peak indicating presence of multilayer graphene, as $I_{2D}/I_G$ is less than 0.5.

**3.4 Electrochemical Properties**

Electrochemical window of the *Gr on GC* microelectrode was defined by linear sweep voltammetry by sweeping the working electrode potential between −1.5 and 2 V, with a scan rate of 50 mV/s (**Figure S3**). Electrochemical impedance (**Figure 6**) at 1 kHz of 18.58 ± kΩ indicates an acceptable range for μECoG recording application **[2].** Phase plot shows a dominance of resistive component for impedance values at frequencies higher than 6 kHz. Results from cyclic voltammetry of *Gr on GC* microelectrodes demonstrate an approximately rectangular shape which is a characteristic of microelectrodes exhibiting a predominantly double-layer capacitance [**2-4**]. The modified Randle's equivalent circuit was curve-fitted with EIS impedance spectra and showed shapes similar to our previously reported results [**2-4**]. The capacitive charge injection mechanism is ideal for understanding neural stimulation and was investigated with voltage transient response to a biphasic symmetric current pulse of 400 μA for 400 μs pulse width. The calculated charge injection capacity was **0.226 mC/cm$^2$**. The voltage transient response showed access voltage **(*Va*) of -0.9V**, maximum positive voltage of **1.6V**, maximum negative voltage of **-1.75V**, $\boldsymbol{E_{mc}}$ (most negative polarization voltage) across electrode-electrolyte interface of **-0.85V** and $\boldsymbol{E_{ma}}$ (most positive polarization voltage) close to **0.7V**. The $E_{mc}$ = **-0.85V** and $E_{ma}$ = **0.7V** values are within the water window range for *Gr on GC* microelectrodes. The charge storage capacity (CSC) of *Gr on GC* microelectrodes was calculated by integrating the cyclic voltammogram curve and was found to be **56.48± 0.770 mC/cm$^2$** (**Figure 6**).

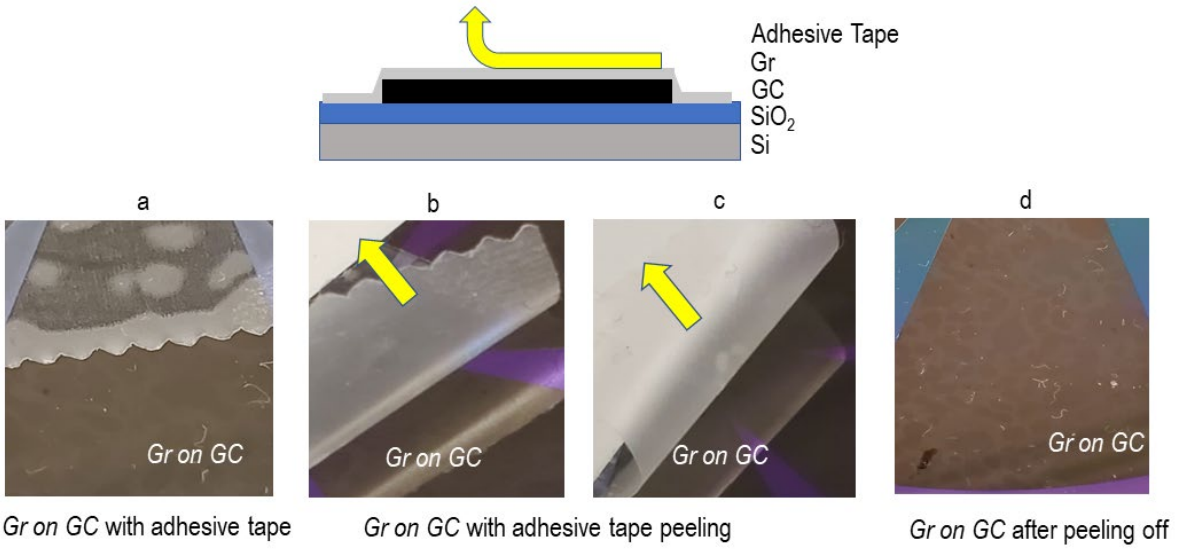



**Figure 5.3** Adhesive tape peeling test on *Gr on GC* microstructure, (a) Adhesive tape attached on *Gr on GC* microstructure surface (b and c) During peeling off of the tape (d) *Gr on GC* microstructure after peel off of the test.

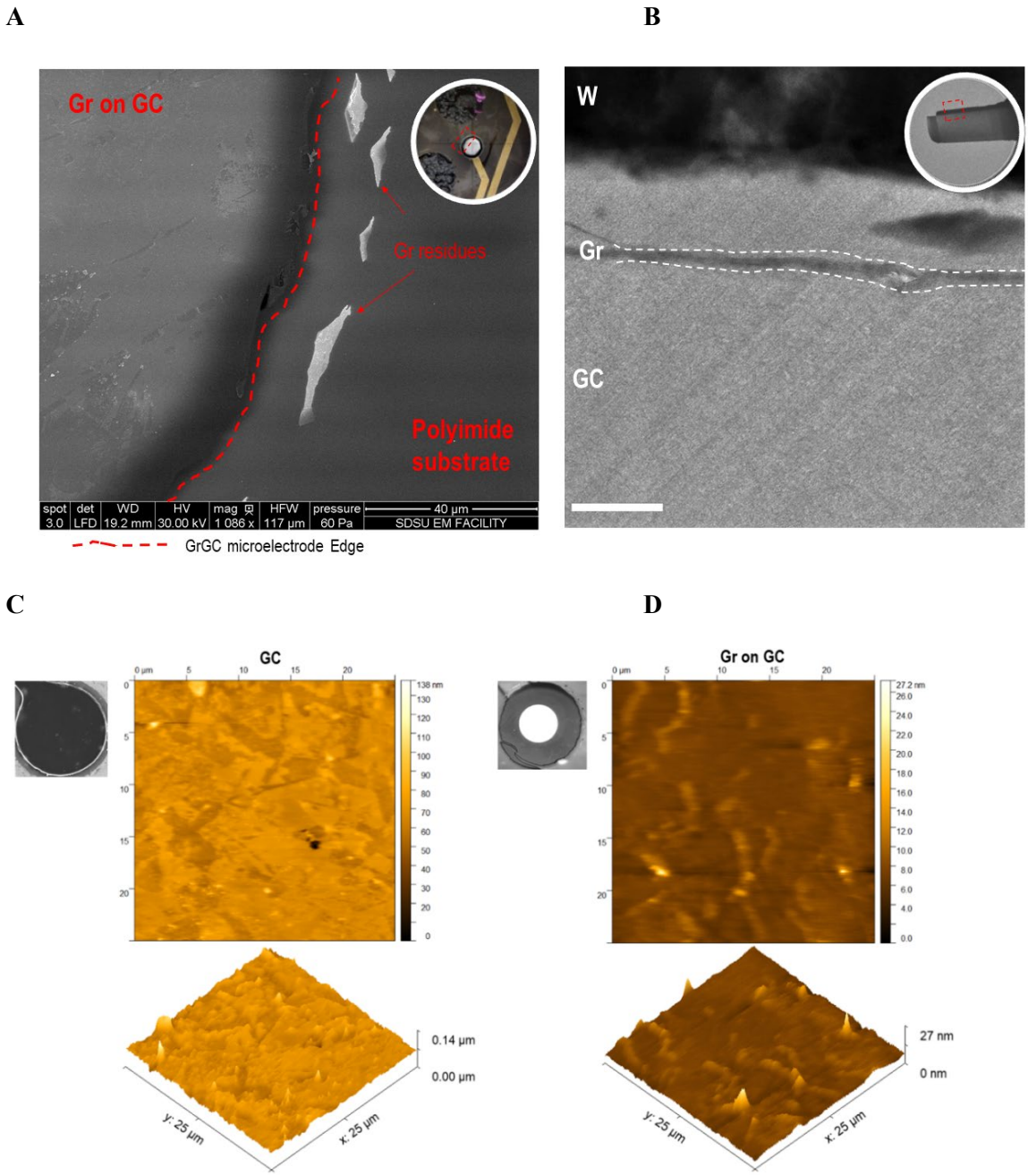
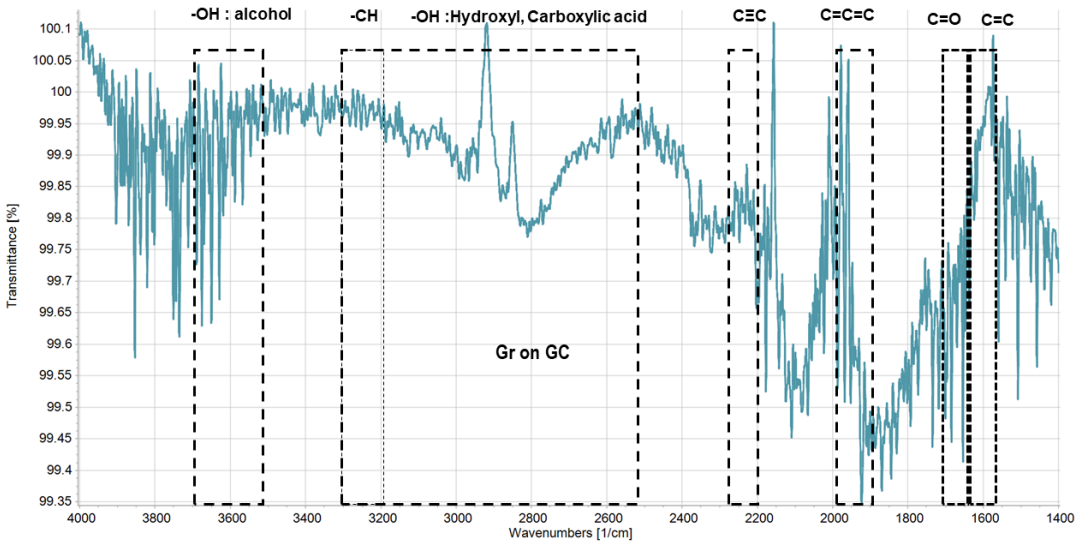



**Figure 5.4** (a) SEM image indicating Gr patches on the GC microelectrode surface (inset image: microscopic image of *Gr on GC* microelectrode). (b) STEM image showing clear distinction between *Gr and GC* interface. Scale bar = 25 nm (Inset Image: *Gr on GC* sample prepared by FIB for STEM, Tungsten (W) was used as protective layer and (c) comparison of mean surface roughness by AFM between GC and (d) *Gr on GC* microelectrode surface**.**

**A**




**B**

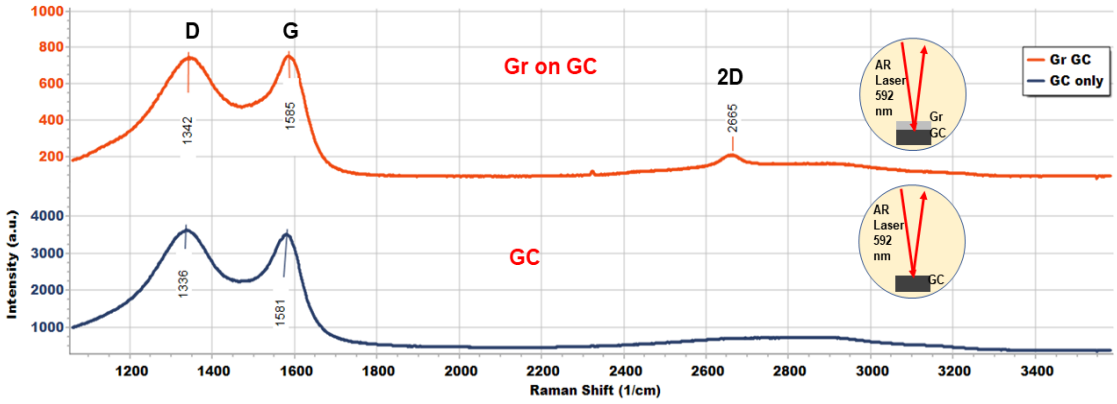



**Figure 5.5** (a) FTIR spectrum of *Gr on GC* microstructure and corresponding hydroxyl, carboxyl, and carbonyl peaks, (b) Raman Spectrum for GC vs. *Gr on GC* microelectrode. $I_D/I_G = 1.03$ for GC and 0.99 for *Gr on GC*. $I_{2D}/I_G$ for *Gr on GC* = 0.27.

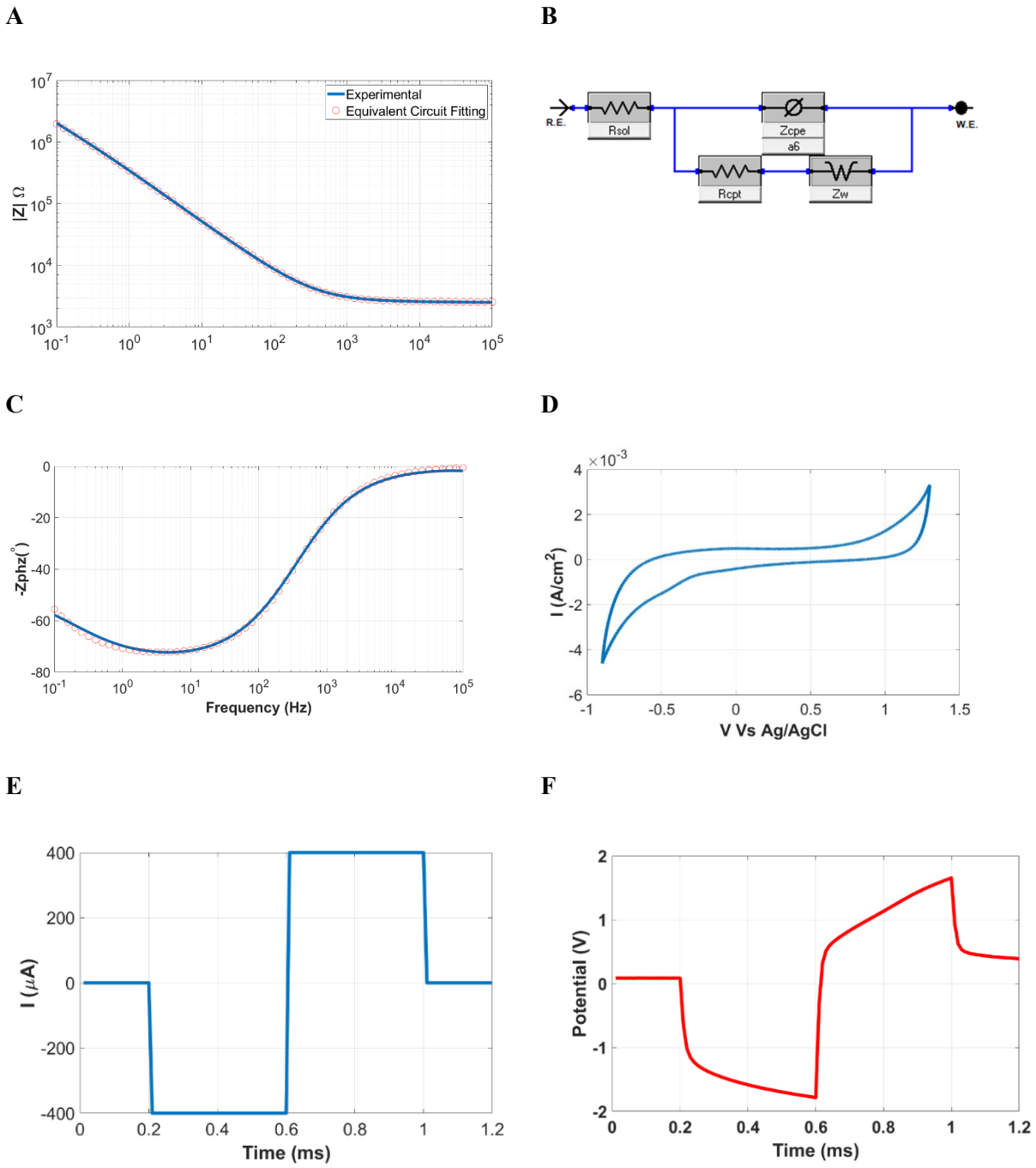



**Figure 5.6: (a)** Electrochemical Impedance Spectroscopy (measured and curved fitted), (b) Equivalent Modified Randle's Circuit, (c) phase indicating capacitive behavior, (d) representative cyclic voltammogram, (e) biphasic pulse of 400 µA for 400 µs pulse-width, (f) voltage transient response of *Gr on GC* microelectrode.

### 3.5 Neurophysiological Recordings

#### Acute *In Vivo* Validation

We then focused on the *in vivo* evaluation of the ECoG microarray. We designed the ECoG probe to perform multimodal function on the brain. First, we tested the acute recording quality of three ECoG probes (*Device 1-3*). Each probe was tested in a different animal. We removed electrodes with $|Z| > 600$ kΩ from all analyses due to likely mechanical or connection failure **[5].**

The impedance of the electrodes across all devices were evaluated at 1kHz in vivo ($|Z|$ @1kHz = 94.5 ± 5.6 kΩ, n = 30; **Figure 7a**). The three devices showed no significant difference in impedance ($\chi^2(2) = 0.86$, $p = 0.6505$, Kruskal-Wallis test). Furthermore, subcutaneous biceps electrical stimulation elicited SEPs in all electrodes (Supplementary **Figure S4**). By using the SEPs, the signal to noise ratio (SNR) was calculated as peak-to-peak amplitude of the bicep's stimulation-induced responses divided by two standard deviations of spontaneous activity (average SNR: 9.76 ± 0.25, for n = 30). There was a significant difference of the SNR among three devices ($\chi^2(2) = 8.44$, $p = 0.0147$, Kruskal-Wallis test). Wilcoxon rank-sum test revealed a significant difference only between Device 1 and Device 2 (*$p = 0.0104$; **Figure 7b**). The average SNR across three devices were over 9.76 which confirms high resolution for the recording (**Figure 7b**). These observations confirmed the repeatability of fabrication for the new *Gr on GC* microarrays.

Second, we tested the performance of stimulation through one channel located on the forelimb motor area in three ECoG probes (*Device 4-6*) in one animal. The stimulation train through the ECoG electrodes elicited the MEPs in the biceps muscle using the EMG recording in the same animal. The maximum stimulation current, 2.65 mA, was determined considering safety of the neural tissues based on Shannon's Equation for 300 μm electrode diameter and 100 μs stimulation pulse width [**29-30**].

We found evoked responses in the biceps muscle within the tested parameters. Three devices similarly showed increased responses as the current increased above 2.4 mA (**Figure 8a**). There was a significant difference of the peak to peak responses among three devices at 2.2 mA, 2.4 mA, and 2.65 mA ($\chi^2(2) = 101$, 105, and 55.2, respectively, $p < 0.001$, Kruskal-Wallis test). Wilcoxon rank-sum test revealed a significant difference only between Device 4 and Device 5 and, between Device 4 and Device 6 (*$p < 0.001$; **Figure 8b**). However, the MEPs across three devices were consistently detectable within the safe parameter settings which confirms the performance of the ECoG stimulation (**Figure 8b**).

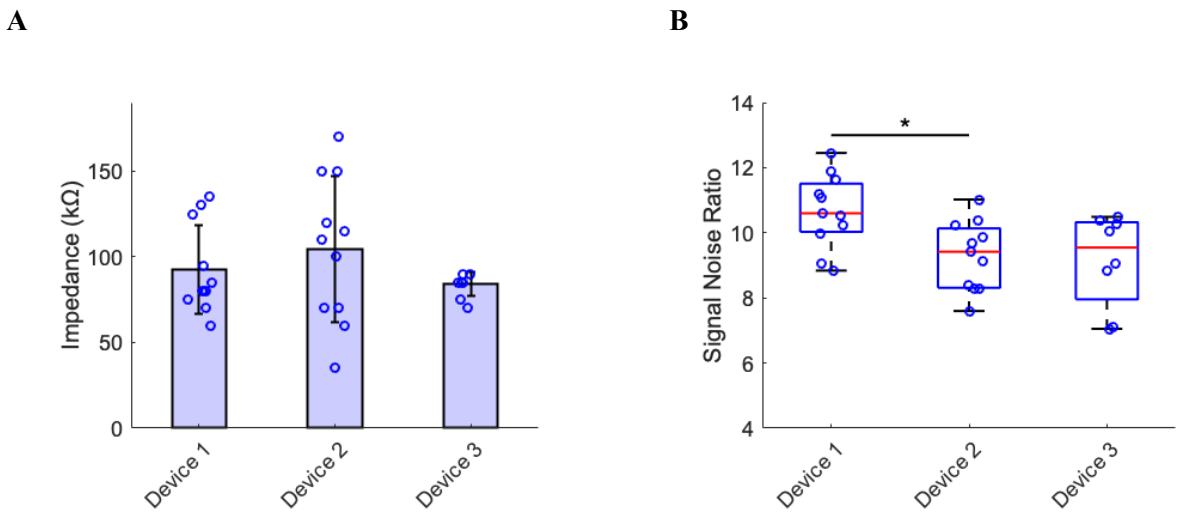



**Figure 5.7** Acute *in vivo* validation of the *Gr on GC* device consistency. (a) Electrode impedance |Z| at 1 kHz for all microelectrodes of each device. Circles present individual data points. Error bars indicate standard error of mean. (b) Signal to noise ratio for all microelectrodes of each device. Electrodes per device; Device 1: $n = 11$ electrodes, Device 2: $n = 11$ electrodes, Device 3: $n = 8$ electrodes. Red lines, boxes, Whiskers, and empty circles present median, 25th-75th percentile, minimum values & maximum values, individual data points, respectively.

### Chronic *In Vivo* Functional Evaluation

Stability of the *Gr on GC* microelectrodes was evaluated by chronic implantation for 18 weeks in one animal. We implanted the *Gr on GC* ECoG arrays over the forelimb sensorimotor cortex and then conducted impedance and SEP testing for the signal noise ratio (SNR) assessment until 18 weeks post implant.

The impedance measured on all eight microelectrodes was generally stable over time *in vivo* except for the first post-implantation week ($\chi^2(4) = 21.35$, $p = 0.0003$, Friedman's test; **Figure 9a**). Week 1 showed significantly higher impedance compared to Week 10, Week 16, and Week 18 ($^*p = 0.0078$, Wilcoxon signed-rank test). This was likely due to changes in the electrode tissue interface around the time of implantation, as there was no significant change from week 6 to week 18. The SNR through the SEPs with the contralateral biceps muscle stimulation was also relatively stable except for Week 18 ($\chi^2(4) = 16.1$, $p = 0.0029$, Friedman's test; **Figure 9b**). We observed a significant decline of the SNR only at Week 18 (SNR: 10.86 ± 0.30) compared to Week 1 and Week 6 (SNR: 13.37 ± 0.45, 12.82 ± 0.64, respectively;

*$p$ = 0.0078, Wilcoxon signed-rank test). Despite the slight decline of the SNR 18 weeks after the implantation, the high recording quality was maintained for at least 16 weeks.

### 3.6 Tissue Histology

To assess the responses of glial cells to the microelectrodes, we labeled the brain sections with antibodies against glial fibrillary acidic protein (GFAP) for astroglial responses and ionized calcium binding adaptor molecule (IBA-1) for microglial responses.

The brain tissue close to the surface showed high GFAP positive processes in both the implanted and control sections, although we observed a trend of slightly higher GFAP responses in the implanted sections (**Figure 10a-c**). There was a statistically significant increase in GFAP positive responses in the implanted section compared to the control section only at 300 μm, and 400 μm form the brain surface (Z = -3.21, $p$ = 0.0013 at 300 μm, Z = -3.32, $p$ = 0.0001 at 400 μm, Wilcoxon singed-rank test; **Figure 10c**). Overall, while the deeper brain presented inconsistent increased GFAP responses, 18-week electrode implantation on the brain did not increase the reaction of astrocytes in the brain close to the surface compared to the control hemisphere in the animal. Meanwhile, IBA-1 positive cells, indicating activated microglia and macrophage, tended to be high around the implant, only at 25 μm from the brain, in the implanted hemisphere compared to the control hemisphere despite non-significant difference after Bonferroni correction (Z = -2.73, $p$ = 0.0064 at 400 μm, Wilcoxon singed-rank test; **Figure 10f**). However, the IBA-1 positive cells showed normal responses based on the control section of the brain (**Figure 10d-f**). Therefore, the prolonged implantation of the *Gr on GC* ECoG led to minimum glial responses of the brain compared to the control hemisphere in the animal.

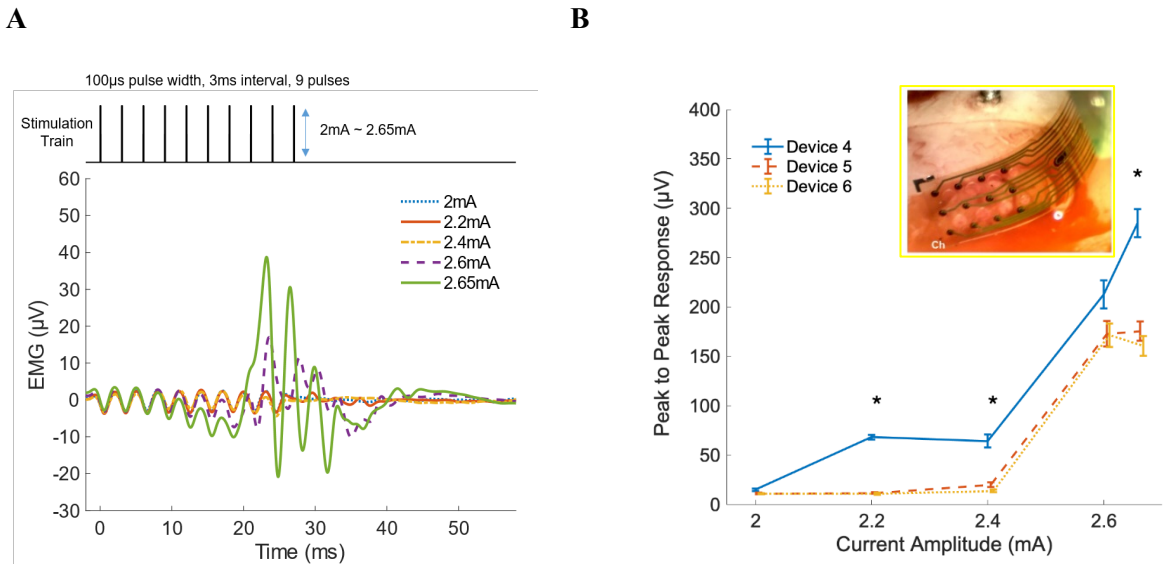



**Figure 5.8** Acute stimulation *in vivo* validation of the *Gr on GC* device (Device 4-6). (a) Example of graded filtered electromyographic signals from Device 5 (0-60 ms after the ECoG stimulation onset) recorded in the biceps following the brain stimulation. (b) Recruitment curve of the ECoG induced motor evoked potentials (MEPs) recorded in the contralateral biceps.

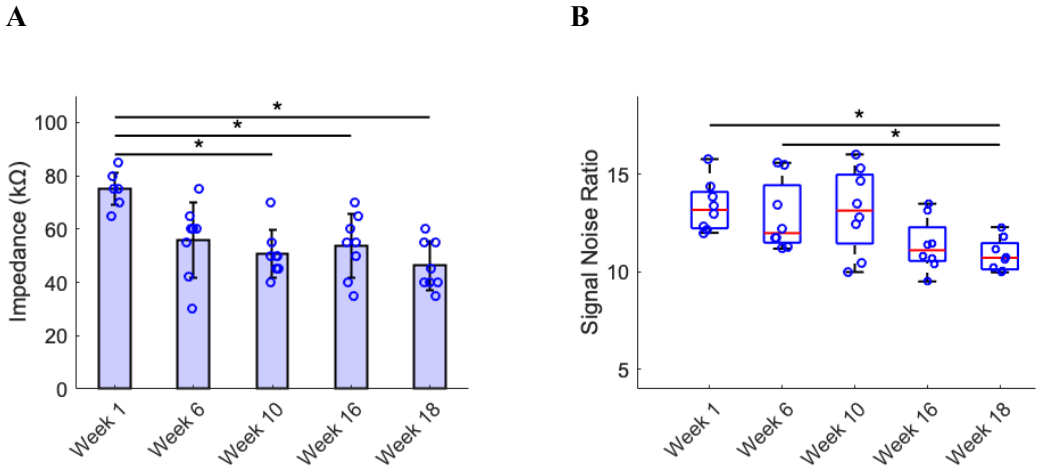



**Figure 5.9** Chronic *in vivo* validation of the *Gr on GC* microelectrode device stability. (a) Impedance at 1 kHz for all 8 electrodes of the chronic implant over 18 weeks (n = 8). Circles present individual data points. Error bars indicate standard deviation. (b) Signal to ration (SNR) for all functioning microelectrodes over 18 weeks. Red lines, boxes, Whiskers, and empty circles present median, 25th-75th percentile, minimum values & maximum values, individual data points, respectively.

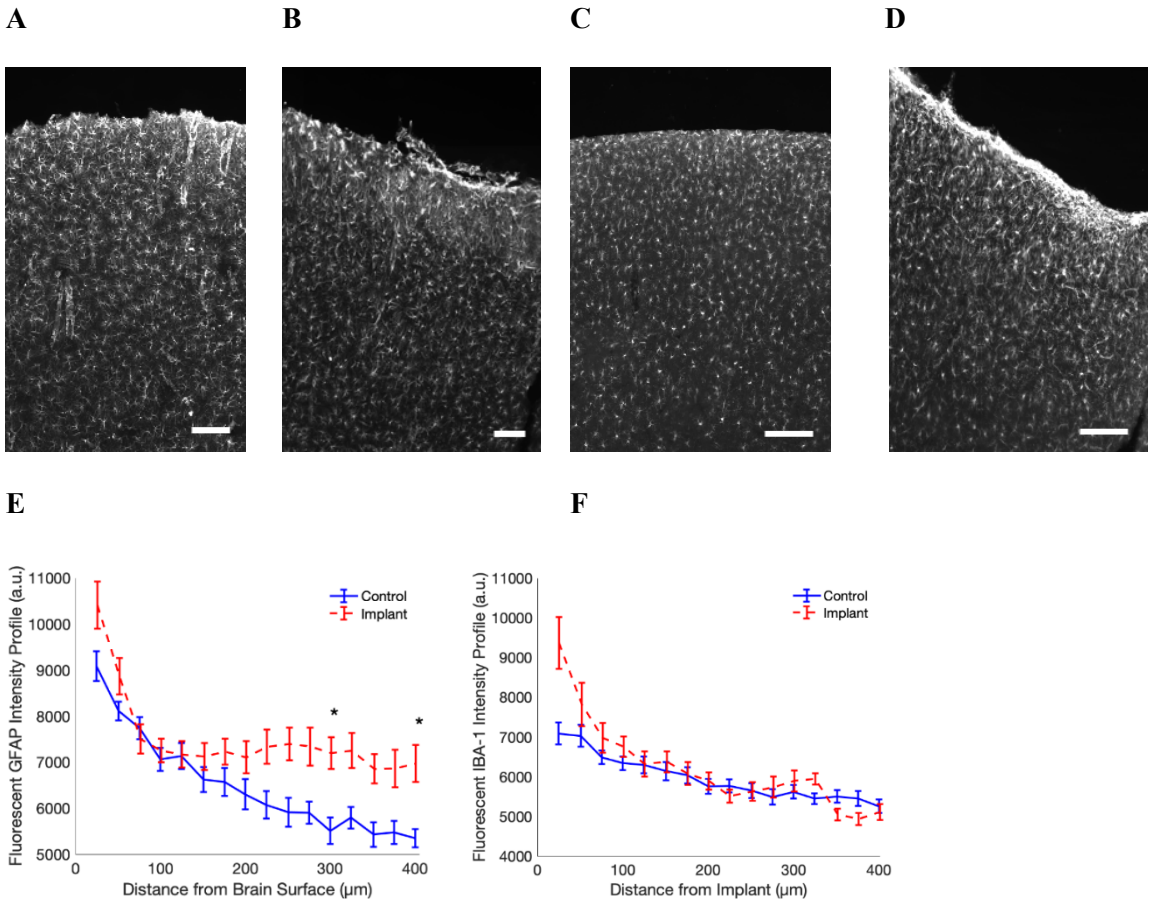



**Figure 5.10** Representative GFAP and IBA-1 images. (a) section from the control hemisphere. (b) section from the brain after 18 weeks post-implantation. Scale bar = 300 μm (c) An example of the IBA-1 expression image from the control hemisphere. (d) An example of the IBA expression image from the brain after 18 weeks post-implantation. (e) Plot of the GFAP+ cells with respect to depth below the brain surface. Normalized fluorescent GFAP intensity at 18 weeks after implantation in the brain (red dashed line) compared to the control brain (blue line). Each data point is the average of n = 20 samples (implant: 7195 ± 348, control: 5509 ± 287 at 300 μm; implant: 6969 ± 402, control: 5346 ± 198 at 300 μm; Wilcoxon signed-rank test, * p-value < 0.05,). (f) Plot of the IBA-1+ cells with respect to depth below the brain surface. Normalized fluorescent IBA-1 intensity at 18 weeks after implantation in the brain (red dashed line) compared to the control brain (blue line). Each data point is the average of n = 20 curves.

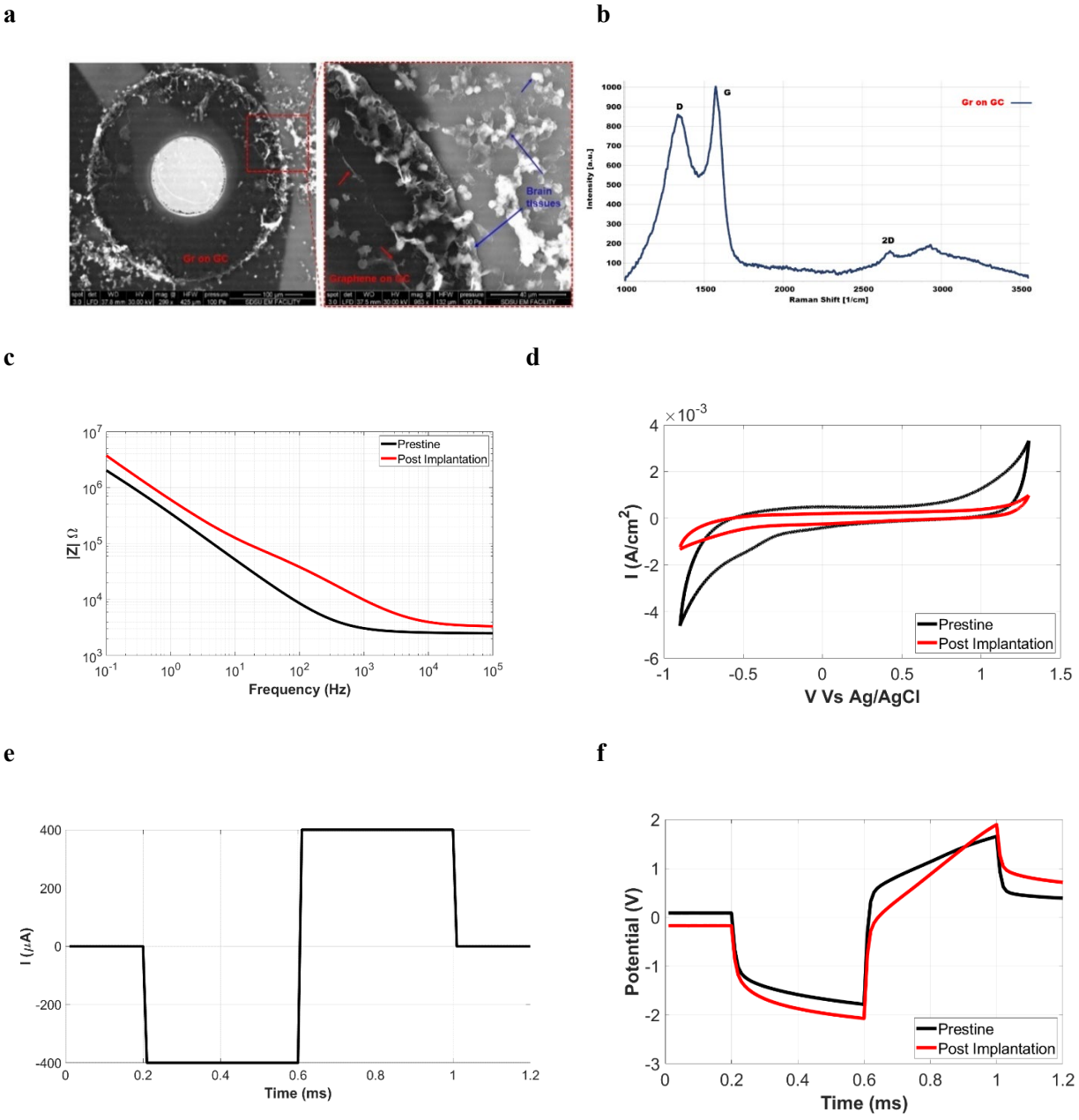



**Figure 5.11** *Gr on GC* microelectrode surface morphology post explant after 18 weeks. (a) Magnified image of the *Gr on GC* microelectrode surface indicating tissue grown and salts accumulation during implantation (b) Raman Spectrum of *Gr on GC* microelectrode indicating similar peaks compared to pre-implantation. (c) EIS spectra of *Gr on GC* electrode post explant (d) cyclic voltammogram post explant (e) biphasic pulse of 400 µA for 400 µs pulse-width (f) Voltage transient response recorded post explant.

### 3.7 Post-Explant Characterization of Microelectrodes

After *in vivo* validation tests for 18 weeks, we investigated the material and electrical characteristics of the explanted electrode. The SEM image shows the tissue growth around the edge of the microelectrode Ch 4. There were no defects observed on both the *Gr on GC* material surface and the polyimide substrate, indicating structural stability of microelectrode material as well as that of the whole probe. The Raman Spectra indicated G and D peaks as well as presence of multilayer graphene at 2D peak similar to pristine *Gr on GC* microelectrode (**Figure 11**). Average impedance of the microelectrode at 1 kHz was recorded to be **8.758 kΩ ± 10.26** for $n = 6$ in PBS 0.01M. This increase in impedance value as compared to pristine *Gr on GC* is due to attached brain tissue traces visible on the microelectrode surface. Linear sweep voltammogram and CV showed the functionality of microelectrode within the water window range -0.9 V to 1.3 V (Supplementary **Figure S5**) and the calculated CSC was **51.45 ± 6.739 mC/cm$^2$**. The lowered CSC value post implantation could be due to decreased charge transfer capability while the increased impedance value was due to tissue growth on the electrode surface. The $E_{mc}$ = -0.94 V and $E_{ma}$ = 1.25 V values obtained from the voltage transient response for a biphasic pulse of 400 μA and 400 μs pulse-width were observed to be within the water window. Altogether, the *Gr on GC* microelectrode array showed remarkable structural and functional stability in terms of electrical and material characteristics over 18 weeks of implantation.

## 4. Discussion and Conclusion

By introducing a thicker backing for graphene microelectrodes (and hence out-of-plane rigidity), we addressed, in this study, a major gap in the potential further expansion of the capabilities of Gr in neural probe applications with long term stability. A novel microfabrication methodology and pattern transfer technology followed by pyrolysis of a negative-tone polymer is presented here resulting in a versatile probe with *Gr on GC* microelectrodes on a flexible polyimide substrate. STEM image of the new microelectrodes clearly indicated a distinct zone of Gr layers on top of GC and a separate zone of GC. Raman spectra also indicated graphene structure with 2D peak. The pyrolysis of SU8 layer located on top of a patterned graphene layer was observed to have created an excellent bond between the two layers that is further

strengthened by transitional Gr type intermediate layers. This intriguing outcome has opened up further possibilities in exploring interplay between these two allotropes of carbon. This will be reported separately in the future.

Further, the new *Gr on GC* material introduced here for neurological sensing and stimulation was demonstrated to be rich in carbonyl, carboxyl, and hydroxyl functional groups. Electrochemical impedance spectroscopy, and cyclic voltammogram showed electrophysiological compatibility of *Gr on GC* microelectrodes. The capacitive behavior of *Gr on GC* microelectrode was demonstrated with voltage transient response to biphasic pulse of 400 μA for 400 μs pulse width. Further, the new probes demonstrated comparable electrical characteristics as their GC counterpart microelectrodes. The charge storage capacity of *Gr on GC* was found to be (**56.48± 0.7704 mC/cm$^2$**), which is comparable to (**61.4 ± 6.9 mC/cm$^2$**) that corresponds to ultra-capacitive *all-GC* microelectrodes (GC microelectrodes and GC traces) of same size introduced by our group recently [**3**]. Further, *Gr on GC* microelectrodes were noted to have relatively less surface roughness (**9.64 ±2.67 nm**) as compared to the *all-GC* ultra-capacitive microelectrodes (**43.55 ± 3.09 nm**), but comparable roughness to hybrid microelectrodes (GC microelectrodes and metal traces) (**3.3 nm** (*n = 5*)) [**2**]. The double-sided etching of *all-GC* microelectrodes could account for their rather high surface roughness.

Overall, the electrical and electrochemical properties of the new *Gr on GC* microelectrodes compare very well with what has been reported in the literature. For example, a porous graphene microelectrode arrays patterned on polyimide film by laser pyrolysis method had a reported impedance value at 1 kHz within 2-8 kΩ [**8**]. These microelectrodes were used for sensing brain activity patterns with high spatio-temporal resolution and to control leg muscles with high-precision electrical stimulation from the cortical surface [**8**]. On the other hand, the impedance of Gr microelectrodes was shown to be fundamentally limited by quantum capacitance. For example, an approach where a parallel conduction path was created using platinum nanoparticles reported 100 times reduction in graphene electrode impedance **[31].** An alternative approach that used three-dimensional fuzzy graphene (NT-3DFG) MEA helped create a very significant surface area and a subsequent large reduction in electrode impedance **[32].**

With regard to *in vivo* studies, this study is a first demonstration of the consistency and longevity of neural recording of *Gr on GC* microelectrodes over a period of 18 weeks. The acute *in vivo impedance and* SNR recordings showed repeatability of the *Gr on GC* microarrays, replicating the recordings in three devices and animals. A previous report on Gr microelectrodes for recording neuronal activity showed SNR of **10.31 ± 1.2** for action potential recordings [**33**] which was comparable to our SNR results. We also conducted cortical stimulation through the *Gr on GC* microelectrodes that successfully evoked targeted forelimb muscles in all three devices within the safe current range under the Shannon constant, $k < 2.0$ [**28**]. The maximum safety current is 2.66 μA which was converted from the safe charge per phase [**29**]. This level of current is also reasonably close (< 10% difference) to what a recent work had recommended in terms of taking the following into consideration for tissue safety: lower Shannon constant (e.g., $k < 1.85$), stimulation protocols including waveform and interval, and surface morphology of electrodes [**30**]. This, therefore, has demonstrated for the first-time cortical stimulation with *Gr on GC* microelectrode in comparison to previous studies on GC microelectrodes where *in vivo* stimulation capability of GC microelectrodes was discussed [**2,3**]. Furthermore, stable SNR measurements were observed up to 16 weeks during *in vivo* implantation, and long-term stable tissue interface impedance for 18 weeks. Our *Gr on GC* microelectrodes functionality lasted longer than previously reported Gr applications [**34-36**]. The longest brain implantation of Gr probes previously reported was only ten weeks [**34**].

Tissue histology nearby the implant and tests of the explanted *Gr on GC* device supported the functional stability of the device. The histological analysis showed - only on the surface of the brain - trends of slightly high glial responses with the implanted electrodes compared to the control section of the brain. A previous study reported that there is a correlation between increased impedance and the presence of increased GFAP expressions in the implanted area of the brain [**37**]. Thus, although there were inconsistent high astrocyte responses, the tissue histology analysis supports the stable tissue interface ability of the ECoG probe indicated with the stable impedance of the electrodes over 18 weeks [**37**].

Other research groups have pursued biomimetic coatings for pristine graphene such as polypeptide coasting to intervene with inflammation [**38**]. The exploitation of biocompatible Gr probe with coatings

that minimize inflammatory response could, therefore, further help expand the clinical applications of this class of neural interfaces [**39**]. Further, material and electrical properties of the microelectrode implanted for 18 weeks showed similar characteristics as that of pristine *Gr on GC* microelectrode demonstrating material longevity for *in vivo* recording. Post-explant SEM imaging showed intact lamination between the *Gr on GC* microelectrode and polyimide (PI) substrate indicating reliable adhesion at the interface of PI and *Gr on GC* microelectrodes. A recent study has shown use of silicon carbide as adhesion promoting layer in long term *in vivo* recording and stimulation [**40**]; however, this current study has demonstrated intact bonding without use of any adhesion promoter between *Gr on GC* microelectrode and PI interface. The strong covalent bonds between GC and polyimide discussed in Hirabayashi *et al*, [**25**] may have contributed to the intact adhesion of the microelectrodes to the substrate during 18 weeks of implantation.

In summary, based on its excellent impedance values, strong in-plane and out-of-plane mechanical stiffness, and relatively high SNR acute and chronic *in vivo* recordings, the *Gr on GC* microelectrodes presented here offers a compelling case for expanding the potentials of graphene-based technology in the broad areas of neural probes.

## 5. Multimodality of Graphene on GC microelectrodes:

In order to investigate multimodality of Gr on GC microelectrodes similar to GC microelectrode as studied in chapters 2 and 3, we studied magnetic resonance compatibility and neurotransmitter detection capability of Graphene on GC microelectrode in this section.

### 5.1 Methods:

We used magnetic resonance imaging (MRI) and fast scan cyclic voltammetry methods for studying multimodality of Graphene on GC microelectrodes.

#### 5.1.1 Magnetic Resonance Imaging

The MR images of Gr on GC and GC microelectrodes of identical dimensions (2 cm × 1 cm) shown in (Chapter 3, Fig. 1a) were acquired by a Siemens 3 T Prisma scanner (Siemens GmbH, Erlangen, Germany). The microelectrodes were immersed in phosphate-buffered saline (PBS, 0.01 M) solution and entrapped air bubbles were released. Similar to Chapter 3, in Fig. 2, the phantom with the microelectrodes was then placed on top of the MRI phantom (solution N per 1000 g $H_2O$ dist.: 3.75 g $NiSO_4 \times 6H_2O$, 5 g NaCl, 5300 ml, Siemens Healthcare GmbH, Germany) to position the microelectrode near the isocenter of the coil. MR images of the PBS-agarose phantom with Gr on GC and GC microelectrodes were collected to test for MRI artifacts (Fig. 5a). The following MR sequences were run with the 3 T scanner: (i) T1-weighted images were acquired using an inversion-prepared 3D gradient-echo sequence (MPRAGE) with $0.8 \times 0.8 \times 0.8\ mm^3$ resolution, flip angle = 9°, echo time (TE) = 3.15 ms, repetition time (TR) = 7.7 ms, inversion time (TI) = 900 ms, field of view (FOV) = $200 \times 200 \times 179\ mm^3$, and inversion repeat time = 2300 ms; (ii) T2-weighted images were collected using a variable flip angle 3D turbo spin echo (TSE) sequence with $0.9 \times 0.9 \times 0.9\ mm^3$ resolution, TE = 408 ms, TR = 3200 ms, FOV = $230 \times 230 \times 173\ mm^3$, and averages = 1.4; (iii) a 2D dual echo $B_0$-field map was obtained with $3 \times 3 \times 2\ mm^3$ resolution, TE1 = 4.92 ms, TE2 = 7.38 ms, TR = 600 ms, FOV = $192 \times 192\ mm^2$, and flip angle = 60°; and (iv) gradient-echo multiband EPI sequence (functional MRI) images were acquired using a multiband echo planar imaging sequence with $2 \times 2 \times 1\ mm^3$ resolution, TR = 1.02 s, TE = 31 ms, and flip angle = 60°.

### 5.1.2 Fast Scan Cyclic Voltammetry

Similarly discussed in chapter 2, fast-scan cyclic voltammetry (FSCV) was used to evaluate the dopamine (DA) detection performance with a WaveNeuro Potentiostat System (Pine Research, NC). For *in-vitro* dopamine calibration, the FSCV waveform was used with a pyramidal excursion from −0.5 V to +1.3 V potential and back to baseline with respect to the Ag/AgCl reference electrode at a scan rate of 400 V/s and 10 Hz frequency. The duration of each scan was 9 ms (900 data points). Measured

concentrations of dopamine (50 nM–1 μM) were then added over 15 seconds while changes in current were recorded for 60 seconds in PBS solution (0.01 M)

## 5.2 Results and discussion

We analyzed and compared the results between Gr on GC and GC microelectrodes for MRI and FSCV.

### 5.2.1 MR Images

The imaging artifacts produced in the 3 T scanner by the GC and Gr on GC microelectrodes were compared in the phantom using clinical MRI sequences. In Fig. 12, the first row shows T1-weighted images taken with the MPRAGE sequence, T1- and T2-weighted images are commonly used in clinical sequences and are represented in axial, sagittal, and coronal views in Fig. 12. The darkened rectangular shape on the right side of the phantom artifact shows loss of signal or hyperintense signals corresponding to an imaging artifact produced by the tape attaching electrodes to petri dish. There is no visible differentiation between the $B_0$-field maps of the GC and GrGC microelectrodes, as shown in Fig. 12

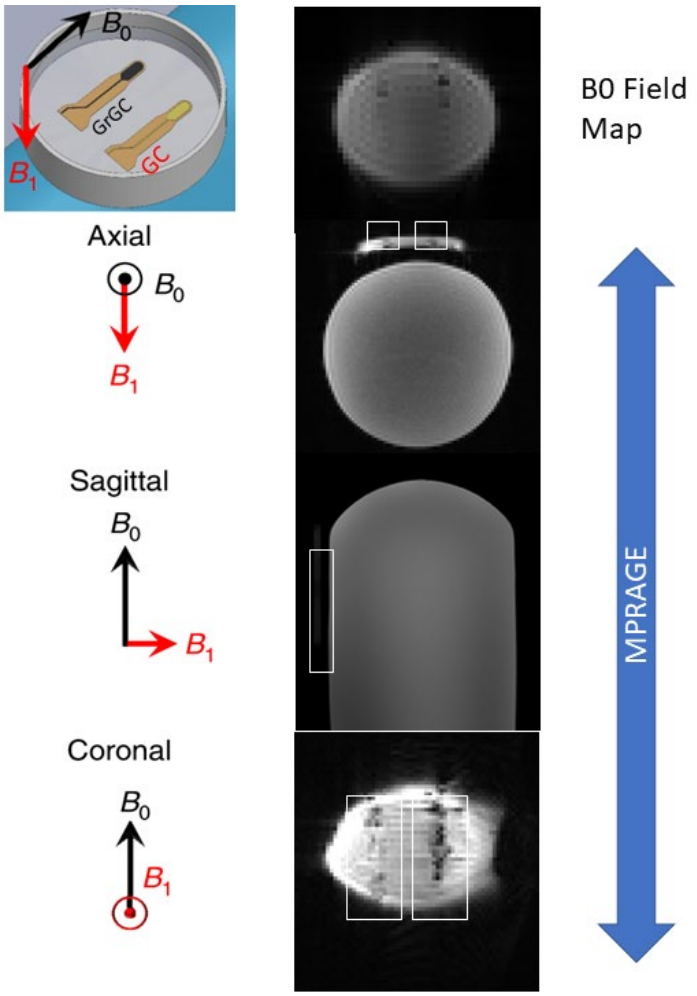



**Figure 5.12** Comparison of magnetic resonance imaging artifact of Gr on GC and GC microelectrode from T1 -weighted images captured with MPRAGE. No significant imaging artifacts were observed for both the samples.

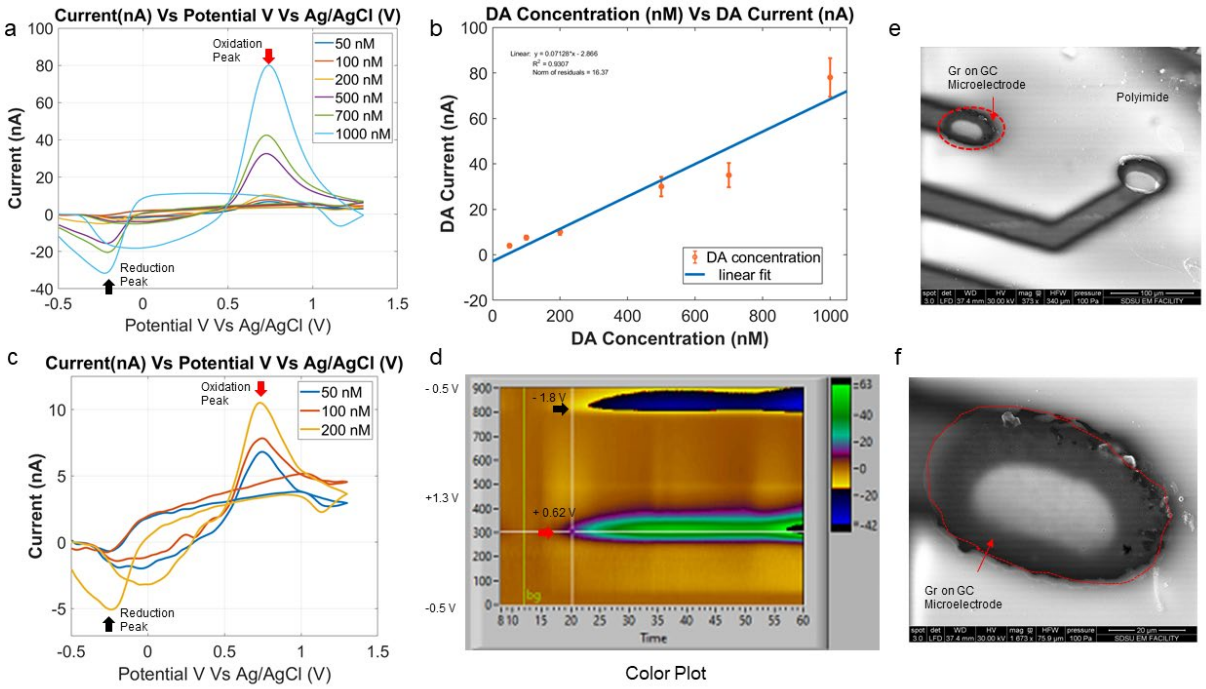



**Figure 5.13** Background subtracted CV showing reduction (−0.18 V) and oxidation (0.62 V) peaks of DA. Dopamine signals were measured using a standard pyramidal FSCV waveform in which the applied voltage was ramped from the holding potential of −0.5 V to the switching potential of +1.3 V and then back to −0.5 V at 400 V/s. (a) Background subtracted CVs for 50, 100, 200, 500, 700 nM and 1 µM DA concentration in PBS, showing reduction (−0.18 V) and oxidation (0.62 V) peaks, (b) Calibration curve corresponding to conditions in figure 5.13 (a), (c) Background subtracted CVs for 50, 100, 200, 500 nM DA concentration in PBS, (d) corresponding representative color plot of 100 nM detection injected at 5 s and detected at t =15 s (e and f) Graphene on GC microelectrode designed for DA detection with 1800 1800 µm$^2$ surface area

Figure 13 summarizes the results obtained from a series of FSCV characterizations on a 1800 µm$^2$ surface area Gr on GC microelectrode. Figure 5.13 d shows an example of dopamine signals detected using a standard pyramidal FSCV waveform in which the applied voltage was ramped from the holding potential of −0.5 V to the switching potential of +1.3 V and then back to −0.5 V at 400 V/s scan-rate. In particular, the color plots show changes in current following the injection of 50 nM of dopamine (DA) at t = 15 secs first. These changes in currents occurred at the known reduction and oxidation peaks of DA (i.e., −0.18 V and 0.62 V), as clearly shown in the background subtracted CVs for 50 nM, 100 nM and 200 nM DA given in Fig. 13 (c). Further, to determine a calibration curve over a wider range of concentrations, additional sets of FSCV were carried out at 50, 100, 200, 500, 700 nM and 1 µM

concentration of dopamine in PBS. As shown in Fig. 5 a and c, the background subtracted CVs corresponding to these range of concentrations demonstrate reduction and oxidation peaks at (−0.18 V) and (0.62 V). In addition, the calibration curve for these concentrations of DA varying from 50 nM to 1 μM follows a linear trend as reported in Fig. 13 b

**5.3 Multimodality Discussion**

As the resistivity of the GrGC and GC are comparable, induced voltage and current in GrGC electrodes would be in the similar range as that of GC electrode (Chapter 3, Figure 8). As torque per slew rate is function of conductivity, gradient induced vibration on GrGC electrode would be also in similar range as compared to GC (Chapter 3, Figure 9).

Limit of detection for neurotransmitter (DA) for the GrGC electrode is 50 nM, less sensitive as compared to GC electrode (Chapter 2). Here, to protect the Gr monolayer, dry oxygen plasma cleaning treatment was not employed. As seen from STEM imaging, basal planes of the graphene stacks were arranged parallel to surface of the electrode (Chapter 4, Figure 4). While edge plane is considered to have more electronic density and better electron transfer for surface sensitive probes, the edge planes in the case of GrGC electrode are not exposed to DA injected in PBS for in-vitro experiments. These edge plane defects can also be measured from D/G ratio from Raman spectrum. If D/G ratio is higher in Raman spectrum, it depicts more defects and edge plane sites in carbon electrode. For GrGC microstructure, D/G ratio was almost equal to 1 (Chapter V, Figure 5).

In FSCV, the dopamine redox reaction is adsorption-controlled by electrostatic attraction between cationic dopamine and negative oxide groups on carbon electrodes. Only increasing surface area is not effective way of enhancing adsorption, because capacitance increases with surface area which results in increased noise. Defects sites on the electrode can be strategically introduced. Chemical treatment such as oxidative etching of carbon nanomaterials [41,42], and treatments such as laser [43], oxygen plasma etching [44] generate defects and surface oxide groups to promote adsorption.

**References**


1. Chen, Yung-Chan, Hui-Lin Hsu, Yu-Tao Lee, Huan-Chieh Su, Shiang-Jie Yen, Chang-Hsiao Chen, Wei-Lun Hsu et al. "*An Active, Flexible Carbon Nanotube Microelectrode Array for Recording Electrocorticograms*." Journal of Neural Engineering, 8, no. 3 (2011): 034001.

2. Vomero, M., Castagnola, E., Ciarpella, F., Maggiolini, E., Goshi, N., Zucchini, E., Carli, S., Fadiga, L., Kassegne, S., and Ricci, D., "*Highly Stable Glassy Carbon Interfaces for Long-term Neural Stimulation and Low-noise Recording of Brain Activity*." Scientific Reports 7, no. 1 (2017): 1-14.

3. Nimbalkar, S., Castagnola, E., Balasubramani, A., Scarpellini, A., Samejima, S., Khorasani, A., Boissenin, A., Thongpang, S., Moritz, C., and Kassegne, S., "*Ultra-capacitive Carbon Neural Probe Allows Simultaneous Long-term Electrical Stimulations and High-Resolution Neurotransmitter Detection*," Scientific Reports 8, no. 1 (2018): 1-14.

4. Castagnola, E., Maiolo, L., Maggiolini, E., Minotti, A., Marrani, M., Maita, F., Pecora, A., *et al.* "*PEDOT-CNT-coated Low-Impedance, Ultra-Flexible, and Brain-Conformable Micro-ECoG arrays.*" *IEEE Transactions on Neural Systems and Rehabilitation Engineering* 23, no. 3 (2014): 342-350.

5. Park, D-W, Schendel, A.A., Mikael, S., Brodnick, S.K., Richner, Ness, J.P., Hayat, M.R., *et al. "Graphene-based Carbon-layered Electrode Array Technology for Neural Imaging and Optogenetic Applications.*" *Nature Communications* 5, no. 1 (2014): 1-11.

6. Wang, K., Fishman, H.A., Dai, H., and Harris, J.S., "*Neural Stimulation with a Carbon Nanotube Microelectrode Array*," Nano Letters 6, no. 9 (2006): 2043-2048.

7. Vitale, F., Samantha R. Summerson, Behnaam Aazhang, Caleb Kemere, and Matteo Pasquali. *"Neural Stimulation and Recording with Bidirectional, Soft Carbon Nanotube Fiber Microelectrodes*." ACS Nano 9, no. 4 (2015): 4465-4474.

8. Lu, Y., Lyu, H., Richardson, A.G., Lucas, T.H., and Kuzum, D., *"Flexible Neural Electrode Array Based-on Porous Graphene for Cortical Microstimulation and Sensing*." *Scientific Reports* 6, no. 1 (2016): 1-9

9. Nimbalkar, S., Fuhrer, E., Silva, P., Nguyen, T., Sereno, M., Kassegne, S., & Korvink, J. (2019). "*Glassy Carbon Microelectrodes Minimize Induced Voltages, Mechanical Vibrations, and Artifacts in Magnetic Resonance Imaging*," Microsystems & Nanoengineering, 5(1), 1-11

10. Castagnola, E., Winchester, N., Nimbalkar, S., Rudraraju, S., Thielk, M., Zucchini, E., Cea, C., *et al*. "*In Vivo Dopamine Detection and Single Unit Recordings Using Intracortical Glassy Carbon Microelectrode Arrays*." *MRS Advances* 3, no. 29 (2018): 1629-1634.

11. Castagnola, E, Thongpang, S., Hirabayashi, M., Nava, G., Nimbalkar, S., Nguyen, T., Lara, S., et al. "*Glassy Carbon Microelectrode Arrays Enable Voltage-Peak Separated Simultaneous Detection of Dopamine and Serotonin Using Fast Scan Cyclic Voltammetry*." *Analyst,* (2021).

12. Zachek, Matthew K., Pavel Takmakov, Benjamin Moody, R. Mark Wightman, and Gregory S. McCarty. "*Simultaneous Decoupled Detection of Dopamine and Oxygen Using Pyrolyzed Carbon*

*Microarrays and Fast-Scan Cyclic Voltammetry*." *Analytical Chemistry* 81, no. 15 (2009): 6258-6265.

13. Zachek, MK, Takmakov, P., Park, Wightman, R.M., and McCarty, G.S., "*Simultaneous Monitoring of Dopamine Concentration at Spatially Different Brain Locations In Vivo*." *Biosensors and Bioelectronics* 25, no. 5 (2010): 1179-1185.

14. Cheng, Y., Trikantzopoulos, E., Jacobs, C.B., and Venton, B.J., "*Evaluation of Carbon Nanotube Fiber Microelectrodes for Neurotransmitter Detection: Correlation of Electrochemical Performance and Surface Properties*." *Analytica Chimica Acta* 965 (2017): 1-8.

15. Cheng, Y., Cao, Q., Puthongkham, P., Lee, ST., Ganesana, M., Lavrik, N.V., and Venton. B.J., "*3D-Printed Carbon Electrodes for Neurotransmitter Detection*." *Angewandte Chemie International Edition* 57, no. 43 (2018): 14255-14259.

16. Demuru, S., Nela, L., Marchack, N., Holmes, S.J., Farmer, D.B., Tulevski, G.S., Lin, Q., and Deligianni, H., "*Scalable Nanostructured Carbon Electrode Arrays for Enhanced Dopamine Detection*." *ACS Sensors* 3, no. 4 (2018): 799-805.

17. Stankovich, S., Dikin, D., Dommett, G., Kohlhaas, K.M., Zimney, E.J., Stach, E.A., Piner, R.D., Nguyen, S.T., and Ruoff, R.S., "*Graphene-based Composite Materials*." *Nature* 442, no. 7100 (2006): 282-286.

18. Bose, S., Kuila, T., Mishra, A.K., *et al.,* "*Carbon-based Nanostructured Materials and their Composites as Supercapacitor Electrodes.,"* J. Mater. Chem. **22**, 767 (2012).

19. Xia, J., Chen, F., Li, J. & Tao, N. "*Measurement of the Quantum Capacitance of Graphene*," Nat. Nanotechnolpgy, 4, 505–509 (2009).

20. Shearer CJ, Slattery AD, Stapleton AJ, Shapter JG, Gibson CT. "*Accurate Thickness Measurement of Graphene,*" Nanotechnology. 2016

21. Sharma, S., Shyam Kumar, C.N., Korvink, J.G. *et al.* "*Evolution of Glassy Carbon Microstructure: In Situ Transmission Electron Microscopy of the Pyrolysis Process*", Sci Rep 8, 16282 (2018).

22. Jurkiewicz, K., Pawlyta, M., Zygadło, D. *et al*. *"Evolution of Glassy Carbon Under Heat Treatment: Correlation Structure–Mechanical Properties*", J Mater Sci 53, 3509–3523 (2018).

23. Schueller, O.J., Brittain, S. T., Marzolin, C. and Whitesides, G. M. "*Fabrication and Characterization of Glassy Carbon MEMS,*" Chem. Mater. 9, 1399–1406 (1997).

24. Ranganathan, S., McCreery, R. L., Majji, S. M. and Madou, M. "*Photoresist-Derived Carbon for Microelectromechanical Systems and Electrochemical Applications*," *J. Electrochem. Soc.* 147(1), 277–282 (2000).

25. Hirabayashi, M., Logan, K., Deutschman, C.P., McDowell, TW., Torres, M.Z., Pullman, D., and Kassegne, S., "*Investigation of Interface Bonding Mechanisms Between Glassy Carbon Microelectrodes and Polyimide Substrate through Fourier Transform Infrared Spectroscopy,*" Journal of The Electrochemical Society 165, no. 8 (2018): B3060

26. Robert D. Hall, Ernest P. Lindholm, "*Organization of Motor and Somatosensory Neocortex in the Albino Rat,*" Brain Research, Volume 66, Issue 1, 1974, Pages 23-38, ISSN 0006-8993.

27. Hara, K., and Harris, R.A., *"The Anesthetic Mechanism of Urethane: The Effects on Neurotransmitter-gated Ion Channels,"* Anesthesia & Analgesia, Vol. 94, No. 2, pp. 313-318, 200227.

28. Nordhausen, Craig T., Edwin M. Maynard, and Richard A. Normann. "*Single Unit Recording Capabilities of a 100-Microelectrode Array*." *Brain Research* 726, no. 1-2 (1996): 129-140.

29. Merrill DR, Bikson M, Jefferys JGR. "*Electrical Stimulation of Excitable Tissue: Design of Efficacious and Safe Protocols,*" *J Neurosci Methods* 141: 171–198, 2005.

30. Shannon, R., "*Model of Safe Levels for Electrical Stimulation*," *IEEE Trans Biomed Eng* 39: 424–426, 1992

31. Lu, Yichen, Xin Liu, Ryoma Hattori, Chi Ren, Xingwang Zhang, Takaki Komiyama, and Duygu Kuzum. "*Ultralow Impedance Graphene Microelectrodes with High Optical Transparency for Simultaneous Deep Two-photon Imaging in Transgenic Mice*," Advanced Functional Materials 28, no. 31 (2018): 1800002.

32. Rastogi, S.K., Bliley, J., Matino, L., Garg, R., Santoro, F., Feinberg, A.W., and Tzahi Cohen-Karni. "*Three-dimensional Fuzzy Graphene Ultra-microelectrodes for Subcellular Electrical Recordings*." Nano Research 13, no. 5 (2020): 1444-1452.

33. Du X, Wu L, Cheng J, Huang S, Cai Q, Jin Q, Zhao J. "*Graphene Microelectrode Arrays for Neural Activity Detection*," J Biol Phys. 2015 Sep;41(4):339-47.

34. Bourrier A, Shkorbatova P, Bonizzato M, Rey E, Barraud Q, Courtine G, Othmen R, Reita V, Bouchiat V, Delacour C. *"Monolayer Graphene Coating of Intracortical Probes for Long-Lasting Neural Activity Monitoring*," Adv Healthc Mater. 2019, 8(18).

35. Park, D.-W.; Schendel, A.A.; Mikael, S.; Brodnick, S.K.; Richner, T.J.; Ness, J.P.; Hayat, M.R.; Atry, F.; Frye, S.T., Pashaie, R. "*Graphene-based Carbon-layered Electrode Array Technology for Neural Imaging and Optogenetic Applications*," Nat. Commun. 2014, 5, 5258

36. Shokoueinejad M, Park DW, Jung YH, Brodnick SK, Novello J, Dingle A, Swanson KI, Baek DH, Suminski AJ, Lake WB, Ma Z, Williams J. *"Progress in the Field of Micro-Electrocorticography*," Micromachines (Basel). 2019 Jan 17;10(1):62.

37. Williams JC, Hippensteel JA, Dilgen J, Shain W, Kipke DR. "*Complex Impedance Spectroscopy for Monitoring Tissue Responses to Inserted Neural Implants*," J. Neural Eng. 2007;4:410–423.

38. Veliev F, Briançon-Marjollet A, Bouchiat V, Delacour C. "*Impact of Crystalline Quality on Neuronal Affinity of Pristine Graphene Biomaterials*," 2016, 86:33-41.

39. Bramini M, Alberini G, Colombo E, Chiacchiaretta M, DiFrancesco ML, Maya-Vetencourt JF, Maragliano L, Benfenati F, Cesca F. "*Interfacing Graphene-Based Materials with Neural Cells*," Front Syst Neurosci. 2018, 11;12:12.

40. Čvančara, Paul, Tim Boretius, Víctor M. López-Álvarez, Pawel Maciejasz, David Andreu, Stanisa Raspopovic, Francesco Petrini et al. "*Stability of Flexible Thin-film Metallization Stimulation Electrodes: Analysis of Explants After First-in-Human Study and Improvement of In Vivo Performance*," Journal of Neural Engineering 17, no. 4 (2020): 046006.

41. Puthongkham, Pumidech, Cheng Yang, and B. Jill Venton. "Carbon Nanohorn-modified Carbon Fiber Microelectrodes for Dopamine Detection." Electroanalysis 30, no. 6 (2018): 1073-1081.

42. Xiang, Ling, Ping Yu, Jie Hao, Meining Zhang, Lin Zhu, Liming Dai, and Lanqun Mao. "Vertically aligned carbon nanotube-sheathed carbon fibers as pristine microelectrodes for selective monitoring of ascorbate in vivo." Analytical chemistry 86, no. 8 (2014): 3909-3914.

43. Yang, Cheng, Elefterios Trikantzopoulos, Michael D. Nguyen, Christopher B. Jacobs, Ying Wang, Masoud Mahjouri-Samani, Ilia N. Ivanov, and B. Jill Venton. "Laser treated carbon nanotube yarn microelectrodes for rapid and sensitive detection of dopamine in vivo." ACS sensors 1, no. 5 (2016): 508-515.

44. Yang, Cheng, Ying Wang, Christopher B. Jacobs, Ilia N. Ivanov, and B. Jill Venton. "O2 plasma etching and antistatic gun surface modifications for cnt yarn microelectrode improve sensitivity and antifouling properties." Analytical chemistry 89, no. 10 (2017): 5605-5611.

**Acknowledgments**

Chapter 5, in partial (Sections 1 to 4), is in preparation or submission for publication as: Surabhi Nimbalkar, Soshi Samejima, Viet Dang, Trevor Hunt, Omar Nunez, Chet Moritz, Sam Kassegne., "*Graphene on Glassy Carbon* Microelectrodes Demonstrate Long-Term Structural and Functional Stability in Neurophysiological Recording and Stimulation". The dissertation author was the primary author of this chapter.

# CHAPTER VI

# Discussion and Conclusion

## 1. Future of Nanomanufacturing

A metamaterial that consists of a layer of glassy carbon (GC) and layer of graphene (Gr) derived from the same and common polymer precursor (or polymer of similar hydrocarbon content) and bound at the interface at a molecular level through covalent chemical bonds was introduced here. The suite of characterizations presented here demonstrate that the new metamaterial consists of graphene and glassy carbon material seamlessly joined together with clear and identifiable interface layer. STEM imaging revealed stacks of graphene multilayers close to surface of the material that was verified by molecular dynamics simulation. The stacks of graphene are crosslinked by the presence of defects in the form of non-hexagonal rings, vacancies, isolated $sp^3$ bonds or chains which introduce curvature in the interlayer connections. The interlayer distance from imaging was calculated to be ~0.38 nm whereas MD simulation showed 0.35 nm. Both EELS and MD simulation showed the presence of several functional groups like epoxides or cyclic ether (C-O-C), carbonyl (C=O), carbonyl, and hydroxyl groups. GrGC has shown comparable mechanical strength to GC as found in literature based on Young's Modulus. Addition of Gr monolayer to GC microstructure may increase mechanical strength of the material.

## 2. Glassy Carbon (GC) material for neurophysiology

In this dissertation, demonstration of the multimodal capability of GC, one of the carbon's allotropes, was addressed to lay the ground work for further exploration on the use of a new metamaterial in neural probes. It was demonstrated that the microelectrode showed charge injection capacity of 3mC/cm$^2$, charge storage capacity of 61.4 mC/cm$^2$, in vivo acute recording SNR of ~16. The multi-modality of the glassy carbon was proved based on neurotransmitter detection capability, magnetic resonance compatibility and in vitro long-term stimulation capability for 3 billion pulses at 0.25mC/cm$^2$ charge density [1,2].

The CSC value obtained here 61.4 mC/cm$^2$ is slightly lower than that of carbon nanotubes (CNT) directly grown on metal microelectrodes (70.8 ± 1.1 mC/cm$^2$) [3,4], but much larger than porous graphene (50 mC/cm$^2$) with impedance of 2-8 kΩ at 1 kHz frequency [5]. CSC for PEDOT-PSS coatings is

$40.4 \pm 4.8$ mC/cm$^2$ while it is $893.5 \pm 137.8$ mC/cm$^2$ for PEDOT-PSS-CNT coatings and ~90 mC/cm$^2$ for AIROF (Activated Iridium Oxide Film) microelectrodes [6-10]. To understand stimulation capability of the electrode, charge storage capacity (CSC) which provides estimated value of charge an electrode is capable of transferring was introduced by Beebe and Rose et al [10]. CSC of the electrode is dependent on of material properties of the electrode such as presence of oxide layer, surface topography, etc. Surface modification of the electrode by electroplating or surface cleaning has resulted into higher charge injection capacity for Pt electrodes [11-12], Similarly, Vomero et al has demonstrated that addition of PEDOT-PSS to GC electrode resulted into high charge density of the injection input for the electrode ~10 mC/cm$^2$[13].

Lu et al have shown that CNT fibers, 20 μm in diameter with $41.95 \pm 3.62$ kΩ impedance at 1 kHz frequency also demonstrated MRI compatibility [14]. Zhao et al also fabricated MRI compatible graphene electrodes by one-step dimensionally confined hydrothermal process using suspensions of graphene oxide with diameter of 75 μm, demonstrated CIC of $10.1 \pm 2.25$ mC/cm$^2$. Activation pattern of stimulation was studied using functional MRI imaging. [15]

Biologically relevant dopamine (DA) concentration in living systems is within 26–40 nM [16] CNT grown on metal microelectrodes (CNT-Nb) have shown dopamine detection limit of $11 \pm 1$ nM [17], whereas SWCNT (Single Walled CNTs) on metal microelectrodes have shown detection limit of 17 nM [18]. Carbon nanofibers modified by PEDOT/graphene oxide coating demonstrated detection limit of 85 nM was reported [19]. Laser-treated CNT yarn microelectrodes (CNTYMEs) have been shown to have LOD of $13 \pm 2$ nM for DA [20].

Zhao *et al* have shown that porous graphene fibers microelectrodes demonstrated *in vivo* DBS capability in hemi-Parkinsonian rats during MR imaging [15]. Vara et al has shown that PEDOT with poly(4-styrenesulfuric acid co-maleic acid) coated on carbon microfibers are capable of *in vivo* spinal cord stimulation, however, resulted in delamination of the surface coating after being pulsed for 6000 times at biphasic pulse of 100 μA [21]. Carbon fiber electrode arrays (each ~7 μm in diameter) with PEDOT:PSS [22-24] site have shown promising results with low immune response at electrode tissue interface . Single

carbon fiber electrode has demonstrated compelling results in chronic recording. Chronic DA recording was also studied with these electrodes for over a year [25-27].

### 3. GrGC Metamaterial for Neurophysiology

Encouraged by GC's performance, we introduced a new GrGC metamaterial synthesis process. To address demanding need of long-term stimulation capability in carbon-based electrodes for neurophysiology, we investigated effect of addition of Gr monolayer to GC electrodes during the pyrolysis process. The resultant process has synthesized GrGC metamaterial and hypothesized that the metamaterial would be suitable for neurophysiology testbed with comparable or improved material, surface, electrochemical properties as compared to GC. The effect of addition of Gr monolayer to GC fabrication process was studied by understanding surface morphology, surface topography. Surface defects and functional groups, nanostructures were examined. Testbed for GrGC for neurophysiology was introduced on polyimide substrate. Performance of the GrGC test bed for ECoG application showed comparable charge storage capacity, in vivo SNR as that of GC electrode. The motor evoked potential recording also indicated stimulation capability of the GrGC testbed. Table 6.1 provides the comparison between GC and GrGC material properties and testbed results.

### 4. Comparative Study: GC Vs GrGC

The microfabrication methodology for GrGC involved starting with Gr monolayer on $SiO_2$ substrate and pyrolyzing Gr and SU8 photoresist whereas, GC is obtained from pyrolysis process of SU8 photoresist only. The surface roughness of the GC microelectrode is observed to be ~ 40 nm while, it is examined to be ~ 10 nm for GrGC. Multilayer graphene was indicated by 2D peak in GrGC Raman spectrum. Hydroxyl and carbonyl functional group peaks were the predominantly observed in FTIR spectrum of GrGC. Disordered graphene 2-3 layers were stacked in GC whereas multilayer Gr stacking was depicted in GrGC cross section at the material surface. Likewise, MD simulation results of pyrolysis

process indicated disordered graphene layers (2-3) stacking for GC whereas multilayer stacking of Gr sheets was seen in GrGC.

We validated application of neural probe for GrGC testbed with same geometry (Ø =300 μm) showed lower impedance at 1 kHz as compared to GC electrode. The GrGC and GC microelectrodes showed comparable impedance. CSC for GrGC electrode has shown comparable value as compared to GC. Based on limit of detection for DA neurotransmitter, GrGC has demonstrated less sensitivity as compared to GC. The relationship between graphene multilayer stacking at GrGC surface and roughness as well as surface activation of GrGC surface by dry oxygen plasma etching should be investigated for enhancing sensitivity of GrGC microelectrodes. Similar to GC, GrGC has demonstrated magnetic resonance compatibility due to its comparable resistivity to GC. In vivo results have demonstrated 18 weeks chronic implantation capability with SNR ~12 (at 6 weeks). This is recorded to be one of the longest chronic studies for graphene-based electrodes (Chapter V).

**5. Summary:**

In the summary, we compared material, electrical, electrochemical properties of the GC and GrGC materials. Additionally, we analyzed performance of the GC and GrGC material as neural probe test bed. Thus, the GrGC microelectrodes have shown better conductivity and impedance values in comparison with GC microelectrodes and CSC values of GC and GrGC microelectrodes are comparable [Table 6.1].

**Table 6.1** GrGC Vs Gc material properties and testbed results

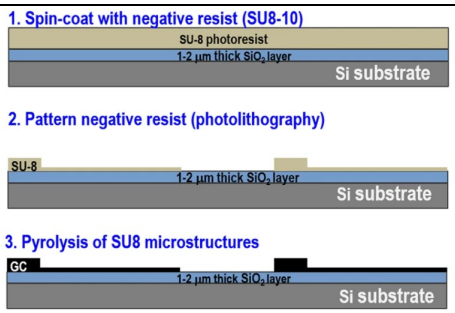
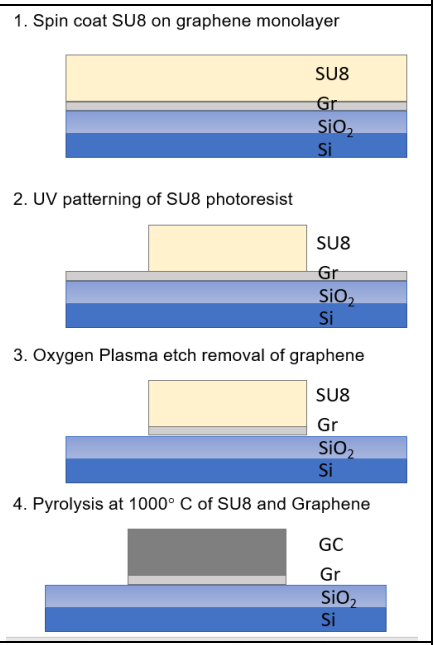
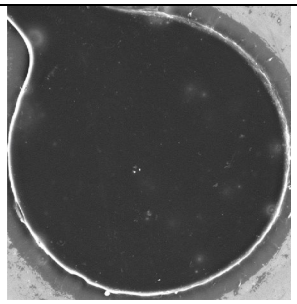
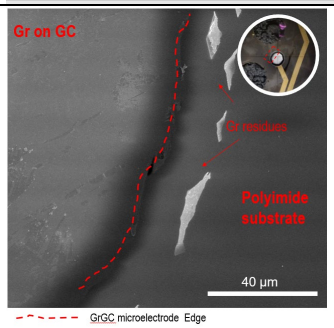
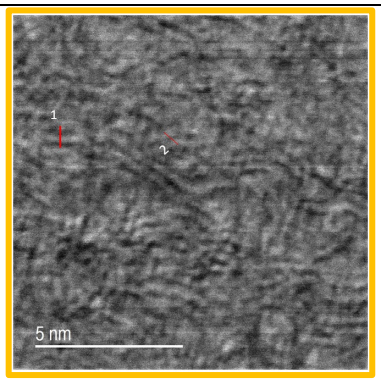
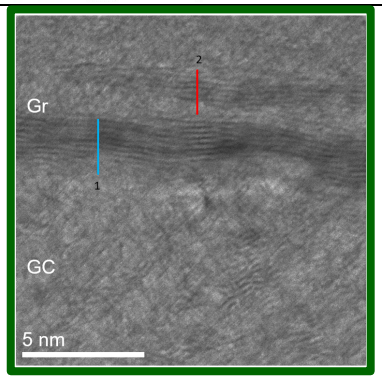
| Methods | | GC | GrGC |
|---|---|---|---|
| **Micro-fabrication** | |  |  |
| **Surface Morphology** | SEM |  |  |
| | |  |  |

**Table 6.1** GrGC Vs Gc material properties and testbed results (Continued)

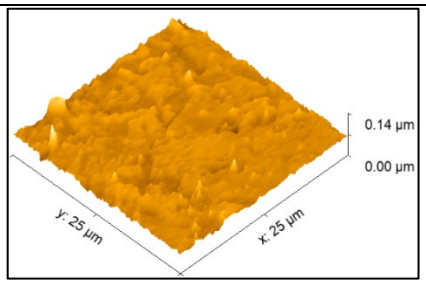
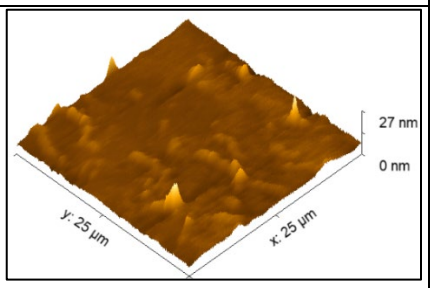
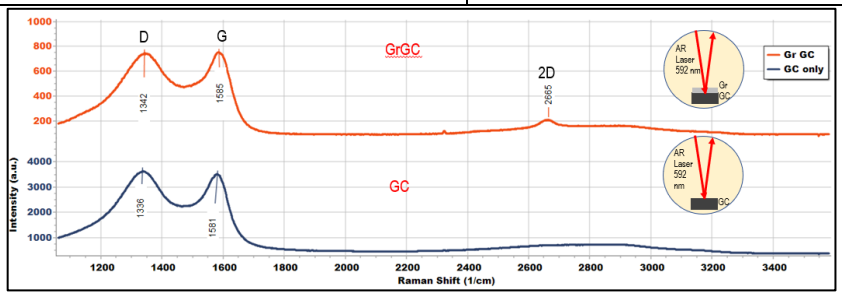
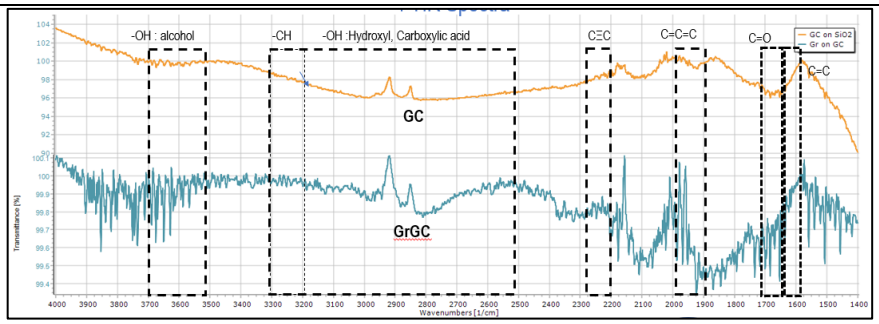
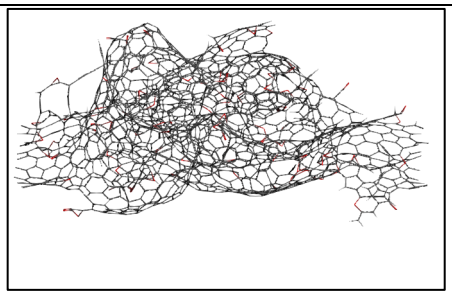
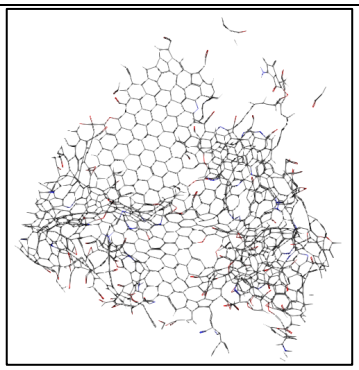
| Methods | | GC | GrGC |
|---|---|---|---|
| **Surface Topo-graphy** | |  40.15 ± 6.25 nm |  9.64 ±2.67 nm |
| **Surface Defects** | |  | |
| **Surface bonds** | FTIR Spectrum |  GrGC : presence of hydroxyl, carbonyl, alkenes functional groups | |
| **Molecular Dynamics Simulation** | |  GC: double layer graphene with highly curved microstructure |  GrGC: multilayer graphene grown at original monolayer Gr edges |

**Table 6.1** GrGC Vs Gc material properties and testbed results (Continued)

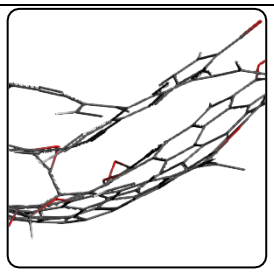
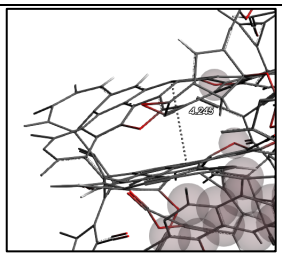
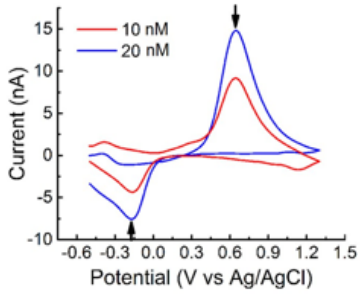
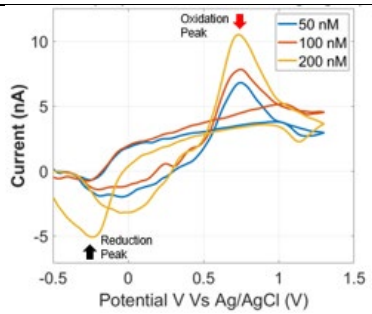
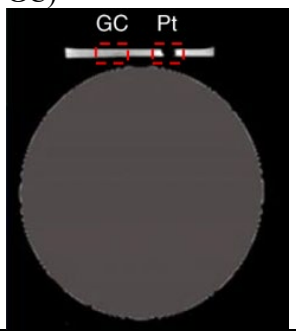
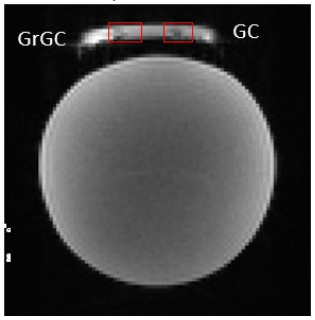
| Methods | | GC | GrGC |
|---|---|---|---|
| **Molecular Dynamics Simulation** | |  Double layer |  3-4 layers of graphene sheets |
| | Resistivity (Ω.cm) | 6.862e-3 (T. Hunt 2020) | 6.738e-3 (T. Hunt 2020) |
| **Micro-electrode-In vitro** | Impedance at 1 kHz | 5.8 ± 1.2 kΩ in 0.01 M PBS (Nimbalkar et al, 2018) | 4.948±1.47 kΩ in 0.01 M PBS |
| | Charge Storage Capacity ($mC/cm^2$) | 61.4 ± 6.9 [ Nimbalkar et al, 2018] | 51.45 ± 6.739 |
| | |   LOD = 10 nM [Nimbalkar et al] |   LOD = 50 nM |
| | MRI | No imaging artifact for GC (Pt Vs GC)   | No imaging artifact for both (GC Vs GrGC)   |
| ***In vivo*** | Impedance | 81 ± 16 kΩ (n=8) [Nimbalkar et al, 2018] | 94.5 ± 5.6 kΩ (n = 30) |
| | SNR Acute SEP | 16 ± 6(n = 8) [Nimbalkar et al, 2018] | 9.76 ± 0.25, for n = 30 |
| | SNR SEP Chronic | - | 12.82 ± 0.64 (n =8) after WK 6 |

**Table 6.1** GrGC Vs Gc material properties and testbed results (Continued)

| Methods | | GC | GrGC |
|---|---|---|---|
| ***In vivo*** | MEP | - | Mean peak to peak voltage of 50 μV recorded for stimulation current of 0.24 mA |

## 6. Conclusion:

The new metamaterial introduced here will find applications in the broader areas of semi-conductor technology, sensors, photovoltaics, energy storage and the like. In semi-conductors, graphene's exceptional conductivity and zero band-gap along with GC's capability to form 3D and complex conducting components (3D electrodes, antennas, resonators, etc.,) will offer a compelling platform that could enable new possibilities in TTF (thin-film transistors) FET (field effect transistors), OFET, etc. The exceptional electrochemical sensing capability of GC together with the exceptional electrical conductivity of graphene could also offer pathway to ultra-sensitive biochemical sensors that could substantially extend current detection limits. In energy storage, Gr layer will offer its superior electrical conductivity while GC will allow high charge storage capacity.

## References:


1. Nimbalkar S, Castagnola E, Balasubramani A, Scarpellini A, Samejima S, Khorasani A, Boissenin A, Thongpang S, Moritz C, Kassegne S. Ultra-capacitive carbon neural probe allows simultaneous long-term electrical stimulations and high-resolution neurotransmitter detection. Scientific reports. 2018 May 3;8(1):1-4.

2. Nimbalkar S, Fuhrer E, Silva P, Nguyen T, Sereno M, Kassegne S, Korvink J. Glassy carbon microelectrodes minimize induced voltages, mechanical vibrations, and artifacts in magnetic resonance imaging. Microsystems & nanoengineering. 2019 Nov 18;5(1):1-1.

3. Ansaldo A, Castagnola E, Maggiolini E, Fadiga L, Ricci D. Superior electrochemical performance of carbon nanotubes directly grown on sharp microelectrodes. Acs Nano. 2011 Mar 22;5(3):2206-14.

4. Castagnola E, Ansaldo A, Fadiga L, Ricci D. Chemical vapour deposited carbon nanotube coated microelectrodes for intracortical neural recording. physica status solidi (b). 2010 Dec;247(11-12):2703-7.

5. Lu Y, Lyu H, Richardson AG, Lucas TH, Kuzum D. Flexible neural electrode array based-on porous graphene for cortical microstimulation and sensing. Scientific reports. 2016 Sep 19;6(1):1-9.

6. Castagnola E, Biso M, Ricci D. Improvement of polypyrrole and carbon nanotube co-deposition techniques for high charge-transfer electrodes. physica status solidi (b). 2009 Dec;246(11-12):2469-72.

7. Castagnola V, Bayon C, Descamps E, Bergaud C. Morphology and conductivity of PEDOT layers produced by different electrochemical routes. Synthetic metals. 2014 Mar 1;189:7-16.

8. Castagnola E, Maiolo L, Maggiolini E, Minotti A, Marrani M, Maita F, Pecora A, Angotzi GN, Ansaldo A, Fadiga L, Fortunato G. Ultra-flexible and brain-conformable micro-electrocorticography device with low impedance PEDOT-carbon nanotube coated microelectrodes. In2013 6th International IEEE/EMBS Conference on Neural Engineering (NER) 2013 Nov 6 (pp. 927-930). IEEE.

9. Venkatraman S, Hendricks J, King ZA, Sereno AJ, Richardson-Burns S, Martin D, Carmena JM. In vitro and in vivo evaluation of PEDOT microelectrodes for neural stimulation and recording. IEEE Transactions on Neural Systems and Rehabilitation Engineering. 2011 Jan 31;19(3):307-16.

10. Beebe X, Rose TL. Charge injection limits of activated iridium oxide electrodes with 0.2 ms pulses in bicarbonate buffered saline (neurological stimulation application). IEEE transactions on biomedical engineering. 1988 Jun;35(6):494-5.

11. Park S, Song YJ, Boo H, Chung TD. Nanoporous Pt microelectrode for neural stimulation and recording: in vitro characterization. The Journal of Physical Chemistry C. 2010 May 20;114(19):8721-6.

12. Weremfo A, Carter P, Hibbert DB, Zhao C. Investigating the interfacial properties of electrochemically roughened platinum electrodes for neural stimulation. Langmuir. 2015 Mar 3;31(8):2593-9.

13. Vomero M, Castagnola E, Ciarpella F, Maggiolini E, Goshi N, Zucchini E, Carli S, Fadiga L, Kassegne S, Ricci D. Highly stable glassy carbon interfaces for long-term neural stimulation and low-noise recording of brain activity. Scientific reports. 2017 Jan 13;7(1):1-4.

14. Lu L, Fu X, Liew Y, Zhang Y, Zhao S, Xu Z, Zhao J, Li D, Li Q, Stanley GB, Duan X. Soft and MRI compatible neural electrodes from carbon nanotube fibers. Nano letters. 2019 Feb 24;19(3):1577-86.

15. Zhao S, Li G, Tong C, Chen W, Wang P, Dai J, Fu X, Xu Z, Liu X, Lu L, Liang Z. Full activation pattern mapping by simultaneous deep brain stimulation and fMRI with graphene fiber electrodes. Nature communications. 2020 Apr 14;11(1):1-2.

16. Jackowska K, Krysinski P. New trends in the electrochemical sensing of dopamine. Analytical and bioanalytical chemistry. 2013 Apr;405(11):3753-71.

17. Yang C, Jacobs CB, Nguyen MD, Ganesana M, Zestos AG, Ivanov IN, Puretzky AA, Rouleau CM, Geohegan DB, Venton BJ. Carbon nanotubes grown on metal microelectrodes for the detection of dopamine. Analytical chemistry. 2016 Jan 5;88(1):645-52.

18. Xiao N, Venton BJ. Rapid, sensitive detection of neurotransmitters at microelectrodes modified with self-assembled SWCNT forests. Analytical chemistry. 2012 Sep 18;84(18):7816-22.

19. Taylor IM, Robbins EM, Catt KA, Cody PA, Happe CL, Cui XT. Enhanced dopamine detection sensitivity by PEDOT/graphene oxide coating on in vivo carbon fiber electrodes. Biosensors and Bioelectronics. 2017 Mar 15;89:400-10.

20. Yang C, Trikantzopoulos E, Nguyen MD, Jacobs CB, Wang Y, Mahjouri-Samani M, Ivanov IN, Venton BJ. Laser treated carbon nanotube yarn microelectrodes for rapid and sensitive detection of dopamine in vivo. ACS sensors. 2016 May 27;1(5):508-15.

21. Vara H, Collazos-Castro JE. Enhanced spinal cord microstimulation using conducting polymer-coated carbon microfibers. Acta biomaterialia. 2019 May 1;90:71-86.

22. Kozai TD, Langhals NB, Patel PR, Deng X, Zhang H, Smith KL, Lahann J, Kotov NA, Kipke DR. Ultrasmall implantable composite microelectrodes with bioactive surfaces for chronic neural interfaces. Nature materials. 2012 Dec;11(12):1065-73.

23. Patel PR, Na K, Zhang H, Kozai TD, Kotov NA, Yoon E, Chestek CA. Insertion of linear 8.4 μm diameter 16 channel carbon fiber electrode arrays for single unit recordings. Journal of neural engineering. 2015 Jun 2;12(4):046009..

24. Patel PR, Zhang H, Robbins MT, Nofar JB, Marshall SP, Kobylarek MJ, Kozai TD, Kotov NA, Chestek CA. Chronic in vivo stability assessment of carbon fiber microelectrode arrays. Journal of neural engineering. 2016 Oct 5;13(6):066002.

25. Schwerdt HN, Kim M, Karasan E, Amemori S, Homma D, Shimazu H, Yoshida T, Langer R, Graybiel AM, Cima MJ. Subcellular electrode arrays for multisite recording of dopamine in vivo. In2017 IEEE 30th International Conference on Micro Electro Mechanical Systems (MEMS) 2017 Jan 22 (pp. 549-552). IEEE.

26. Schwerdt HN, Shimazu H, Amemori KI, Amemori S, Tierney PL, Gibson DJ, Hong S, Yoshida T, Langer R, Cima MJ, Graybiel AM. Long-term dopamine neurochemical monitoring in primates. Proceedings of the National Academy of Sciences. 2017 Dec 12;114(50):13260-5.

27. Alvarez NT, Buschbeck E, Miller S, Le AD, Gupta VK, Ruhunage C, Vilinsky I, Ma Y. Carbon Nanotube Fibers for Neural Recording and Stimulation. ACS Applied Bio Materials. 2020 Aug 19;3(9):6478-87.

28. Hunt, Trevor. Investigation of Glassy Carbon-Graphene Metamaterial-Through FET and Associated Micro-Structures. Diss. San Diego State University, 2020.

# Appendix

Supplementary Tables and Figures: Chapter II

# Ultra-Capacitive Carbon Neural Probe Allows Simultaneous Long-Term Electrical Stimulations and High-Resolution Neurotransmitter Detection

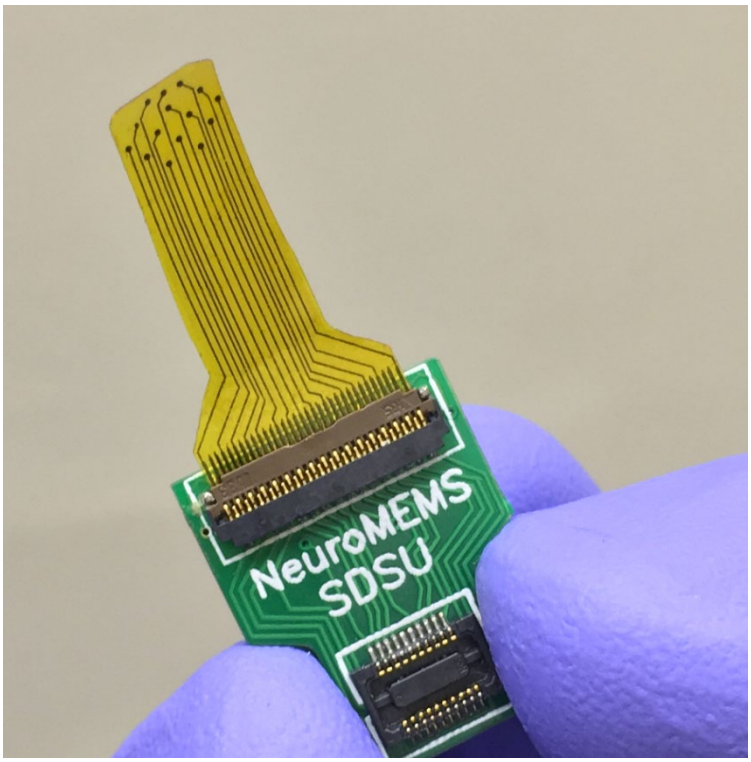



**Figure S2.1** 15-channel aGC ECoG recording microelectrode array mounted on PCB with GC microelectrodes, GC traces and GC bump-pads microfabricated through 2-step double-sided patterning. The probe has microelectrodes with 300 μm diameter, 180 μm wide traces and a total width of 3.5 mm at the electrode locations. ZIF (Zero Insertion Force) connectors are used to connect the probes to PCB which is eventually connected to TDT (Tucker-Davis Technologies) multichannel data acquisition system via a DF30 connector (bottom).

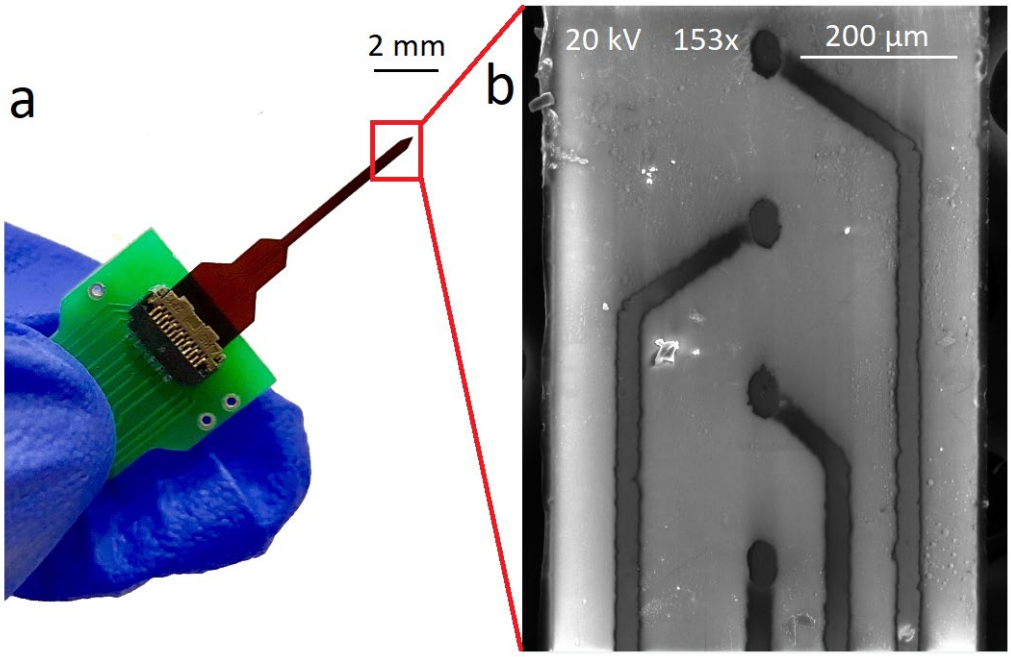



**Figure S2.2** 4-channel aGC penetrating (intracortical) microelectrode array used for dopamine detection (a) Probe mounted on a PCB with ZIF connector (b) SEM image of aGC probe showing four GC microelectrodes with exposed area of 25 µm x 20 µm (500 µm$^2$) spaced at 220 µm. Total width of the probe near the microelectrodes is 500 µm. Length of probes is 17 mm with width of 50 µm.

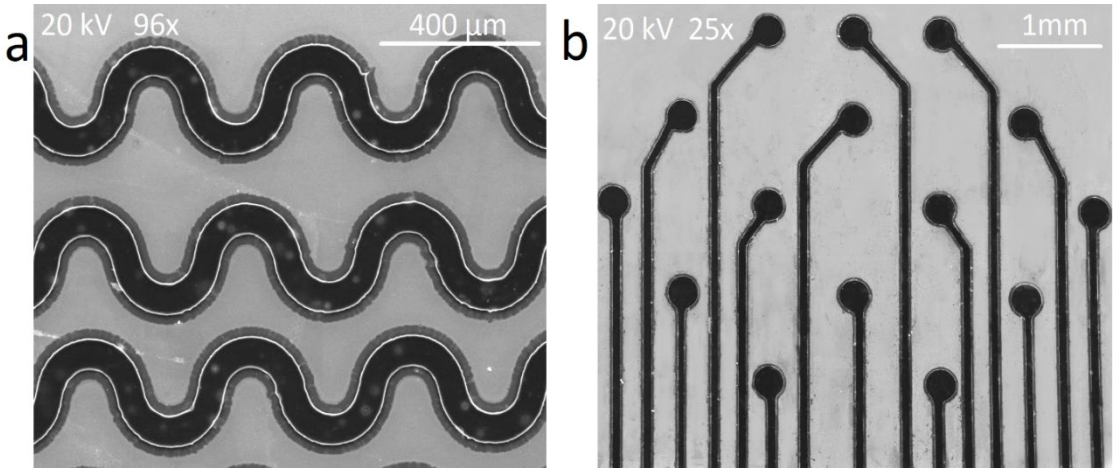



**Figure S2.3** SEM Imaging after pyrolyzing SU8 photopolymer as precursor for GC traces and electrodes (a) Serpentine-shaped GC interconnects (b) Close-up view of GC microelectrodes (Ø = 300 µm) and GC interconnects.

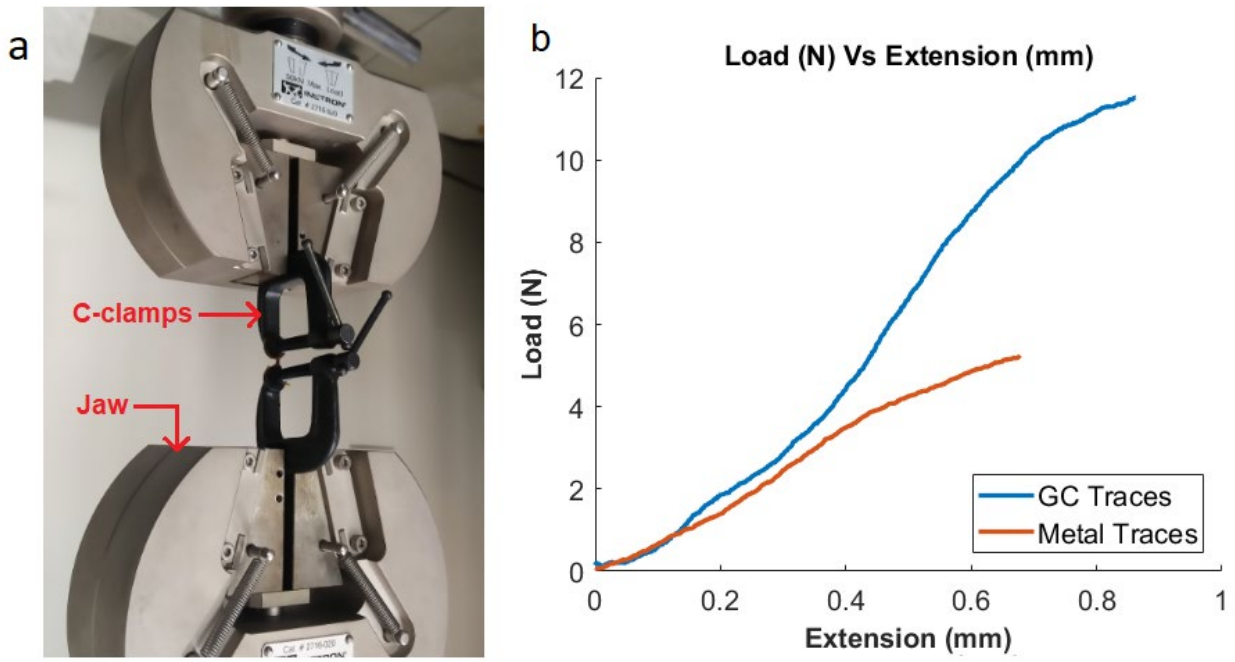



**Figure S2.4** (a) Experimental setup of Instron Universal Testing Machine for axial tensile loading of aGC electrode probe (b) Comparison of load-deflection curve of aGC probes with that of thin-film metal probes of similar geometry. Tensile test specimen probes with 17 mm in length, 3 mm in width, and 50 mm in thickness were used.

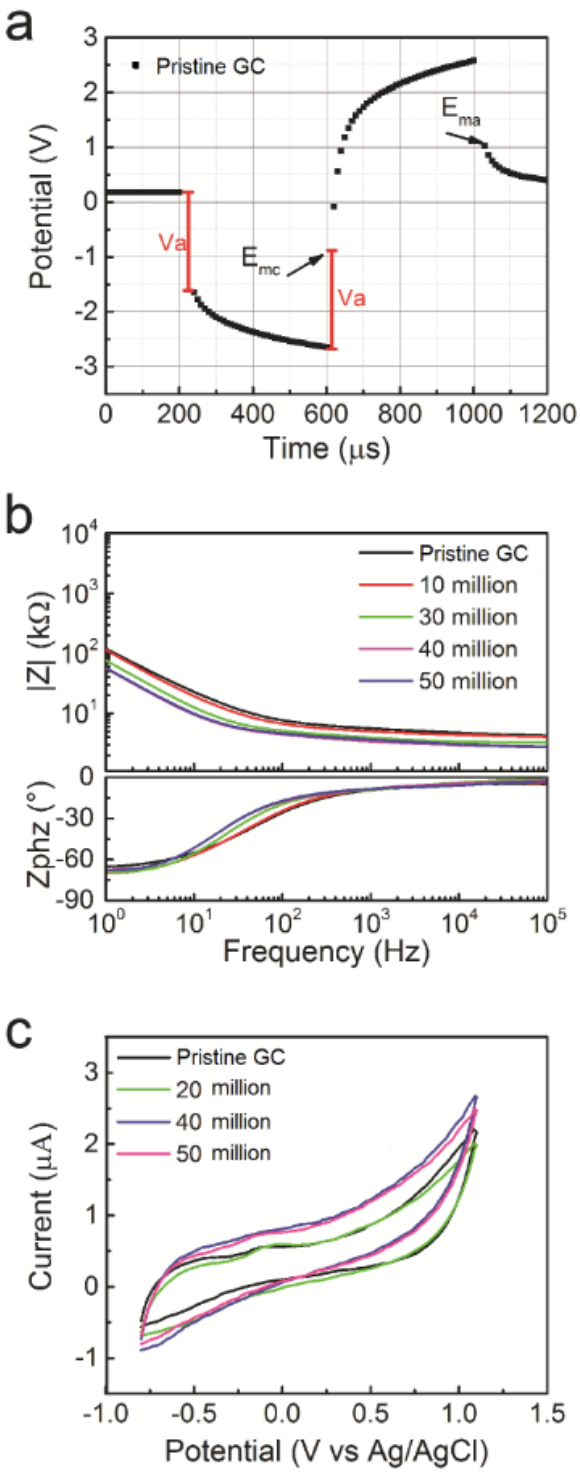



**Figure S2.5** (a) Voltage transients of a GC microelectrodes in response to a 5.2 mA biphasic pulse corresponding to 3 mC/cm$^2$ charge density (b) Impedance spectra before and after 20, 40, 50 billion cycles of 3 mC/cm$^2$ stimulation pulses in PBS, and (C) Corresponding cyclic voltammograms. Qinj is calculated as the time integral of current in the loading phase normalized by the geometric area.

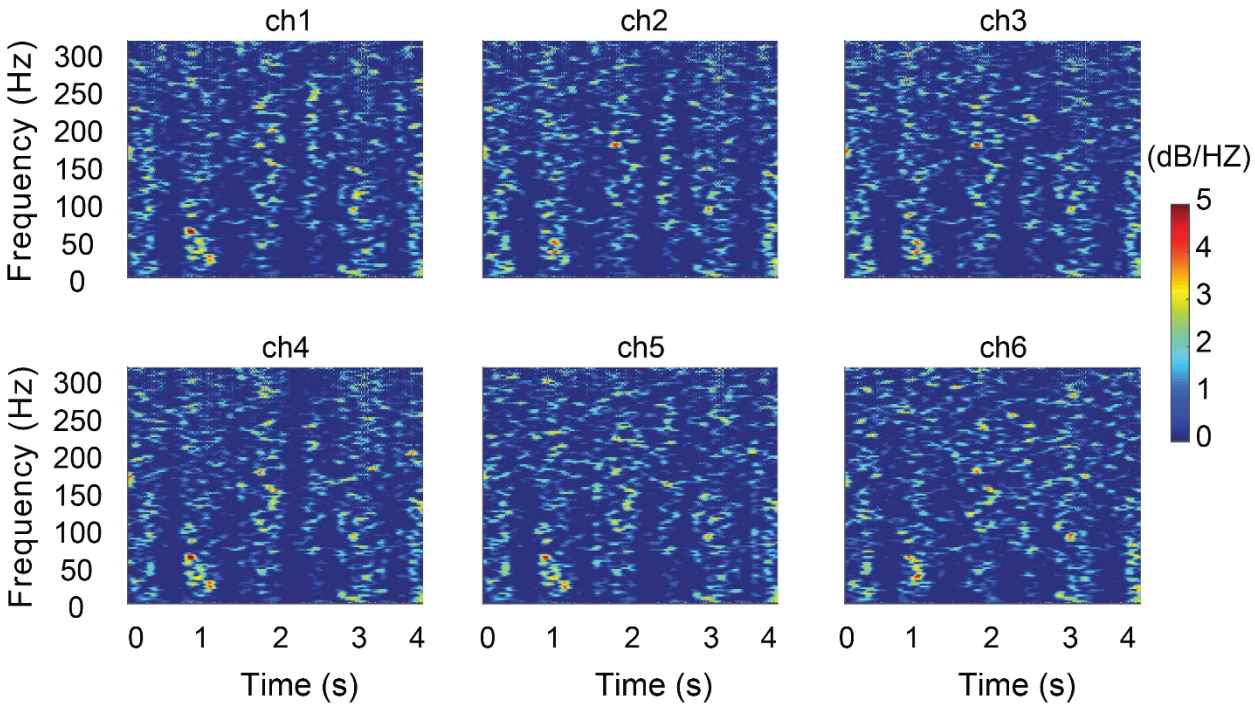



**Figure S2.6** Spectrogram of six ECoG channels during SEP stimulation shown in Figure 8b. Short time Fourier Transform was applied to the 256 ms section of each ECoG time series and smoothed by 200 ms overlapped windows to obtain this temporal-spectral representation of ECoG data.

**Table S2.1** Summary of Charge Injection Limits (Qinj), CSC and Potential Limits of Microelectrode Materials Reported in Literature

| Material | Coating | CSC ($mC/cm^2$) | Qinj limit ($mC/cm^2$) | Potential limit (V vs. Ag/AgCl) | Ref. | Mechanism |
|---|---|---|---|---|---|---|
| CNT pillars | no | -- | 1−1.6 | -1.5 - 1 | (1) | capacitive |
| CNT CVD | no | 70.8 ± 1.1 at 100 mV/s | 4 | -1 - 1.15 | (2) | capacitive |
| Porous Graphene | no | 50 at 100 mV/s | 3.2 | -1.3 - 0.8 | (3) | capacitive |
| PEDOT-CNT | yes | 40.4 ± 64.8, 158.7 ± 8.1, 540.7 ± 70.3 at 100 mV/s | 2.5 - 7 | -1 - 0.8 | (4-7) | pseudocapacitive |
| PPY-CNT | yes | 212.3 ± 23.9 | 7 | -0.9 - +0.6 | (2) | pseudocapacitive |
| PEDOT | yes | 75.6 ± 5.4, 893.5 ± 137.8 at 100mV/s | 2.3 - 15 | −0.8 - +0.6 | (6,8-10) | pseudocapacitive |
| IrOx | yes | 28.8 ± 0.3 at 50 mV/s | 0.9 - 3.3 | −0.8 - +0.6 | (8, 11-12) | faradaic |
| Pt | no | 0.5 ± 0.1, 8.6 ± 3.5 | 0.05 - 0.15 | -0.8 - +0.6 | (6, 8 ,9 13) | pseudocapacitive |
| GC (Current) | no | 61.4 ± 6.9 | 3.0 | -0.9 - +1.3 | | capacitive |

**Table 2.2** Summary of Detection Limits and Sensitivity to Dopamine Detection Reported in Literature

| Material | Detection Limit | Sensitivity at 1 mM DA | Ref |
|---|---|---|---|
| CNT yarn microelectrodes | 25 ± 2 nM | -- | (14) |
| Laser treated CNT yarn microelectrodes | 13 ± 2 nM | -- | (14) |
| PEDOT/graphene oxide modified CF | 85 ± 9 nM | ca. 50 $nA/\mu m^2$ | (15) |
| CF | 19 ± 4, 218 ± 20 nM | -- | (15,17,18) |
| Self-assembled SWCNT forests | 17 ± 3 nM at 10 Hz, 65 ± 7 nM at 90 Hz | 184 ± 19 $pA/\mu m^2$ | (16) |
| CNT-Nb | 11± 3 nM | 197 ± 16 $pA/\mu m^2$ | (17) |
| GC (Current) | 10 nM | 450 ± 30 $pA/\mu m^2$ | |

**References**


1. K. Wang, H. A. Fishman, H. Dai, and J. S. Harri, *Neural Stimulation with a Carbon Nanotube Microelectrode Array*, Nano Lett., 2006, 6 (9), pp 2043–2048.

2. A. Ansaldo, E. Castagnola, et al., *Superior Electrochemical Performance of Carbon Nanotubes Directly Grown on Sharp Microelectrodes*, ACS Nano, 2011, 5 (3), pp 2206–2214.

3. Y. Lu, H. Lyu, A. G. Richardson, T. H. Lucas & D. Kuzum, *Flexible Neural Electrode Array Based-on Porous Graphene for Cortical Microstimulation and Sensing* Scientific Reports, 6:33526, DOI: 10.1038/srep33526

4. X. Luo , C.L. Weaver, D.D. Zhou, R. Greenberg, X.T. Cui. *Highly stable carbon nanotube doped poly(3,4-ethylenedioxythiophene) for chronic neural stimulation*. Biomaterials.;32(24):5551-7, 2011, doi: 10.1016/j.biomaterials.2011.04.051.

5. E. Castagnola, L. Maiolo, E. Maggiolini, A. Minotti, M. Marrani, F. Maita, A. Pecora, G.N. Angotzi, A. Ansaldo, M. Boffini, L. Fadiga, G. Fortunato, D. Ricci, *PEDOT-CNT-Coated Low-Impedance, Ultra-Flexible, and Brain-Conformable Micro-ECoG Arrays*. IEEE Trans Neural Syst Rehabil Eng. ;23(3):342-50, 2015, doi: 10.1109/TNSRE.2014.2342880.

6. E. Castagnola, A. Ansaldo, E. Maggiolini,T. Ius, M. Skrap, D. Ricci, and L. Fadiga, *Smaller, softer, lower-impedance electrodes for human neuroprosthesis: a pragmatic approach*, Front. Neuroeng. 8, 2014 doi: 10.3389/fneng.2014.00008

7. E.Castagnola, E. Maggiolini, L. Ceseracciu, F. Ciarpella, E. Zucchini, S. De Faveri, L. Fadiga,and D. Ricci, *pHEMA Encapsulated PEDOT-PSS-CNT Microsphere Microelectrodes for Recording Single Unit Activity in the Brain*, Front Neurosci.; 10: 151, 2016. doi: 10.3389/fnins.2016.00151

8. S. F. Cogan, *Neural stimulation and recording electrodes*. Annu. Rev. Biomed. Eng. 10, 275–30910, 2008, 1146/annurev.bioeng.10.061807.160518

9. M. Vomero, E. Castagnola, F. Ciarpella, E. Maggiolini, N. Goshi, E. Zucchini, S. Carli, L. Fadiga, S. Kassegne and D. Ricci. *Highly Stable Glassy Carbon Interfaces for Long-Term Neural Stimulation and Low-Noise Recording of Brain Activity*, *Nature Sci. Rep.* **7**:40332 (2017) doi: 10.1038/srep40332.

10. S. Venkatraman, J. Hendricks, Z. A. King, A.J. Sereno, S. Richardson-Burns, D. Martin, and J. M. Carmena, *In Vitro and In Vivo Evaluation of PEDOT Microelectrodes for Neural Stimulation and Recording*, IEEE Trans Neural Syst Rehabil Eng., VOL. 19, NO. 3, JUNE 2011 307.

11. S. F. Cogan, P.R. Troyk, J. Ehrlich, T.D.Plante, D.E. Detlefsen, *Potential-biased, asymmetric waveforms for charge-injection with activated iridium oxide (AIROF) neural stimulation electrodes*. IEEE Trans. Biomed. Eng. 53, 327–33210, 2006.

12. S. J. Wilks, S. M. Richardson-Burns, J. L. Hendricks, D.C. Martin, and K. J. Otto, *Poly(3,4-ethylenedioxythiophene) as a Micro-Neural Interface Material for Electrostimulation*, Frontiers in Neuroengineering., 2: 7., 2009; doi: 10.3389/neuro.16.007.

13. L. Bullara, D. McCreery, T. Yuen, W. Agnew, A microelectrode for delivery of defined charge densities. Journal of Neuroscience Methods 9, 15–21, 1983.

14. C. Yang, E. Trikantzopoulos, M. D. Nguyen, C. B. Jacobs, Y. Wang, M. Mahjouri-Samani, I. N. Ivanov, and B. J. Venton, *Laser Treated Carbon Nanotube Yarn Microelectrodes for Rapid and Sensitive Detection of Dopamine in Vivo*, DOI: 10.1021/acssensors.6b00021 ACS Sens. 2016, 1, 508−515

15. I.M. Taylor, E.M. Robbins, K.A. Catt, P.A. Cody, C.L. Happe, X.T. Cui. *Enhanced dopamine detection sensitivity by PEDOT/graphene oxide coating on in vivo carbon fiber electrodes, Biosens Bioelectron*., 89 (Pt 1):400-410, 2017. doi: 10.1016/j.bios.2016.05.084.

16. N. Xiao and B. J. Venton, *Rapid, sensitive detection of neurotransmitters at microelectrodes modified with self-assembled SWCNT forests*, Anal Chem. 84(18): 7816–7822, 2012,.doi: 10.1021/ac301445w

17. C.Yang, C. B. Jacobs, M. D. Nguyen, M. Ganesana, A. G. Zestos, I. N. Ivanov, A. A. Puretzky, C. M. Rouleau, D. B. Geohegan, and B. J. Venton, *Carbon Nanotubes Grown on Metal Microelectrodes for the Detection of Dopamine*, Anal. Chem., 88, 645−652, 2016, DOI: 10.1021/acs.analchem.5b01257

18. W. Yi, Y. Yang, P. Hashemi, M. M.-C,Cheng, *3D carbon nanofiber microelectrode arrays fabricated by plasma-assisted pyrolysis to enhance sensitivity and stability of real-time dopamine detection*, Biomed Microdevices 18: 112, 2016, DOI 10.1007/s10544-016-0136-1.

Supplementary Tables and Figures: Chapter III

# Glassy Carbon Microelectrodes Minimize Induced Voltages, Mechanical Vibrations and Artifacts in Magnetic Resonance Imaging

## A. Microfabrication of Pt microelectrodes on a polymer substrate

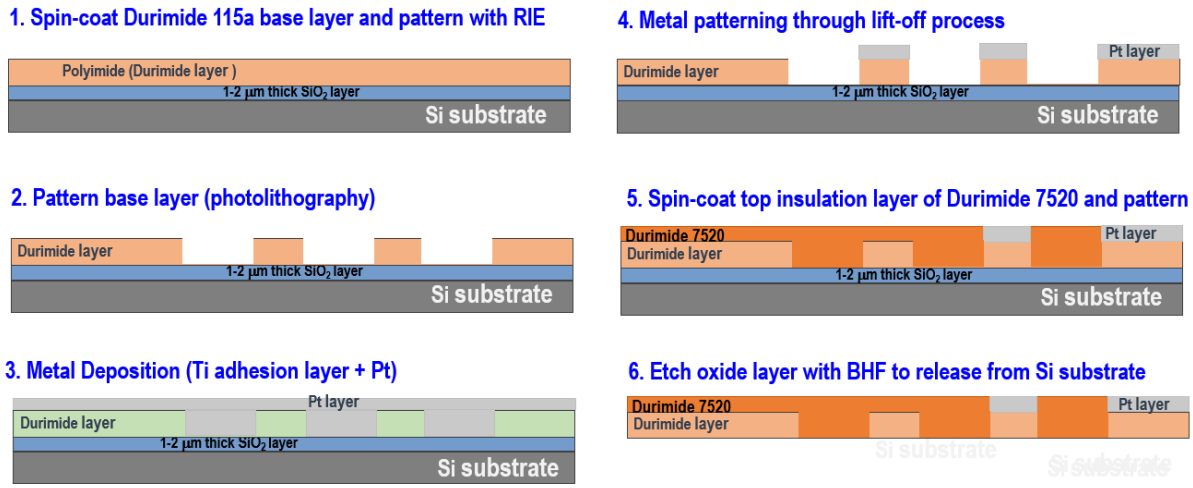



**Figure S3.1** Lithography process for microfabricating Pt microelectrodes on a flexible polymer substrate.

## B. FEA Methods

The FEM simulations of the effects observed were made in COMSOL Multiphysics (COMSOL AB, Sweden). Static magnetic fields ($B_0$ effects) were obtained by solving for the magnetic scalar potential according to Gauss´ law, dynamic electromagnetic behavior (gradient effects) by solving for the magnetic vector potential and current fields according to Ampere's and Faraday's laws and the radiofrequency behavior ($B_1$ effects) by solving for the electric field in the EM-wave equation.

All simulations were made using the structures shown in a much larger (>10x) volume setting the boundary condition on its outside. These were, respectively, a large box with uniform magnetic flux in one direction on its boundaries, a large box with a time-varying magnetic flux in one direction and an electromagnetic single-loop resonator, excited at the desired frequency, inside a much larger box, at whose boundary the electromagnetic field was null.

The materials simulated were Pt ($\varepsilon_r \sim= 0.735$, $\chi$ = 279 ppm, $\sigma= 9.43x10^6$ S/m), GC ($\varepsilon_r \sim= 12.5$, $\chi$ = -1.2 ppm, $\sigma \sim= 6803$ S/m), and PMMA ($\varepsilon_r \sim= 2.6$, $\chi$ = -1.2 ppm, $\sigma \sim= 0$ S/m) in a water phantom ($\varepsilon_r \sim=$ 80, $\chi$ = -9.05 ppm, $\sigma \sim= 0$ S/m) [21-24].

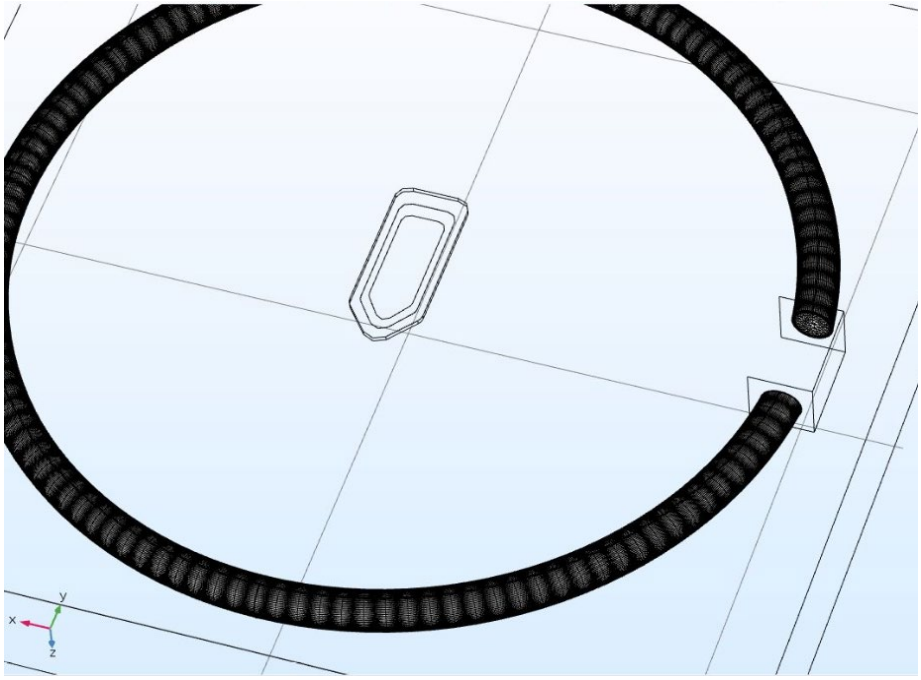



**Figure S3.2** FEA domain used for solving static magnetic effects, magnetic potential vectors, and electric fields.

**C. Three-step measurement protocol to determine the torque produced by the implants**

Connect the actuation coil to the external frequency-controlled voltage supply:

i. Determine the spring constant $\mu$, by sweeping the torque $\tau_1$ at a constant low frequency (4 Hz).

ii. Determine the transfer function and the eigenfrequency of the mechanical oscillation by sweeping the frequency of the torque $\tau_l$ at constant amplitude.

Disconnect the actuation coil from the external frequency-controlled voltage supply.

iii. Application of a defined gradient sequence and measurement of deflection.

We recorded the resulting vibration as well as the excitation pulses to enable a proper analysis in the frequency domain. The used devices are: frequency controlled voltage supply: Tektronix AFG3022B, Acquisition devices: NI-USB9215 & RedLab 1408-FS both connected to the computer via USB readout through MatLab interface.

By measuring the transfer function as explained in step (i) + (ii), one can derive the torque acting on the mechanical device due to the electrode ground planes (see Figure S.2.)

To evaluate and distinguish the effect of acoustic vibration from eddy current induced vibration we run the sequence also with no electrodes attached to the PMMA. Therefore, we tested three different PMMA plates each of them in three different measurement cycles to obtain statistically relevant values about the acoustic coupling. Additionally, we used a sample produced from 40 µm copper foil (Chomerics, CCK-18-101-0200) to evaluate the torque produced by a high conductive sample.

In step (iii) we measure the time domain signal of the gradient switching and the consequential deflection. To measure the gradient switching response of the samples we ran a standard 2D gradient echo sequence (axial slice). To simplify the analysis, we applied a one-dimensional gradient along the z-axis, by setting the field-of-view (FOV) of the two orthogonal gradients to 10 m (at 32 pixels). For the Pt and GC sample we set the slice thickness to 0.4 mm, whereas for the Cu sample to 20 mm. In both cases, the excitation bandwidth was set to 3 kHz. To obtain maximal vibration we excited the corresponding samples on mechanical resonance, thus set $\mathrm{TR} = \frac{1}{f_{res}}$. Using the Fast-Fourier-Transform (FFT) we analyze the signal in the frequency domain which allows to compensate for the mechanical transfer function and to calculate the external torque. From step (i) + (ii) we know the transfer function and the spring constant,

and we can derive the torque produced by gradient switching. The results were normalized in reference to the static magnetic field and the gradient slew rate which leads to an implant specific parameter, the position and the field strength we measured. This results in a specific number or figure of merit for an implant namely the specific torque per field slew rate (TPSR $\left[\frac{Nm}{T \cdot T/s}\right]$). The worst case torque produced by an implant obtained in any MR scanner is obtained by multiplying this number with the slew rate of the target scanner, the maximal possible distance from the gradient center and the corresponding field strength.

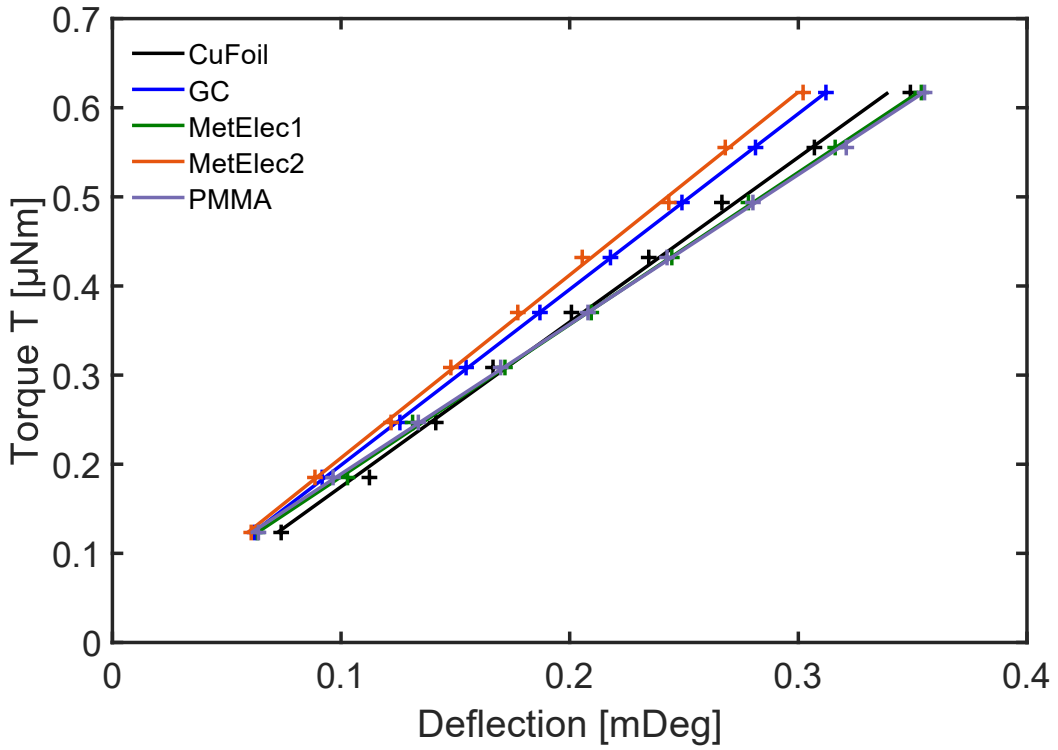



**Figure S3.3** Result of the spring constant measurements of the different samples using the same sample holder. Variations arise due to the maladjustment of the sample holder when exchanging the samples. This leads to a shift of the angle α between the sample holder and the $B_0$-field and thus to a different torque (see Equation 2 in the main document). The spring constant of the sample holder is μ = (1.85 ± 0.15) µNm/mDeg.

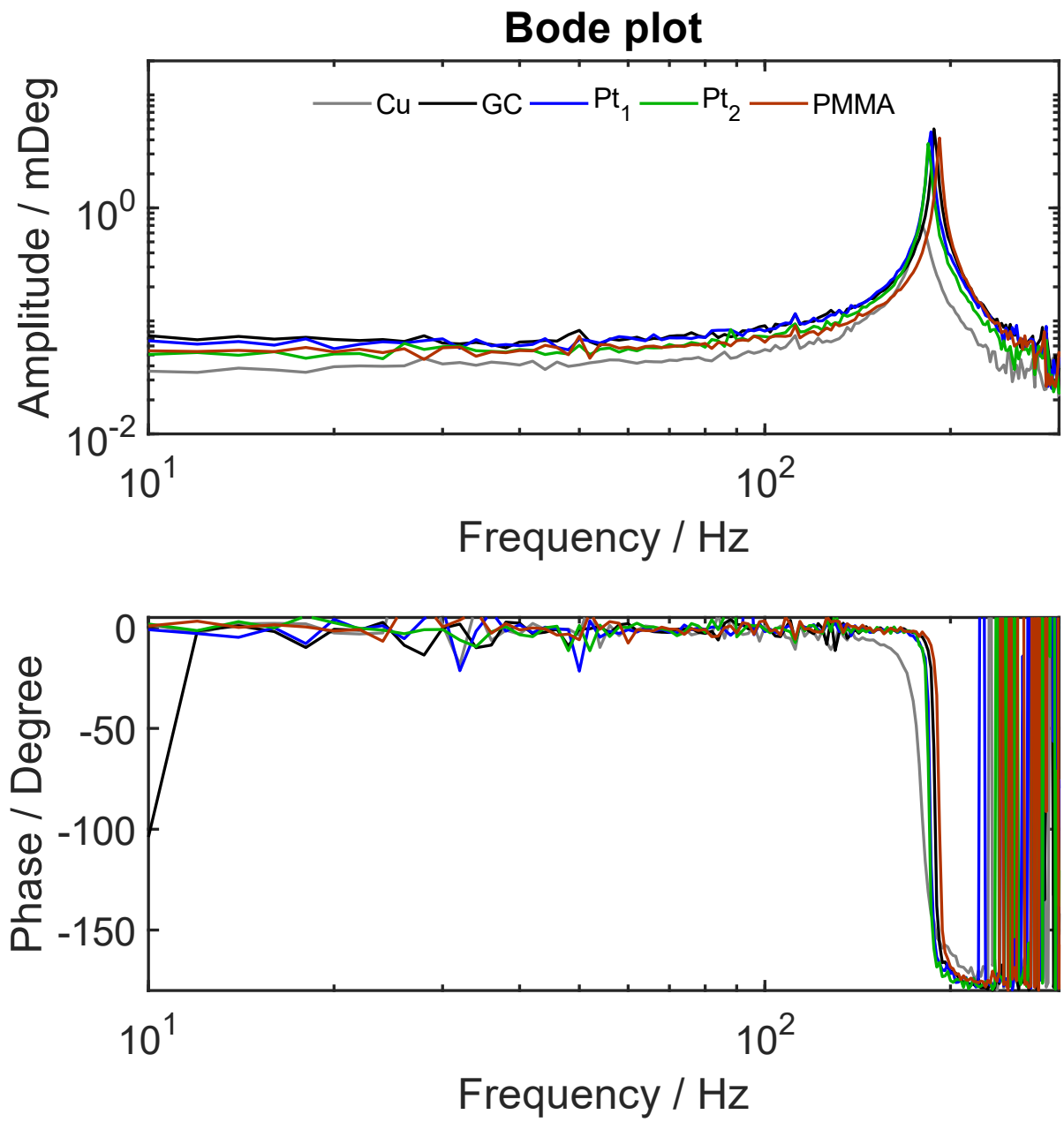



**Figure S3.4** Measured transfer functions of different samples. The harmonic-oscillator-like behavior of the damped spring-mass system is clearly recognizable.

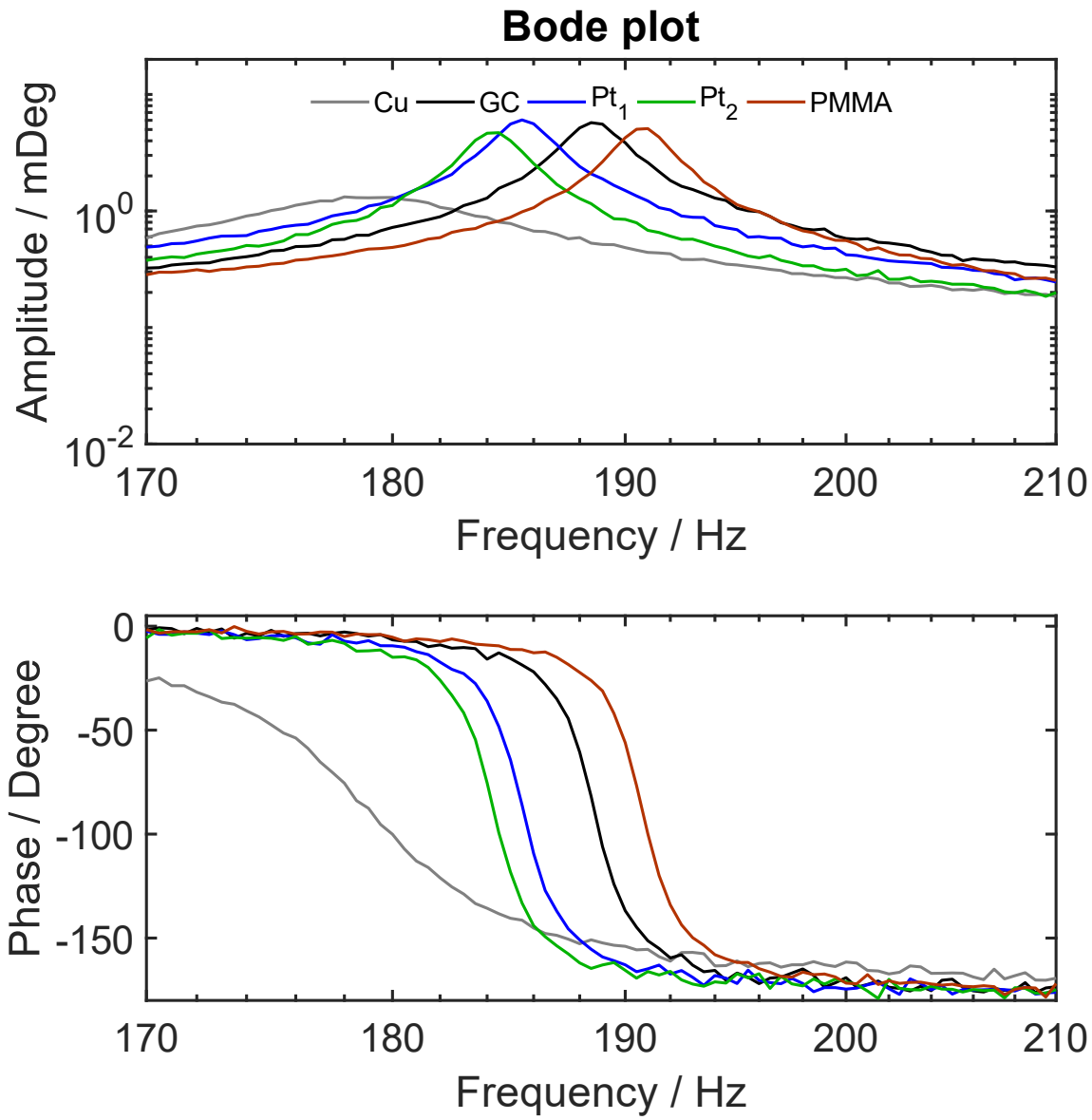



**Figure S3.5** Transfer function with higher frequency resolution around the resonance frequencies. The highest resonance frequency is measured with the PMMA sample holder without an electrode because the moment of inertia is least without an electrode sample attached on the PMMA substrate. The GC microelectrode is lighter than the Pt microelectrodes, hence the resonance frequency of the GC microelectrode is reduced compared to the empty sample holder but larger compared to the Pt microelectrodes. For the copper foil there is, in addition to the reduced resonance frequency, an increased damping observable. The cause is the damping forces due to eddy currents during vibration, induced by the motion of the sample inside the $B_0$-field. Hence, the very precise measurement of changes of the transfer function could be used as an examination tool, too.

## D. Imaging Results of $B_0$ Field Map and EPI Sequence

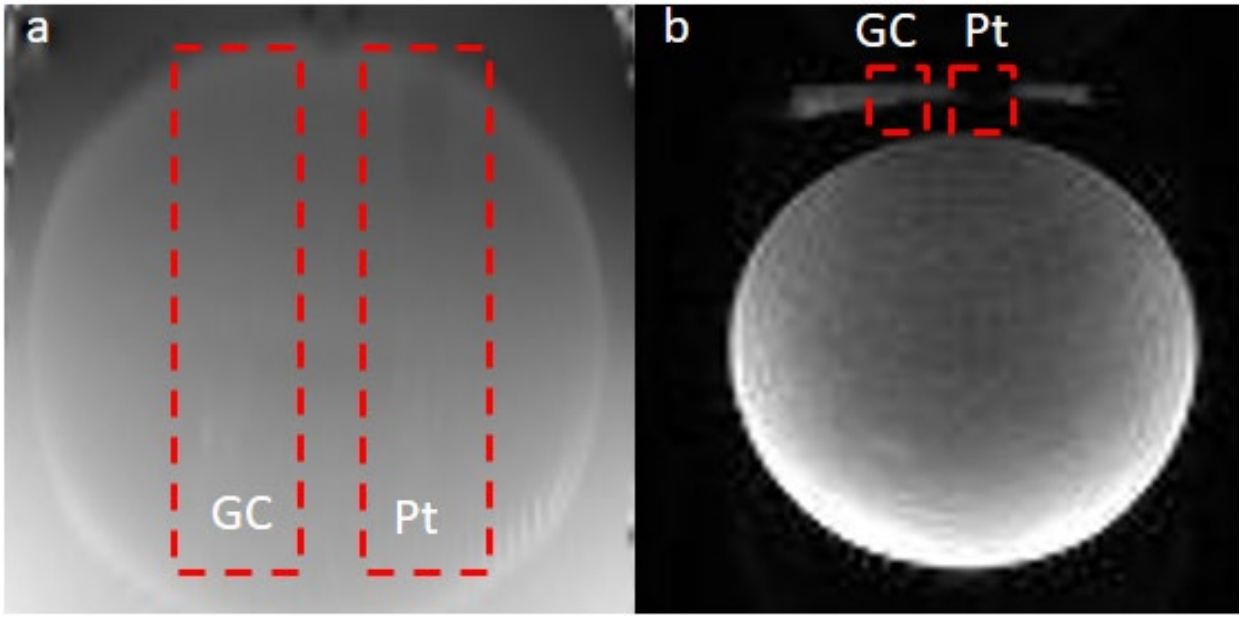



**Figure S3.6 (a)** Bo-field map image showing very little or no signal loss at Pt microelectrode site in the coronal view with 3T scanner and **(b)** Echo planar fMRI image showing loss of signal at Pt microelectrode site in axial view with 3T scanner

Supplementary Tables and Figures: Chapter IV

# Novel Graphene-Glassy Carbon (GrGC) MetaMaterial: Synthesis, Characterization, and Molecular Dynamics Simulation

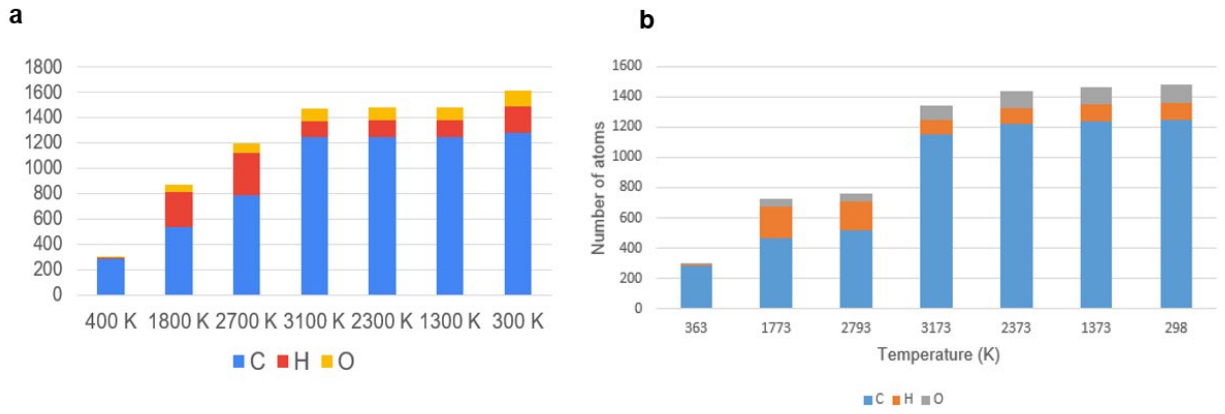



**Figure S4.1** Carbon, Hydrogen and, Oxygen (CHO) contents of the GrGC nanostructure during pyrolysis (a) Model I (b) Model II

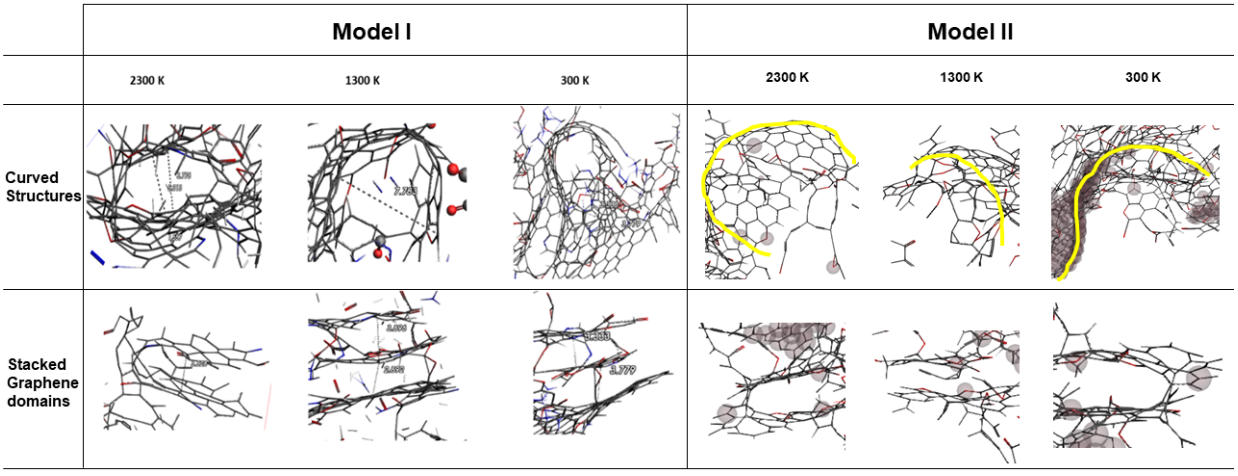



**Figure S4.2** Model I (a) closed cage GrGC structure evolution during ramp down of temperature from 2300K to 300K (b) Gr interlayer stacking spacing changing from 2300K to 300K is observed to be *0.38±0.014 nm* at 300K. Model II (a) closed cage Gr structure evolution during ramp down of temperature from 2300K to 300K (b) Gr interlayer stacking.

Supplementary Tables and Figures: Chapter V

# Graphene on Glassy Carbon Microelectrodes Demonstrate Long-Term Structural and Functional Stability in Neurophysiological Recording and Stimulation

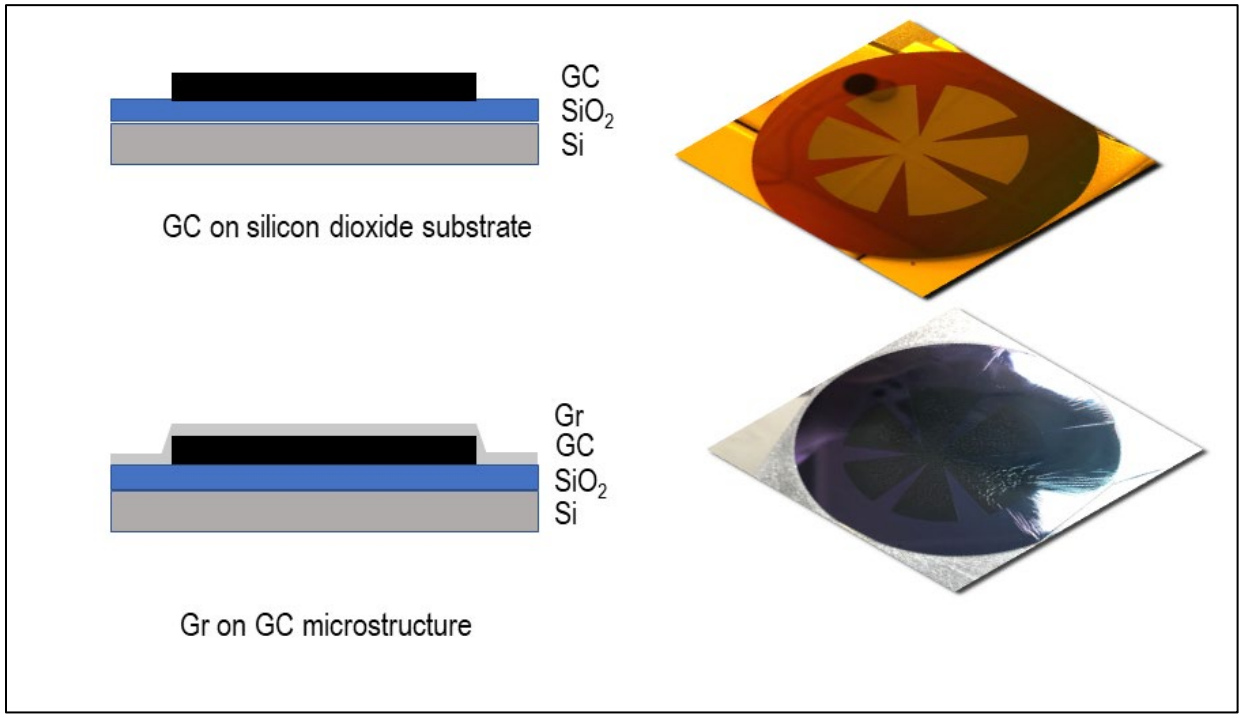
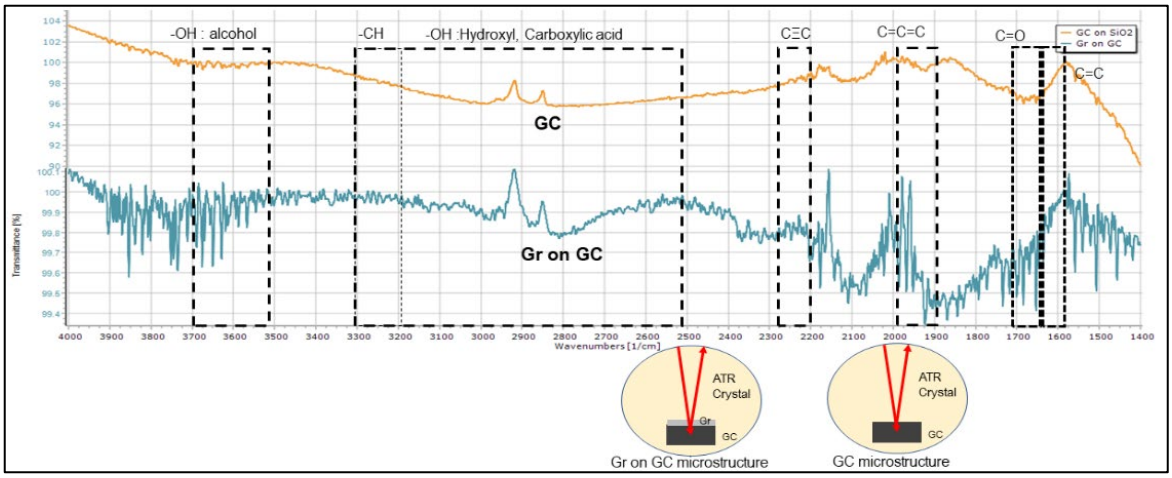



**Figure S5.1** GC and *Gr on GC* microstructures for FTIR spectroscopy.

**a**




**b**

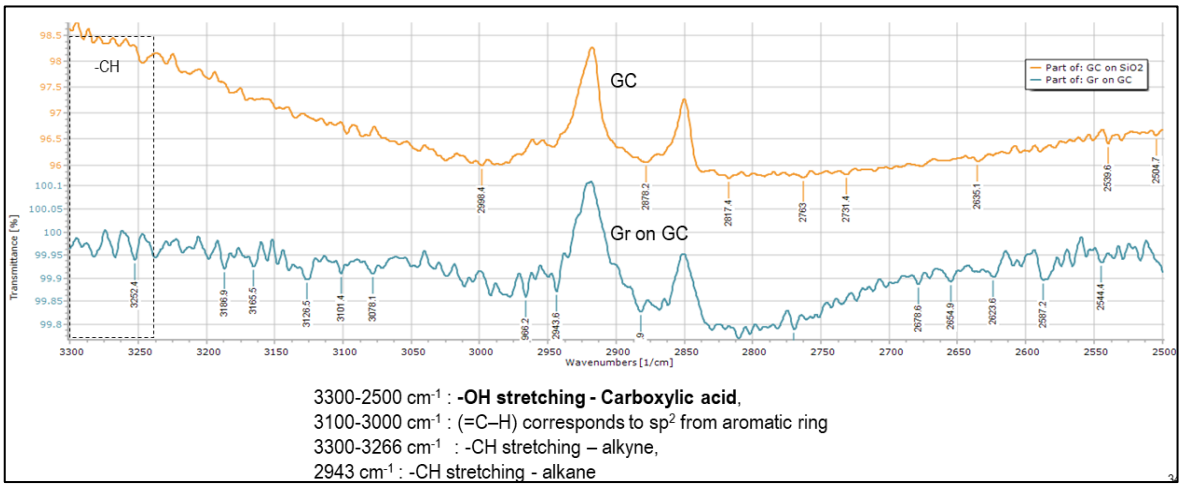
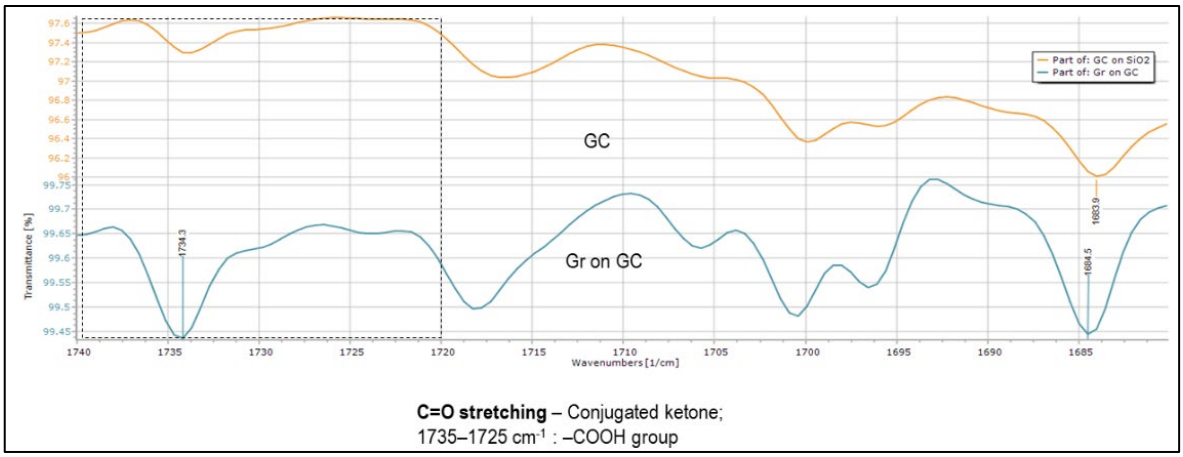



**Figure S5.2** (a) FTIR Spectra corresponding to function group peaks for GC and *Gr on GC* microstructure. (b) close-up showing hydroxyl (-OH) stretching, =C-H, alkyne (-CH), and alkane stretching

a




b

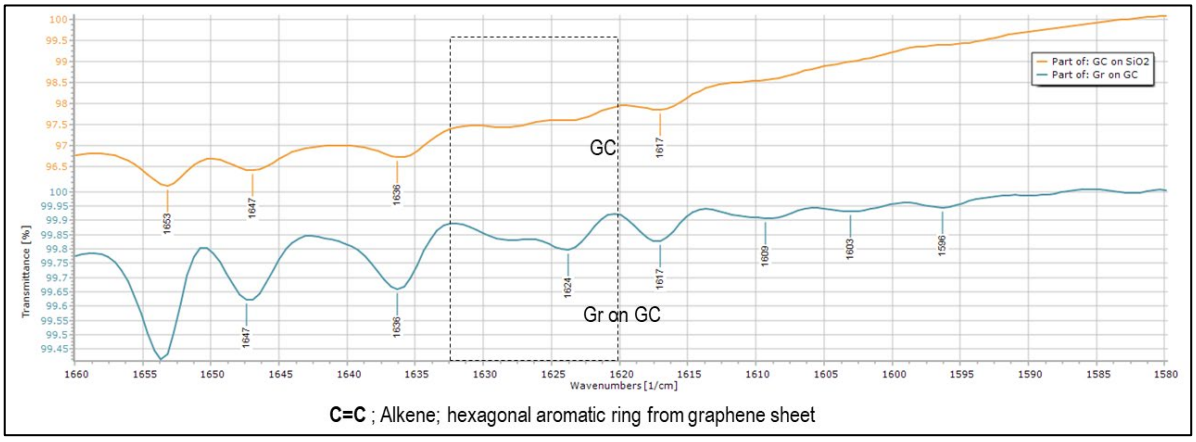



**Figure S5.3** (a) close-up showing C=O stretching and -COOH group, and (b) alkene (C=C) groups.

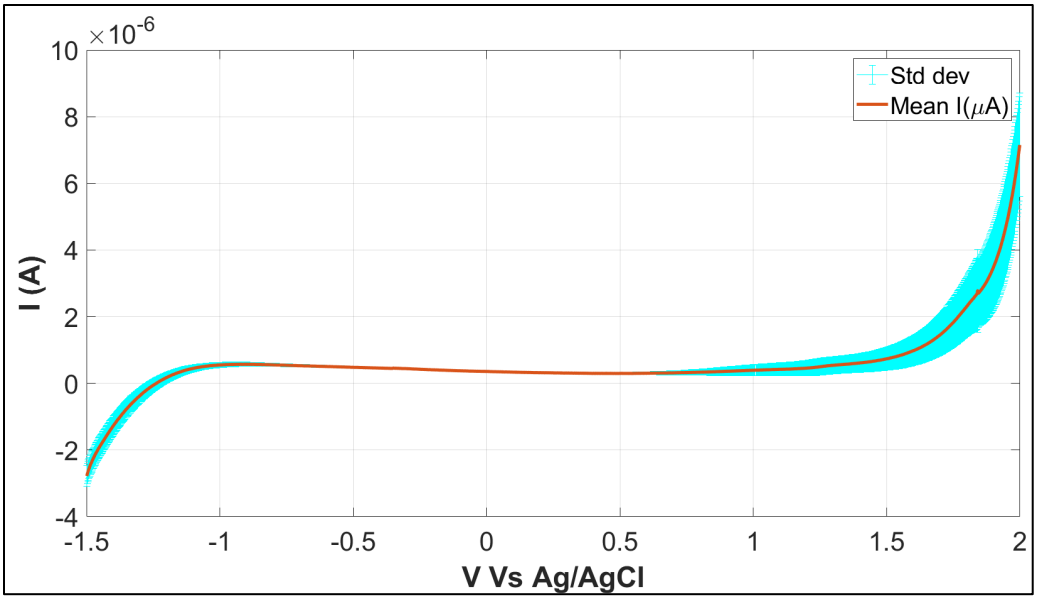



**Figure S5.4** Linear sweep voltammetry of *Gr on GC* microelectrode swept between 2 and −1.5 V vs. Ag/AgCl, scan rate of 50 mV/s). The light blue color indicates the standard deviation.

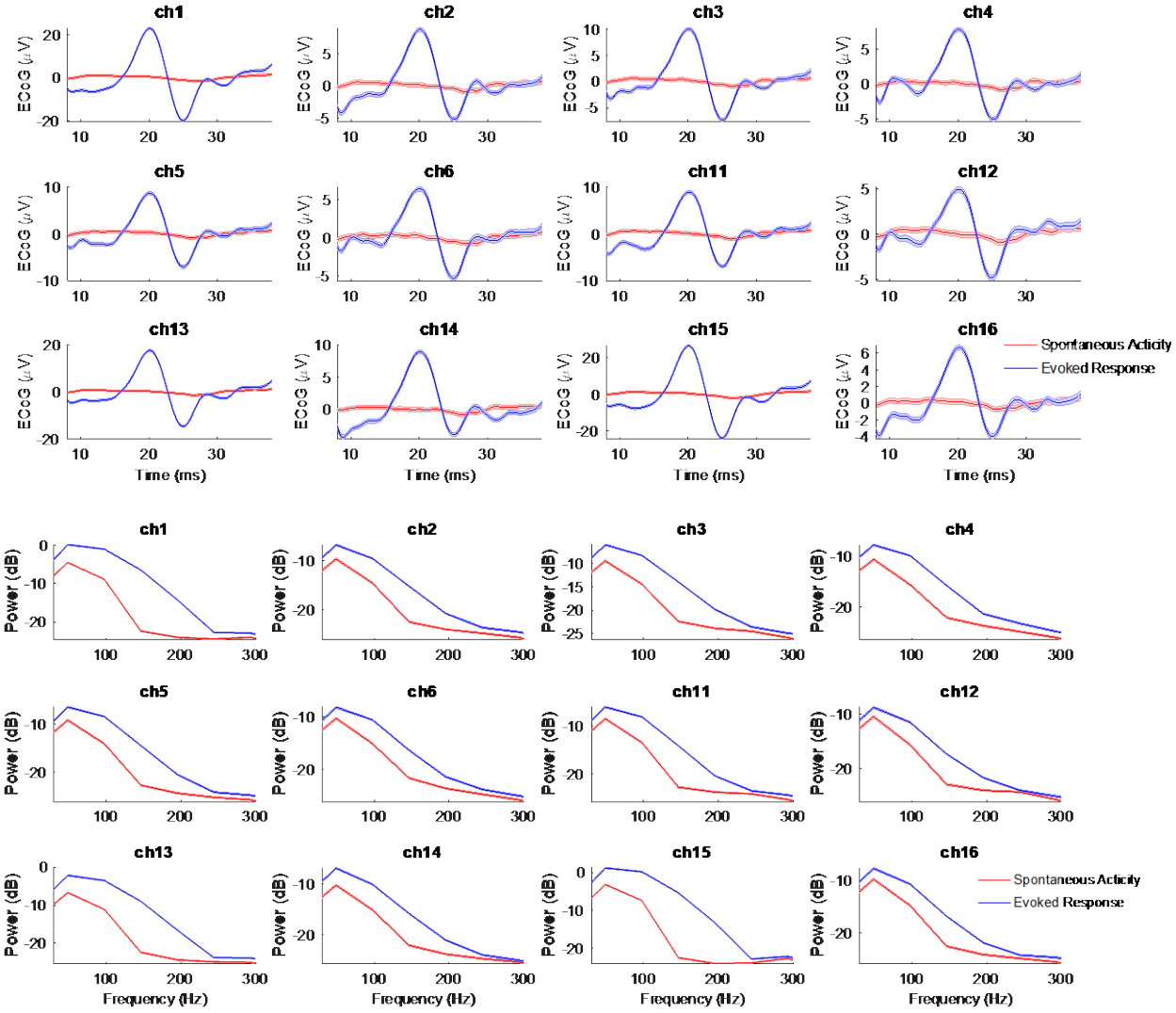



**Figure S5.4** Example of averaged sensory evoke potentials (SEPs) in an acute recording of 12 electrodes. (a) averaged SEPs response (blue) displayed 7–37 ms after the biceps muscle stimulation with the average-spontaneous activity (red) with shaded error (standard error), (b) the power spectrum for sensory evoked response (blue) and spontaneous activities (blue) corresponding to the same signals shown in (a).

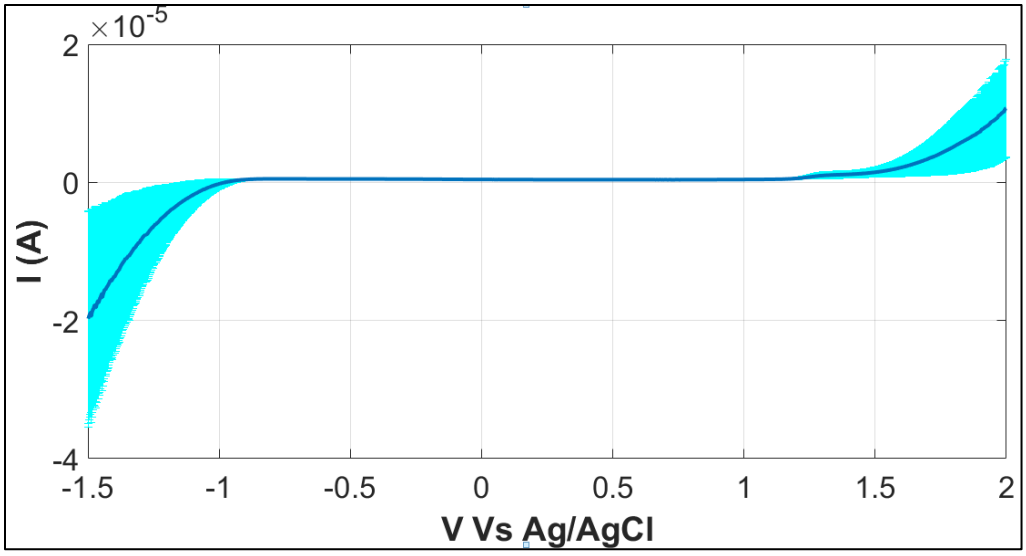



**Figure S5.5** Linear sweep voltammetry of *Gr on GC* microelectrode swept between 2 and −1.5 V vs. Ag/AgCl, scan rate of 50 mV/s) post-chronic implantation of 18 weeks. The light blue color indicates the standard deviation.

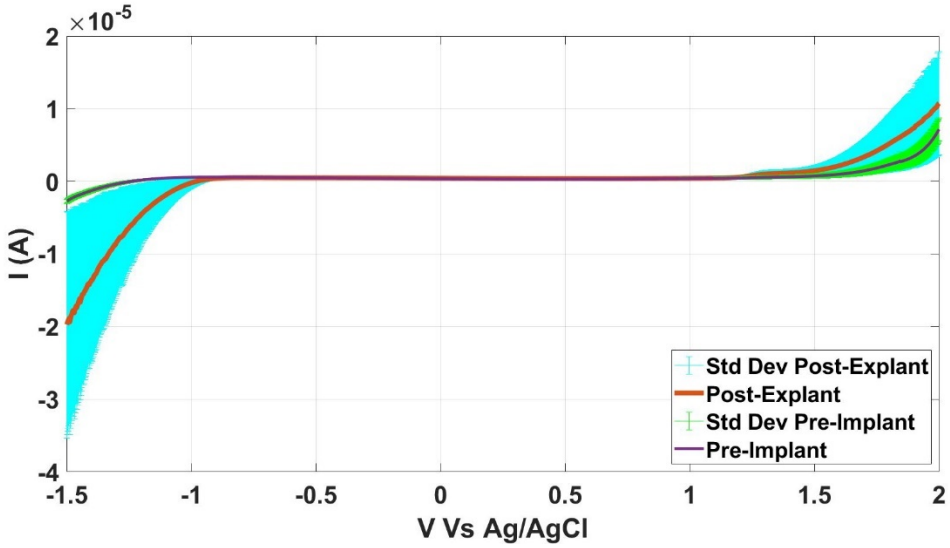



**Figure S5.6** Plot S3 and S5 together – Superposition of linear sweep voltammetry of *Gr on GC* microelectrode swept between 2 and −1.5 V vs. Ag/AgCl, scan rate of 50 mV/s) pre- and post-chronic implantation of 18 weeks.

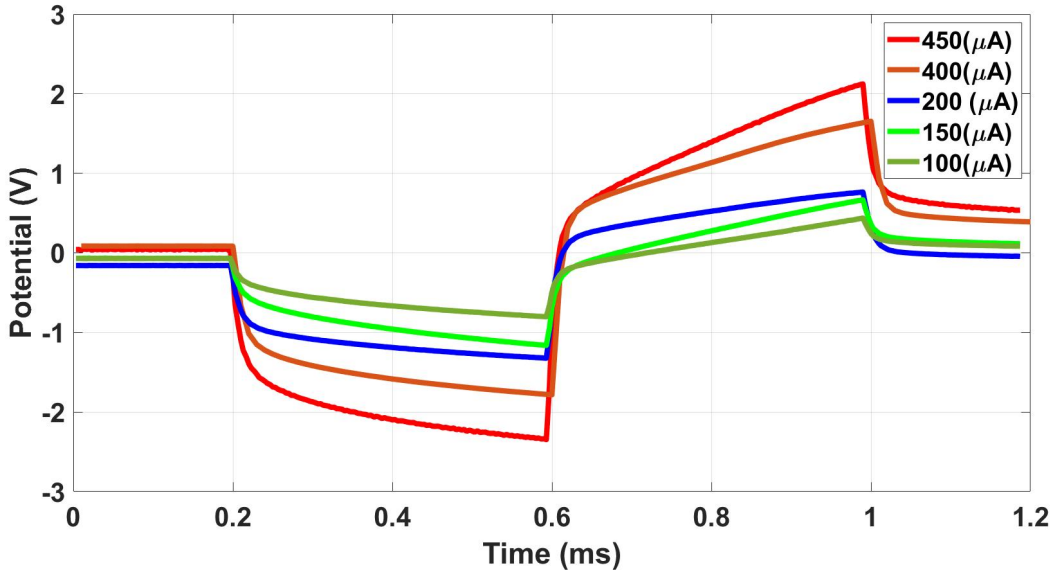



**Figure S5.7** Calculation of CIC. For biphasic cathodic pulse of $I_c = I_a \leq 400$ µA, $E_{ma}$ and $E_{mc}$ values were within the range of water window of the electrode. For $I_c = I_a \geq 400$ µA, $E_{mc}$ and $E_{ma}$ are out of range of water window. So, max CIC at $I_c = I_a = 400$ µA is calculated as 0.2263 mC/cm$^2$